NATIONAL INSTITUTE FOR FUSION SCIENCE

Proceeding of A3 Foresight Program Seminar on Critical Physics Issues Specific to Steady State Sustainment of High-Performance Plasmas 19-22 May, 2015, Chuncheon, Korea

Edited by Yeong-Kook OH, Shigeru MORITA and Liqun HU

(Received - Jun. 6. 2016)

NIFS-PROC-100

Jul. 25. 2016

Proceeding of A3 Foresight Program Seminar on Critical Physics Issues Specific to Steady State Sustainment of High-Performance Plasmas

19-22 May, 2015, Chuncheon, Korea

Edited by

Yeong-Kook OH, Shigeru MORITA and Liqun HU

Abstract

The A3 Foresight Program titled by "Critical Physics Issues Specific to Steady State Sustainment of High-Performance Plasmas", based on the scientific collaboration among China, Japan and Korea in the field of plasma physics, has been started from August 2012 under the auspice of the Japan Society for the Promotion of Science (JSPS, Japan), the National Research Foundation of Korea (NRF, Korea) and the National Natural Science Foundation of China (NSFC, China). The main purpose of this project is to enhance joint experiments on three Asian advanced fully superconducting fusion devices (EAST in China, LHD in Japan and KSTAR in Korea) and other magnetic confinement devices to solve several key physics issues on steady state sustainment of high-performance plasmas. The sixth seminar on the A3 collaboration, as the seventh meeting of A3 program, was held in Chuncheon, Korea, 19-22 May 2015, which was hosted by National Fusion Research Institute, to check joint research results achieved during the past three years and to discuss the future plan. Newly proposed collaborative research was also encouraged as well as the participation of young scientists. The topics in the seminar include steady state sustainment of magnetic configurations, edge and divertor plasma control and confinement of alpha particles.

Key words: superconducting fusion device, magnetic confinement, toroidal plasmas, high-performance plasmas, steady state sustainment, edge plasma, divertor plasma, edge stability, high-energy particle, alpha particle and fusion plasma simulation.

Organization Committee

Yeong-Kook OH (National Fusion Research Institute, Korea)

Shigeru MORITA (National Institute for Fusion Science, Japan)

Liqun HU (Institute of Plasma Physics, Chinese Academy of Sciences, China)

Program Committee

Yeong-Kook OH (National Fusion Research Institute, Korea)

Shigeru MORITA (National Institute for Fusion Science, Japan)

Liqun HU (Institute of Plasma Physics, Chinese Academy of Sciences, China)

Youngmu Jeon (National Fusion Research Institute, Korea)

Conference Secretariats

Noh-Yeong OH (National Fusion Research Institute, Korea)

Hideoi HOSOKAWA (National Institute for Fusion Science, Japan)

Shaohua DONG (Institute of Plasma Physics, Chinese Academy of Sciences, China)

Preface

Steady-state sustainment of high-performance plasmas is one of the crucial issues needed to be addressed for fusion reactor development. To enhance close collaborations among scientists in three Asian countries (China, Japan and Korea), A3 foresight program on Plasma Physics started from August 2012 under the auspice of JSPS (Japan), NRF (Korea) and NSFC (China). The main purpose of this project is to solve several key physics issues through joint experiments on three Asian advanced fully superconducting fusion devices (EAST in China, LHD in Japan, KSTAR in Korea) and other magnetic confinement devices to carry out multi-faceted and complementary physics researches.

The first meeting of A3 foresight program on Plasma Physics hosted by NFRI (Korea) was held in Jeju Island, Korea on 22nd August, 2012 as coordinator meeting to initiate the A3 program. As a result, the first seminar hosted by NIFS (Japan), the second seminar hosted by ASIPP (China), and the third seminar hosted by NFRI (Korea) were held in Kushiro, Japan during 22-25 January, in Beijing, China during 20-23 May, and in Gyeongju, Korea during 3-4 November, respectively, in 2013. Concrete planning of collaborative research was made and possible scientific progresses done in steady state sustainment of high-performance plasmas were discussed. Also, many young scientists were joined in these seminars. The fourth seminar hosted by NIFS and the fifth seminar hosted by ASIPP were held in Kagoshima, Japan during 23-26 June in 2014, and in Nanning, China during 6-9 January in 2015, to discuss achievements and summarize intermediate report within the A3 scientific framework.

The sixth seminar as the seventh meeting, hosted by NFRI (Korea), was held in Chuncheon, Korea during 19-22 May, 2015 to continuously report the progress and achievement in on-going A3 collaboration. In total 48 participants attended in this seminar (13 from China, 14 from Japan, and 21 from Korea) and 44 scientific reports were presented for five categories; I. Steady state sustainment of magnetic configurations, II. Edge and divertor plasma control (IIa. Transport of edge and divertor plasmas and IIb. Stability of edge plasma), III. Confinement of alpha particles and IV. Theory and simulation. Especially, Dr. Keeman Kim (President of NFRI, Korea) and Prof. Hyeon K. Park (Director of KSTAR center in NFRI, Korea) participated in this seminar giving special speeches for the opening.

The seminar was closed with great success, clarifying remarkable progress in researches along A3 program physics subjects and also contributing to the fostering of younger scientists. The organizing and program committees are deeply grateful to all

participants and to strong and continuous support from foundation of three countries (NSFC in China, JSPS in Japan, and NRF in Korea), with those support and corporation the seminar was smoothly and successfully concluded.

Yeong-Kook OH, Shigeru MORITA, and Liqun HU
Chairpersons of the Organizing Committee

Contents

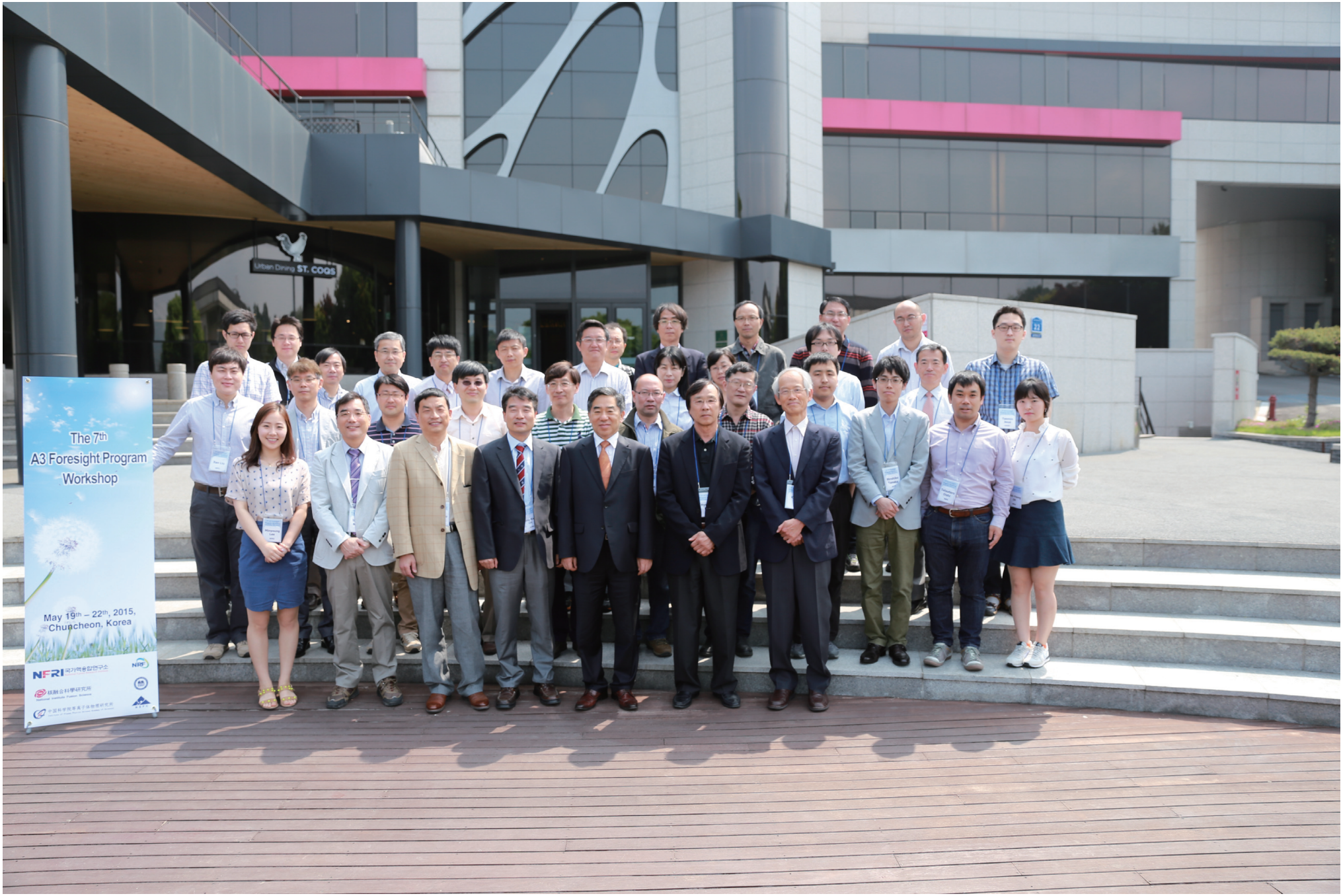
Urban Dining ST. COQS
The 7th
A3 Foresight Program
Workshop
May 19th – 22th, 2015,
Chuncheon, Korea
NFRI 국가핵융합연구소
NRF

Chinese Achievements in the A3 Program

Liqun Hu, on Behalf of Chinese Principal Investigators and researchers

lqhu@ipp.ac.cn, Institute of Plasma Physics, Chinese Academy of Sciences

The implementation process focused on the international frontier requirements of the subjects and followed a goal-limitation and key-breakthrough principle based on the domestic existing foundation. Great importance was attached on the combination between theoretical and numerical simulation and physical experiment research. Enthusiasm and specialty were fully stimulated in domestic partners by cooperating closely with the scientists of other universities and research institutes to improve physical research level, share joint research results, and successfully complete the planned tasks.

Following research work has been mainly carried out: 1) Experimental research of steady-state discharge of high-performance plasma; 2) A variety of lithium wall processing and recycling control technology; 3) Edge localized modes (ELM) mitigation; 4) Mechanism research of the L－H transition physics; 5) Current drive and profile control; 6) MHD instability and its dynamics; 7) Experimental and theoretical research of high-energy runaway electron dynamics.

1. Important progress of collaborative research work since being funded

During the project implementation, based on the advantages of heating technology, diagnostic techniques and data analysis at home and abroad, we learned from each other and improved together by a variety ways of communication. We made great progress and obtained rich fruits on many internationally advanced subjects, such as long pulse high confinement model physics, ELMs mitigation, high-energy runaway electronic behavior and simulation, resonant magnetic perturbation (RMP) field penetration and advanced key diagnostic system studies. The project team completed a number of experimental and theoretical researches at internationally frontier level, the main achievements of which were discussed at international conferences many times and published or prepared to publish in major journals home and abroad. Some important results, such as the progress on steady-state high-temperature plasma and high-performance H mode, etc., were reported in the most important world fusion energy conference and have drawn great attention and recognition among domestic and foreign counterparts. Since the project execution, a total of 41 SCI articles in major fusion journals have been published which were marked clearly with project grant number.

The technological breakthroughs and scientific innovation have been obtained:

1) EAST Tokamak firstly achieved in the world 411-second high-temperature

divertor plasma which gets close to steady-state maintenance, 35-second long-pulse H mode and 28-second high performance long pulse H mode.

2) It was found in the steep pressure gradient of edge transport barrier exists an electrostatic quasi coherent model (ECM), which drives particles transport and heat transport in continuous radial outwards direction, and plays an important role in maintenance of the long pulse H mode.

3) It was found that lower hybrid wave produces helical current in plasma edge, which changes magnetic topology, affects edge heat flow deposition, and has an inhibiting or mitigating effect on ELMs similar to RMP.

4) A variety of lithium wall processing technology was developed, which has been successfully used in achieving boundary recycling control.

5) The heat load in divertor target plate was dispersed by supersonic molecular beam injection and divertor impurity gas puffing under the heating of lower hybrid wave.

6) ELMy H mode was successfully mitigated on EAST by respectively applying deuterium pellet injection, lithium pellet injection, supersonic molecular beam injection, lower hybrid power modulation and resonant magnetic perturbation.

The smooth implementation of the project has rapidly improved the understanding and development of subject "key physical studies of high-performance plasma steady maintenance", promoted the level of domestic existing tokamak plasma physical research and engineering technology, and will accelerate physical experiment research of high-performance plasma steady maintenance in EAST over next several years. It will play a pivotal role in the pre-research for ITER construction and the maintenance of leading position in international related research.

2. The milestones achieved

1) EAST Tokamak firstly achieved in the world 411-second L-mode divertor plasma which gets close to steady-state maintenance and 35-second long-pulse H-mode plasma.

The elaborate control of the peak heat flux of divertor target plate, low particle recycling and impurity production, as well as the stability of plasma density contributed to the achievement of long-pulse high-performance quasi-steady-state plasma in EAST. The thermal load of the first wall was relieved by Li coating in advance and real-time Li powder dusting on the wall, high-intensity divertor exhausting to effectively control particle flux and recycling, active water cooling to minimize divertor thermal load, together with precise controlling of plasma shape and periodic scanning striking-point location. A series of key techniques, such as effective fueling and coupling of lower hybrid wave and plasma, were implemented. Eventually it was achieved repeatable 400-second more L-mode divertor plasmas under full drive

of lower hybrid wave, with $2 \times 10^{19} m^{-3}$ center plasma density and higher than twenty million degree center electron temperature. Under the conditions of low recycling with lithium wall processing and edge pedestal maintaining, lower hybrid wave drive and ion cyclotron resonance heating were applied to control current profile. EAST realized a long pulse H mode with good confinement performance and more than 30-second stable repetition, in which the confinement improvement factor $H_{98\,(y,\,2)}$ was close to 0.9 [1, 2].

2) EAST Tokamak obtained 28-second long-pulse high-performance H mode.

To realize steady operation of high-confinement plasma is an important scientific goal of EAST Tokamak, and also a difficult issue that requires verification before ITER conducting experiment. In 2014, EAST tokamak received overall upgrading: doubling auxiliary heating power, installing ITER-type tungsten/copper divertor and many systems such as resonance helical magnetic field controlling coils, which greatly extended EAST operation region and control capability, and further improved plasma performance and quality. With a newly-built 4.6Hz lower hybrid wave system, 28-second high-performance long-pulse H mode (about 200 times energy confinement time) was achieved through regulating the EAST plasma current distribution, in which the energy confinement improvement factor $H_{98\,(y,\,2)}$ topped 1.2, center electron temperature reached 3keV, and the peak heat load on divertor target plate was relieved to $3MW/m^2$ with 25 kHz long time edge coherence mode (ECM) and small-amplitude ELM [3].

3) EAST obtained high-temperature plasma close to 50 million degrees and realized full wave drive of 450kA plasma current.

In 2014, wave reflection was reduced and better wave and plasma coupling was achieved through plasma configuration optimization and puffing at the mouth of lower hybrid wave antenna. The maximum injection power of 4.6 GHz lower hybrid wave was 3.5 MW (corresponding refractive index $N_{//}^{peak}$ close to 2.04). Full wave drive of 450 kA plasma was realized. The current drive efficiency of lower hybrid wave reached $\eta_{CD} \sim 1.1 \times 10^{19} Am^{-2}W^{-1}$ and wave reflection power was less than 3%. Location of current drive of lower hybrid wave and electron heating were close to the core, the highest electron temperature of which reached 4.5 keV (50 million degrees) measured by Thomson scattering. Meanwhile, with 2.4MW energetic neutral beam injected into 500 kA plasma, the H mode with first-type ELM was obtained, in which normalized specific pressure β_N reached 1.8 with the highest up to 2 ($\beta_p \sim 1.3$), plasma energy storage reached 200 kJ, H_{98} topped 1.2, the loss of the plasma energy storage caused by single ELM collapse amounted to 10%, and the heat load of divertor target plate exceeded 10 MW/m^2 [3].

4) Helical current band was produced by lower hybrid wave in plasma

boundary, which changed boundary magnetic topology, affected boundary heat flow deposition, and had inhibiting or mitigating effect similar to RMP on ELM.

The H mode with first-type ELM had high confinement capability, but ELM collapse caused abundant heat load and particle load transiently depositing on divertor target plate and the wall surface. Single energy loss of first-type ELM in ITER was close to 20 MJ, and the number must be reduced 20 times to avoid material destruction. Therefore, it becomes the most popular topic at present in fusion field to find reliable target plate heat load dispersion method. In EAST experiment, it was found that Lower hybrid wave produced current belt along magnetic line in the scrape-off layer area of plasma boundary. Numerical simulation showed that the current belt in the pedestal area could arouse Gaussian-scale magnetic disturbance, resulting in a big change of magnetic topology of the plasma boundary and leading to hit point bifurcation outside the divertor target plate surface, which were verified by divertor target plate probe, infrared camera and retarding field energy analyzer. Meanwhile, EAST experiment showed that Lower hybrid wave could reduce divertor peak heat flow and particle flow caused by outbreak of ELMs. Compared with the resonance magnetic perturbation coil (RMP), the helical current belt driven by lower hybrid wave was distributed along the magnetic line of scrape-off layer all the time, which did not depend on the relatively narrow boundary safety factor resonance window. This discovery will probably set up a new ELM control method, which is of great significance to ITER [4, 5].

5) A variety of lithium wall processing technology was developed, and boundary recycling control was successfully realized.

As ion cyclotron resonance frequency (ICRF) heating is the main heating method in EAST, it is vitally important for the EAST to control hydrogen-deuterium ratio control under 10%. After years of exploration, EAST has successfully developed a variety of effective Lithium wall processing technology, i.e. Lithium granule injection. The results showed that: one-time Lithium injection could effectively inhibit the amount of H_2O, N_2 and O_2 in the vacuum chamber; continuous Lithium injection could reduce the hydrogen-deuterium ratio below 10%, and boundary recycling could significantly decreased as lithium particles accumulated; real-time lithium injection was beneficial to improve the quality of plasma. Real-time Lithium injection for a long time could help to repair the damage to the wall caused by long-pulse plasma, control plasma corrosion to the first wall, reduce tungsten sputtering and effectively control recycling. With real-time Lithium injection, EAST obtained 18-second quasi steady-state H mode without ELMy (far exceeding the current diffusion time). The main parameters of plasma were steady, boundary radiation was increased, and the peak heat load of target board caused by ELMs was greatly reduced to far less than $2MW/m^2$. It would be a very promising long-pulse high-confinement plasma

operation mode [3].

6) The physical research of long-pulse ELM H mode made important progress.

Further study indicated that EAST long-pulse H mode depended mainly on the following factors: 1) The Wall evenly coated with Lithium effectively reduced boundary recycling, inhibited impurity regurgitation, and benefited the control of density in a stable level; 2) Lower hybrid wave heating and current drive would change the boundary magnetic topology, open a new energy removal channel, and effectively reduce peak heat flow of the target plate; 3) Optimization of plasma configuration and parameter helped EAST to work in the operation range which was beneficial to produce small-scale ELM; 4) The use of the powerful internal cryogenic pump was advantageous to effective expelling of the particles in the long pulse; 5) In the steep pressure gradient zone of boundary pedestal existed boundary quasi-coherence mode which could transport particles and heat outwards so that the pedestal height would not increase to produce large amplitude ELM. At the same time, parallel flow played an important role in particle transport of scrape-off layer and divertor asymmetry; under the condition of ELMy H mode, the deposition width scaling of divertor target plate heat flow did not rely on plasma configuration, in an anti-dependence relation with plasma current; the boundary scrape-off layer width of radio frequency wave heating H mode in the low density operation area was greater than that of neutral beam heating. These results have directive significance in active control of divertor heat flow in advanced steady operation [2, 4, 6, and 7].

7) Multiple ways of ELM moderation

ELMs were successfully relieved in EAST by applying deuterium and lithium pellet injection, supersonic molecular beam injection and lower hybrid wave modulation, with burst frequency increased and amplitude reduced. Lower hybrid wave frequency modulation stimulated high-frequency small-scale ELM, the frequency of which synchronized with lower hybrid wave frequency modulation. Plasma confinement and energy-storage capacity did not drop significantly with modulation. When the modulation of lower hybrid wave increased over 50Hz, the stimulated ELM range decreased obviously compared with usual ELM. Supersonic molecular beam injection could increase the frequency of ELM 5 to 10 times, and inhibited ELM range. Resonance perturbation of magnetic field increased ELM frequency 5 times, the collapse amplitude of boundary temperature and particle flow of target plate decreased about five times. At the same time, with the density expelling effect, fuel pellets successfully triggered H mode without ELM, the frequency of which reached 300Hz. Lithium pellet injection realized the PACE of ELMs [3, 5].

8) Research of MHD instability and its dynamics

In the EAST tokamak metal wall operation, large amount of inherent high-Z

impurities gathered around the core, resulting in the change of electron temperature distribution and sharp cooling of core plasma, which greatly affected plasma confinement. The primary research indicated that: 1) Inherent high-Z impurities gathering around the core produced internal kink mode, leading to large-scale distortion of 3D magnetic profile, damaging magnetic profile structure and affecting plasma performance; 2) The inherent high-Z impurity density gradient stimulated 1/1 mode of larger poloidal size, producing high toroidal rotating damping which was difficult for Tokamak to tolerate; 3) When large sawtooth collapsed, impurity mode would couple with lower beta plasma, generating farther-away 2/1 NTM and bringing worse influence on energy confinement. 4) Large amount of impurities around the core had strong modification effect on core magnetic shear. The snake-like oscillation stimulated by impurities in H-L-H conversion plasma would be destabilized under particular impurity concentration threshold, producing high damping to toroidal rotation in the plasma core. These destabilization of macroscopic MHD instability can effectively avoid impurity gathering around the core, and has important significance on the metal wall tokamak operation under the condition of H mode.

9) The research of L-H conversion physical mechanism made important progress

L-H conversion middle oscillation dynamics was studied with fast-scanning probe, finding the synergistic effect between zonal flow and equilibrium flow driven by plasma turbulence during L-H conversion; gas-puff imaging diagnostic showed that the poloidal flow driven by turbulent flow took effect in L-H conversion. In the L-H conversion middle oscillation state, the turbulent flow in plasma boundary decreased and bursted, providing power for turbulent flow's transport to poloidal flow and eternally driving poloidal flow. In the boundary transport steep gradient zone of H mode, a kind of 300 kHz high frequency quasi-coherent mode was detected, which did not depend on auxiliary heating, and probably was a main unsteady mode in the limiting boundary transport barrier pressure gradient in EAST relatively highly collided H mode plasma; a variety of enhanced recycling H mode with multiple boundary quasi coherent mode under the conditions of lower hybrid wave, ion cyclotron resonance heating and neutral beam heating.

10) Current drive and profile control research

Based on effective inhibition of boundary recycling and maintenance of boundary pedestal with Li wall processing technology, the current profile was controlled by combining **LHCD and LHCD, ICRF, NBI as well as NBI**, achieving longer-pulse high-performance H mode. Active real-time control of current profile was critically important for obtaining steady-state high-performance Tokamak plasma. In order to accurately measure current profile, both EAST and J-TEXT (Huazhong University of Science and Technology, HUST) developed advanced three waves

multi-channel polarization interferometer (POINT) diagnostics, which successfully obtained equilibrium profiles such as current density and electron density profile, etc. by measuring Faraday rotation angle and reconstructing plasma magnetic equilibrium. J-TEXT conducted studies in RMP field penetration, density sawtooth with its advanced diagnostics. In 2014, under collaboration with HUST, 11ch. POINT system was constructed in EAST, data processing & feedback control algorithm in the PCS framework completed and off-line real-time current density distribution successfully achieved. In 2015 summer EAST campaign, such algorithm will be used in the current density feed-back distribution in LHCH and ECRH plasmas.

11) Theoretical calculation and numerical simulation research.

By combining of international cooperation and independent research, we developed a wide variety of computing simulation programs, carried out data analysis and experiment prediction work, built up computer simulation platform for radio frequency wave heating and current drive, and conducted comparing simulation study of lower hybrid wave discharge under different densities in EAST by using the ray tracing program GENRAY, full wave program TORLH and CQL3D (Fokker - Plank program); With coupled transport program ONETWO and GENRAY, we simulated and analyzed EAST lower hybrid wave experimental data. Based on geometric theory, we constructed advanced volume algorithm which could be applied to the research of runaway electron dynamics multi-scale problems, ensuring the accuracy and stability of long-term numerical simulation; and also investigated runaway electron phase space dynamics evolution process and neoclassic drift process through dynamics simulation research for a long time. With MEGA program we simulated fishbone mode motivated by high-energy particles from EAST neutral beam injection, finding that the toroidal precession resonance of high-energy electrons stimulated fishbone mode with the frequency of 3 kHz propagating against direction of toroidal current and mainly within the q = 1 surface, which was consistent with the soft X-ray diagnostic result in the EAST core.

3. Personnel training

Through joint experiment, academic exchanges and international cooperation, we expanded the breadth and depth of foreign cooperation and exchanges, and increased the level of independent innovation and scientific research of a large number of youth talents. Many doctors and masters learned quickly in cooperation and exchanges, which played a great role in promoting the study of key physical problems and substantial progress. Until now, our two young people finished doctoral and post-doctoral studies in Japan and returned to ASIPP. Three of our talented youth were invited to Japan for PhD degree. A number of outstanding young plasma scientists and senior engineers gradually stepped onto the stage of international fusion

research and have aroused the concern of international fusion experts.

Through lectures, academic research and participation in the experiment, our team has invited internationally well-known professors and experts in fusion energy field to visit China many times. Obvious progress have been made in neutral beam injection device, high-energy particle diagnostics, extreme ultraviolet spectrum imaging, 2D X-ray and microwave imaging technology, and also numerical simulation study of boundary plasma transport by introducing a number of advanced key technology and procedures.

Until now, totally 41 SCI articles marked with project grant number were published in Chinese side. Many people participated in large and medium-sized international academic conferences. The academic communication meeting between China, Japan and South Korea was held six times, the details of which are as follows. Moreover, five doctors and three masters graduated. Two students won respectively 2014 dean excellence award of Chinese academy of sciences, and 2014 Dr Zhu Li Yuehua outstanding graduate award of University of Chinese Academy of Sciences.

4. Summary

In order to fundamentally improve plasma performance and parameters, EAST Tokamak has conducted comprehensive upgrading since 2013. The divertors in EAST were upgraded to ITER-type tungsten ones so as to substantially increase divertors' heat removal and anti-sputtering capability. Modularized divertor structure posed unprecedented challenge to material, technology and manufacturing. Because of the manufacturing difficulty of high-power steady-state electron cyclotron tube as well as delivery delay from foreign suppliers, ECRH physical experiment was put off until 2015 EAST summer campaign. At present EAST works smoothly in all aspects and starts to conduct physical experiment in April. The experiments of present project will run smoothly as expected.

Acknowledgments

The author would like to thanks all contributors both in domestic and international facilities for their great efforts to this A3 project. This work is undertaken partially under the support of the JSPS-NRF-NSFC A3 Foresight Program in the field of Plasma Physics (NSFC No.11261140328 and NRF No. 2012K2A2A6000443).

References

[1] Nature Phys. 9 (2013) 817.

[2] H.Y. Guo, J. Li, X.Z. Gong, B.N. Wan, et al., "Approaches towards long-pulse divertor operations on EAST by active control of plasma–wall interactions", Nuclear Fusion 54 (2014) 013002.

[3] B.N. Wan for the EAST team and collaborators, "Advances in H-mode Physics for Long Pulse Operation on EAST", 25th IAEA Fus. Energy Conf., Saint Petersburg,

Russian Federation, 0V/3-3, Oct.2014.
[4] H. Y. Guo, J. Li, B. N. Wan, X. Z. Gong, et al., “Recent advances in long-pulse high-confinement plasma operations in Experimental Advanced Superconducting Tokamak”, Phys. Plasmas 21 (2014) 056107.
[5] L. Wang, J.Nucl. Mater., 2014, in press.
[6] L. Wang, H.Y. Guo, G.S. Xu, S.C. Liu, et al., “Scaling of divertor power footprint width in RF-heated type-III ELMy H-mode on the EAST superconducting tokamak”, Nuclear Fusion 54(2014) 114002.
[7] L. Wang, G.S. Xu, H.Y. Guo, H.Q. Wang, et al., “Characterizations of power loads on divertor targets for type-I, compound and small ELMs in the EAST superconducting tokamak”, Nuclear Fusion 53(2013) 073028.

Extended LHCD Capability towards Steady-State Plasma in EAST

B J Ding, F K Liu, J G Li and B N Wan **for LHCD group, EAST team and collaborators**

Institute of Plasma Physics, Chinese Academy of Sciences, Hefei 230031, P. R. China

Email: bjding@ipp.ac.cn

Abstract In addition to 2.45GHz/4MW lower hybrid current drive (LHCD) system, a 4.6GHz LHCD system has been firstly commissioned in EAST in 2014 campaign. First LHCD results with 4.6GHz show that LHW can be coupled to plasma with low reflection coefficient, drive plasma current, modify plasma current profile, and heat plasma effectively. Also, CD efficiency and current profile depend on the launched wave spectrum, suggesting the possibility of controlling current profile by changing phase difference. Repeatable H-mode plasma is obtained by either 4.6GHz LHCD system alone, or together with the 2.45GHz LHCD system, the NBI (neutral beam injection) system.

1. Introduction

Lower hybrid current drive (LHCD) [1–3] plays a key role in controlling current profile in tokamak experiments aimed at achieving important goals relevant to fusion plasma. For steady-state plasma with LHCD in EAST [4], high LH power is necessary. Also, at high density, LH wave with higher frequency is preferred so as to avoid the interaction between LH wave and ions. To obtain EAST scientific goal (long pulse and high performance), a new LHCD system (4.6GHz/6MW, CW), which consists of 24 klystrons, has been installed in EAST and commissioned in 2014. Up to now, together with 2.45GHz/4MW LHCD system, the total available LHCD power is up to 10MW in EAST. For the 2.45GHz system, many LHCD results have been reported[5, 6-11], including coupling and current drive at different conditions.

In this paper, the preliminary experimental results with 4.6GHz system and some investigations are presented, in which the toroidal magnetic field (B_t) is about 2.3T.The working gas is with deuterium (D_2) and usual configuration mentioned in this paper is lower single null (LSN).

2. Description of 4.6GHz LHCD system

In EAST, the 4.6GHz LHCD system consists of power supply, klystrons (total 24), transmission line (circulator, directional coupler, ceramic windows, waveguide, etc), and antenna. LHW from micro-wave source to transmission line is launched into the tokamak plasma by a multi-junction grill [12, 13] type of antenna with 24 modules arranged in an array of 4 rows and 6 columns. Each module (main waveguide), supplied by one power system, is divided into 3 sub-rows in poloidal direction and, in each sub-row, consists of 8 active sub-waveguides between which there is a 90^0 phase difference generated by a built-in phase shifter, which is composed of quarter wavelength step transformers and a straight waveguide with reduced height. In each sub-row of the launcher, there are 7 passive waveguides inserted between the adjacent

main waveguides. Therefore, the whole launcher is composed of 660 sub-waveguides (576 active and 84 passive sub-waveguides). The height and the width of each sub-waveguide are 5cm and 0.6 cm for wave propagation, respectively. The system is cooled by water during the operation. The calculated power spectrum by a linear coupling code ALOHA [14] is displayed in Fig.1, where $N_{//}^{peak}$ is the peak index of parallel refraction of the launched wave. The power spectrum of launched waves can be adjusted by changing the phase difference ($\Delta\Phi$) between the adjacent main waveguides from -180^0 to 180^0.

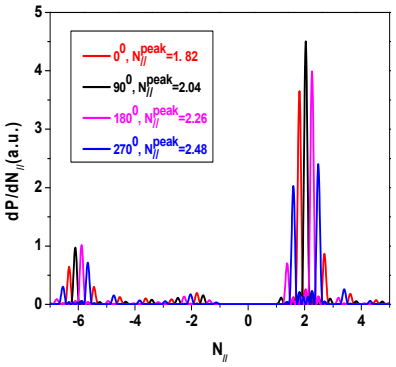

Fig. 1 Power spectrum (4.6GHz antenna) calculated by ALOHA code

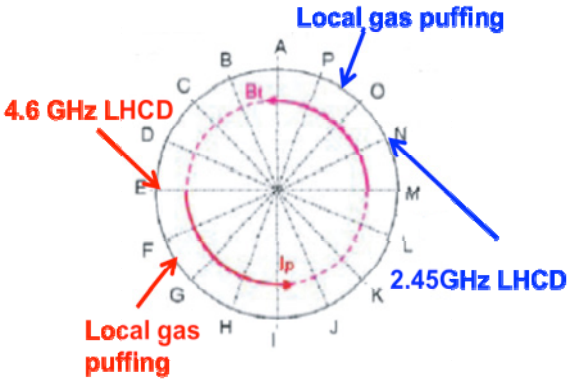

Fig. 2 Top view of ports of local gas puffing and LHCD antenna (the directions of Ip and Bt are indicated)

3. LHW-plasma coupling experiments

In EAST, LHW antenna with 4.6 GHz and 2.45GHz are installed in E port and N port (see Fig. 2), respectively. In order to improve LHW–plasma coupling for 2.45GHz and 4.6GHz LHW as shown in Fig. 2, two local gas pipes covering the whole grill in the poloidal direction have been installed at the electron-drift side of the LHW antenna for the new campaign, between the port of O and P port, and F and G port in EAST, respectively. The layout of the top view is shown in Fig.2, in which the direction of plasma current (Ip) and toroidal magnetic field (Bt) are also shown. The major radius of the pipe location is about 2400 mm and the radial position of LH antenna is about 2355mm in routine experiments.

First of all, the coupling experiments with and without local gas puffing with the typical phase difference of 90^0 between the main waveguides are performed in EAST. Coupling characteristics by means of the reflection coefficient (RC) and grill density measurements are shown in Fig. 3, where the grill density (n_{e_grill}) is measured by a Langmuir probe installed on the top of the LH antenna, and cut-off density (n_{e_co}) is also plotted. It is shown that with a grill density larger than the cut-off density, RC is relative low (~6%), whereas RC increases quickly when the density is below the cut-off value. The reflection coefficient without local gas putting is higher than that with local gas puffing, implying that the good coupling is obtained by the local gas puffing. The coupling characteristics between L-mode and H-mode are also compared in Fig. 4, showing that, though the RC in H-mode is higher than that in L-mode, its level remains acceptable and does not much affect the coupling.

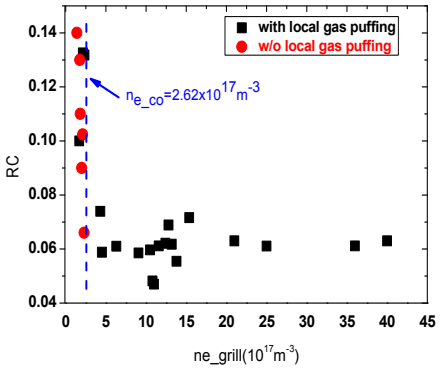

Fig. 3 Coupling characteristics of 4.6GHz LH antenna with/without local gas puffing

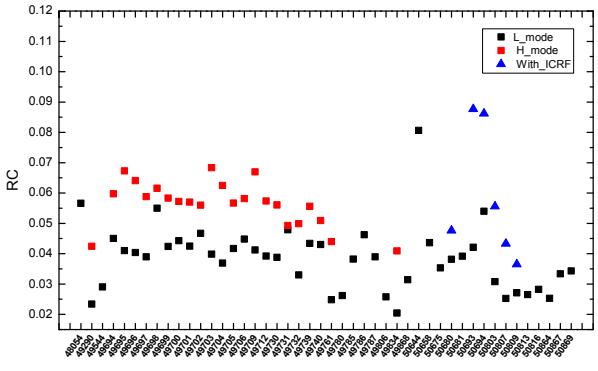

Fig. 4 Coupling characteristics comparison between L-mode and H-mode

Typical waveform (with phase difference of 90^0) including coupling and current drive are shown in Fig.5, indicating that good coupling is obtained by means of local gas puffing and configuration optimization. The maximum power of coupled to plasma is up to 3.5MW in this campaign, suggesting that by means of configuration optimization and local gas puffing, LHW can be effectively coupled into plasma with the present system.

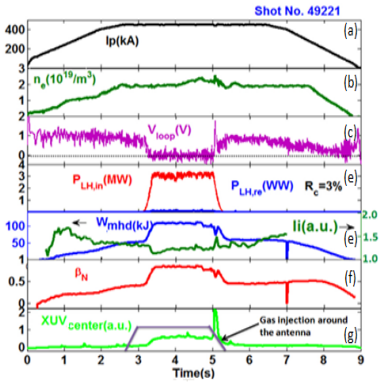

Fig. 5 Typical waveform of coupling, current drive and plasma heating

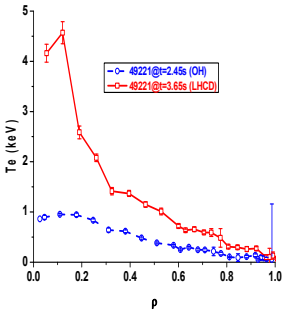

Fig. 6 Te profile measured with Thomson scattering system

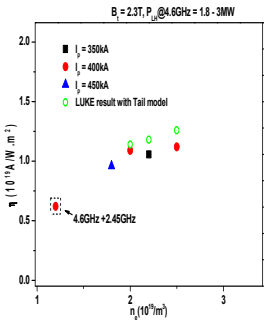

Fig. 7 Experimental and simulated CD efficiency with 4.6GHz LHCD system

4. Experiments of current drive and plasma heating

As shown in Fig.5, the loop voltage decreases quickly to zero approximately, meaning that LHW can drive plasma current effectively. Also, the energy increase from 50kJ to 100kJ and normalized beta increases from 0.4 to 0.8 due to LHCD, suggesting that LH power is effectively coupled to plasma and fully transferred plasma. In addition, the internal inductance (li) decreases after LHCD is applied compared to Ohmic plasma, implying the plasma current profile is broadened by the application of the LH wave.

The electron temperature profile measured by Thomson scattering (TS) [15] is plotted in Fig.6.As compared to the Ohmic plasma, the electron temperature increases much during the LHCD phase and the temperature in core region increases from 1.0keV to

4.5keV, suggesting that plasma is effectively heated by LHW by mean of slowing down of fast electrons and that LHW is mainly deposited in core region.

In the experiments, fully driven current plasma is obtained with different plasma current, which is very convenient to investigate the CD efficiency since we do not need to consider the effect of the Ohmic electric field. Assuming the absorption efficiency of LHW power is 75%, the estimated CD efficiency is shown in Fig. 7. It shows that the CD efficiency is up to $1.1\times10^{19}Am^{-2}W^{-1}$,which is a little higher than that of 2.45GHz LHW [7]. The experimental CD efficiency is weakly evolving with the electron density, which is consistent with the calculated estimate from C3PO/LUKE code shown in Fig. 7 [16]. In the simulation, the experimental parameters and tail model [17] referring to considering broadened spectrum are used.

5. Effect of power spectrum on current drive

To explore long pulse and high performance with LHCD, high current drive efficiency and the capability of controlling current profile are necessary. The related experiments are carried out with toroidal different phase difference ($\Delta\varphi=0^0$, 90^0, 180^0, -90^0) between the main waveguides in EAST, and correspondingly the calculated launched wave spectrum was shown in Fig.1. The target plasmas and plasma configurations, which are kept the same, were displayed in Fig. 8, in which Ip, the distance between the two magnetic surfaces passing through the upper X-point and the lower X-point in the mid-plane in low field side (Drsep), n_e, P_{LH_in}, and $P_{LH_re}$are plotted from (a) to (e). In the experiments, Drsep>0, =0, and <0 means upper single null (USN), double null (DN) and lower single null (LSN), respectively.

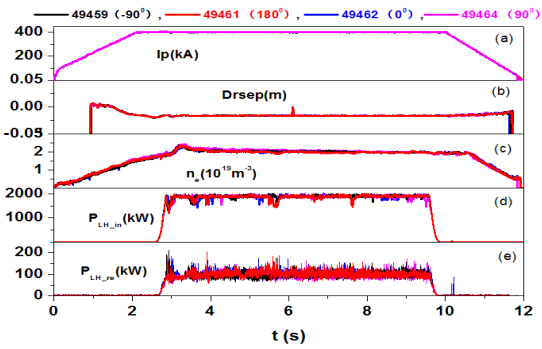

Fig. 8 Target plasmas for effect of power spectrum on current drive

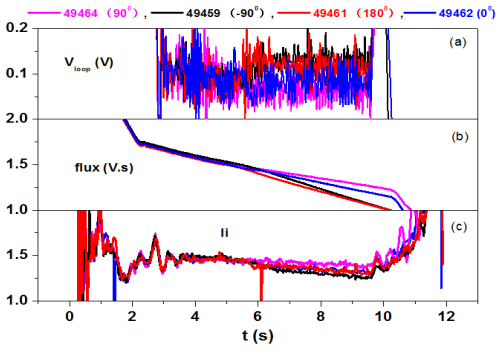

Fig. 9 Effect of spectrum on CD efficiency and current profile

Loop voltages and consumptions of magnetic flux (flux) plotted in Figs. 9 (a) and (b), are the key parameters to investigate the effect of spectrum on CD efficiency, since the total plasma current is feedback controlled by the Ohmic heating power. As shown from Fig.9, though the differences between the various phasings are rather small, the loop voltage is the lowest with $\Delta\varphi=90^0$, which is consistent with the smallest consumptions of magnetic flux, suggesting the highest CD efficiency in this case. The internal inductance is shown in Fig. 9 (c). The value of li is the largest with $\Delta\varphi=90^0$, whereas it is the lowest for $\Delta\varphi=-90^0$, implying the most peaked current density profile with $\Delta\varphi=90^0$.

Note that present differences in loop voltage, consumptions of magnetic flux and li between the cases are not obvious, possibly because the temperature of target plasma is a little low. This could be improved by means of increasing electron temperature, hence enhancing the single pass absorption efficiency. Anyway, above results that current profiles are different with different $\Delta\rho$ indicates the possibility of profile control by change the wave spectrum as shown in previous LH experiments in many tokamaks [18-23]. Further experiments will be continued with hotter target plasma, e.g., preheated with 2.45GHz LHW, ECRH (electron cyclotron resonance heating), or NBI (neutral beam injection).

6. H-mode plasma with LHCD

To obtain long pulse and high performance plasma, various heating systems are used in EAST, including LHCD, NBI and ion cyclotron radio frequency (ICRF). Based on the above experiments, repeatable H-mode plasmas [24] are obtained by either 4.6GHz LHCD system alone, or together with 2.45GHz LHCD system, NBI system or ICRF system.

Firstly, with the injected LH power of 2.8MW, the longest H-mode plasma with grassy (very small or free) edge localized mode (ELM) up to 28s obtained by 4.6GHz LHCD system alone is shown in Fig. 10, in which Ip, n_e and V_{loop}, P_{LH_in} and P_{LH_re}, W_{mhd} and β_N, and D_a are plotted in (a)-(e). It is observed that the loop voltage remains close to zero, stored energy increases to 130kJ, and the normalized beta is about 1.2. From the statistics of the discharges using the LH system at 4.6GHz shown in Fig. 11, the threshold power for L-H transition is about 1MW in the experiments, which is comparable with the H-mode plasmas obtained with the LH system at 2.45GHz[10]. Further comparison between them will be investigated with a same experimental condition later. The lossed power defined as $P_{loss}= P_{LH} + P_{OH} - P_{rad}$ (P_{LH}, P_{OH}, and P_{rad} are the coupled LH power, Ohmic power and radiation power, respectively)roughly evolves as the scaling law $P_{th}=0.042n_{20}^{0.73}B_t^{0.74}S^{0.98}$ (MW)[25],where *S* is the plasma surface area in m^2. The operating window for the H-mode is very narrow, the operation space was not varied very much during the experiments, which is to be extended later.

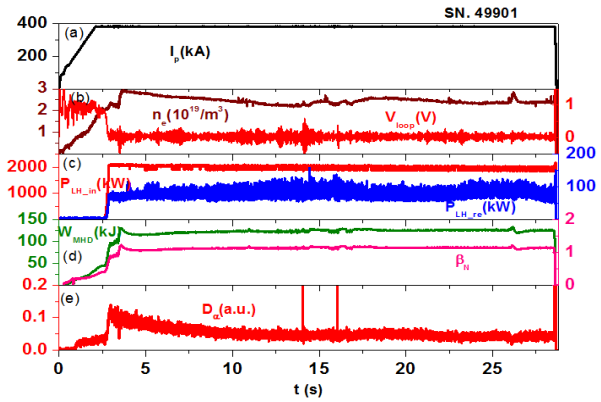

Fig. 10 Typical wave form of H-mode plasma with 4.6GHz LHCD system

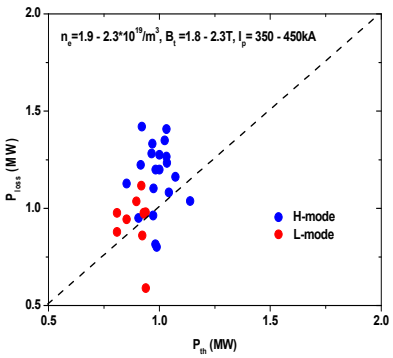

Fig. 11 Threshold power for L-H transition with 4.6GHz LHCD system

Secondly, H-mode is obtained by the LHCD combination of 2.45GHz and 4.6GHz, which is shown in Fig. 12, in which Ip and electron temperature in central region (T_{e0}) measured by Soft X-ray spectrum , n_e and V_{loop}, P_{LH_in}, P_{LH_re}, W_{mhd}, β_N, local gas puffing, and D_a are plotted from (a) to (h), as well as the L-H transition. The H-mode plasma is not observed with the 2.45GHz LH wave alone. A possible explanation is that the LH power injected by this system has not reached the L-H transition threshold. After the application of the LH power at 4.6GHz, the loop voltage decreases somewhat, possibly due to the temperature increase and the additional driven current by LH wave at 4.6GHz. Also, , the electron temperature in core region, the stored energy and normalized beta continue increase after the LH wave application, and then the transition of L-H occurs, indicated the sharp increase in electron density, stored energy and normalized beta, and the sharp decrease in D_a The normalized beta increases from 0.5 to about 1. Around the L-H transition, there is another sharp decrease in loop voltage implying that non-inductive current increases in the H-mode phase, even if the density ($\sim 3.7\times10^{19}m^{-3}$) is much higher than that ($\sim 2.7\times10^{19}m^{-3}$) in the L-mode. This may come from three effects. One is the increase in temperature, which cannot be identified at present due to the time resolution of temperature measurement is not enough. The second is the bootstrap current, which is enhanced due to the pedestal structure. The third is the enhanced CD efficiency, which could be improved by the increased temperature in the edge region due to the pedestal formation. As reported in Ref. 26, high edge temperature may reduce parametric instability behaviour, hence making more waves propagate to core region and enhance CD efficiency. Similar results that higher CD efficiency in H-mode with 2.45GHz LHCD system in EAST have been reported in Refs. 5 and 11. Therefore, high temperature in edge region is expected to improve CD efficiency at high density, e.g., lithium coating or local heating by ECRH in edge region.

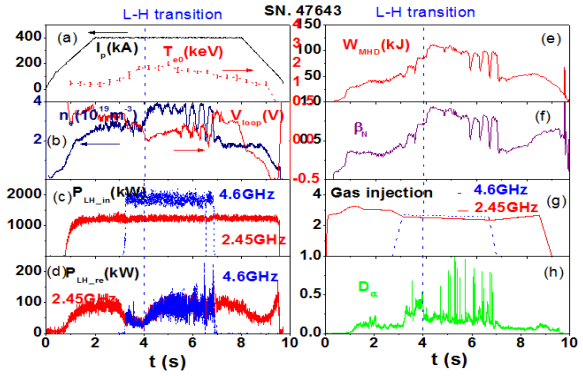

Fig. 12 Typical H-mode with 4.6GHz and 2.45GHz LHCD system

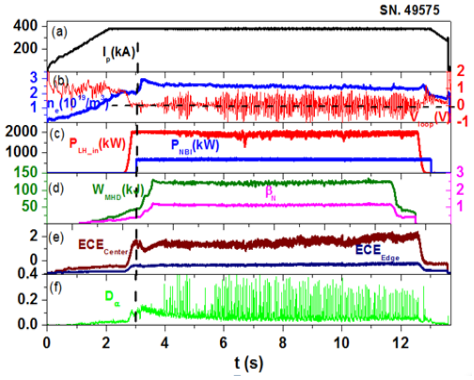

Fig. 13 Typical H-mode with 4.6GHz LHCD and NBI

Lastly, together with NBI system, repeatable H-mode plasmas are also obtained and the typical waveforms are shown in Fig. 13, in which Ip, n_e and V_{loop}, P_{LH_in} and NBI power (P_{NBI}), W_{mhd} and β_N, electron cyclotron emission in core and edge region (ECE_{Center}, ECE_{Edge}), D_a are plotted from (a) to (f). From Fig.13 (d), it is shown that the plasma energy increases to 150kJ when both the LH and NBI power are injected.

Consequently, the normalized beta reaches up to 1.2. From Figs. 13 (b) and (f), during the ELM phase, a large fluctuation in the loop voltage takes place, implying that the current drive is possibly affected by the density fluctuation in the edge region due to ELM burst. Finally, ECE measurements shown in Fig. 13 (e) indicate that the plasma emission is much stronger in the center line than that in the edge region, suggesting that wave remains mainly deposited in the core region, as in the L-mode. This is consistent with the lack of change of the loop voltage during LHCD phase and LHCD plus NBI phase .

By further comparing the D_a signal, ELM behaviors are different between the above three cases (4.6GHz alone, 4.6GHz plus 2.45GHz, and 4.6GHz plus NBI). In the H-mode with 4.6GHz, the ELMs are very small (almost ELM-free regime), possibly due to the small level of the injected power. In the case with LH at 4.6GHz and 2.45GHz, the amplitude of the ELMs is the largest (~0.9) with a frequency about 6~7 Hz. For the H-mode with LH at 4.6GHz plus NBI, the amplitude is reduced to 0.4 with an increased frequency of ~ 20Hz. The difference between the two later cases has no clear explanations yet. It may arise from different H-mode mechanisms between LHCD and neutral beam current drive (NBCD), which will be studied further later. Full time analysis of these discharges must be carried out for this purpose.

7. Conclusion and discussion

A 4.6GHz LHCD system has been firstly installed and commissioned in EAST in 2014. First LHCD results with 4.6GHz shows that LHW can be coupled to plasma with low reflection coefficient, drive plasma current and plasma rotation, modify plasma current profile, and heat plasma effectively, suggesting that it is possible to explore high performance at high density relevant to ITER.

By means of configuration optimization and local gas puffing near the LHW antenna, good LHW-plasma coupling with reflection coefficient less than 5% is obtained. The maximum LHW power coupled to plasma is up to 3.5MW.Current drive efficiency is up to $1.1\times10^{19}Am^{-2}W^{-1}$, which is a little higher than that of 2.45GHz LHW, assuming the absorption efficiency of LHW power is 75%. Plasma is simultaneously effectively heated by LHW and the central electron temperature is above 4keV, suggesting that LH power is mainly deposited in the core region. Experiments show that current profile is effectively modified, which could improve plasma confinement. Also, CD efficiency and current profile is related to launched wave spectrum, suggesting the possibility of controlling current profile by change phase difference with the system if the target plasma is enhanced further, eg., preheated by NBI or ECRH.

Repeatable H-mode plasma is obtained by either 4.6GHz LHCD system alone, or together with 2.45GHz LHCD system, NBI system. The ELM feature of H-modes is different and the related reason is under investigation.

Current drive efficiency with high density (~$3.7\times10^{19}m^{-3}$) in H-mode is higher than that with low density (~$2.7\times10^{19}m^{-3}$) in L-mode. This is possibly because CD efficiency is enhanced by less parametric instability due to the increased temperature in the edge region when the pedestal is formed. If so, CD efficiency at high density could be improved by increasing edge temperature, e.g., lithium coating

or local heating by ECRH in edge region. This could be performed in EAST later.

Acknowledgements:
This work is supported by the National Magnetic Confinement Fusion Science Program of China (Grant No. 2015GB102003, 2013GB106001, 2013GB112003), the National Natural Science Foundation of China under Grant No. 11175206, 11305211 and 11275233, and the JSPS-NRF-NSFC A3 Foresight Program in the field of Plasma Physics (NSFC No. 11261140328). It is partly supported by the China-France Collaboration program.

References:

[1] Fisch N.J. 1978 *Phys. Rev. Lett.* **41**873.
[2] Bernabei S. *et al* 1982 *Phys. Rev. Lett.* **49**1255.
[3] Fisch N.J. 1987 *Rev. Mod.Phys.* **59**175.
[4] Wan Y. X., Weng P. D., Li J. G., *et al*, "Overview progress and future plan of EAST Project" 2004 *21st International Atomic Energy Agency (IAEA) Fusion Energy Conference,* Chengdu, China, OV/1-1.
[5] Ding B. J., et al., 2013 Nucl. Fusion **55** 113027.
[6] Ding B. J. et al., 2012 *Phys. Plasma* **19** 122507.
[7] B J Ding et al., 2011 *Phys. Plasma* **18** 082510.
[8]Zhang L., et al, 2013 *Phys. Plasma***20** 062507.
[9]Kong E. H., et al., 2013*Plasma Phys. Control. Fusion* **55** 065008**.**
[10] Li M. H., et al., 2011 *Chin. Phys. B* **20**125202**.**
[11] Li M. H., et al., 2014 *Phys. Plasmas***21**062510.
[12] Moreau D.and Nguyen T. K., in Proceedings of the International Conference on Plasma Physics, Lausanne, Switzerland, June 27–July 3, 1984, Vol. 1 (1984), p. 216.
[13] Litaudon X. and Moreau D., 1990 *Nucl. Fusion***30** 471.
[14] Hillairet J. et al.,*Nucl. Fusion***50** (2010) 125010.
[15] Zang Q. et al., 2011 *Rev. Sci. Instrum.* **82** 063502**.**
[16] Peysson Y. and the Tore Supra Team 2001 *Nucl. Fusion* **41** 1703
[17] Decker J., et al.2014*Phys. Plasmas*, **21**, 092504
[18] Soldner F. X. et al., 1994 *Nucl. Fusion* **34** 985.
[19] Ide S. et al., 1996 *Plasma Phys. Contr. Fusion* **38** 1645.
[20] Peysson Y. et al., 2001 *Nucl. Fusion* **41** 1703.
[21] Litaudon X. et al., 2001 *Plasma Phys. Contr. Fusion* **43** 677.
[22] Ding B. J. et al., 2007 *Plasma Phys. Contr. Fusion.* **49** 563**.**
[23] Kuang G. L. et al., 1999 *Nucl. Fusion* **39** 1769.
[24] Wan B. N. *et al.,* 25th Fusion Energy Conference, Saint Petersburg, Russia, 13 -18 October 2014, OV/3-3
[25] Doyle E J et al., 2007 *Nucl.Fusion* **47** S18.
[26]Cesario R., et al 2010*Nature Commun*.**55** 1.

Effect of trapped electrons on lower hybrid current drive

Nong Xiang, Yuheng Huang, Guozhang Jia
Institute of Plasma Physics, CAS, Hefei, Anhui 230031, P.R.China
Xueyi Wang, Yu Lin
Physics Department, Auburn University, AL 36849-5311, USA

Abstract:

The interaction of electrons with two lower hybrid waves (one is resonant mode and the other one is off-resonant mode) has been studied via PIC simulations. As the second wave amplitude is increased, it is shown that the motion of the trapped electrons becomes stochastic. As a result, the damping of the resonant mode is greatly enhanced, and the resonant plateau is significantly broadened.

I ▪ Introduction

Lower hybrid current drive (LHCD) has been widely used in Tokamak devices for current generation and plasma control [1-2].Generally the power spectrum of a launched lower hybrid wave (LHW) from an antenna has a finite width.Since the ray trajectory strongly depends on the wave parallel refractive index$n_{//}$, we have to divide the power spectrum into many small intervals or bars so that each interval can be treated as a monochromatic wave. The interaction of electrons with these waves is then described by the quasi-linear theory, which assumed that the electron orbit is unperturbed. For present LHCD experiments, the input lower hybrid wave is typically up to a few mega-watts, and nonlinear plasma-wave interactions have been observed in many LHCD experiments. Therefore it is necessary to study the nonlinear processes during LHCD. In this work, we investigate the interaction of electrons with two lower hybrid waves by taking perturbed orbit into account. To efficiently achieve plasma current the lower hybrid wave and electrons should be in Landau resonance. Therefore, we consider two LHWs.

$$E_1(x,t) = A_1 \sin(k_1 x - \omega_1 t), E_2(x,t) = A_2 \sin(k_2 x - \omega_2 t),$$

$$\frac{\omega_1}{k_1 v_{te}} = 3.8, \text{ and } \frac{\omega_2}{k_2 v_{te}} = 6.8$$

Apparently the second wave with higher phase velocity is undamped since resonant electrons are few.

If A_2=0, for a large A_1, the effect of the perturbed orbit needs to be taken into account which causes the wave amplitude oscillates as the time is larger than the trapped electron bouncing period [3]. For particles move in two fields, it is found that the trapped particle motion becomes stochastic as the resonances overlap [4-6].However, most published work focused on the trapped particle motion and

the perturbed fields were assumed unchanged during the interaction. Menyuk et al investigated the interaction of electrons with a Langmuir wave via PIC simulations [7]. It is found that the wave propagating obliquely with respect to a magnetic field has many resonances. When they overlap, there is a transition between regular and stochastic particle motion, which leads to a strong decrease in the final wave amplitude. In this work we conduct PIC simulations to study the interaction of electrons with the above two LHWs.

II ▪ Simulation model

The simulations are conducted in the framework of GEFI, in which electrons are described by the gyro-kinetic equation while ions by the fully kinetic equation [8,9]. The plasma is uniform and the magnetic field is along x and z directions with $B_z/B=0.075$. Two perturbations $E_1(x, t=0)$ and $E_2(x,t=0)$ given in the above section is initially launched. The excited lower hybrid waves are confirmed by comparing with the linear dispersion relation.

III ▪ Simulation results

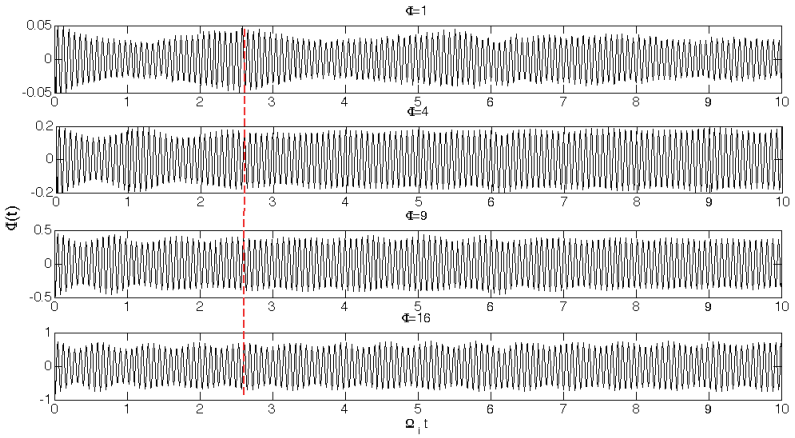

Fig.1 Evolution of Ex with time for different perturbation amplitudes.

A. Nonlinear Landau damping for a single mode

For $A_2 = 0$, the damping of the wave is described by O'neil theory which has taken the perturbed orbit into account. Fig.1 shows variation of Ex as a function of time for different perturbation amplitudes. The linear Landau damping occurs only in a short time much less than the bouncing period (τ_B) of trapped electrons. For $t>\tau_B$, the wave amplitude oscillates. This oscillation comes from the momentum conservation of the resonant electrons, and occur at a frequency near the bouncing frequency [10]. The wave amplitude becomes constant for sufficiently long time as predicted by O'neil [3].

The electron velocity distribution function f_e and phase space plot at different

times are shown in fig.2. It can be seen that a plateau, which oscillates with time, is formed near the resonance.

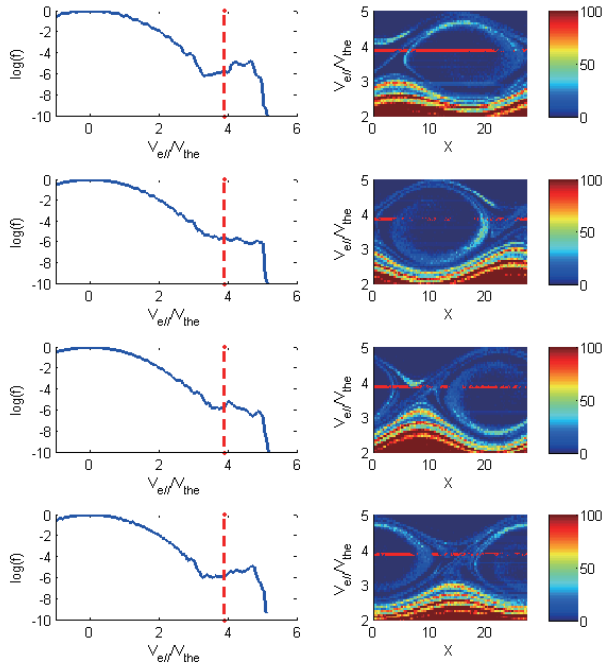

Fig. 2 Electron velocity distribution function f_e and phase space plot at different times.

B. Damping in the presence of another LHW

The presence of other LHW can affect the electron motions and the trapped electrons may become stochastic provided the wave amplitudes are sufficiently large so that the resonance overlap occurs, as shown in previous work. The electron motion in two LHWs is

$$m\ddot{x} = -eE_1 \sin(k_1 x - \omega_1 t) - eE_2 \sin(k_2 x - \omega_2 t) \quad (1)$$

$$H = H_1 + H_2, H_1 = \frac{p^2}{2m} - (eE/k_1)\cos(k_1\xi), \quad (2)$$

$$Actiton: I_1 = \oint p\, d\xi.$$

$$Angle: \theta_1 = \frac{\partial W}{\partial I_1}, W: Hamilton's\ characteristic\ function, W = \int p\, d\xi$$

$$\dot{\theta}_1 = \frac{\partial H_1}{\partial I_1} (When\ \ \varepsilon=0, I_1 = const, \dot{\theta}_1 = const).$$

$$H_2 = -(eE/k_2)\cos\theta_2, \theta_2 = k_2\xi - k_2\Delta v_\varphi t, \dot{\theta}_2 = k_2\Delta v_\varphi.$$

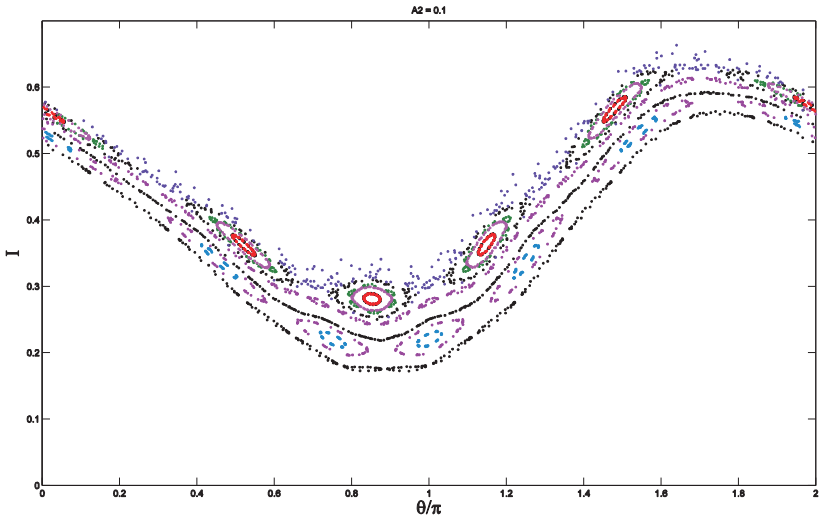

Fig. 3.Surface of section plot showing a divided phase space.

For the parameters $\omega_2 = 0.8\omega_1 k_2 = 2k_1$, and $A_2 = 0.8$, we solve the motion equation of the electrons near the separatrix. The surface of section plot clearly shows the stochastic motion of the trapped electrons.

Since the motion of trapped electrons becomes stochastic. It is expected that the damping of the wave should be affected. Thevariations of the wave amplitudes with time for $A_2 = 0.2$ and $A_2 = 0.8$ are shown in Fig.4. It can be seen that the wave A_1 is similar to the case of single wave as $A_2 = 0.2$. But its damping isgreatly enhanced as the second wave field becomes strong. The change of the trapped electron motion from regular to stochastic can also be seen in the phase space plot, as shown in fig.5. The spiral structure of the trapped electron is formed for small A_2, and it is destroyed as A_2 is increased. The electrons are then trapped near the second resonance $\omega/(k_{//}v_{te}) = 6.8$ and a newspiral structure is formed.

The velocity distribution functions of electrons for different A_2 are plotted in fig.6. One can see that the resonant plateau is greatly broadened due to the existence of the second wave. The broadening increases with A_2. Therefore it is expected that the driven current will also be greatly increased.

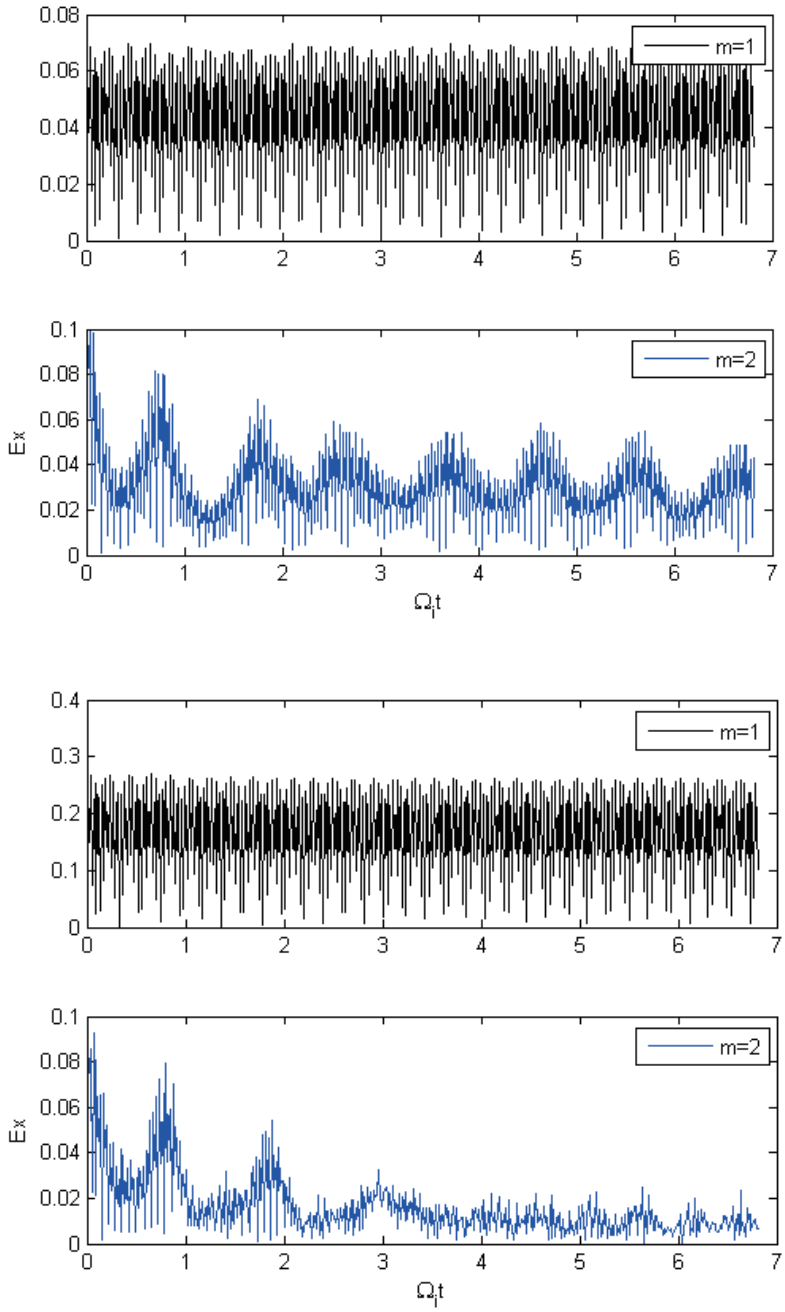

Fig.4 Variation of the wave amplitudes with time for A_2 = 0.2 (top two) and A_2 = 0.8.

If the amplitude of the non-resonant mode is small, the damping of the resonant mode is not affected. However, the damping is strong enhanced as the amplitude increases.

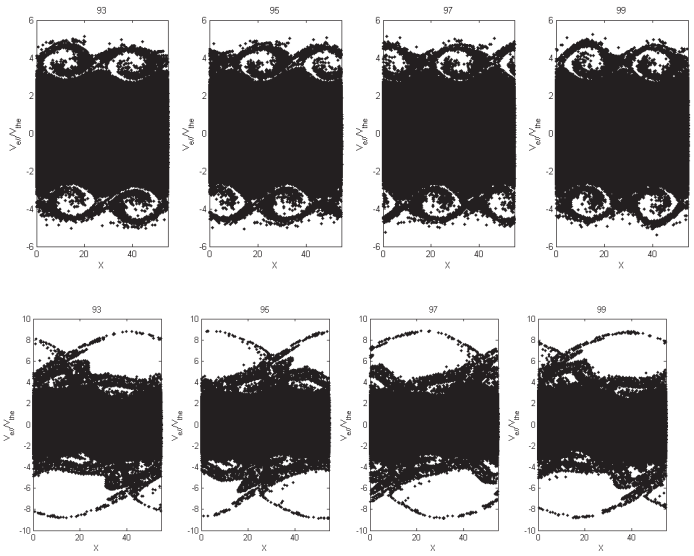

Fig.5 Phase space plot at different times for A_2 = 0.2 (top) and A_2 = 0.8.
Explanation:

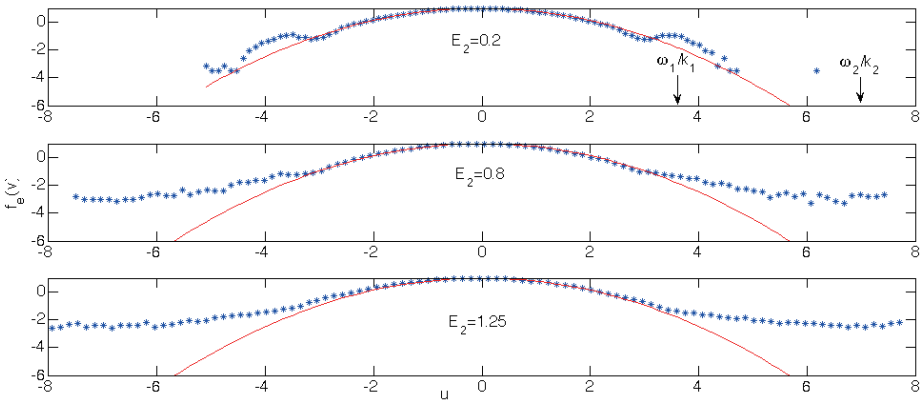

Fig.6.Velocity distribution functions of electrons for different A_2 . The two resonances are indicated by arrows.

IV ▪ Summary

The interaction of electrons with two lower hybrid waves has been studied via PIC simulations. The variation of the wave amplitude can be exactly described by O'neil theory if the second wave amplitude is not large. As the second wave amplitude is increased, it is shown that the motion of the trapped electrons becomes stochastic. As a result, the damping of the resonant mode is greatly enhanced, and the resonant plateau is significantly broadened.

Acknowledgment

This work is supported partially under the JSPS-NRF-NSFC A3 Foresight Program in the field of Plasma Physics (NSFC No.11261140328).

References

[1] N.J. Fisch, Phys. Rev. Lett. 41, 873 (1978).
[2] Paul T. Bonoli and Ronald C. Englade, Phys. Fluids 29, 2937 (1986).
[3] T. O'neil, Phys. Fluids 8, 2225 (1965).
[4] G.M. Zaslavskii and N.N. Filonenko, Sov. Phys. JETP 27, 851 (1968).
[5] G.R. Smith and A. N. Kaufman, Phys. Rev. Lett. 34, 1613 (1975).
[6] A. Fukuyama, et al., Phys. Rev. Lett. 38, 701 (1977).
[7] C. R. Menyuk et al., Phys. Rev. Lett. 48, 1104 (1982).
[8] Lin Y, et al, Plasma Phys. Control. Fusion 47, 657 (2005).
[9] Qi L, et al, Plasma Phys 20, 122102 (2013).
[10] J.T. Morales and T.M. O'neil, PRL 28, 417 (1972)

Simulation Study of Off-Midplane LHCD in KSTAR

Young-soon Bae[a], S. Shiraiwa[b], P. Bonoli[b], J.C. Wright[b], R. Parker[b], J.H. Kim[a], W. Namkung[c], M.H. Cho[c], B.H. Park[a], S.W. Yoon[a], Y.K. Oh[a], H. Park[a,d]

[a] National Fusion Research Institute, Daejeon, Korea
[b] Plasma Science Fusion Center, MIT, MA, 02139, USA
[c] Pohang University of Science and Technology, Pohang, Korea
[d] Ulsan National Institute of Science and Technology, Ulsan, Korea

Email: ysbae@nfri.re.kr

A new concept of lower hybrid (LH) wave launching scheme is suggested for efficient current drive aiming for high performance H-mode operation in KSTAR.This new concept is based onoff-midplane launcher to have a quick upshift of the parallel component of refractive index hence the efficient single pass absorption via Landau damping. In order to locate an appropriate position of the launcher on the poloidal direction, the ray tracing and Fokker-Planck codes have been employed to calculate the pah and absorption rate. Based on survey of the LH wave launch parameters and operation conditions including the interfacing issues with the existing in-vessel components, the LH wave launch from the top position near upper X-point of plasma separatrix would be free of the accessibility problem and reduce a parasitic edge loss for the KSTAR high performance H-mode operation scenario using 5 GHz LHCD.

1. Introduction

In LHCD, power damping of the LH wave is mainly due toelectron Landau damping (ELD) resulting in electron acceleration to the parallel direction with respect to the magnetic field. This was experimentally demonstrated for the first time in Alcator C-Mod [1]. Therefore, the LHCD has a high current drive efficiency and considered as anattractive current drive tool foroff-axis current drive necessary forsustaining tokamak plasmas in steady state including ITER [2]. However, as the density increases, the LHCD efficiency was found to be decreased more quickly than prediction(ray-tracing code) in a diverted configuration of the C-Mod tokamak experiment [3]. They reported thatthe main causes of the degradation of the curernt drive efficiency areastrong interaction of the scrape-off layer (SOL) region leading to aparasitic collisional power loss, which does not contribute to the current drive, and parametric decay instability at the edge [4, 5].In addition, asteep density gradient near the edge makes the accessibility to ELD domain more difficult. It is well known that the typical H-mode plasma has steep density gradient with pedestal formation ranged about ~ 1 cm inward from the last closed flux surface (LCFS).

The target operation mode in KSTAR is an “advanced tokamak” (AT) operation mode which aims to demonstrate β_N ($=\beta_t[\%]/(I_p/aB_t)$) ~ 5 and bootstrap current fraction, f_{BS}> 0.5, where I_p is the plasma current, a is the minor radius, B_t is the toroidal magnetic field, and β_t is defined as a ratio of the plasma stored energy to the toroidal magnetic energy. This target is preferrable requirement in fusion reactor in terms of high fusion output power and minimized recirculating power for auxiliar heating and current drive system. This operation regime is being investigated using the time dependent integrated simulation code with off-axis current drive source which is a mixture of off-axis neutral beam injector (NBI), electron cyclotron current drive (ECCD), and lower hybrid current drive (LHCD). The attractiveness of off-axis NBI is well demonstrated in DIII-D experiments for the steady state high performance plasma with enhanced MHD stability limit [6, 7]. But, due to the limited off-axis NBI power upgrade in KSTAR, the target performance of β_N ~ 5 and high bootstrap current fraction require additional far off-axis current drive using lower hybrid current drive (LHCD). Also, the LHCD current drive efficiency should be sufficient enough to provide the low magnetic shear (s ~ 0) in a layer close to extended the internal transport barrier (ITB) radial foot with limited LHCD power in KSTAR.

Since the AT operation mode in KSTAR is based on H-mode with pedestal, it would be difficult to sustain such a high performance plsma due to the lower single pass absorption if the LH wave is launched at the outer midplane. Presently, the 5 GHz KSTAR LHCD is being operated with a 500 kW CW klystron prototype, which hasrecently demonstrated with 1000 s pulse operation at 500 kW output power at the window, and a conventional fully active waveguide grill launcher with fixed $n_{||}$ ~ 2 installed a the low field side midplane. In ELMy H-mode discharge, it is observed that there is a strong response of edge ECE

diagnostic channels with high rf reflection. For the better coupling and accessibility, the higher fixed $n_{||}$ will be availabe by changing the power dividing section before the launcher. The frequency of LH wave, 5 GHz in KSTAR will not be susceptible to the parametric decay instability in the high density operation regime of 1 x $10^{20}/m^3$in which $\omega/\omega_{LH}(0) > 5$ for B_t = 2 T, where $\omega_{LH}(0)$is the lower hybrid wave frequency at the plasma center. It implies that the KSTAR 5 GHz LHCD is completely out of range of unstable spectra [8] or has much higher density threshold where the parametric decay instabilities can be excited with cold lower hybrid side bands and low frequency ion-cyclotron quasi-modes near the edge if $\omega/\omega_{LH}(0) \leq 2$ [4].Note that$\omega/\omega_{LH}(0) \approx 5$ for B_t = 3 T with the same central density as above.

In order to overcome this difficulty, we need to enhance the single pass absorption. When we review the accessibility limit and ELD condition to the parallel refractive index, $n_{||}$which is given below [9, 10].

$$\sqrt{1-\frac{\omega_{pi}^2}{\omega^2}+\frac{\omega_{pe}^2}{\omega_{ce}^2}}+\frac{\omega_{pe}}{\omega_{ce}} < n_{||} < \sqrt{\frac{30}{T_e(keV)}} \quad (1)$$

The left-handed side is the accessibility condition and right-handed side is strong ELD condition with electrons having parallel velocity of electron with ~3 ×v_{th}, where v_{th} is the electron thermal velocity defined by$\sqrt{2T_e/m_e}$. Figure 1 shows the plot of Eq. 1 as a function of major radius in KSTAR tokamak with typical H-mode density and temperature profile with SOL. The window at the low field side has very narrow region between the onset of strong ELD and the wave accessibility limit. It requires the high launched $n_{||}$ or quick upshift of $n_{||}$ after the launch. The window at the high field side which allows lower $n_{||}$for penetration to the plasma center improves the current drive efficiency, since it is proportional to $1/n_{||}^2$ and provides an easy access to strong ELD.

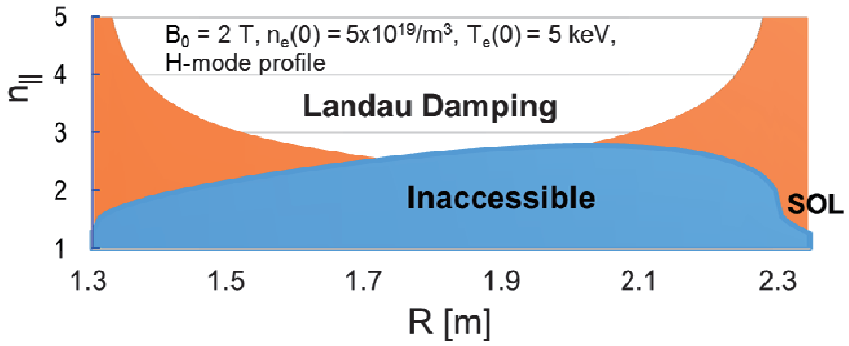

Fig. 1. The window of $n_{||}$ defined by the accessibility limit and Landau damping with typical H-mode density and temperature profiles in KSTAR for toroidal magnetic field of 2 T and central density of $5\times10^{19}/m^3$ and the central temperature of 5 keV, which are expected operation parameters for high β mode near future.

The inside launch system at the high field side is very attractive for fusion reactor with advantage of quiescent plasma avoiding plasma material interaction and better wave coupling. However, it is very unlikely to utilize inside launch system in KSTAR tokamak due to the space for launcher and waveguide penetration. On the other hand, the off-midplane launch system above the midplane will be a feasible to have efficient current drive at far off-axis using the toroidal effect of quick up-shift of $n_{||}$. Based on this motivation, we present the result of simulation study including enhanced current drive efficiency of the off-midplane launch system using GENRAY ray-racing code and CQL3D Fokker-Planck code [11, 12].

2. Accessibility in KSTAR H-mode

Difficulty in accessibility to the plasma center at the outer midplane launch system is viewed by GENRAY ray tracing simulation with typical H-mode density and temperature profile. In GENRAY simulation, the density is assumed with $(n_e(0)-n_e(1))(1-\rho^{\alpha_n})^{\beta_n}+n_e(1)$and temperature profile is assumed with$(T_e(0)-T_e(1))(1-\rho^{\alpha_T})^{\beta_T}+T_e(1)$, where rho is the normalized minor radius, $n_e(0)$ and $T_e(0)$ are values at the center, and $n_e(1)$ and $T_e(1)$ are values at the LCFS.

Figure 2 shows the ray tracing simulation results for the outer midplane launch system with the above plasma profiles. As seen in the ray tracing results, there are many multi-reflections in SOL region for B_t = 2 T due to accessibility limit even for higher launched central value of the parallel refractive index $n_{||0}$= 2.5

which is being considered the maximum value limited by power flux density in the waveguide grill. Even for the case of higher B_t = 3 T and $n_{||0}$ = 2.5, the strong single-pass absorption is not obtained with H-mode like density profile. Note that the launched power spectrum is specified with $\sin^2(x)/x^2$.

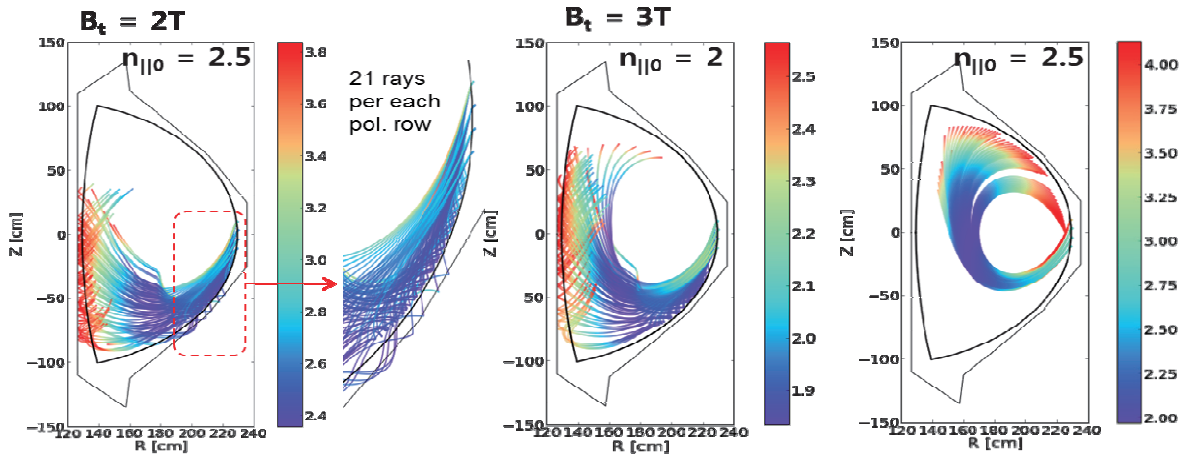

Fig. 2. The ray tracing results of outer midplane launch for H-mode plasma profile given in fig. 3.The color bar indicates the $n_{||}$ variation along the wave propagation. Here, SOL model in GENRAY and CQL3D simulation is included with exponential fall-off distances in density and temperature (λ_n = 1.5 cm, λ_T = 3 cm) *based on the measurement in KSTAR ELMy H-mode operation [13].*

3. Inside and off-midplane launch

As seen in Fig. 1, the inside launch system from inboard side is expected to provide high current drive efficiency without accessibility limit even with the lower $n_{||}$. Furthermore, it can take advantage of no plasma material interactions due to quiescent plasma and hence better LH wave coupling. It would provide a new possibility to LHCD in DEMO or beyond as a steady state current drive tool. Although the inside launch system provides an efficient current drive at the far off-axis even with lower $n_{||}$,as described in introduction, the inside launch is not realistic in KSTAR due to space limitation although it seems very attractive. In the off-midplane launch systems, the locations at 60^0 and 90^0 also appear to have a good accessibility, but difficult interface issues with the existing in-vessel control coils and passive plates. The in-vessel control coil and passive plate are very important component and are not feasible to remove in KSTAR. On the other hand, the off-midplane launch system on the top near the upper X-point of the separaterix shows very strong ELD by quick upshift of $n_{||}$ owing to the toroidal geometry effect even in the case of low B_t, and there is no difficult issues with in-vessel control coils and passive plates. Instead, it is unavoidable to remove the upper in-vacuum cryo-pump and upper divertor. This means that only the lower single null operation is allowed.Figure 3 shows that the proper locations of the launcher grillsshould be ranged from 1.5 m to 1.7 m in major radius. The interfaces of the grill launcher with in-vessel components inside KSTAR machine are also seen in Fig. 3.

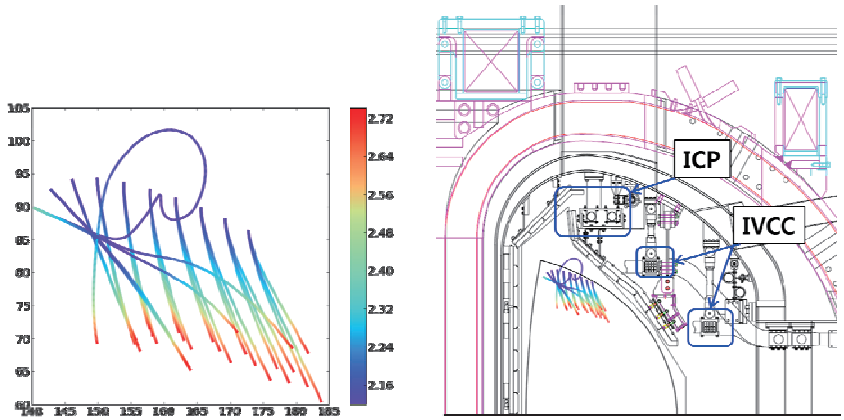

Fig. 3. Ray tracing from the several grill launcher locations on the top.

4. Current drive performance of top off-midplane launch

The current drive performance of the5 GHz LH wave from the top off-midplane launch system has been studied with more realistic setup of the launcher grill on the top side near X-point discussed in previous section. For this study, total 84 rays (21 rays x 4 rows) are launched from 4 poloidal waveguide rows. Each poloidal waveguide row is positioned far from the LCFS, and the cut-off and reflections in SOL in front of launcher grill is not calculated in the ray tracing calculations. For the density at the LCFS, it is assumed with 10% of the central density. Figure 4 shows the current density profile driven by the 5 GHz LH wave launched from the top off-midplane for various densities and two representative magnetic fields. We obtain very high current drive performance from the Fokker-Planck calculation utilizing ray tracing with high density range for both low and high toroidal magnetic field. But the peak position of the current density profile is toward the outer minor radii, from ρ(r/a) = 0.82 to 0.95 with density. The radial peak position control appears less flexible with a density and $n_{||}$ due to the strong quasi-linear electron Landau damping. The "figure of merit" $\eta = R_0[m]I_{CD}[A] < n_e[\times 10^{19}m^{-3}] > P_{abs}[W]$is very large and increases with the plasma density (1.17 – 1.76 A/W/m^2).

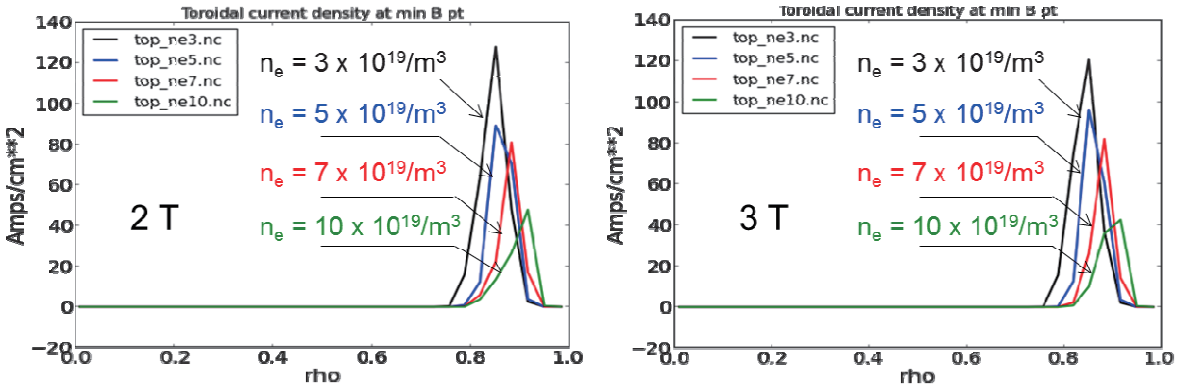

Fig. 4. The flux-averaged current density profile driven by 5 GHz LH wave from the top off-midplane launch for various densities and two representative magnetic fields. The launched $n_{||}$ = 2.5, the temperature is fixed with 5 keV.

5. Conclusions

In KSTAR, an efficient LHCD is essential for steady state advanced tokamak operation scenario using limited off-axis LHCD power (~ 4 MW source power) at I_p> 1 MA and n_e ~ 5x10^{19}/m^3. However, In the conventional low field side launcher system, degradation of LHCD efficiency is expected due to the accessibility limit and hence collisional damping, and the parametric decay instability. High performance H-mode with a steep density gradient at low field side will be detrimental for the LH wave absorption and current drive. Then, an off-midplane launch system will be an alternative to provide higher LHCD efficiency in KSTAR. From GENRAY/CQL3D simulation studies, 5 GHz LH wave with refractive index $n_{||}$ = 2.5 meets good damping condition for off-midplane launch near upper X-point for both low and high B_t up to density of 10x10^{19}/m^3 at the large outer minor radii. It turns out the strong quasi-linear electron Landau damping restricts propagation of the LH wave to r/a ~ 0.8 to 0.9. So, it should be noted that at this stage the further simulation studies for the different density profiles characterized with density peaking, $n_e(0)/\langle n_e \rangle$ is needed to see the change of the current drive efficiency and peak positions. An integrated modeling approach is also needed to account for the effects of the top off-midplane launch system for advanced tokamak operation mode in future KSTAR operation. However, there are a few physical and technical challenging issues; many hardware works to remove the upper divertor plates and in-vessel cryo-pump for the installation of the steady state launcher through the long vertical upper port, double null shape operation is not allowed, and possibly damage risk by disrupted plasma by vertical displacement event. Finally, we would like to mention that the off-midplane launch (and inside launch) could provide alternative and new possibility in LHCD for DEMO and beyond with a benefit in terms of avoiding significant absorption of the injected LH wave via α particle damping because of the spatial peaking of its density profile near the plasma center [14, 15].

Acknowledgement

This research was supported by Ministry of Science, ICT, and Future Planning under KSTAR project, and

was partly supported by the JSPS-NRF-NSFC A3 Foresight Program in the field of Plasma Physics (NRF No. 2012K2A2A6000443 and NSFC No.11261140328), and partly supported by DOE/Office of Science Program Office, DE-FOA-0000714.

References

[1] M. Porkolab et al., Phys. Rev. Lett. **53**, 1229 (1984).
[2] G.T. Hoang et al., Nucl. Fusion **49**, 075001 (2009).
[3] G.M. Wallace et al., Phys. Plasmas **19**, 062505 (2012).
[4] Y. Takase et al., Phys. Fluids **28**, 983 (1985).
[5] S.G. Baek et al., Plasma Phys. Control. Fusion **55**, 052001 (2013).
[6] C.T. Holcomb et al., EX/1-5, IAEA FEC, San Diego, Oct. 8-13, 2012.
[7] J.R. Ferron et al., Phys. Plasmas**20**, 092504 (2013).
[8] M. Porkolab, Phys. Fluids **20**, 2058 (1977).
[9] M. Brambilla, Nucl. Fusion **18**, 493 (1978).
[10] V.E. Golant, Sov. Phys. – Tech. Phys. **16**, 1980 (1972).
[11] A.P. Smirnov and R. Harvey, Bull. Am. Phys. Soc. **40**, 1837 (1995)
[12] R.W. Harvey and M. McCoy, in Proc. Of the IAEA TCM on Simulation and Modeling of Thermonucelar Plasmas, Montreal, pp. 489-526 (IAEA, Vienna, 1992). (http://compxco.com/050520_cql3d_manual.pdf)
[13] J.G. Bak et al., 19th ITPA Divertor-SOL Topical Group Meeting (ITPA, Kanazawa, 2014).
[14] P.T. Bonoli et al, Nucl. Fusion **27**, 1341 (1987).
[15] M. Schneider et al., Nucl. Fusion **49**, 125005 (2009).

Analysis of tungsten density in plasma core of LHD

S.Morita[1,2], X.L.Hunag[2], T.Oishi[1,2], I.Murakami[1,2], H.M.Zhang[2] and M.Goto[1,2]

[1]National Institute for Fusion Science, Toki 509-5292, Gifu, Japan

[2]SOKENDAI (Graduate University for Advanced Studies), Toki 509-5292, Gifu, Japan

Abstract

The tungsten ion density measurement has been attempted in LHD using EUV emissions from highly ionized tungsten ions based on the tungsten pellet injection. For the purpose the radial profile of W^{45+} ion spectrum ($4p\ ^2P_{1/2}$ - $4s\ ^2S_{1/2}$) is measured at 126.998Å with absolute intensity. The measured profile is reconstructed to a local emissivity profile as a function of normalized radius, ρ. The intensity coefficient of the W^{45+} transition is calculated from HULLAC code [1]. The tungsten density profile of W^{45+} ions is finally obtained with consideration of electron temperature and density profiles. The measured density of W^{45+} ions is $1.0\times10^{9}cm^{-3}$ at the plasma center and the ratio of the W^{45+} ion to the electron density is 2.5×10^{-5}. The result is very reasonable when we consider the number of total tungsten particles ($N_W=8.67\times10^{16}$ particles) injected with the tungsten pellet. The result also indicates that the intensity coefficient of the W^{45+} ion transition obtained from the HULLAC code gives an accurate value.

1. Introduction

The density measurement of tungsten ions in fusion plasmas is very important for accurate understanding of the tungsten transport [2]. Until now the tungsten density measurement has not been done because the tungsten emission is not so strong for the profile measurement in addition to the lack of a sufficient diagnostic system. In LHD, an injection of carbon pellet with tungsten wire of 0.1mm in diameter and 0.7mm in length is possible because of the absence of plasma current [3]. Therefore, a bright source of tungsten emissions can be produced which enables to measure the radial profile of tungsten EUV spectra. The profile observation is absolutely necessary for the density measurement of impurity ions. On the other hand, the ionization stage of tungsten ions which is suitable for the density measurement is very limited. The electronic configuration of tungsten ions is listed in table 1. Since most of tungsten ions have many electrons in the outer electron orbit, the resultant spectral structure is very complicated. In order to measure the tungsten density, the number of electrons at the outer electron orbit should be one or two because of the high intensity, a limited number of transitions and accurate intensity calculation.

When we see the table 1, the tungsten ion having one or two electrons at the outer orbit is only W^{44+}, W^{45+}, W^{62+}, W^{63+}, W^{70+} and W^{71+} ionic configuration. Since the W^{62+}, W^{63+}, W^{70+} and W^{71+} ions have high ionization energy ($E_i\geq7keV$), it is difficult to produce such ions in LHD. The production of such ions is possible in ITER. In the present study, therefore, the tungsten density measurement is focused on the W^{44+} and W^{45+} ions.

Table 1 Ionic configuration of tungsten ions

W^{0+}: $1s^2 2s^2 p^6 3s^2 3p^6 3d^{10} 4s^2 4p^6 4d^{10} 4f^{14} 5s^2 5p^6 4d^6$

W^{6+}: $1s^2 2s^2 p^6 3s^2 3p^6 3d^{10} 4s^2 4p^6 4d^{10} 4f^{14} 5s^2 5p^6$

W^{12+}: $1s^2 2s^2 p^6 3s^2 3p^6 3d^{10} 4s^2 4p^6 4d^{10} 4f^{14} 5s^2$

W^{15+}: $1s^2 2s^2 p^6 3s^2 3p^6 3d^{10} 4s^2 4p^6 4d^{10} 4f^{11} 5s^2$

W^{17+}: $1s^2 2s^2 p^6 3s^2 3p^6 3d^{10} 4s^2 4p^6 4d^{10} 4f^{11}$

W^{28+}: $1s^2 2s^2 p^6 3s^2 3p^6 3d^{10} 4s^2 4p^6 4d^{10}$

W^{38+}: $1s^2 2s^2 p^6 3s^2 3p^6 3d^{10} 4s^2 4p^6$

W^{44+}: $1s^2 2s^2 p^6 3s^2 3p^6 3d^{10} 4s^2$

W^{45+}: $1s^2 2s^2 p^6 3s^2 3p^6 3d^{10} 4s$

W^{46+}: $1s^2 2s^2 p^6 3s^2 3p^6 3d^{10}$

W^{56+}: $1s^2 2s^2 p^6 3s^2 3p^6$

W^{62+}: $1s^2 2s^2 p^6 3s^2$ (3p3s-$3s^2$: 79.91Å)

W^{63+}: $1s^2 2s^2 p^6 3s$ (3p-3s: 77.69Å)

W^{64+}: $1s^2 2s^2 p^6$

W^{70+}: $1s^2 2s^2$

W^{71+}: $1s^2 2s$

W^{72+}: $1s^2$ (2p2s-$1s^2$: 0.204Å)

W^{73+}: 1s (2p-1s: 0.201Å)

2. Tungsten spectra of Zn-like XLV (W^{44+}) and CU-like XLVI (W^{45+})

Tungsten spectra in EUV range are relatively simple at Te>2keV, while those are very complicated due to the presence of unresolved transition array (UTA) at Te<2keV [2]. A typical example of the spectra is shown in Fig.1. The W^{44+} and W^{45+} ions have two EUV spectra as the major transition, respectively, as follows;

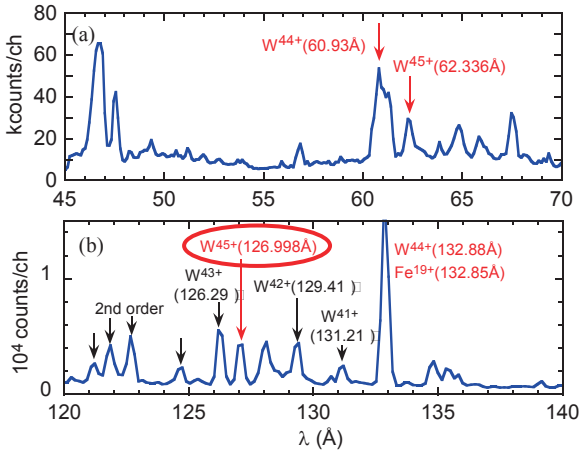

Fig.1 Tungsten EUV spectra at Te2keV in wavelength ranges of (a) 45-70Å and (b) 120-140Å. W^{44+} and W^{45+} ion spectra are indicated by arrows with their transition wavelengths.

W^{44+}: 4s4p $P_{3/2}$-$4s^2\ ^1S_0$ (60.93 Å)

4s4p $P_{1/2}$-$4s^2\ ^1S_0$ (132.88Å)

W^{45+}: 4p $^2P_{3/2}$-4s $^2S_{1/2}$ (62.336Å)

4p $^2P_{1/2}$-4s $^2S_{1/2}$ (126.998Å)

The W^{44+} ion spectrum at 132.88Å is completely blended with Fe^{19+} ion spectrum at 132.85Å. The W^{44+} ion spectrum at 60.93Å and W^{45+} ion spectrum at 62.336Å are also a little blended with another W ion spectrum. Therefore, the W^{45+} ion spectrum at 126.998Å is only isolated from other W ion spectra. Then, we attempt to measure the tungsten density of W^{45+} ions using the EUV spectrum at 126.998Å.

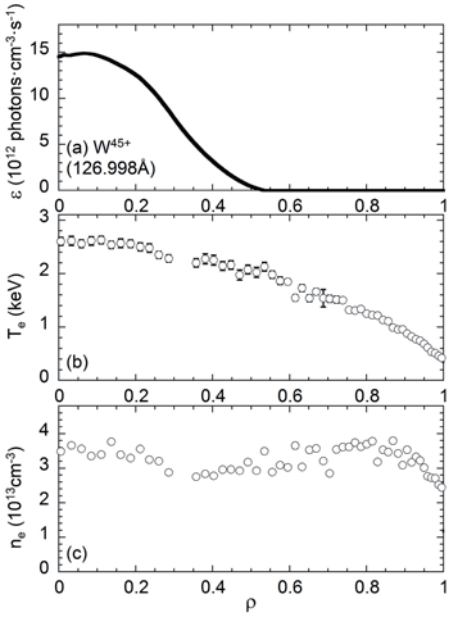

Fig.2 Radial profiles of (a) local emissivity of W^{45+} ion spectrum at 126.998Å, (b) electron temperature and (c) electron density.

3. Radial profile and intensity coefficient of W^{45+} ion spectrum

Radial profile of local emissivity of W^{45+} ion spectrum is shown in Fig.2(a) as a function of normalized radius, which is obtained with a space-resolved EUV spectrometer [4]. The intensity is absolutely calibrated using bremsstrahlung continuum in high-density discharges of LHD [5]. The electron temperature and density profiles are also shown in Figs.2 (b) and (c), respectively. Since the central electron temperature is high, the tungsten can be ionized up to the W^{46+} ionization stage. The W^{45+} ion is then localized in the plasma center as shown in Fig.2(a).

The intensity coefficient of the W^{45+} ion transition is calculated with HULLAC code [1]. The result is shown in Fig.3. Since the transition energy of the W^{45+} spectrum is roughly 100eV at 126.998Å, the intensity coefficient also has the maximum at T_e~100eV. However, the intensity coefficient is practically a low value because the W^{45+} ion exists at a radial location where the ionization is equal to the electron temperature. Then, it takes a value of 5×10^{-10} phs.cm^3/s.

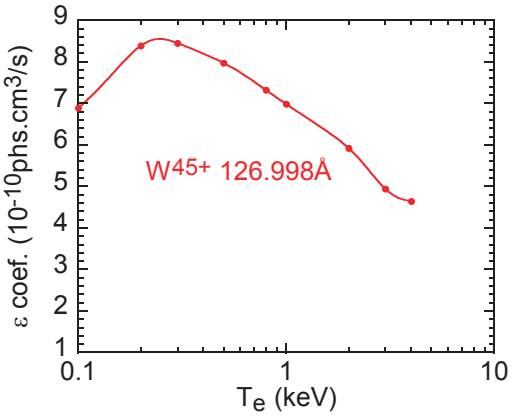

Fig.3 Intensity coefficient of W^{45+} transition at 126.998Å calculated with HULLAC code.

4. Density of W^{45+} ions

The density of W^{45+} ions calculated from Figs. 2 and 3 is $1.0\times10^{9}cm^{-3}$ at the plasma center. When the electron density is $4\times10^{13}cm^{-3}$, the ratio of the W^{45+} ion to the electron density is 2.5×10^{-5}. In order to observe the tungsten emission a carbon pellet with tungsten wire is injected in NBI discharges. In the present study the tungsten wire with sizes of 0.1mm in diameter and 0.7mm in length is used. The number of tungsten particles of $N_W=8.67\times10^{16}$ are injected in the LHD plasma. Since the plasma volume of the LHD plasma is approximately $V_p=30m^3$ when the magnetic axis position is $R_{ax}=3.60m$, the average number density of the tungsten particle is $2.89\times10^{9}cm^{-3}$ ($=N_W/V_p$) if all the injected tungsten particles are well confined in the LHD plasma. If we consider the tungsten ion density in other ionization stages of tungsten ions, e.g. W^{43+}, W^{44+}, W^{46+}, at the plasma center, the measured density ($n(W^{45+})=1.0\times10^{9}cm^{-3}$) indicates a reasonable value in comparison with the estimated value ($N_W/V_p=2.89\times10^{9}cm^{-3}$).

Acknowledgements

The authors thank all the members of the LHD team for their cooperation through the LHD experiment. This work was partially carried out under the LHD project financial support (NIFS13ULPP010) and partly supported by the JSPS-NRF-NSFC A3 Foresight Program in the field of Plasma Physics (NSFC: No.11261140328, NRF: No.2012K2A2A6000443).

References

[1] A.Bar-Shalom, M.Klapisch and J.Oreg, J.Quant.Spectr.Radiant.Trans. 71 (2001) 169.

[2] S.Morita, C.F.Dong, M.Goto, et al., AIP Conference Proceedings **1545** (2013) 143.

[3] X.L.Huang, S.Morita, T.Oishi, et al., Rev. Sci. Instrum. **85** (2014) 11E818.

[4] C.F.Dong, S.Morita, M.Goto and H.Y.Zhou, Rev. Sci. Instrum. **81** (2010) 033107.

[5] C.F.Dong, S.Morita, M.Goto and E.H.Wang, Rev. Sci. Instrum. **82** (2011) 113102.

Hydrogen depth profiles using laser-induced breakdown spectroscopy (LIBS) on graphite target of divertor in LHD

N. Ashikawa[1], Dongye Zhao, Cong Li[2], Hongbin Ding[2] and LHD experimental group[1]

[1] National Institute for Fusion Science, Gifu, Japan

[2] Dalian University of Technology, Dalian, China

1. Introduction

Investigations on hydrogen isotope inventories in plasma facing walls are important with the view of controls of fuel recycling and in-vessel tritium inventories in fusion devices. But, removal processes of hydrogen isotopes have not been optimized yet and still serious problems in ITER and DEMO. In particular, retained hydrogen isotopes in deposition layers are higher than that in bulk materials. Depth profiles in target materials are different between the retained hydrogen isotopes originating from energetic hydrogen isotopes during plasma discharges and the molecular hydrogen isotopes.

Laser-induced breakdown spectroscopy (LIBS) is one of useful analytical methods for hydrogen isotopes with depth profiles on materials [1-2]. Advantages of LIBS as ex-situ measurements are (1) short time analysis, (2) elements can be detected including hydrogen isotopes and helium, and (3) intensities mappings at 2-D positions. For research topics of hydrogen removal experiments for ITER, analyses of hydrogen isotope depth profiles are important. In this study, a demonstration of hydrogen depth profile analyses on graphite target exposed to LHD divertor plasmas was done using LIBS. From a comparison with LIBS and other analyses, effective approaches are discussed.

2. Experimental setup

YAG laser that a wavelength of 1064 nm is injected to a target material under low pressure in a vacuum chamber as shown in Fig.1. A laser energy per pulse is 100 mJ and a pulse length is 5 ns. A spectrometer has seven silicon CCD array detectors. A gas extraction system was installed to create a controlled Ar atmosphere.

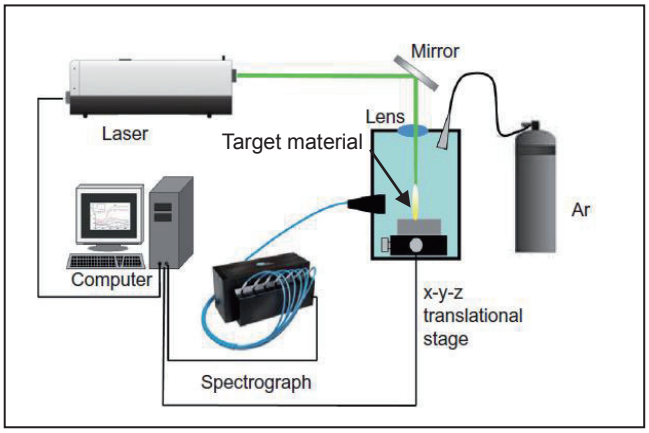

Figure 1. Systematic drawing about LIBS

An isotropic graphite (IG-430U, Toyo Tanso Corp.) exposed to hydrogen divertor plasmas using the material probe system at the 4.5 lower

port in LHD. A size of IG-430 target sample is 10 mm x 50 mm x 1 mm and three targets set on a sample holder made by molybdenum as shown in Fig.2 (a). A target “C” which located at right side of the holder in Fig. 2(a), was selected to LIBS measurement. Figure 2 (b) shows a picture of target "C" after LIBS analysis. A spot size of analyzed position is about 1 mm and each interval between analyzed points is about 1 mm. Analyzed points are written as circles in Fig.2 (b). Number of positions from 1 to 25 are written from an upper side to a lower side on this picture. Positions 4 or 5 (P4 or P5) are located at the divertor footprint of LHD and smaller numbers from P1 to P3 are located at private regions of the divertor configuration. For one position, total 20 pulses by Nd:YAG laser were injected and detected intensities at each pulse indicates different depth positions on the target.

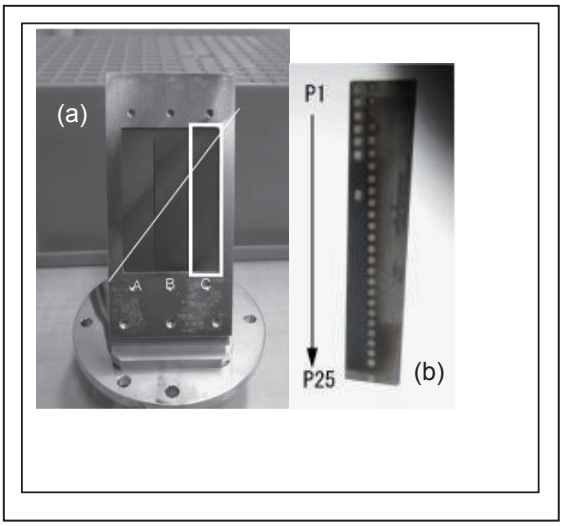

Figure 2 (a) A picture of a sample holder with IG-430U targets after plasma exposure in LHD. A line indicated the divertor footprint. (b) A picture of target “C” after LIBS analyses. Circles at 25 positions from P1 to P25 are analyzed traces by erosions of Nd:YAG laser.

3. Results

3-1. Hydrogen depth profile on graphite target exposed to LHD

Figure 3 shows spatial distributions of hydrogen, molybdenum, carbon and oxygen elements on the target sample C in Fig.2 (b). Figure 3 (a) is results at the first laser pulse and (b) is the second laser pulse by ex-situ LIBS. On the first layer such as in Fig.3 (a), deposited impurities and air contaminations are mixing. Higher hydrogen intensity is observed at private region of divertor plasma configuration. Positions from P1 to P13 show higher molybdenum intensities due to deposition from eroded sample holder made by molybdenum. Deposited molybdenum is observed at the first layer only and deeper regions does not show higher intensities such as the second layer as shown in Fig.3 (b).

Figure 4 shows depth profiles of H, Mo, C and O elements at the position 11 on the target sample C in Fig.2 (b). A sputtering rate by a laser pulse is not calibrated yet, but it is estimated about 100 nm / a laser pulse. Higher hydrogen intensities are detected from the top surface until 500 nm. In this analytical setup, a counting of 150 (a.u) is background signal level and sufficient counts were detected near top surface regions. This result of a depth distribution is consistent with effective areas of interactions from divertor geometry. Carbon intensities are uniform on this depth distribution.

3-2. A comparison with ex-situ LIBS and other analyzers

A detection limit of hydrogen is lower than that of glow discharge optical emission spectroscopy (GD-OES). For depth regions less than 100 nm, GD-OES data supports such as sensitive depth profiles near the top surfaces. For bulk target materials, such as ferritic steel alloys, thicknesses of iron/chromium oxide layers measured by GD-OES and XPS were compared and both thicknesses were about 30 nm. Hence, a good agreement based on an analytical result is shown. XPS can analyze elements with atomic number more than 3 and can not detect hydrogen and helium. On the other hand, GD-OES can detect elements with all atomic numbers due to a detection using s spectroscopy. A depth resolution of GE-OES is about 1 nm and it is good advantage of this analyzer. However, signal intensities depend on glow discharge parameters, and a stability of glow discharges is required.

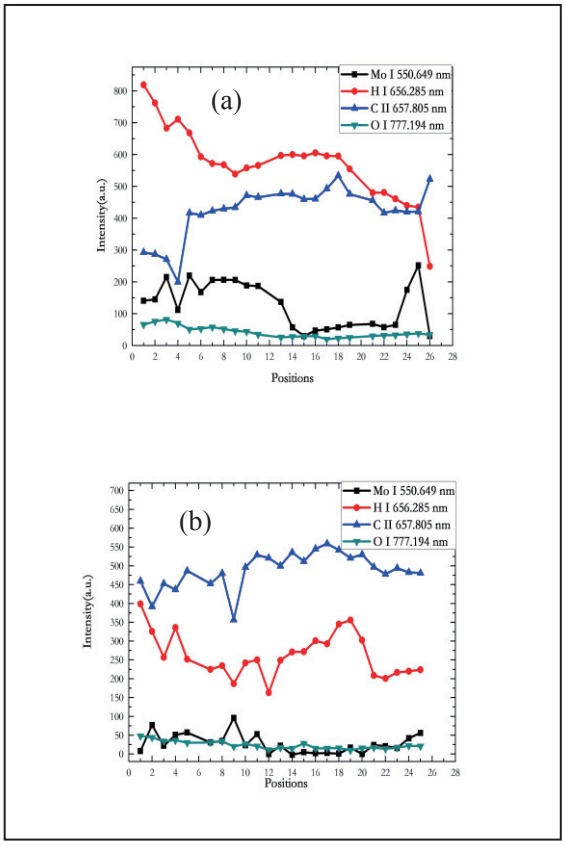

Figure 3. Spatial distributions of H, Mo, C, and O elements on the target sample C in Fig.2 (b).

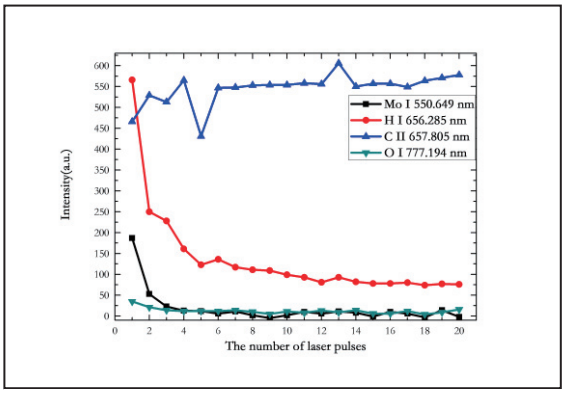

Figure 4. Depth distributions of H, Mo, C, and O elements at position 11 on the target sample C in Fig.2 (b).

Advantages of ex-situ LIBS are a good detection sensitivity, a small spot size of a detection area and detected elements with all atomic numbers. A detection sensitivity of LIBS is two order of magnitude higher than that of GD-OES. Detection areas have erosions in both analyzers, and then smaller detection area by LIBS is better. A minimum depth resolution by LIBS is about 50 nm and it is depending on materials, and it is difficult to observe an order of 1 nm.

Two analyzers, LIBS and GD-OES, have different characterizations, and good advantage for hydrogen and helium detections. A comparison between GD-OES and LIBS data is planned near future.

4. Summary

Hydrogen and impurities depth profiles on the IG-430U target exposed to hydrogen divertor plasmas of LHD were measured by LIBS and a proper results is obtained. At present, quantitative values cannot be analyzed using LIBS, but this results using the graphite target show one of an advantage of LIBS, such as good sensitivity with low detection limit of analyzers. In future work, a comparison with LIBS and other analyzers, such as GD-OES are planned.

Acknowledgments

This work was supported by the NIFS budgets ULFF004, KUHR010 and. the JSPS-NRF-NSFC A3 Foresight Program in the field of Plasma Physics (NSFC: No.11261140328, NRF: No.2012K2A2A6000443).

References

[1] Cong Li, et al., J. Nucl. Mater. (2015) 915.

[2] Ran Hai, Cong Li, et al., J. Nucl. Mater. (2013) S1168.

Observation of Central Toroidal Rotation Induced by ICRF on EAST

Bo Lyu[1)], [)]Xiayun Pan[2)], Fudi Wang[1)], Xinjun Zhang[1)], , Jun Chen[1, 2)], Yingying Li[2)], Jia Fu[2)], Yuejiang Shi[1, 3)], Yi Yu[1)], Minyou Ye[1)], Baonian Wan[2)]

[1)] *Institute of Plasma Physics, Chinese Academy of Sciences, Hefei, 230031, China*
[2)] *University of Science and Technology of China, Hefei 230026, China*
[3)] *Department of Nuclear Engineering, Seoul National University, Seoul, 151-742, Korea*

Core plasma rotation of both L-mode and H-mode discharges with ion cyclotron range of frequency (ICRF) minority heating (MH) scheme were measured with a tangential X-ray imaging crystal spectrometer on EAST. Co-current central impurity toroidal rotation change was observed in ICRF-heated L- and H-mode plasmas. Rotation increment as high as 30 km/s was generated at ~ 1.7 MW ICRF power. Scaling results showed similar trend as the Rice scaling but with significant scattering especially in L-mode plasmas. We varied plasma current, toroidal field and magnetic configuration separately to study their effect on L-mode plasma rotation, while keeping other major plasma parameters and heating unchanged during the scanning. It was found that larger plasma current could induce plasma rotation more efficiently. A scan of toroidal magnetic field indicated that the largest rotation was obtained for on-axis ICRF heating. The comparison between lower-single-null (LSN) than (double-null) DN configurations showed that LSN discharges rendered larger rotation change for the same power input and plasma parameters.

1. Introduction

Plasma rotation and velocity shear have been shown to be beneficial for tokamak plasma performance. Strong rotation can significantly affect the transition from L to H mode [1-3], help the formation of internal transport barriers (ITBs) [4], and stabilize destructive magneto-hydrodynamic (MHD) instabilities (i.e. resistive wall modes (RWMs)) [5-7], while rotation gradients can improve plasma confinement by suppressing turbulence [8, 9]. In the current generation of tokamak devices, neutral bean injection (NBI) is the most effective method to produce plasma rotation. However, for International Thermonuclear Experimental Reactor (ITER) and future reactors, this approach may be impractical due to the large machine size and high plasma density. Other alternative rotation drive methods were widely examined without external momentum input. One potential rotation driving scheme was to use ion cyclotron range of frequency (ICRF) heating, and substantial intrinsic rotation induced by ICRF waves has been observed on a number of tokamaks. On JET, co-current toroidal rotation was first observed to be induced by ICRF waves and the driving mechanism was considered to be fast ion pressure gradient [10]. ICRF driven co-current rotation was also observed on Alcator C-Mod for both minority heating (MH) and mode conversion (MC) regimes [11-15], and the mechanism driving rotation was thought to be the edge temperature gradient [16]. On Tore Supra, ICRF-heated plasma toroidal rotation was accelerated in both co- and counter-current direction. A close relationship between rotation change and ion pressure was found and the driving source might be due to the improved confinement [17]. On EAST, ICRF was used as one of the major auxiliary heating schemes and self-generated co-current flows were induced in both L-mode and H-mode plasmas with ICRF heating. These experiment results implied that ICRF heating might be an applicable flow drive method for ITER, which requires significant rotation level for RWM stabilization in typical operation regimes [18]. This paper presents experimental results of the toroidal plasma rotation produced by ICRF as the only auxiliary heating on EAST. ICRF were typically used to deuterium-hydrogen (D-H) plasmas via MH scheme, where the H-minority concentration was typically around 5%.

2. Experimental Description

Rotation measurements were performed on EAST, which is a fully superconducting tokamak (major radius R ~ 1.85 m, minor radius a = 0.45 m, toroidal magnetic field Bt < 3.5 T, plasma current Ip < 1MA) with flexible magnetic configurations (diverted and limited) and advanced wall conditioning techniques for long-pulse (1000s) high-performance steady-state operation [19]. All of these experiments were performed with a molybdenum first wall and lithium wall conditioning. ICRF with a total source power of 12MW was used to heat deuterium plasmas. During the normal ICRF experiments, the antenna was powered at predominantly symmetric spectrum for heating purposes. Both 2D TORIC full-wave simulation and ECE imaging measurement indicated that the ICRF power deposition profile was normally peaked near the magnetic axis for on-axis heating (ϱ ~ 0.1) for Bt ~ 2.0 T and ICRF frequency of 27 MHz [20].

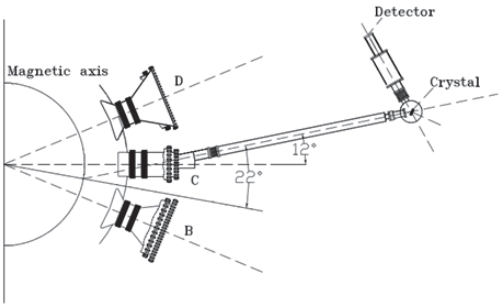

Figure 1. Layout of tangential X-ray crystal spectrometer on EAST

The rotation measurements presented in this paper were all derived from the tangential X-ray crystal spectrometer (TXCS) on EAST (Figure 1). Due to the unavailable absolute wavelength calibration, rotation measurements in this paper were presented in the form of relative velocity increment ($\Delta V0$), i.e. the rotation velocity magnitude was subtracted by the average pre-ICRF value, which was presumed to be nearly zero. The positive sign of rotation velocity means that the rotation increases in the co-current direction, while the negative sign of rotation velocity means the opposite increasing direction.

3. Plasma rotation characteristics for ICRF heated discharges

H-mode plasmas with only ICRF heating were recently obtained with double-null (DN) magnetic shape. The ICRF heated H-mode plasmas were generally characterized by type-III edge localized mode (ELM). Figure 2 shows an ELMy ICRF H-mode discharge (B_t = 2.0 T, I_p = 0.5 MA). The deuterium DN plasma was heated on axis by 27 MHz ICRF. As shown in Figure 2, the pre-ICRF plasma line-averaged density was about 2.0×10^{19} m^{-3} and ICRF power of 1.6 MW was coupled to the plasma from 3.1 to 6.8 s. The L-H transition took place at 3.4 s as indicated by a sudden drop of Dα emission and a successive increase in electron density and stored energy, which occurred at ~ 300 ms after ICRF power was applied and the duration of H-mode was about 3.4 s. After the application of ICRF power, substantial changes in plasma parameters were observed. Electron density rise to ~ 3.54×10^{19} m^{-3}, stored energy increment was about 55 kJ, core ion and electron temperature showed an increase

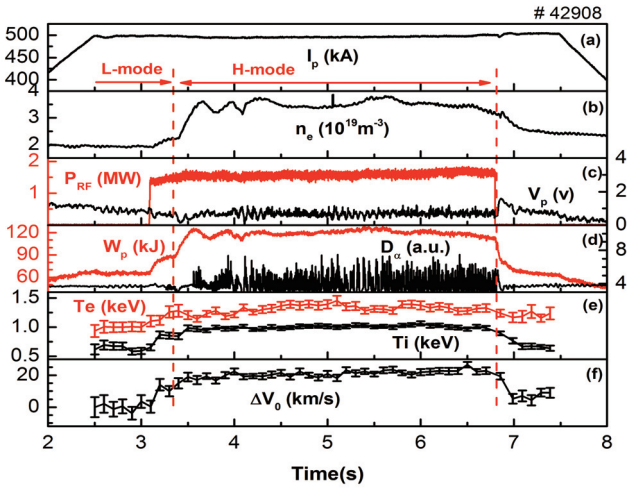

Figure 2. Time histories of plasma parameters for an ICRF heated H-mode discharge: (a) plasma current; (b) electron density; (c) ICRF injection power (red) and loop voltage; (d) stored energy (red) and Dα emission; (e) electron (red) and ion temperature; (f) central toroidal rotation.

of 370 eV and 330 eV, respectively. The increase in core plasma toroidal rotation was about 20.0 km/s relative to pre-ICRF phase and remained elevated during the entire H-mode phase.

Toroidal rotation generally increases with stored energy consistently, which showed close relationship between rotation and confinement [11, 12]. Figure 3 showed a scatter plot of central toroidal rotation increase versus the change of stored energy normalized to plasma current for ICRF-heated plasmas. The dataset included both H- and L-mode discharges with ICRF minority heating covering plasma parameters from I_p = 0.3-0.6 MA, n_e = 1.5-3.6×10^{19} m^{-3}, 1.0 MW < P_{ICRF} < 2.0 MW, DN H-mode and LSN and DN L-mode. As shown in Figure 3, these points fell into two groups: plasmas with the normalized stored energy increases below 0.8 J/A were of L-mode, while plasmas with the normalized stored energy increases above 0.8 J/A were of H-mode. The general trend of rotation increase versus stored energy increase was obvious for a wide range of plasma parameters, implying again the close relation between energy and momentum confinement as summarized by Rice et al [21]. Rice scaling is a global scaling between global plasma parameters, it doesn't include too much physics. When looking at L-mode data alone, the data scattering was not small, and the rotation increase even faster than a linear rate over ΔW/Ip, while H-mode data were more closely grouped. To further investigate plasma rotation behaviour in L-mode cases, plasma current, toroidal field and magnetic configurations were scanned during a sequence of deuterium discharges on EAST with only ICRF minority heating to study their effect on the rotation change. The experimental results were summarized in the follow section

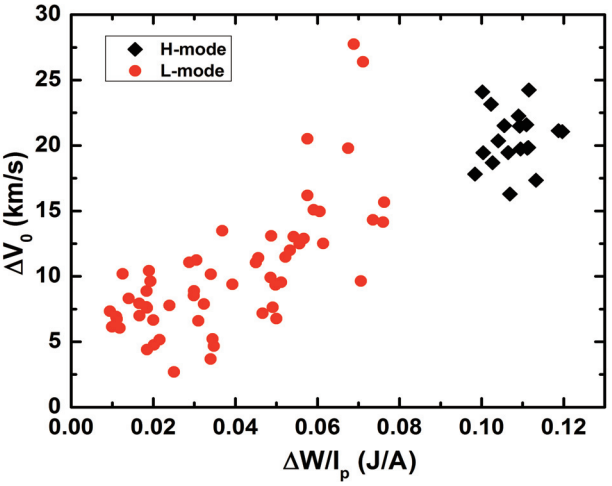

Figure 3. Rotation change as a function of the change in the stored energy normalized to the plasma current.

4. Effect of plasma current, toroidal magnetic field and magnetic configuration on the ICRF-heated plasma rotation

To study the effect of plasma current, toroidal magnetic field, electron density and ICRF power were also fixed at the same value while Ip was varied from 0.3 MA to 0.5 MA. Figure 4 plots the waveforms of several representative plasma parameters for deuterium LSN L-mode discharges (B_t = 2.0 T) at different plasma current (0.3 MA, 0.4 MA and 0.5 MA). The line-averaged densities were ~ 1.7×10^{19} m^{-3}. It could be seen that the rotation change depended on plasma current, where larger Ip generated larger rotation. For I_p ~ 0.3 MA, 0.4 MA and 0.5 MA, the stored energy increment was ~ 20 kJ, ~ 30 kJ and ~ 40 kJ, and toroidal rotation increment were ~ 10 km/s, ~ 16 km/s and ~ 30 km/s, respectively. For these three cases, the change of stored energy increased with plasma current,

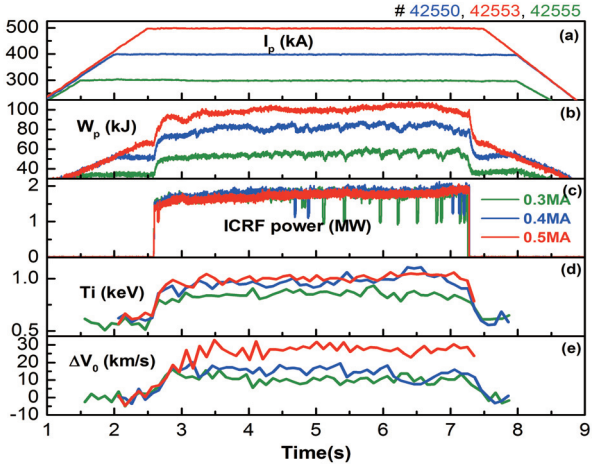

Figure 4. Time histories of several parameters for ICRF heated discharges with different Ip: (a) plasma current; (b) stored energy; (c) ICRF injection power; (d) ion temperature; (e) central toroidal rotation.

resulting in similar values of $\Delta W/I_p$. In this case, larger plasma current generated larger toroidal rotation, it may be due to the better coupling efficiency between ICRF power and plasmas with larger current. Although the global scaling law showed a general trend of rotation increase versus $\Delta W/I_p$, the rotation change did not increase with $\Delta W/I_p$ linearly. The result showed that for the same ICRF power, change in target plasma parameters affected the resulting rotation, but could still be roughly described by Rice scaling

The effect of ICRF resonance location on the rotation was also investigated by changing the toroidal magnetic field at fixed ICRF frequency (27 MHz) and plasma current (0.4 MA). Figure 5 showed the results of toroidal magnetic field scan for a series of deuterium DN L-mode discharges. The plasma densities were ~ 2.0×10^{19} m^{-3}, and ICRF at ~ 1.5 MW was delivered to the plasma. It could be seen that the largest core rotation increment was obtained for B_{t0} ~ 1.9-2.0 T, for which on-axis ICRF heating was occurred. Off-axis heating generally resulted in less rotation increment in the core. At fixed frequency, the H ion cyclotron (IC) resonance was on the magnetic axis for B_{t0} ~ 1.9-2.0 T, while the IC resonance was on the high-field side (HFS) of the axis for B_{t0} = 1.8 T and on the low-field side (LFS) of the axis for B_{t0} = 2.13 T, 2.26 T. When the ion cyclotron resonance was away from the magnetic axis, the flow drive was not as effective as on-axis heating in the core region. Due to limited diagnostic capabilities, it was hard to evaluate the rotation changes in off-axis positions, but from JET results it was showed that varying resonance location did not change off-axis rotation substantially and the most change was still in the core [19].

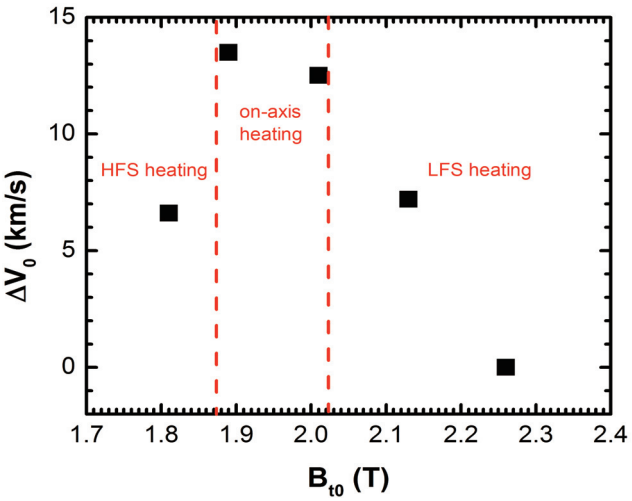

Figure 5. Dependence of rotation increment on toroidal magnetic field: ΔV_0 versus B field.

The flow drive efficiency was also found to be affected by the plasma shape. Figure 6 compared time traces of plasma parameters for an LSN plasma (red) and DN plasma (blue) on EAST. Both discharges were heated by 27 MHz ICRF with the same Ip = 0.5 MA, same density (ne ~ 1.75×10^{19} m^{-3}), toroidal magnetic field (B_t = 2.0 T), similar RF power (P_{RF} = 1.75 MW). After the application of ICRF, both stored energy and ion temperature increased significantly at similar magnitude, however, the driven rotation velocities were very different for LSN and DN plasmas: LSN plasma rotation increase was much higher than plasma rotation increase in DN plasma. Core rotation increases were 30 km/s and 15 km/s, both in the co-current direction.

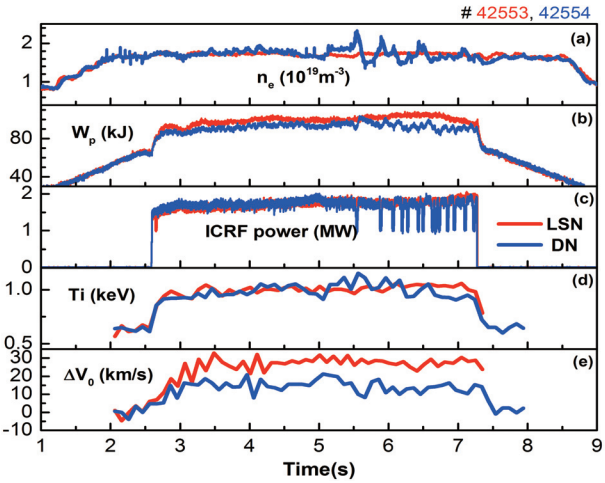

Figure 6. Time histories of several parameters for LSN and DN L-mode discharges: (a) electron density; (b) stored energy; (c) ICRF injection power; (d) ion temperature; (e) central toroidal rotation.

5. Conclusions

Core plasma rotation and ion temperature in both H-mode and L-mode discharges with 27 MHz ICRF minority heating alone were measured using a high-resolution X-ray imaging crystal spectrometer on the EAST. Significant co-current toroidal rotation increases in both H-mode and L-mode plasmas were observed. The flow drive was found to be sensitive to plasma current, toroidal field and plasma shape. The toroidal rotation was higher in plasmas with larger current. For a fixed RF frequency, the largest core rotation increase was obtained at an optimized toroidal field which makes the IC resonance on the magnetic axis. Additionally, LSN plasma produced larger rotation increase than DN shape while keeping other parameters the same plasmas

Acknowledgement

The authors thank the diagnostic group, vacuum group, ICRF group and the operation team of EAST. The work is partly supported by National Magnetic Confinement Fusion Science Program of China (2013GB112004 and 2015GB103002), National Natural Science Foundation of China (11175208, 11261140328) and Brain Korea 21 Program for Leading Universities & Students (BK21 PLUS).

References

[1] Shaing K C, Crume E C. 1989, Phys. Rev. Lett., 63: 2369

[2] Groebner R J, Burrell K H, Seraydarian R P. 1990, Phys. Rev. Lett., 64: 3015

[3] Ida K, Hidekuma S, Miura Y, et al. 1990, Phys. Rev. Lett., 65: 1364

[4] Wolf R C 2003, Plasma Phys. Control. Fusion 45: R1

[5] Bondeson A, Ward D J. 1994, Phys. Rev. Lett., 72: 2709

[6] Betti R, Freidberg J P. 1995, Phys. Rev. Lett., 74: 2949

[7] Strait E J, Taylor T S, Turnbull A D, et al. 1995, Phys. Rev. Lett., 74: 2483

[8] Hahm T S, Burrell K H. 1995, Phys. Plasmas, 2: 1648

[9] Burrell K H. 1997, Phys. Plasmas, 4: 1499

[10] Eriksson L G, Righi E, Zastrow K-D. 1997, Plasma Phys. Control. Fusion, 39: 27

[11] Rice J E, Bonoli P T, Goetz J A, et al. 1999, Nucl. Fusion, 39: 1175

[12] Rice J E, Lee W D, Marmar E S, et al. 2004, Phys. Plasmas, 11: 2427

[13] Rice J E, Lee W D, Marmar E S, et al. 2004, Nucl. Fusion, 44: 379

[14] Lin Y, Rice J E, Wukitch S J, et al. 2008, Phys. Rev. Lett., 101: 235002

[15] Lin Y, Rice J E, Wukitch S J, et al. 2011, Nucl. Fusion, 51: 063002

[16] Rice J, Hughes J W, Diamond P H, et al. 2011, Phys. Rev. Lett., 106: 215001

[17] Eriksson L G, Hoang G T, Bergeaud V. 2001, Nucl. Fusion 41: 91

[18] Liu Y, Bondeson A, Gribov Y, et al. 2004, Nucl. Fusion, 44: 232

[19] Wan B Y, Li J G, Guo H Y, et al. 2013 Nucl. Fusion, 53: 1040006

[20] Zhang X J, Zhao Y P, Wan B N, et al. 2013, Nucl. Fusion, 53: 023004

[21] Rice J E, Ince-Cushman A, deGrassie J S, et al. 2007, Nucl. Fusion, 47: 1618

Current status of Density limit studies in KSTAR

J. Son[1], Yong-Su Na[1], C.S. Byun[1], Y.K. In[2], Y.M. Jeon[2], J.H. Kim[2], D.H. Na[1], M.G. Yoo[1], S.W. Yoon[2] and KSTAR Team
1. Department of Nuclear Engineering, Seoul National University, Seoul, Korea
2. National Fusion Research Institute, Daejeon, Korea

The operation regime of KSTAR was investigated via Hugill diagram. The factors which affect the low density limit and the high density limit were revealed. The low density limit was investigated by focusing upon the locked mode limit due to the error field effect, indicating that the KSTAR has very low error field to reach very low density regimes. The high density limit was analyzed by the auxiliary power dependency and Greenwald density limit where the maximum density is found to be $0.6n_G$ and $0.8n_G$ in L-mode and in H-mode, respectively.

1. Introduction

As the fusion power is strongly related with the density, it is important to develop the operation scenarios which can maximize the density, and to investigate the underling background physics of density limit. In this point of view, density limit studies have been studied from early ages of magnetic fusion research. The operational space of a tokamak can be characterized by Hugill diagram [1]. The boundary of Hugill diagram is set by four limits, the lower density limit which is set by the runaway electron or the locked mode, the upper current limit set by the low edge-q or MHD instabilities, the Murakami limit set by power balance [2], and the Hugill limit which later replaced by Greenwald density limit [3]. The Hugill diagram is plotted between the normalized plasma density or Murakami number in abscissa and the normalized plasma current expressed as reciprocal number of the cylindrical safety factor in ordinate.

In this paper, the operation regime of KSTAR was revealed via Hugill diagram. The overall operation regime of KSTAR is explained in Section 2. The two of the density limit, low density limit and high density limit are discussed in Section 3 and Section 4, respectively. Types of disruption during density rise are explained in Section 5. A short summary is given in Section 6.

2. Operation regime of KSTAR

The overall operation regime of KSTAR is shown in Figure 1. Experimental database of KSTAR from year 2011 to 2013 were collected. Five time points were taken from each shot in the plasma current flattop phase. To plot the Hugill diagram, shots were carefully selected and those don't have proper data of plasma current(I_P), line averaged density(n_e), toroidal magnetic field(B_T), major radius(R), minor radius(a), and elongation(κ) were excluded.

3. Low density limit

3.1 Runaway electron

One of the main reasons determining low density limit of Hugill diagram is disruption by runaway electron. In low density plasmas with low collisionality, the electron does not

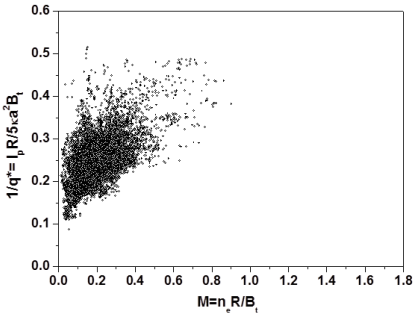

collide

Figure 1 *Overall operation regime of KSTAR on Hugill diagram*

with other electrons or ions so that it can be significantly accelerated by the electric field in a tokamak. This fast electron can give a severe damage to the wall when escaping from the plasma along the magnetic field line. The criterion on the electric field which is needed to generate runaway electrons is known to be "Dreicer field" [4]. According to the Dreicer field, to generate runaway electrons, the electric field of the tokamak E must be larger than critical value E_c, where $E_c = \frac{nq^3 ln\Lambda}{4\pi\varepsilon_0^2 mc^2} \cong 0.08 n_{20}$ and $E = V_{loop}/2\pi R$. As the critical electric field is proportional to the line average density, it is clear that the possibility of generating runaway electrons is higher in low density regimes, rather than high density regimes.

3.2 Error field effect

Another reason for limiting access to the low density regime is locked modes mainly triggered by the error field of the tokamak. It was reported in DIII-D that locked modes were occurred in low density discharges because of the high error field which resulting in the high limit of the low density. However, after minimizing the error field by using error field correction coils, the operation regime could be expanded to the low density regime [5].

In this point of view, the error field effect of KSTAR is investigated. Figure 2(a) shows the overlapped plot of KSTAR and DIII-D operation regime. KSTAR could reach far low density regime than DIII-D because of the low intrinsic error field in KSTAR [6]. So we tried to find out the error field effect by applying an error field using resonant magnetic perturbation (RMP). Figure 2(b) shows the comparison of two different discharges, one with no RMP (shot 9063) shown in black line and the other with n = 1 RMP (shot 9064) shown in red line. When the RMP applied, the plasma was immediately locked and disrupted. It is noteworthy that this locked mode is very rarely seen in low density discharges in KSTAR. The triangle points in Figure 2(a) indicate the discharges disrupted by the locked modes by applying RMP, where the white points are with n=1 RMP and black points are with n=2 RMP. It is clear that they set a new low density limit in KSTAR. It seems that the n=1 RMP shows greater impact than n=2 RMP to the low density limit.

This modified low density limit by RMP can affect the access of L- to H-mode transition. It is beneficial to achieve L-H transition with a minimum input power and it is strongly related with the density. KSTAR exhibits a roll-over behavior of the L-H threshold power against the density [7]. If the specific density where the L-H threshold power rolls over stays close to the low density limit set by RMP, the minimum transition power could not be achieved.

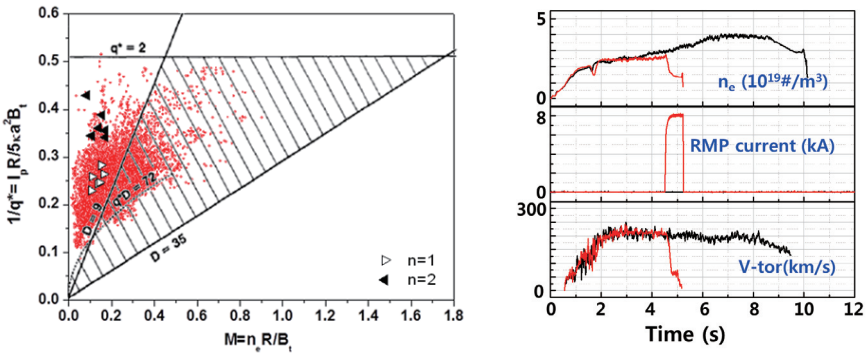

Figure 2 (a) Comparison between KSTAR and DIII-D operation regime (b) Comparison between RMP induced shot and no RMP shot

4. High density limit

4.1 power dependency

One factor that associates with the high density limit is the auxiliary input power. The input power is known not to affect the Hugill limit or Greenwald limit which express the density limit as $n \sim I_P$. But the expansion of the operation regime in terms of the Murakami limit is appeared in Figure 3(a) because of the power balance and the core fuelling effect of NBI. But the ECH effect was unclear possibly because ECH in KSTAR has much less input power than NBI (about 0.3MW) and subsequent low absorption power.

4.2 Greenwald density limit

The Greenwald density, which is expressed as $n_G = \frac{I_P}{\pi a^2}$, is widely used in many tokamak devices to figure out the high density limit. The Hugill plot of KSTAR was replotted between the density and the Greenwald density in Figure 3(b) to find out the maximum achievable Greenwald fraction in KSTAR. As shown in the figure, the Greenwald fraction of the H-mode is slightly higher than that of L-mode, as H-mode shows 80% fraction and L-mode shows 60% fraction. The higher fraction of H-mode is thought as due to the peaked density profiles and high triangularity. Because Greenwald density limit uses global parameter, it misses the local effect and profile dependency of the plasma. As the physics of the density limit is believed to be associated with the edge plasma condition, the density can be over Greenwald density with core fuelling which does not affect the plasma edge like pellet injection. And the strong plasma shaping represented as high elongation shows better confinement and higher density, due to pedestal stability related to the plasma shape

5. Types of disruptions during density rise

There are several types of plasma disruptions during density rise, which are related with MARFE, divertor detachment, drop of H-mode confinement, H-L back transition, blobs, etc. In KSTAR two disruption phenomena were discovered during the density rise, one is locked modes and the other is MARFE. The locked mode was shown in #6376 which had the Greenwald fraction of 55%. Sudden n=1 locked mode appeared just before disruption, caught by the locked mode signal.

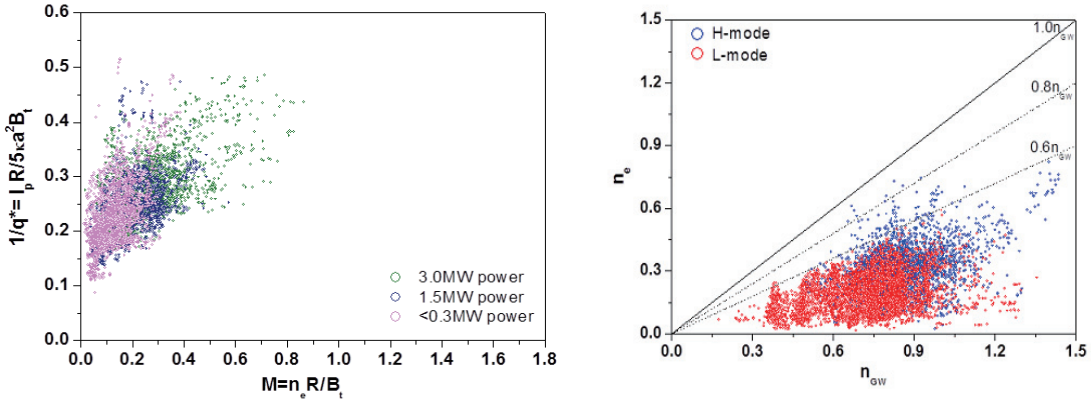

Figure 3 (a) Operation regime expansion by power dependency (b) Greenwald fraction in L-mode and H-mode

The locked mode amplitude which induces disruption can be predicted by DeVries scaling, as the scaling formula is $B_{ML} = 7.35{I_P}^{1.1}{q_{95}}^{-0.97}li(3)^{1.35}{\rho_c}^{-3}$[8]. If the magnitude of locked mode signal is greater than this scaled B, the disruption is likely to appear. This scaling is ongoing research in KSTAR.

The other one is MARFE. The Greenwald fraction was 61% when MARFE appears in KSTAR, far below the density limit like Alcator C-Mod, DITE, and TFTR. But some tokamaks like ASDEX-U, JT-60U, DIII-D, JET suggested that MARFE can appear just below the density limit [9].

6. Summary

In this study the operation boundary of the KSTAR was revealed with Hugill diagram with particular focus upon the density limits. For the low density limit, the runaway electron effect and the error field effect with RMP were investigated. In the high density limit, power dependency and Greenwald fraction in L-mode and H-mode were revealed. Causes of disruptions during density rise are analyzed and they were found to be locked mode and MARFE in KSTAR.

Acknowledgement

This research was supported by Ministry of Science, ICT, and Future Planning under KSTAR project and was partly supported by the JSPS-NRF-NSFC A3 Foresight Program (NRF No. 2012K2A2A6000443).

References

[1] S. J. Fielding et al., Nuclear Fusion **17,** 1382 (1977)
[2] M. Murakami et al., Nuclear Fusion **16,** 347 (1976)
[3] M. Greenwald et al., Nuclear Fusion **28,** 2199 (1988)
[4] R. S. Granetz et al., Physics of Plasmas **21**, 072506 (2014)
[5] Y. In et al., Nuclear Fusion **55**, 043004(2015)
[6] J. T. Scoville et al., Nuclear Fusion **31,** 875 (1991)
[7] J. W. Ahn et al., Nuclear Fusion **52**, 114001(2012)
[8] P.C de Vries, *"MHD perturbation amplitudes required to trigger disruptions"*, 41st EPS Conference (2014)
[9] M. Greenwald, Plasma Physics and Controlled Fusion **44,** R27 (2002)

Observation of flow and ion temperature of carbon impurities in the ergodic layer of LHD

T. Oishi[1,2], S. Morita[1,2], X. Huang[2], H. Zhang[2], M. Goto[1,2], and the LHD Experiment Group[1]

[1] *National Institute for Fusion Science, 322-6 Oroshi-cho, Toki 509-5292, Japan*
[2] *SOKENDAI (Department of Fusion Science, Graduate University for Advanced Studies), 322-6 Oroshi-cho, Toki 509-5292, Japan*

Abstract
A space-resolved spectroscopy using a 3 m normal incidence Vacuum ultraviolet (VUV) spectrometer was developed to measure the VUV emission profiles in wavelength range of 300-3200 Å from impurities in the ergodic layer in the Large Helical Device (LHD). The emission intensity, the ion temperature, the impurity ion flow, and their vertical profiles are derived by measuring the Doppler profile of impurity line spectra. The carbon impurity flows were derived by the Doppler shift of the CIV spectra with the wavelength of 1548.20 × 2 Å. The flow in the ergodic layer clearly increased when the averaged electron density was increased from 0.8 to 5.5 × 10^{13} cm^{-3}. A three-dimensional simulation code EMC3-EIRINE predicts that the flow is driven by a friction force between bulk ions and impurity ions which becomes dominant in the parallel impurity momentum balance in the ergodic layer when the electron density increases.

I. INTRODUCTION

Control of the impurity transport in the edge region of magnetically-confined plasmas has attracted an attention in the fusion research to sustain high-performance plasma and mitigation of the divertor heat flux. In the studies of the impurity transport, spectroscopy plays significant roles such as spectrum identification and impurity monitoring, which contributes to transport analysis and modeling. Moreover, investigation on the relationship between the edge magnetic fields and impurity transport becomes important recently. For example, reduction of the cross-field impurity transport, so called "impurity screening", has been observed in Large Helical Device (LHD) which has a thick stochastic magnetic field layer called "ergodic layer" located outside the core plasma [1]. In theoretical studies of the impurity screening in LHD, intrinsic carbon impurities generated from the divertor plates are accumulated close to the last closed flux surface (LCFS) in the electron density is low while the carbon impurities are pushed toward the outermost region of the ergodic layer [2]. The screening effect has been also observed experimentally using the extreme ultraviolet (EUV) spectroscopy for emissions from intrinsic carbon impurity ions indicating that the screening effect is enhanced in the magnetic field configuration with a thick ergodic layer [3]. It has been also found that iron impurities are more effectively screened, which results that the iron density in core plasmas of LHD is extremely low despite the stainless steel vacuum vessel [4].

A transport model for the impurity behavior in the ergodic layer has been proposed considering the parallel momentum balance on impurity ions along a magnetic field line connecting the core plasma and the divertor plate based on the following equation;

$$m_Z \frac{\partial V_{Z//}}{\partial t} = -\frac{1}{n_Z}\frac{\partial T_Z n_Z}{\partial s} + ZeE_{//} + m_Z \frac{V_{i//} - V_{Z//}^{imp}}{\tau_s} + 0.71Z^2 \frac{\partial T_e}{\partial s} + 2.6Z^2 \frac{\partial T_i}{\partial s}, \qquad (1)$$

where five terms in the right-hand side are contributions of impurity ion pressure gradient, parallel electric field, friction force between bulk ions and impurity ions, electron thermal force, and ion thermal force, in the order. Among these terms, the friction force terms and the ion thermal force term are the dominant terms. When the ion density gradient increases, the friction force increase resulting the impurity flow is directed toward divertor plates, which means the impurity screening. On the other hand, when the ion temperature gradient increases, the ion thermal force increases resulting that the impurity flow is directed toward the core plasmas, which means the impurity accumulation. Therefore, it is important to understand what kind of impurity flows can be observed related to changes of experimental parameters.

A precise measurement on the spatial profile of impurity line emissions in the ergodic layer is required to investigate the impurity transport in such stochastic magnetic field. The vacuum ultraviolet (VUV)

lines from impurity ions are significantly emitted in the ergodic layer because the electron temperature around the LCFS ranges from 10 to 500 eV. Therefore, space-resolved spectroscopy using a 3 m normal incidence VUV spectrometer was developed to measure the intensity profiles of the VUV emission in wavelength range of 300-3200 Å from impurities in the ergodic layer in LHD [5]. In the present study, we try to measure impurity flows in the ergodic layer by using the VUV spectroscopy.

II. EXPERIMENTAL SETUP

The LHD coil system consists of a set of two continuous superconducting helical coils with poloidal pitch number of 2 and toroidal pitch number of 10 and three pairs of superconducting poloidal coils. Figures 1 (a), (b), and (c) show the poloidal cross sections at horizontally-elongated plasma position of LHD for different magnetic axis configurations of R_{ax} = 3.6 m, 3.75 m, and 3.9 m, respectively. The stochastic magnetic fields in the edge ergodic layer are plotted with color scale indicating the magnetic field connection length in addition to the magnetic surfaces. The ergodic layer mainly consists of stochastic magnetic field lines with connection lengths from 10 to 2000 m, which correspond to 0.5 - 100 toroidal turns in the LHD. Radial thickness of the ergodic layer varies toroidally and poloidally. When the magnetic axis is shifted outwardly, the ergodic layer is wider and the plasma size within LCFS is smaller.

The 3m normal incidence VUV spectrometer (McPherson model 2253) is installed on an outboard midplane diagnostic port. The working wavelength range of the spectrometer is of 300 to 3200 Å. Figure 2 shows an observation range of the VUV spectroscopy and edge magnetic fields with magnetic axis of R_{ax} = 3.9 m and the toroidal magnetic field B_t = 2.539 T. The optical axis was arranged perpendicular to the toroidal magnetic field in the bottom edge at holizontally-elongated plasma cross section to adjust the observation range, in which the vertical profile of VUV emissions was measured, to the ergodic layer. A mirror unit which consists of a convex mirror and a flat mirror is mounted in front of the entrance slit of the spectrometer, which expands the view angle so that the elliptical plasma of LHD can be fully observed at the horizontally-elongated plasma cross section. A back-illuminated CCD detector (Andor model DO435-BN: 1024 × 1024 pixels) is placed at the position of the exit slit of the spectrometer. A high wavelength dispersion of 0.037 Å/pixel enables measurements of the Doppler profile of the line spectra of impurity

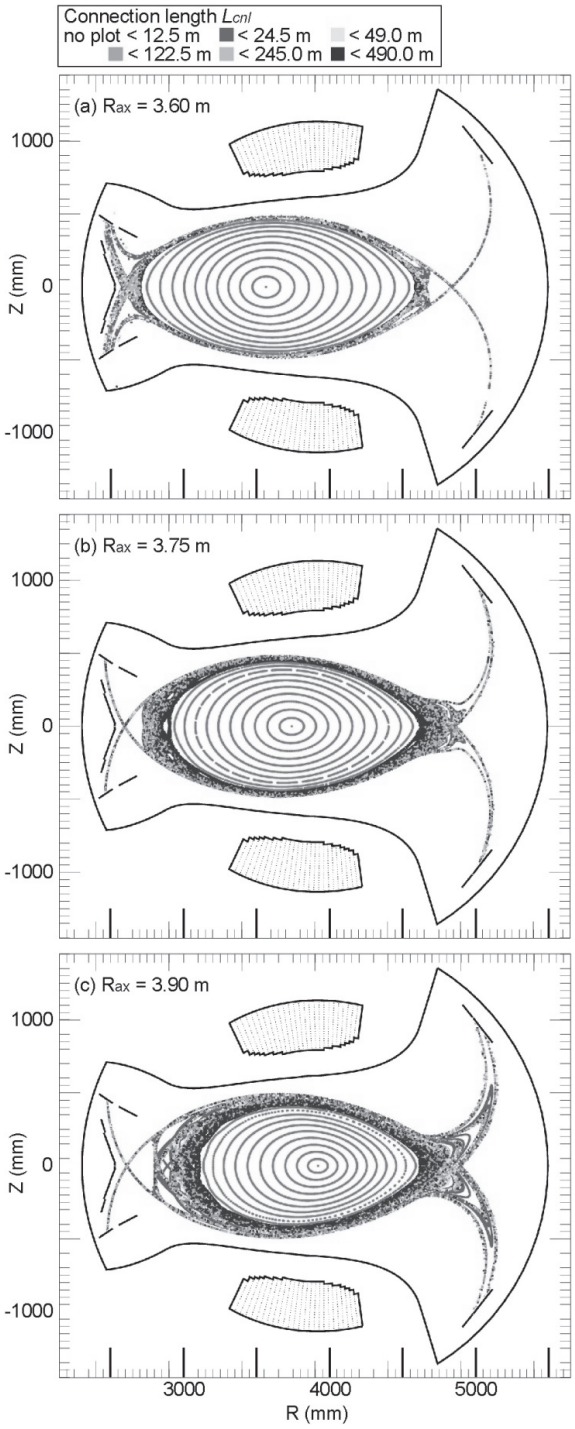

Fig.1 Poloidal cross sections at horizontally-elongated plasma position of LHD for different magnetic axis configurations of R_{ax} = (a) 3.6 m, (b) 3.75 m, and (c) 3.9 m, respectively.

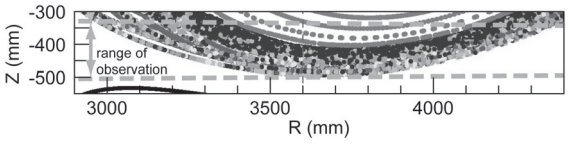

Fig.2 Observation range of the VUV spectroscopy and edge magnetic fields with R_{ax} = 3.9 m.

emissions. In the present study, the emission intensity, the ion temperature T_i, the impurity ion flow Δv, and their vertical profiles are derived by measuring the Doppler profile of CIV spectra from C^{3+} carbon impurity ions with the wavelength λ_0 of 1548.20 × 2 Å. Figure 3 shows a wavelength spectra of CIV lines with wavelength of 1548.20 × 2 Å together with the Gaussian profile as a fitting function. T_i and Δv are derived from the following equations, respectively;

$$T_i = 1.68 \times 10^8 M_i \left(\Delta_{FWHM} / \lambda_0\right)^2, \quad (2)$$

$$\Delta v = c\left(\Delta\lambda / \lambda_0\right). \quad (3)$$

where M_i is the atomic mass number, Δ_{FWHM} is the Doppler width at full width at half maximum (FWHM), c is the light velocity, and $\Delta\lambda$ is the Doppler shift. Note that the flow derived by the Doppler shift of the CIV spectrum is in a relative value taking a peak of a spectrum measured in a certain experiment condition as a reference of the flow. For example in Fig.3, a spectrum measured in a low density plasma denoted "reference" was taken as a flow reference case, and the Doppler shift from the reference to a peak of a spectrum measured in a high density plasma denoted "target" was used to evaluate the relative flow.

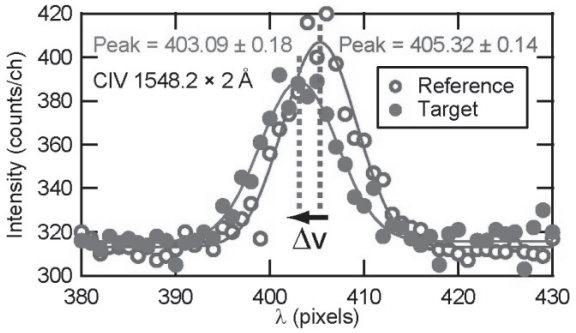

Fig.3 Wavelength spectra of CIV 1548.20 × 2 Å line together with the fitted Gaussian function for a low density case (reference) and a high density case (target).

III. CIV LINE SPECTRA MEASUREMENT

We conducted an experiment with a magnetic configuration with R_{ax} = 3.9 m and B_t = 2.539 T. The averaged electron density n_e was scanned from 0.8 to 5.5 × 10^{13} cm^{-3}. Figure 4 (a) shows the vertical profiles of CIV line intensity with the wavelength of 1548.20 × 2 Å for n_e = 1.0, 2.0, and 4.0 × 10^{13} cm^{-3}. It is known that the spatial profile of the CIV intensity has a steep peak in the ergodic layer. CIV emission is released only in the outermost region of the ergodic layer in LHD plasmas because the low ionization energy of 65eV for C^{3+} ions causes less fractional abundance in the core plasma. Therefore, the peak of the intensity profile outside LCFS shown in Fig. 4 (a) is a result of line integration in a long path along the sightline through the ergodic layer at the bottom edge of the holizontally-elongated elliptical plasma [6]. Figure 4 (b) shows the profiles of ion temperature T_i derived from the Doppler broadening of CIV spectra. The T_i profile also indicates the edge T_i in the ergodic layer at corresponding vertical position. T_i has a negative correlation with n_e.

Figure 5 shows a vertical profile of relative flow with n_e = 4.0 × $10^{13}$$cm^{-3}$. The relative flows were derived by the Doppler shift of the CIV spectra taking the spectra measured in the case of n_e = 0.8 × 10^{13} cm^{-3} as references of the flows. Negative values in the vertical axis indicate increment of flows directing toward the outer horizontal diagnostics port, which corresponds to radially outward direction. The result indicates that the flow increases radially outward compared to the flow reference case over the observation range. Figure 6 shows relative flows measured in the observation chords located at vertical positions of Z

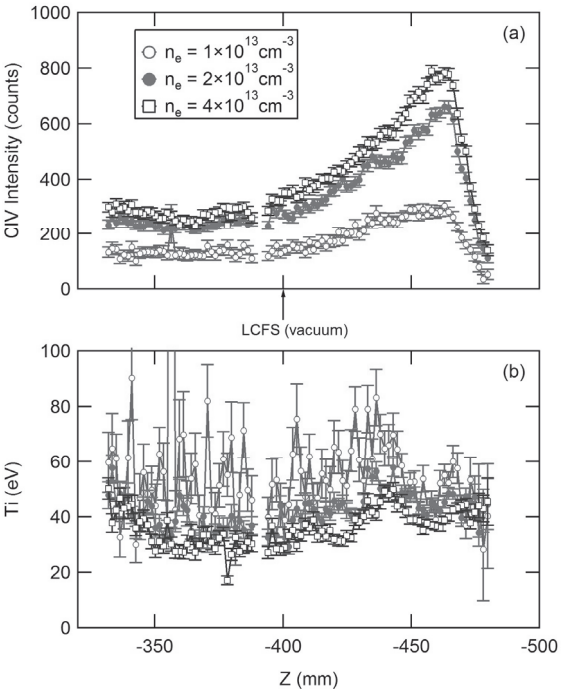

Fig.4 Vertical profiles of (a) CIV line intensity and (b) ion temperature derived from the Doppler broadening of CIV spectra.

= -454, -403, and -369 mm on the horizontal axis of Fig. 5 as a function of the averaged electron density. As shown in Fig. 5, the relative flow increased with the electron density. A three-dimensional simulation code EMC-EIRINE3 predicts that flow changes from low n_e thermal force dominant regime (impurity accumulation) to high n_e friction force dominant regime (impurity screening) considering the parallel impurity momentum balance in the ergodic layer when the electron density is increased. Now we are comparing the results of experiment and calculation to validate the measurements of the impurity flows.

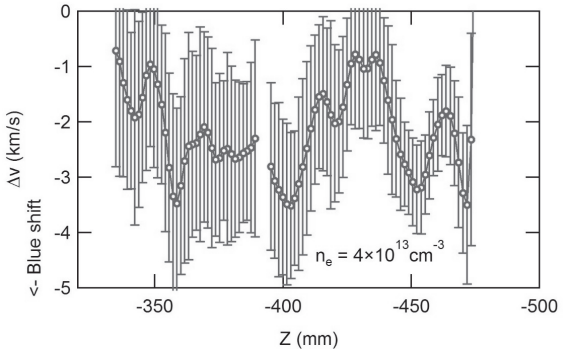

Fig.5 Vertical profile of relative flow with $n_e = 4.0 \times 10^{13}cm^{-3}$ taking the spectra measured in the case of $n_e = 0.8 \times 10^{13}$ cm^{-3} as references of the flows.

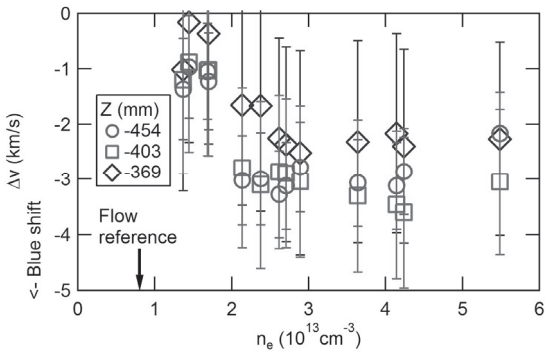

Fig.6 Relative flow along the observation chords located at several vertical positions as a function of the averaged electron density.

IV. SUMMARY

Spatial profiles of VUV lines from impurities emitted in the ergodic layer of LHD were measured by a space-resolved VUV spectroscopy using a 3 m normal incidence spectrometer in wavelength range of 300-3200 Å. The carbon impurity flows were derived by the Doppler shift of the CIV spectra with the wavelength of 1548.20 × 2 Å. The flow in the ergodic layer clearly increased when the electron density was increased from 0.8 to 5.5 × 10^{13} cm^{-3}. A three-dimensional simulation code EMC3-EIRINE predicts that the flow is driven by a friction force between bulk ions and impurity ions which becomes dominant in the parallel impurity momentum balance in the ergodic layer when the electron density increases. Results of experiment and calculation are under comparison for quantitative evaluation of the edge impurity flows.

ACKNOWLEDGEMENT

The authors thank all the members of the LHD team for their cooperation with the LHD operation. This work is partially conducted under the LHD project financial support (NIFS14ULPP010). This work was also supported by Grant-in-Aid for Young Scientists (B) 26800282 and partially supported by the JSPS-NRF-NSFC A3 Foresight Program in the Field of Plasma Physics (NSFC: No.11261140328, NRF: No.2012K2A2A6000443).

REFERENCES

[1] T. Morisaki *et al.*, J. Nucl. Mater. **313-316**, 548 -552 (2003).
[2] M. Kobayashi *et al*., Nuclear Fusion **53**, 033011 (2013).
[3] M. B. Chowdhuri *et al*., Physics of Plasmas **16**, 062502 (2009).
[4] S. Morita *et al.*, Nucl. Fusion **53**, 093017 (2013).
[5] T. Oishi *et al*., Applied Optics **53**, 6900 (2014).
[6] C. F. Dong *et al.*, Physics of Plasmas **18**, 082511 (2011).

Plasma Current and Electron Density Profile Measurements using POINT Diagnostic on EAST

H. Q. Liu,[1]Y.X. Jie[1,b)], W.X. Ding[2], D.L. Brower[2], Z.Y. Zou[1], W.M.Li[1], Z.X. Wang[1], J.P. Qian[1], Y. Yang[1], L. Zeng[1], T. Lan[1,3], X.C. Wei[1], G.S.Li[1,3], L.Q. Hu[1], and B.N. Wan[1]

[1] *Institute of Plasma Physics, Chinese Academy of Sciences, Hefei, Anhui 230031, P.R. China*

[2] *Department of Physics and Astronomy, University of California Los Angeles, Los Angeles, CA 90095, USA*

[3]*University of Science and Technology of China, Hefei, Anhui 230026, P.R. China*

Abstract.

A multichannel far-infrared laser-based **PO**larimeter-**INT**erferometer (POINT) system utilizing the three-wave technique has been implemented for current density and electron density profile measurements in the EAST tokamak. Double-pass, horizontal, radially-viewing chords access the plasma via an equatorial port. The laser source consists of three CW formic acid (HCOOH) FIR lasers at nominal wavelength 432.5 μm which are optically pumped by independent infrared CO_2 lasers. Each of the three FIR lasers can generate output power of more than 30 mW per cavity. Two lasers, with slight frequency offset (~1 MHz), are made collinear with counter-rotating circular polarization in order to determine the Faraday effect by measuring their phase difference in the plasma. The third laser, frequency offset (~ 2 MHz), is used as a reference providing local oscillator (LO) power to each mixer so that one can obtain the phase shift caused by the plasma electron density. Novel molybdenum retro-reflectors are mounted in the inside wall for the double-pass optical arrangement. The retro-reflectors can withstand baking temperature up to 350^{o}C and discharge duration more than 1000s. VDI planar-diode Integrated Conical Horn Fundamental Mixers optimized for high sensitivity, ~750 V/W, are used in the heterodyne detection system. A five-chord layout has been installed with expansion to 11 chords anticipated to fully diagnose the core region of EAST plasmas in next campaign. A Digital Phase Detector with 250 kHz bandwidth, which will provide real-time Faraday rotation angle and density phase shift output for use in plasma control, have been developed for use on the POINT system. Reliability of both polarimetric and interferometric measurement are obtained in 22s H mode discharge and 52s long pulse discharge, indicating the density gradient in H-mode discharge does not impact POINT measurements and that system works for any heating scheme on EAST so far. The electron line-integrated density resolution of POINT is less than 1×10^{16} m^{-2} (<1^o), and the Faraday rotation angle rms phase noise is <0.1^o. With the high temporal (~1 μsec) and phase resolution (<0.1^o), perturbations associated with the sawtooth cycle and MHD activity have been observed. The current profile, density profile and safety factor(q) profile are reconstructed by using EFIT code from the external magnetic and the validation POINT data. Realtime EFIT with Faraday angle and density phase shift constraints will be implemented in the plasma control system in the future.

1. Introduction

Achievement of long pulse and steady-state plasma regimes is a major challenge for both ITER and prospective fusion power reactors. Presently-operating devices have produced candidate scenarios for many relevant fusion targets, including the ITER baseline, alternate **ITER** inductive scenarios, and a variety of high performance steady state regimes. While establishing the optimization and parameters of future reactor operating scenarios has been addressed, a critical step before **ITER** requires qualification of these high-performance scenarios in long-pulse plasmas (i.e. time scale of many resistive relaxation times and longer than the wall equilibration time). A primary goal of the **EAST** device is to develop long-pulse high-performance plasmas near the operational (MHD and beta) limits using **ITER** relevant actuators (NBI and RF current drive and heating) and sensors. The goal of plasma discharge extension to long pulse is important for demonstrating that the current profile relaxes to a steady-state and that no stability boundary is crossed during this evolution that would compromise performance.

Knowledge of the poloidal magnetic field profile, $B_\theta(r)$, along with the associated toroidal current distribution, $J_\phi(r)$ and safety factor $\left(q(r) = rB_\phi / RB_\theta\right)$ is essential to the understanding of both tokamak plasma stability and confinement. The stability of the plasma to tearing modes and other magnetohydrodynamic (MHD) events such as the sawtooth perturbation and disruptions are largely determined by the current density profile. In order to address the critical issues of current profile distribution and temporal evolution, a laser-based Faraday effect polarimetry-interferometry diagnostic is being developed on EAST. The realtime output of this system will be used to monitor the fast profile dynamics of electron density, current density and q (safety factor) and ultimately be integrated into the realtime plasma control system. Here it will be critical to assess the utility and explore the limits of line-integrated measurements (density and Faraday effect) for plasma optimization and control.

In this paper, we present initial experimental results from the mulitchord, double-pass, **PO**larimetry-**INT**erferomettry **(POINT)** being developed on EAST, During the most recent experimental campaign, the POINT system has been employed for the first time to measure the electron density, current density and safety factor profiles for long-pulse EAST plasmas.[1,2] Multichord output provides internal plasma constraints to EFIT reconstructions allowing the temporal dynamics of key equilibrium profiles to be determined. Examples are shown for long-pulse plasmas with RF current drive as well as for high-performance H-mode plasmas. Of particular interest are the temporal dynamics of the L to H transition in EAST where current relaxation occurs and MHD modes evolve. Fast time response of POINT permits not only measurement current relaxation but also magnetic and density fluctuations associated with MHD effects (tearing modes, NTMs, fast-ion driven modes, etc.) and external magnetic perturbations. Interplay between magnetic fluctuations and current relaxation must be investigated and understood for plasma control optimization. Future plans to upgrade the system and integrate results into realtime EFIT (rtEFIT) will also be discussed. Long term goals include using POINT data, in conjunction with other diagnostic systems, for feedback control in order to maintain stable operation of high-performance tokamak plasmas while avoiding deleterious MHD events such as disruptions and ELMS.

2. System description & goals

The three wave polarimeter-interferometer, which may provide poloidal magnetic field distribution with simultaneously measured density distribution, is a popular configuration which was originally proposed by Dodel and Kunz.[3] The three wave configuration has been demonstrated to work successfully on several plasma experiments including RTP, MST, J-TEXT, Alcator C-Mod.[4-7] The POINT system utilizing the three-wave technique, three lasers are used. Two lasers, with slight frequency offset (~1 MHz), will be made collinear with counter-rotating circular polarization in order to determine the Faraday effect by measuring their phase difference. The third laser also frequency offset, will be used as a reference providing

local oscillator power to each detector so that one can obtain the phase shift caused by the plasma electron density.The Faraday rotation angle is proportional to the square of the beam wavelength and the phase shift of density is also proportional to the wavelength. So, three CO_2 pumped HCOOH lasers operating at 432.5μm, at approximately 30 mW each, provides the source power for the POINT system. This wavelength was chosen to avoid refractive effects in the large path through the EAST plasma (~ 3m) and also not to be affected by the mechanical vibrations on the short-wavelength side. Meanwhile, VDI planar-diode Integrated Conical Horn Fundamental Mixers optimized for high sensitivity, typical 750 V/W, are used. It is sufficient to provide good signal quality for the POINT system. In EAST, the most of Faraday angle values are in the range of $5^\circ \sim 10^\circ$ in the core plasma. So a detailed profile measurement of the Faraday rotation angle is completely feasible in the core plasma in EAST.

Initially, a five-chord layout of POINT is installed for testing with expansion to 11 chords anticipated to fully diagnose the core region of EAST plasmas. The layout of the three wave five–chord POINT system is shown in FIG. 1. The triple laser system was placed on the laser table in the laser room in the basement of EAST building, which is just outside the machine hall. The laser room can provide a thermostatic, vibration-free, electromagnetic shielded environment for lasers. Two orthogonal beams are combined here used for probing and sent to the optical tower in the machine hall, together with LO beam through two ~ 20 m length waveguides, which preserves the polarization direction, and what is most important for EAST conditions, it eases the alignment problem. The optical tower is located near the EAST tokamak and besides the diagnostic window for POINT system. It is isolated from the machine and all optics and detectors near the machine are installed on it, as shown in FIG.2.. The probing beams are split up into individual channels. In each individual channel, two combined orthogonal beams pass through a 1/4 waveplate, then they become the R- and L- circularly polarized waves and launched into plasma through the Polymethylpentene (TPX) window. Then the beams pass the plasma twice along the horizontal direction reflecting by the cube corner retro reflectors in the inner

vacuum wall. After pass out windows again, probe beams are combined with LO beam in the probe mixers. At same time, part of probe and LO beams are launched to the reference channel mixer. All intermediate frequency (IF) signals will be processed by an amplifier and filter module and then sent into a high-speed digital phase detector to extract the phase shift information, from which Faraday rotation angle profile and current density profile can be calculated by using EFIT code for EAST.10 Initially five-chord, has already installed on EAST now, is located at -34, -17, 0, 17, 34 cm along the vertical direction.

Optical stability is always an important issue in FIR optical diagnostics. To avoid the vibration caused by the tokamak, an armored concrete optical table and a massive stainless steel tower, independent from the EAST machine, is constructed to ensure the stability of beam-processing optics. All optical components are mounted on the optical table and the optical board on the tower, as shown in FIG.1. and FIG.2.. The careful optical designs, laser stability and mechanical structures are described in detail in another contributed paper.

In the POINT system, retro reflectors are attached to the inner wall of the vacuum chamber and make a double path through the plasma. This introduced sensitivity to vessel movement and required a compensating interferometer which would measure the phase shift due to mechanical displacement. This displacement is especially large during the change of the toroidal field. Vibrations will be compensated using a He-Ne interferometer as the second color. The compensation interferometer is under development for POINT system.

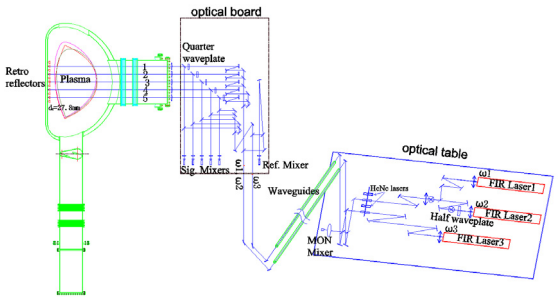

FIG. 1. Schematic view of the FIR POINT system.

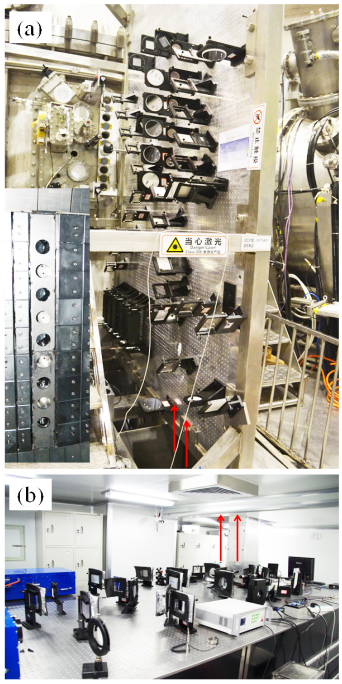

FIG. 2. (a) POINT system optical board in the EAST hall, inlet is the retro-reflector-array in the inner first wall, (b) POINT system optical table. The red arrows indicate the beams transmission

3. **Experimental results**

The first plasma density and plasma current density measurement are obtained in EAST experimental campaign in 2014. Reliability of both polarimetric and interferometric measurement are obtained in 22s H mode discharge and 52s long pulse discharge, indicating the density gradient in H-mode discharge does not impact POINT measurements and that system works for any heating scheme on EAST so far. The electron line-integrated density resolution of POINT is less than 1×10^{16} m^{-2} ($<1^{o}$), and the Faraday rotation angle rms phase noise is $<0.1^{o}$.[2] With the high temporal(~1 μsec) and phase resolution($<0.1^{o}$). The current profile, density profile and safety factor(q) profile are reconstructed by using EFIT code from the external magnetic and the validation POINT data. Sawtooth is a Magnetor-Hydro-Dynamic (MHD) instability in the core plasma region, which is often observed by ECE and SXR. The existence of sawtooth is considered associated with $q_{min}<1$. And also the radius of q=1 rational surface can be approximated by the inversion radius of

sawtooth. As is shown in figure 3, the q_{min} stays well below one during the whole sawtooth period. The quality of the current profile reconstruction is verified with the locations of q=1 rational surface. In discharge 51603, a q=1 surface is established in the plasma. At 3100ms and 5000ms, the inversion radius of sawtooth on 1.8*m* (high field side) and 2.04*m* (low field side) is observed clearly by ECE. This is in good agreement with the q profile reconstructed by using POINT data (shown in figure 3). Another q profile is overlaid at 5800ms when sawtooth disappears. Again, the reconstructed q profile shows good agreement with the experimental observation. The minimum q is well above the unity, in consistent with sawtooth suppression. The q_{min} stays below one during the sawtooth period. This technique can provide a useful alternate method that can be used to provide a reasonably accurate determination of the current and profiles for the tokamaks without MSE diagnostics. It can also be used in conjunction with MSE data and other internal information to provide a more accurate determination of the current and profiles. As shown in Fig. 5, the current profiles and q profile by using EFIT reconstruction with POINT data demonstrated the current profiles temporal evolution just before H-L back transition. POINT can provide a very useful tool for current and q profiles for EAST tokamak.

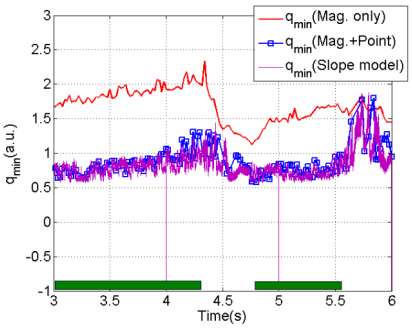

FIG. 3. q_{min}temporal evolution in 51063#. From EFIT and slope mode.

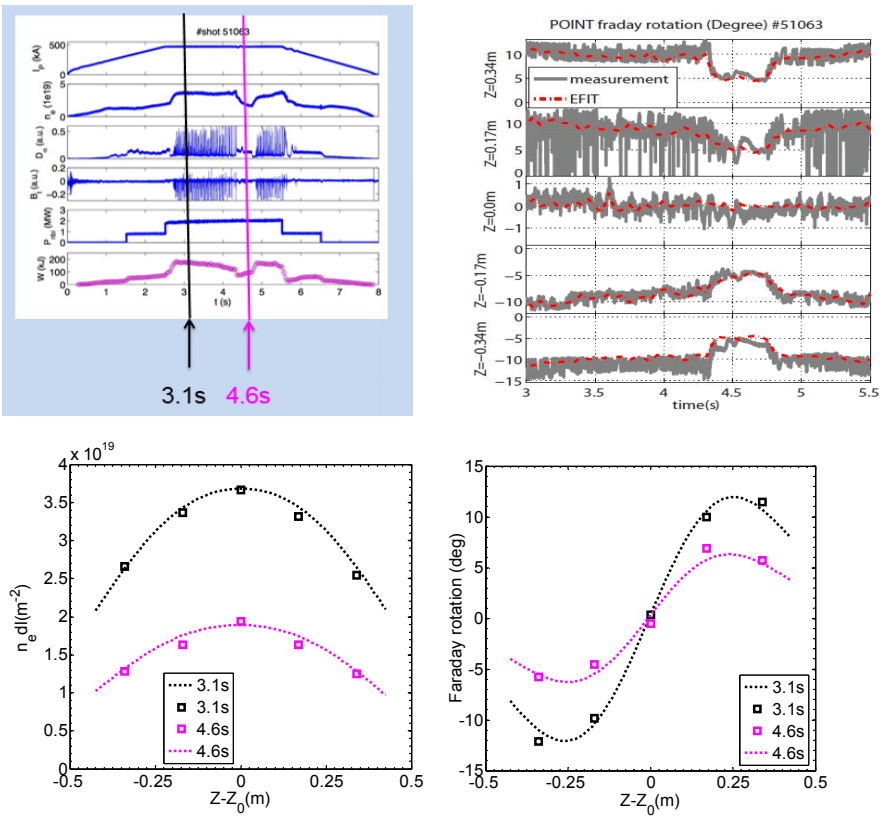

FIG. 4. Line-integrated and inverted profiles w/ and w/o EFIT in 51063#.

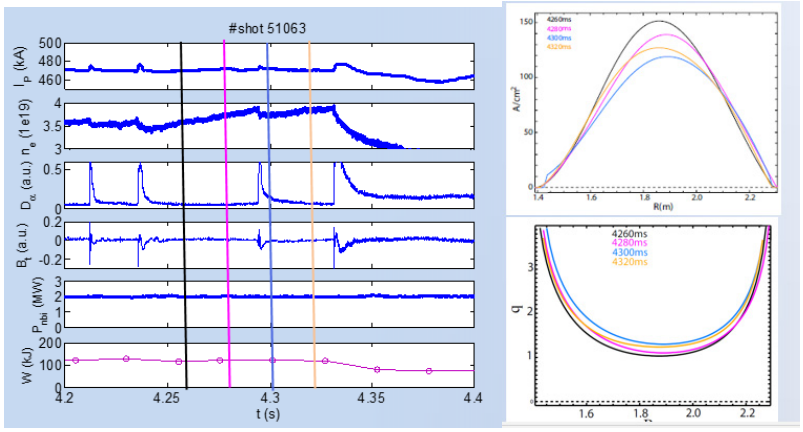

FIG. 5. Temporal evolution of current profiles and q profiles w/ EFIT in 51063#.

4. Summary and Future Plans

A five-chord layout has been installed with expansion to 11 chords anticipated to fully diagnose the core region of EAST plasmas in next campaign. A Digital Phase Detector with 250 kHz bandwidth, which will provide real-time Faraday rotation angle and density phase shift output for use in plasma control, have been developed for use on the POINT system. Reliability of both polarimetric and interferometric measurement are obtained in 22s H mode discharge and 52s long pulse discharge, indicating the density gradient in H-mode discharge does not impact POINT measurements and that system works for any heating scheme on EAST so far. The electron line-integrated density resolution of POINT is less than 1×10^{16} m^{-2} ($<1^{o}$), and the Faraday rotation angle rms phase noise is $<0.1^{o}$. With the high temporal(~1 μsec) and phase resolution($<0.1^{o}$), perturbations associated with the sawtooth cycle and MHD activity have been observed. The current profile, density profile and safety factor(q) profile are reconstructed by using EFIT code from the external magnetic and the validation POINT data. Realtime EFIT with Faraday angle and density phase shift constraints will be implemented in the plasma control system in the future.

Acknowledgments

This work is supported by the National Magnetic Confinement Fusion Program of China with contract No.2012GB101002, No.2014GB106002 and the National Nature Science Foundation of China with contract No.11375237. This work is also partly supported by the US D.O.E. contract DESC0010469 and the Collaborative Research Program of the Research Institute for Applied Mechanics, Kyushu University.

References

[1]H.Q. Liu *et al.*, J. Instrum. **8**, C11002 (2013).
[2]H.Q. Liu *et al.*, Rev. Sci. Instrum. **85**, 11D405 (2014).
[3]G. Dodel and W. Kunz, Infrared Phys. **18**,773 (1978).
[4]W.X. Ding et al., Rev. Sci. Instrum. **81**, 10D508 (2010).
[5]J.H. Rommers et al., Rev. Sci. Instrum. **68**, 1217 (1997).
[6]J. Chen et al., Rev. Sci. Instrum. **83**, 10E306 (2012).
[7] P. Xu et al., Rev. Sci. Instrum. **81**, 10D507 (2010).

Current status and future application of the LHD Thomson scattering system

Ichihiro YAMADA

National Institute for Fusion Science, 322-6 Oroshi, Toki, 509-5292, Japan

INTRODUCTION

The Large Helical Device (LHD) Thomson scattering system has routinely measured electron temperature (T_e) and density (n_e) profiles of LHD plasmas along the LHD major radius since the second LHD experiment campaign, 1999. It is one of the most powerful Thomson scattering systems in the world. During the past 15 years, we have improved the LHD Thomson scattering system for increasing data reliability and accuracy. In this article, we discuss the current status of the LHD Thomson scattering system and future plans.

LHD THOMSON SCATTERING SYSTEM

Figure 1 shows the schematic diagram of the LHD Thomson scattering system. We use four YAG lasers, a 1.6 J/30 Hz laser (Continuum 9030), two 2 J/10 Hz lasers (Thales 230/10), and 0.5 J/50 Hz laser (Continuum 8050). The laser beams are injected from an outer laser input window and travel through LHD plasmas along the major radius. The number of spatial measurement points and spatial resolution are 144 and ~20 mm respectively. The sampling frequency is 10-100 Hz (100-10 msec), which depends on the laser repetition frequency. [1-3]

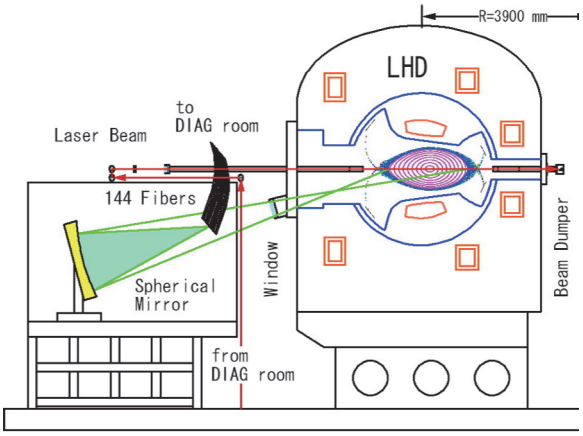

Fig. 1. Schematic diagram of the LHD Thomson scattering system. The LHD Thomson scattring system measures T_e and n_e profiles along the LHD major radius.

Thomson scattering light is collected by a large spherical mirror (1.5m x 1.8m) and analyzed by 144 polychromators having five wavelength channels. The measurable T_e and n_e ranges are T_e = 1 eV - 30 keV and n_e = 10^{18} - 10^{22} m^{-3} respectively. In order to obtain absolute densities, the system has been absolutely calibrated by using the Rayleigh scattering in gaseous nitrogen. [4]

BACKWARD AND FORWARD SCATTERING MEASUREMNETS

In the original design of the LHD Thomson scattering system, a backward scattering configuration, in which a typical scattering angle was 167 degree, was adopted. The laser beam is simply absorbed by a beam dump after traveling through LHD plasma. Recently we removed the beam dump and installed a beam-returning mirror, a relay lens and an optical delay path of 30 m to observe forward Thomson scatting signals as shown in Fig.2. [5, 6] In the forward scattering configuration, typical scattering angle is 13 degree. By combining the backward and forward scattering measurements, two T_e components are obtained at each observation point because the electron velocity along the vector difference of the incident laser direction and observation direction is observed in Thomson scattering measurements as shown in Fig.3. In the original design, we installed an observation window, Window 1. In addition to it, we installed a new window, Window2, an optical fiber, light collection mirror and polychromator, as shown in Fig. 4. The center of the Window 2 is located on the LHD mid-plane. The observation point is set to be the LHD plasma center. By adding optical fibers and polychromators, the number of observation points will be increased in near future.

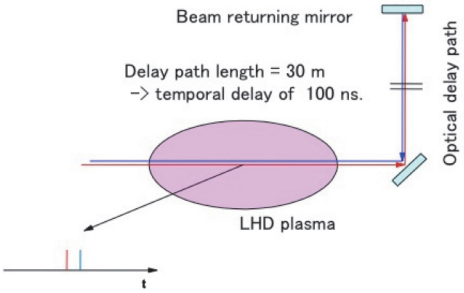

Fig. 2. Schematic diagram of the beam returning system.

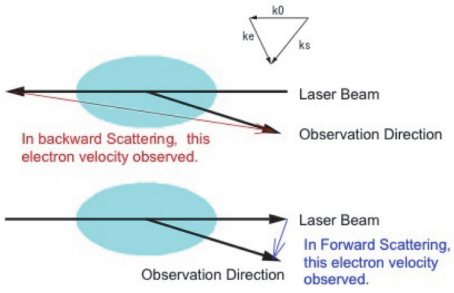

Fig. 3. T_e component obtained in Thomson scattering diagnostics.

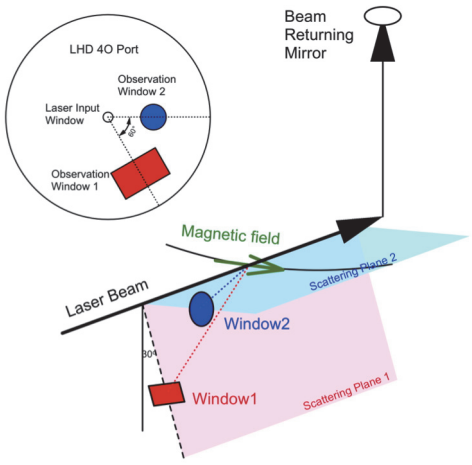

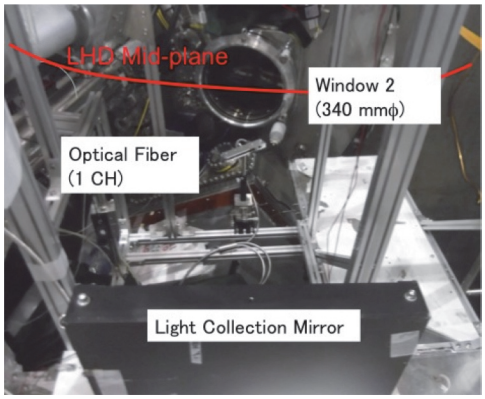

Fig. 4. Schematic diagram of the two observation windows and picture of the newly installed light collection optics.

Z_{eff} MEASUREMENTS USING THE LHD THOMSON SCATTERING SYSTEM

Effective ionic charge, Z_{eff}, is one of the important plasma parameters to characterize the plasma. Since bremsstrahlung light emission is expressed by a function of Z_{eff}, the information of Z_{eff} is obtained by measuring plasma bremsstrahlung. The bremsstrahlung power spectrum, *j(e)*, is given by,

$$\mathrm{j}(\varepsilon) = \frac{8}{3} r_e^3 \frac{m_e c^3}{\lambda_i (1+\epsilon)^2} n_e^2 Z_{eff} \sqrt{\frac{2 m_e c^2}{\pi T_e}} \exp\left[-\frac{hc}{T_e \lambda_i (1+\epsilon)}\right] \ln\left[\frac{4 T_e \lambda_i (1+\epsilon)\gamma}{hc}\right] \qquad (1)$$

where ε is the normalized wavelength, r_e and m_e are the classical electron radius and mass respectively, n_e and T_e are electron density and temperature respectively, h is the Plank constant, and γ is the Euler constant. [7]

Thomson scattering systems observe not only Thomson scattering light but also bremsstrahlung light simultaneously. From the point of view on Thomson scattering diagnostic, the bremsstrahlung light is a background light to be subtracted from measured raw signals, however it includes useful information for the estimation of Z_{eff}. Indeed, some Thomson scattering teams have proposed Z_{eff} measurement using Thomson scattering system. [7-9] We have also installed a plasma light measurement system on the LHD Thomson scattering system. [10] At the present, plasma light signals detected by 80 polychromators have been recorded whereas 144 polychromators are operated for Thomson scattering measurements. The number of measurement points of the plasma light measurement system will be increased up to 144 by adding ADCs.

Figure 5 shows an example of temporal histories of plasma light signals measured by a polychromator that sees the LHD plasma center, R=3.6 m. As a reference, temporal evolutions of T_e and n_e at the same position are also plotted (thick blue and red curves respectively). It is noted that the $T_e s$ and $n_e s$ are local values, however the plasma light signals are line-integrated values. In the plasma discharge, ECH is first applied at t=3-5 sec, and after then, NB is injected. Figures 6 shows plasma light profiles, T_e and n_e profiles at t = 6.0 sec. The plasma light profiles show hollow shapes similar to electron density profiles, and seem to have weak dependence on

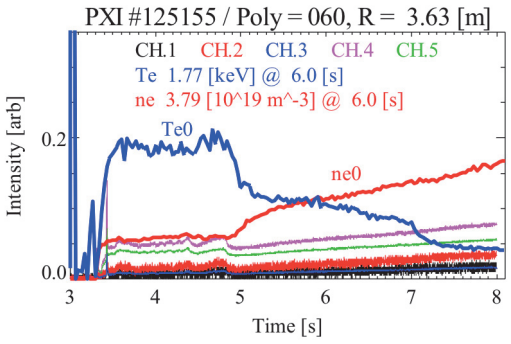

Fig. 5. Temporal behaviors of plasma light and T_e0 and n_e0.

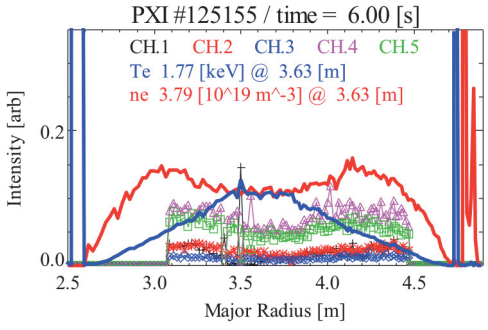

Fig. 6. plasma light profiles, and T_e and n_e profiles at t = 6.0 sec.

electron temperature, as expected. Careful analysis to determine Z_{eff} is now in progress.

SUMMARY

The LHD Thomson scattering system has routinely measured T_e and n_e profiles of LHD plasmas along the LHD major radius. We have improved the LHD Thomson scattering system for increasing data reliability and accuracy. We installed the beam returning system and new light observation optics to carry out backward and forward scattering measurements. In addition, the plasma light monitor system has been installed to estimate Z_{eff} profiles by using the LHD Thomson scattering system.

This work was supported by the NIFS LHD project budgets (NIFS14ULHH005 and NIFS14ULHH801), JSPS KAKENHI Grant Number 25289341, and JSPS-NRF-NSFC A3 Foresight Program in the field of Plasma Physics (NSFC: No.11261140328, NRF: No. 2012K2A2A6000443).

References

[1] K. Narihara *et al.*, Fusion Eng. Design, **34-35**, 67 (1997).
[2] K. Narihara *et al.*, Rev. Sci. Instrum., **72**, 1122 (2001).
[3] I. Yamada *et al.*, Fusion Sci. Tech., **58**, 345 (2010).
[4] I. Yamada *et al.*, Plasma Fusion Res., S1106 (2007).
[5] I. Yamada *et al.*, 40th EPS conference, Espoo, Finland (2013).
[6] I. Yamada *et al.*, 41th EPS conference, Berlin, Germany (2014)
[7] O. Naito and T. Hatae, JAERI Res, 33 (2002).
[8] J. H. Lee *et al.*, Rev. Sci. Instrum. **83**, 10E334 (2012).
[9] M. Aftanas *et al.*, Rev. Sci. Instrum. **83**, 10E350 (2012).
[10] K. Narihara *et al.*, Plasma Fusion Res., **2**, S1107 (2007).

Recent RMPs research on the J-TEXT tokamak

G. Zhuang[1], Q.Q. Yu[2], K.W. Gentle[3], Q.M. Hu[1], Y.H. Ding[1], M. Zhang[1], Z.P. Chen[1], Z.J. Yang[1], L. Gao[1], X.Q. Zhang[1], Z.F. Cheng[1], Y. Pan[1], X.W. Hu[1], K.X. Yu[1], H. Huang[3], the J-TEXT team[1]

[1]*State Key Laboratory of Advanced Electromagnetic Engineering and Technology, School of Electrical and Electronic Engineering, Huazhong University of Science and Technology, Wuhan 430074, P.R. China*
[2]*Max-Planck-Institut für Plasmaphysik, 85748 Garching, Germany*
[3]*Institute for Fusion Studies, University of Texas at Austin, Austin, 78712, USA*

Abstract. The recent resonant magnetic perturbations (RMPs) research progress on the J-TEXT tokamak is introduced. On one hand, the study aiming for unlocking the m/n = 2/1 locked mode (LM) is carried out by using rotating RMPs. After mode locking by using static RMPs, another rotating RMP with several kilo-Hz frequency is applied to drive the static LM to rotate. The unlocking of LM is realized by using rotating RMP with different frequency and amplitude. In addition, the unlocking process is sensitive to both the amplitude and the frequency of the rotating RMP as well as the amplitude of static RMP. On the other hand, the effect of rotating RMPs on particle confinement is studied. It is found that RMPs cause improved (degraded) particle confinement when its frequency is higher (lower) than the natural 2/1 tearing mode frequency, and the amount of change in electron density is proportional to the difference between these two frequencies.

1. Introduction

The Joint-TEXT (J-TEXT) tokamak [1, 2] is a conventional machine with an iron core. It has a major radius R_0 = 105 cm and a minor radius r = 25-29 cm with a movable titanium-carbide coated graphite limiter. The main parameters of a typical J-TEXT discharge are center-line toroidal field B_T ~ 2.0 T, plasma current I_p ~ 200 kA lasting for 400 ms, plasma densities n_e = 1-10×10^{19} m^{-3}, and electron temperature T_e ~ 1 keV. In the last year, Resonant magnetic perturbations (RMPs) are mainly used to study the effect on tearing mode (TM) and electron density.

RMPs generated by external saddle coils have important applications in present tokamak plasmas. RMPs have been shown to be a promising technique in suppression or mitigation of edge localized modes (ELMs) in several devices [1-5], and in active stabilization of resistive wall modes (RWM) [6-12]. RMPs are also used to explore the avoidance of neoclassical tearing mode (NTM) locking and its associated disruption [13], to aid the stabilization of locked modes by modulated or continuous electron cyclotron current drive (ECCD) [14] and re-rotation of locked mode in DIII-D [15]. However, as a drawback, the application of RMPs results in more complicated plasma response. For example, density pump-out is frequently observed in ELMs suppression experiments [1, 2, 16], contrast with which either degradation or improvement of particle confinement are observed in TEXTOR L-mode plasma [17-19]. The application of RMPs can also either decrease or increase the plasma rotation [20-24]. Furthermore, depending on plasma parameters, RMPs exhibit contrast effect on tearing mode stability, such as mode suppression and mode locking [20, 25, 26. 27]. A clear understanding of the physical mechanisms that behind the plasma response caused by RMPs is therefore mandatory for an optimal implementation of RMPs application on ITER.

2. Experimental results

2.1 Experimental setup

J-TEXT has been equipped with two sets of saddle coils. One set is installed outside the vacuum vessel and generates static RMP (named static RMP or SRMP), and another set is installed inside the vacuum vessel, which can generate either static or rotating RMP (named dynamic RMP or DRMP) [22]. Both SRMP and DRMP are used together in the experiments. The field spectrum of SRMP calculated in vacuum condition, which is dominated by the m/n = 2/1 and 3/1 components for edge safety factor q_a ~ 3.5. The 2/1 component at the plasma edge is $b^{2,1}{}_r(r = a) = 0.54$ Gauss/kA. DRMP is used to generate rotating RMP with its frequency ranging from 1 kHz to 6 kHz. The magnetic field of DRMP is calculated for the frequency of 5 kHz, taking the eddy current in the

vacuum vessel into account. The field spectrum of DRMP has a dominant m/n = 2/1 component with its strength $b^{2,1}_r(r = a) = 0.47$ Gauss/kA at plasma edge.

2.2 Locked mode unlocking by rotating RMP

When a static locked mode (LM) is maintained, the rotating RMP is applied with f_{RMP} = 4 kHz and I_R = 3.6 kA for shot 1032199 as shown in figure 1 [28], here f_{RMP} and I_R are the frequency and coil current of rotating RMP, respectively. Figure 1 show that the LM unlocks from the static RMP and locks to the rotating RMP when I_R increases to 3.2 kA at t = 0.32 s, accompanying with which a relatively large magnetic fluctuation appears in Mirnov signal (figure 1(c)) and its frequency is 4 kHz (figure 1(f)). In addition, the 2/1 tearing mode rotates non-uniformly even when it is entrained, since it is modulated by static RMP (together with error field), and there are more than one harmonics as shown in figure 1(f). Besides, b_r signal begins to decline quickly (figure 1(d)) and the plasma toroidal rotation V_{CV} recovers to its initial value (figure 1(e)). Correspondingly, the contour plot of Mirnov signals in the interval of 0.317 s < t < 0.322 s are shown in figure 1 (g), indicating that the unlocking process exhibits two stages, i.e. the oscillating stage and the unlocking stage. As I_R is further increased, the magnetic island oscillates in two periods (marked by the dashed curves) and then transforms to unlocking stage (t >0.32 s).

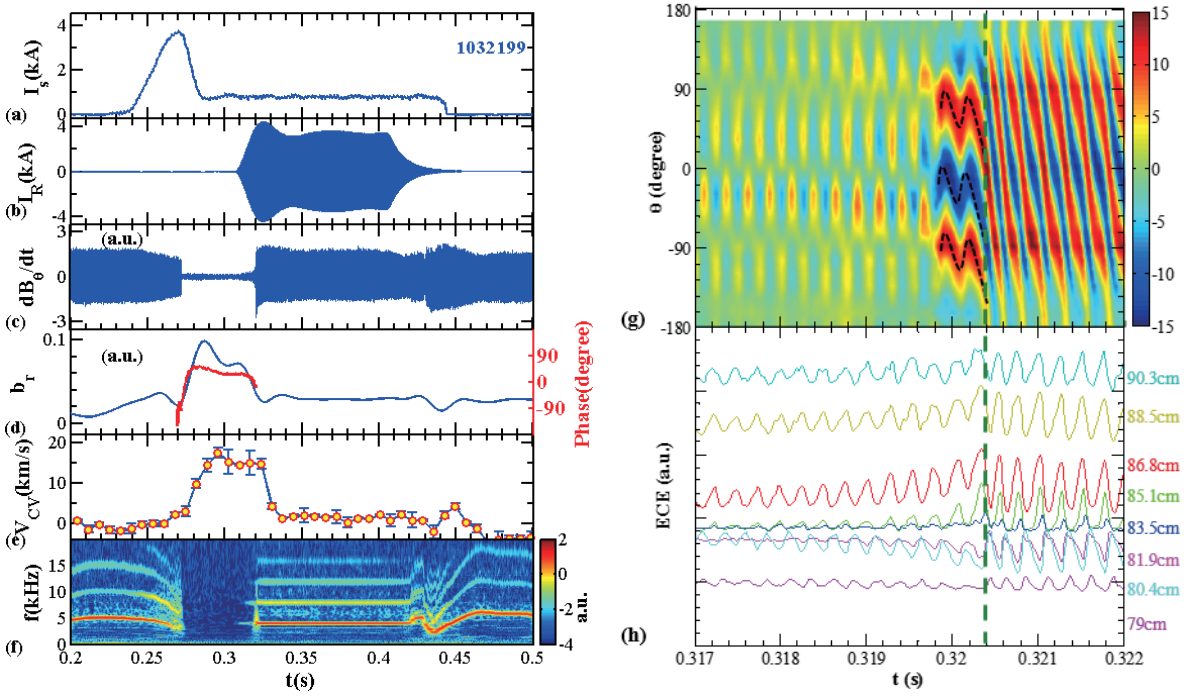

Figure 1 Time evolution of LM unlocking for shot 1032199. (a) static RMP coil current I_s, (b) rotating RMP coil current I_R with a frequency is 4 kHz, (c) Mirnov signal dB_θ/dt, (d) LM detector signal b_r (blue curve) and the phase of magnetic island during mode locking (red curve), (e) plasma toroidal rotation V_{CV}, (f) 2/1 TM frequency f, (g) the contour plot of Mirnov integral signals in the interval of 0.317 s < t < 0.322 s, and (h) time evolution of ECE signals.

Figure 1 (g) indicates that the transformation from mode oscillating to unlocking is in a time period shorter than 1 ms. In figure 1(h), the evolution of ECE signals at different radial positions are presented, which also shows the process from oscillating to unlocking. Based on the result as shown in figure 1, the unlocking process can be conclude as following: the applied rotating RMP firstly drives the static magnetic island to oscillate around its locked phase, and the oscillation amplitude increases as I_R increases, at last the oscillation transforms to unlocking with a sufficiently strong I_R.

Further experiments have been carried out by keeping the background plasma parameters to be the same, while only the amplitude and frequency of rotating RMP, the amplitude of static RMP are changed separately: I_{s0} = 0.7, 0.8, 1, 1.2 kA, f_{RMP} = 1, 2, 4 kHz, and for each I_{s0} and f_{RMP}, I_R is scanned from 2 to 5 kA. The unlocking threshold for ratio of I_R/I_{s0} is shown as a function of f_{RMP} in figure 2. It is seen that there is a clear division between the cases with and without unlocking, and the unlocking threshold for I_R/I_{s0} linearly increases with f_{RMP} with the dependence of I_R/I_{s0} = $0.95f_{RMP}$(kHz)+1.7. Figure 7 indicates that when the amplitudes of static RMP and rotating RMP

are kept the same, unlocking can be more easily realized when f_{RMP} is lower, indicating the unlocking of a LM is sensitive to the amplitude of static RMP (or error field) and the frequency of rotating RMP.

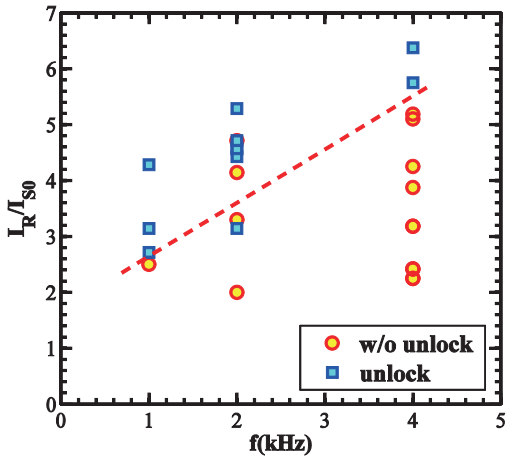

Figure 2 the unlocking threshold for ratio of I_R/I_{S0} is shown as a function of f_{RMP}.

2.3 Influence of rotating RMPs on electron density

An example of the effect of RMP on particle transport is shown in figure 3 with f_{RMP} = 6 kHz and I_c = 2.6 kA at the flattop. Before applying RMPs, a 2/1 TM saturates and rotates at a frequency $f_{2/1}$ = 3.5 kHz (figure 3(f)) [29]. At t = 0.225 s, RMPs are turned on, and mode locking happens later at t = 0.24 s, so that the 2/1 TM is driven to rotate synchronously with RMPs at 6 kHz. The amplitude of the poloidal field perturbation $\tilde{B}_\theta$ becomes larger after mode locking (figure 3(e)), indicating a larger island width. The line-averaged electron density at R = 1.05 m (plasma core) increases from 1.08 to 1.22×10^{19} m^{-3}, with a relative change $\Delta\bar{n}_e/\bar{n}_{e0}$ =13%, where $\bar{n}_{e0}$ is the initial electron density before the application of RMP, $\Delta\bar{n}_e=\bar{n}_e-\bar{n}_{e0}$, and $\bar{n}_e$ is the density in steady state during applying RMPs. The density at plasma edge changes little as indicated by the time trace of $\bar{n}_e$ at R = 1.25 m. The electron temperature decreases as shown by the ECE signal at R = 0.95 m. The edge recycling decreases a little as indicated by the Hα signal at r = 0.27 m. At t = 0.355 s during I_c ramping down, the TM unlocks from the RMP. At the same time $\bar{n}_e$ begins to decrease, and the 2/1 TM frequency slows down to 3.8 kHz. Results shown in Figure 3 indicate that RMPs improves particle confinement in this case, and such an improvement mostly happens in the core region inside q = 2 surface.

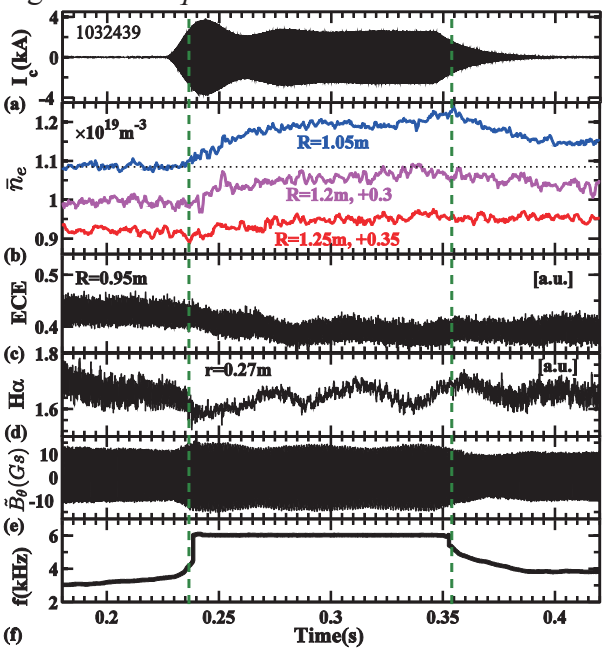

Figure 3 Time traces of (a) RMP coil current I_c, (b)

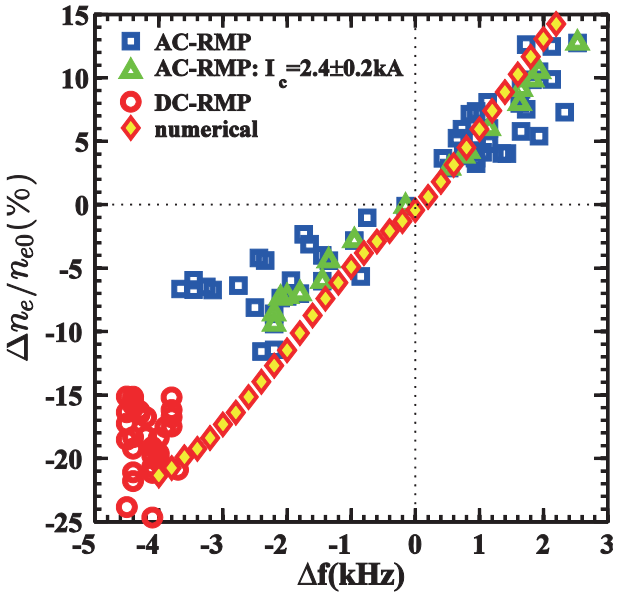

Figure 4 (a) Relative change in line averaged density

line averaged density $\bar{n}_e$ at R = 1.05 m, 1.2 m and 1.25 m, (c) ECE signal at R = 0.95 m, (d) Hα signal at r = 0.27 m, (e) poloidal field perturbations $\tilde{B}_\theta$, and (f) 2/1 TM frequency $f_{2/1}$. The RMP frequency is 6 kHz. For comparison, $\bar{n}_e$ is added by 0.3 and 0.35 for the channels at R = 1.2 and 1.25 m.

$\Delta\bar{n}_e/\bar{n}_{e0}$ at plasma core versus the frequency difference Δf, (b) w/w_0 versus Δf and (c) $\Delta\bar{n}_e/\bar{n}_{e0}$ versus w/w_0, where w_0 and w are the island width before and after applying RMPs, respectively. The TM frequency $f_{2/1}$ ranges from 3.5 kHz to 4.5 kHz, and the RMP coil current I_c ranges from 1.6 kA to 3.2 kA.

Systematical experiments have been carried out by keeping the background plasma parameters to be the same, while only the amplitude and frequency of RMPs are changed: f_{RMP} = 1, 2, 3, 4, 4.85 and 6 kHz, and for each frequency I_c is scanned from 1 kA to 3.2 kA. The mode locking usually happens in experiments for I_c > 1.6 kA. In figure 4(a), $\Delta\bar{n}_e/\bar{n}_{e0}$ is shown as a function of Δf (= f_{RMP}-$f_{2/1}$). $\Delta\bar{n}_e$ is the change in electron density at plasma core in steady state by RMPs with 1.6 kA < I_c <3.2 kA (squares). The results with about the same value of I_c, I_c = 2.4±0.2 kA, are marked by triangles. It is seen that RMPs improve particle confinement ($\Delta\bar{n}_e/\bar{n}_{e0} > 0$) for $\Delta f > 0$ but degrade it for $\Delta f < 0$, and $\Delta\bar{n}_e/\bar{n}_{e0}$ linearly depends on Δf if the RMP amplitude is about the same. The edge recycling is found to decrease for $\Delta\bar{n}_e/\bar{n}_{e0} > 0$ ($\Delta f > 0$) but increase for $\Delta\bar{n}_e/\bar{n}_{e0} < 0$ ($\Delta f < 0$). Figure 4(a) indicates the significant role of the relative frequency Δf in the changed particle confinement by RMPs. The results obtained by static RMPs are also shown in figure 4(a) by circles. A linear dependence of $\Delta\bar{n}_e/\bar{n}_{e0}$ on Δf exists when including the results from both the static and rotating RMPs.

To compare with experimental results, full nonlinear numerical calculations have been carried out based on two-fluid equations, including the mass conservation equation, the generalized Ohm's law and the equation of motion in the perpendicular and parallel (to magnetic field) directions, as described in Ref. [30]. The numerical result of relative change in line-averaged electron density, $\Delta\bar{n}_e/\bar{n}_0$, is shown as a function of Δf by diamond in figure 4. The numerical results approximately agree with experimental ones.

3. Summary

The recent RMP research work on the J-TEXT tokamak emphasizes on the interaction between RMPs and TM and plasma response to RMPs. On one hand, the unlocking of 2/1 LM is realized on J-TEXT tokamak by using rotating RMP of several kilo-Hz frequency. The unlocking process is characterized by oscillating stage and unlocking stage, and the island width is decreased slightly in the oscillating stage. Further studies indicate that the unlocking process is sensitive to f_{RMP}, the ratio of I_R and I_{s0}. On the other hand, both improvement and deterioration of particle confinement caused by rotating RMPs have been observed on J-TEXT discharges in the presence of the m/n = 2/1 TM. The applied rotating RMP causes confinement improvement (deterioration) when its frequency is higher (lower) than the natural frequency of the 2/1 TM, and the applied RMP causes more change in the electron density for a larger difference between these two frequencies. These results reveal the role of relative rotation between the electron fluid and RMPs in affecting the particle transport.

Acknowledgement We are grateful for the help from the Southwestern Institute of Physics and the Institute of Plasma Physics, Chinese Academy of Science. This work is partly supported by the JSPS-NRF-NSFC A3 Foresight Program in the field of Plasma Physics (NSFC No.11261140328).

References

[1] EVANS, T. E., et al. Phys. Rev. Lett. **92** (2004) 235003
[2] LIANG, Y., et al. Phys. Rev. Lett. **98** (2007) 265004
[3] KIRK, A., et al. Nucl. Fusion. **50** (2010) 034008
[4] SUTTROP, W., et al. Phys. Rev. Lett. **106** (2011) 225004
[5] JEON, Y. M., et al. Phys. Rev. Lett. **109** (2012) 035004
[6] LIU, Y. Q., et al. Phys. Plasmas. **7** (2000) 3681
[7] OKABAYASHI, M., et al. Phys. Plasmas. **8** (2001) 2071
[8] SABBAGH, S. A., et al. Phys. Rev. Lett. **97** (2006) 045004
[9] FRASSINETTI, L., et al. Plasma Phys. Control. Fusion **55** (2013) 084001
[10] RATH, N., et al. Nucl. Fusion. **53** (2013) 073052
[11] LIU, Y. Q., et al. Plasma Phys. Control. Fusion **44** (2002) L21

[12] LIU, Y. Q., et al. Nucl. Fusion. **44** (2004) 232
[13] OKABAYASHI, M., et al. 40th EPS Conf. on Plasma Physics (Espoo, Finland, 2013) **P2** 152
[14] VOLPE, F., et al. Phys. Plasmas. **16** (2009) 102502
[15] VOLPE, F., et al. 4th IAEA-TM on ECRH for ITER (2007) **P39**
[16] EVANS, T. E., et al. Nucl. Fusion. **48** (2008) 024002
[17] FINKEN, K. H., et al. Phys. Rev. Lett. **98** (2007) 065001
[18] SCHMITZ, O., et al., J. Nucl. Mat. **390-91** (2009) 330
[19] SCHMITZ, O., et al. Nucl. Fusion. **52** (2012) 043005
[20] HENDER, T. C., et al. Nucl. Fusion. **32** (1992) 2091
[21] FINKEN, K. H., et al. Phys. Rev. Lett. **94** (2005) 015003
[22] KOSLOWSKI, H. R., et al. Nucl. Fusion. **46** (2006) L1
[23] KOSLOWSKI, H. R., et al. Plasma Phys. Control. Fusion **48** (2006) B53
[24] DE BOCK, M. F. M., et al. Nucl. Fusion. **48** (2008) 015007
[25] HU, Q. M., et al. Nucl. Fusion. **52** (2012) 083011
[26] RAO, B., et al. Phys. Lett. A. **377** (2013) 315
[27] RAO, B., et al. Fusion Eng. Des. **89** (2014) 378
[28] JIN, H., et al. Plasma Phys. Control. Fusion (2015) in press
[29] HU, Q. M., et al. Nucl. Fusion. **54** (2014) 122006
[30] HU, Q. M., et al. Nucl. Fusion. **54** (2014) 064013

Exploration of Advanced Tokamak Operation in KSTAR

Yong-Su Na on behalf of the KSTAR Team

Department of Nuclear Engineering, Seoul National University, Seoul, Korea
Email : ysna@snu.ac.kr

The extended advanced regime in 2014 KSTAR campaign is reported in terms of high β_p scenario with $q_{95} \geq 8.5$ and hybrid scenario at q_{95}~5.5. High performance above typical H-modes and full non-inductive current drive have been achieved in both scenarios. The origin of confinement enhancement is investigated and the pedestal improvement is revealed to be the main cause.

1. Introduction

KSTAR has started to address the advanced tokamak (AT) physics since 2012 [1]. The progress made in the AT research is presented in figure 1 (a) where H_{89} above 2.0 and β_N up to 3.5 has been achieved. The enhancement of the energy confinement is clearly seen in these scenarios when plotting against the scaling law derived from KSTAR H-mode plasmas, where the scaling law is $\tau_{E,KSTAR\ H\ scaling} = 0.793\kappa^{-0.68}I_p^{1.41}B_T^{-0.29}P_L^{-0.69}$ [2] (see figure 1 (b)). It is noteworthy that all these advanced regimes have been obtained with low heating power ≤ 4 MW of neutral beam injection (NBI) and low current ramp-up rate ~ 0.4 MA/s. In this paper, experimental results are analysed for two types of advanced scenarios, $q_{95} \geq 8.5$ scenario and $q_{95} \sim 5.5$ scenario. The former is for the steady state operation with high β_p which is described in section 2.1. The latter is for hybrid mode described in section 2.2. The origin of the confinement enhancement observed in these scenarios are discussed in section 3. The conclusion is drawn in section 4.

2. Development of Advanced Scenarios in KSTAR

$q_{95} \geq 8.5$ for steady-state operation with high β_p

In advanced scenarios with $q_{95} \geq 8.5$, the plasma current was lowered to 300-400 kA to increase the non-inductive current drive fractions particularly the bootstrap current fraction by increasing β_p. The toroidal magnetic field strength was 2 T. In the very beginning of the discharge, ECH was injected to increase the electrical conductivity of the plasma, then each NBI was applied one by one during the current ramp-up phase by keeping the plasma density as low as possible to delay the current diffusion. The ECH was turned off during the NBI heating phases to avoid decrease of the toroidal rotation. The representative discharge is presented in figure 2. As shown, the L- to H-mode transition occurred at 1.1 s after the 2nd NBI was injected which helped to prevent decrease of central q-value and to form a target q-profile. The plasma performance was increased after the transition but suddenly collapsed. However, the plasma quickly recovered from this event and the plasma performance was increased again even further up to β_N of 3.0, β_p of 3.5, H_{89} of 2.0, and H_{98} of 1.7 after turning on the 3rd NBI but also cannot be sustained. This strange oscillatory behaviour repeated until 4 s, then the plasma reached stationary conditions at a reduced performance, $\beta_N \sim 1.8$ and $H_{89} \sim 1.5$. These oscillations is found to result from the coupled inner gap and the plasma current control. When the high performance was reached, the loop voltage was significantly dropped. An interpretive ASTRA [3] simulations reveal that the plasma current is driven non-inductively more than 100% as shown in figure 2 (b). Since no measurements were available, an assumed electron density

profile is used here which satisfies the line-averaged density and the total stored energy. We scanned the density peaking to see its impact on the non-inductive current drive fraction but similar results are observed in the ASTRA simulations independent of the density peaking.

q_{95} ~ 5.5 for hybrid mode

In the advanced scenario with $q_{95} \sim 5.5$, the plasma current and the magnetic field strength were 500 kA and 2 T, respectively. A moderate heating is applied during the current ramp-up phase at low density to delay the current diffusion and to avoid an internal transport barrier formation which is the typical experimental recipe of hybrid scenarios [4]. The full heating time is carefully designed to avoid sawtooth activity. A typical discharge is shown in figure 3 (a). When all the beam sources were applied at 2.1 s, the H-mode transition occurred and high performance was achieved, β_N of 3.2, β_p of 2.5, H_{89} of 2.1, and H_{98} of 1.4. The non-inductive current drive fraction of ~100% is also observed in the ASTRA simulation. However, this high performance state couldn't be sustained due to the same radial position control problem addressed in the previous section. The plasma current overshoot technique has been applied to this scenario and the result of which is presented in figure 3 (b). The plasma current was ramped up to 0.6 MA, then linearly ramped down to 0.5 MA. This current overshoot and the heating waveform have been determined by predictive simulations with ASTRA to optimise the s/q profile [1]. As shown in figure 3 (b), the similar high plasma performance was achieved when the full power was applied. However, this regime could be sustained for about 1 s in spite of the position control error. The ASTRA modelling shows fully non-inductive current drive is achieved in this phase for about one second.

3. Investigation of Confinement Enhancement in KSTAR Advanced Scenarios

The origin of the confinement enhancement observed in the advanced scenarios is discussed in this section in terms of the ion stiffness mitigation due to the combined low magnetic shear and strong plasma rotation [5], the increase of ion temperature gradient (ITG) threshold by s/q [6], and the pedestal improvement [7].

Ion stiffness mitigation due to combined low magnetic shear and strong plasma rotation

Investigation in the current overshoot discharge, shot 10962 is described here. The magnetic shear (s), toroidal rotation (V_{tor}), and the normalised ITG length (R/L_{Ti}) are compared in figure 4 for the two different time points; one is in the high performance phase and the other is in the low performance phase. Although both the stronger toroidal rotation and the lower magnetic shear are satisfied in the high performance phase, no considerable difference is found in R/L_{Ti}. It is noteworthy that the normalised ITG lengths in most of advanced scenarios are in the level of that observed in typical H-modes in KSTAR.

Increase of ion temperature gradient threshold by s/q

We investigate the change of the ITG threshold by comparing the two hybrid scenarios at $q_{95} \sim 5$, one without and the other with the plasma current overshoot. The s/q and corresponding R/L_{Ti} profiles are compared in figure 5. As shown, the s/q profile is significantly different between the two scenarios. However, no notable difference is observed in R/L_{Ti} (compare the profiles indicated as blue stars in figure 5). Moreover, R/L_{Ti} stays in the similar level in the entire discharge even though s/q is continuously changing in the current overshoot discharge.

Pedestal improvement

Lastly, we investigate the contribution of the pedestal to the confinement enhancement. The time evolution of the ion temperature profiles are shown in figure 6. It is clearly seen that the pedestal evolves. Since the R/L_{Ti} stays more or less similar, the core temperature changes

according to the change of the pedestal. The same behaviour is also observed in high q_{95} scenarios.

4. Summary

The advanced regime has been extended in 2014 KSTAR campaign. High β_p, H_{89}, and H_{98} above typical H-modes have been achieved with full non-inductive current drive at $q_{95} \geq 8.5$. The high performance regime could not been sustained due to the strong coupling of the radial position control with the plasma current control. Slightly lower performance than $q_{95} \geq 8.5$ scenarios but higher one than typical H-modes have been achieved at q_{95}~5.5. The high performance phase could be sustained in the plasma current overshoot scenario for about 1 s. Fully non-inductive current drive has also been sustained for about 1s. It is noteworthy that all these advanced regimes have been achieved with ~4 MW NBI and 0.4 MA/s of plasma current ramp-up rate. The origin of confinement enhancement is investigated and the pedestal improvement is thought to be the main cause.

Acknowledgement

This research was supported by Ministry of Science, ICT, and Future Planning under KSTAR project and was partly supported by the JSPS-NRF-NSFC A3 Foresight Program (NRF No. 2012K2A2A6000443).

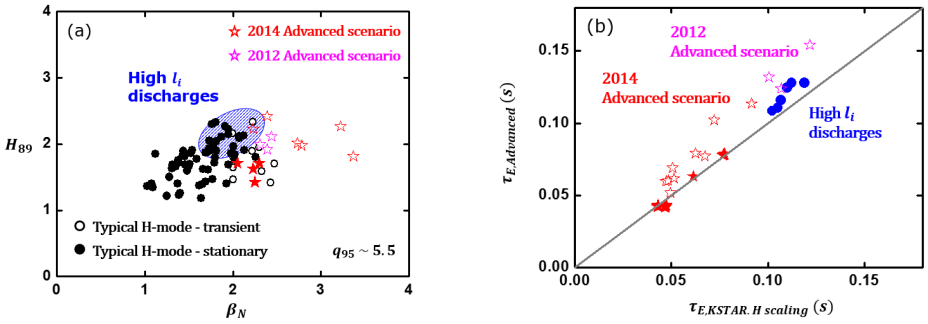

Figure 1. (a) β_N VS. H_{89} for typical H-modes and advanced scenarios in KSTAR. (b) Energy confinement time of advanced scenarios in KSTAR against the H-mode scaling law derived from KSTAR. Typical H-modes with high H_{89} are mostly high l_i discharges.

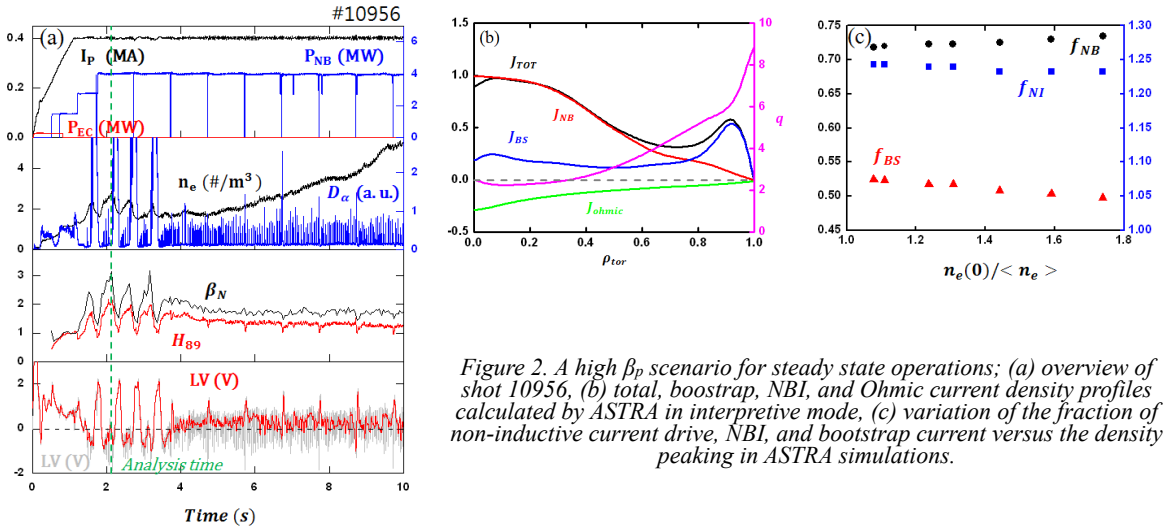

Figure 2. A high β_p scenario for steady state operations; (a) overview of shot 10956, (b) total, boostrap, NBI, and Ohmic current density profiles calculated by ASTRA in interpretive mode, (c) variation of the fraction of non-inductive current drive, NBI, and bootstrap current versus the density peaking in ASTRA simulations.

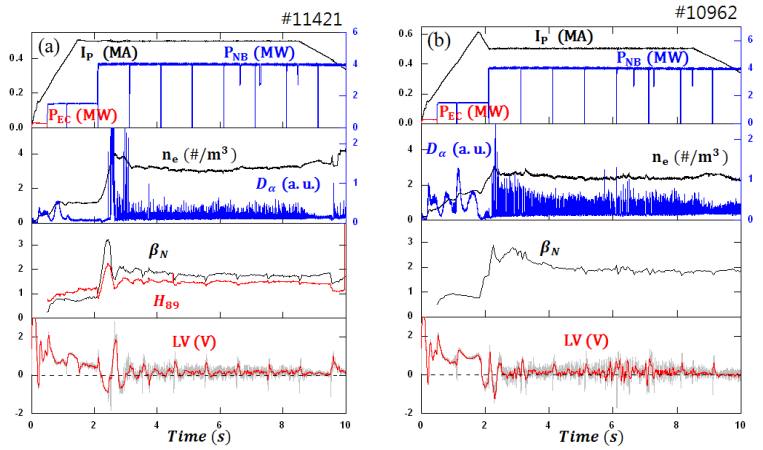

Figure 3. Hybrid scenarios with q_{95} ~ 5.5; (a) shot 11421 and (b) shot 10962 with plasma current overshoot.

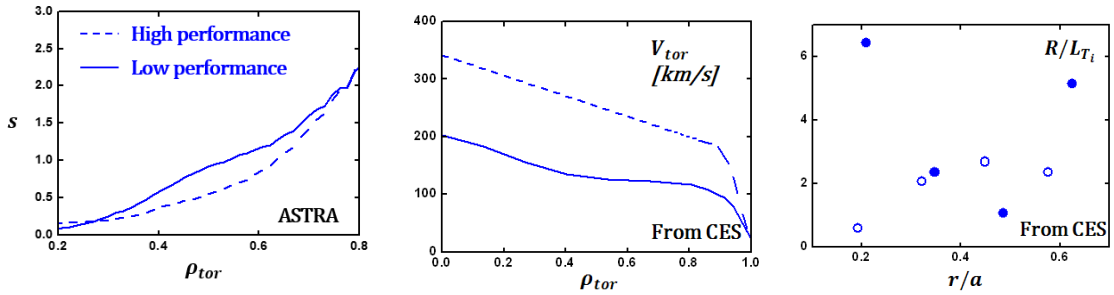

Figure 4. Comparision of magnetic shear (s), toroidal rotation (V_{tor}), and the normalised ion temperature gradient length (R/L_{Ti}) of two different time points; one is in the high performance phase and the other is in the low performance phase in the plasma current overshoot discharge, shot 10962. The dashed line and the open circle represent the high performance phase and the solid line and the closed circle represent the low performance phase.

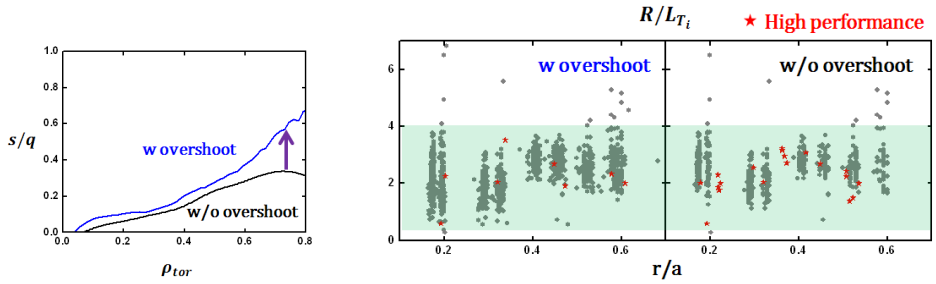

Figure 5. Comparision of s/q and R/L_{Ti} of hybrid scenarios (q_{95} ~ 5.5) with plasma current overshoot (shot 10962) and without plasma current overshoot (shot 11421). R/L_{Ti} taken from all the other time points are overlayed for comparison.

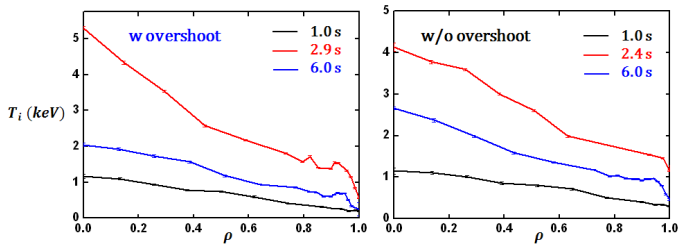

Figure 6. Evolution of ion temperature profiles in hybrid scenarios (q_{95} ~ 5.5) with plasma current overshoot (shot 10962) and without plasma current overshoot (shot 11421).

References

[1] C.S. Byun *et al.*, *Current Appl. Phy.* **14** 144 (2014)
[2] H.-S. Kim *et al.*, Nucl. Fusion **54** 083012 (2014)
[3] G. Pereverzev *et al.*, IPP-Report IPP 5/98 (2002)
[4] T. Luce *et al.*, Nucl. Fusion **54** 013015 (2014)
[5] P. Mantica *et al.*, Phy. Rev. Letters **107** 135004 (2011)
[6] S.C. Guo and F. Romanelli Phys. Fluids B **5** 520 (1993)
[7] Yong-Su Na *et al.*, Nucl. Fusion **46** 232 (2006)

Real Time Electron Temperature Profile Control using NBI and EC in KSTAR

H.-S. Kim[1], Y.-S. Na[1], S.H. Kim[2], Y.M. Jeon[3], Y.S. Bae[3], S.H. Hahn[3], M. Joung[3], H.S. Han[3], K.D. Lee[3], M.H. Woo[3], T.G. Lee[3], S.W. Yun[2], and the KSTAR team

[1]Seoul National University, Seoul, Republic of Korea
[2]ITER Organization, Route de Vinon sur Verdon, 13067 Saint-Paul-Lez-Durance, France
[3]National Fusion Research Institute, Daejeon, Republic of Korea

E-mail: ysna@snu.ac.kr

Abstract. Advanced operation modes require controls of plasma profiles to establish and to sustain the enhanced energy confinement and the non-inductive current fraction. Especially, an electron temperature profile has to be controlled to improve controllability of the safety factor profile as well as to keep the high plasma pressure. A real time electron temperature profile control system has been established in KSTAR and dedicated experiments have been carried out to control the electron temperature profile. The established electron temperature profile control system in KSTAR is composed of three parts. One is a controller for which a physics based non-adaptive control model is developed. The other is a real time measurement system of electron temperature profile which consists of real time EFIT and real time ECE. Another is a real time actuator system which consists of ~0.3 MW 110GHz ECRH and ~2.9 MW NBI. The dedicated control experiments have demonstrated the usefulness of the electron temperature profile response model and feasibility of the real time profile control system in KSTAR.

1. Introduction

Advanced operation modes, promising candidates for DEMO operations, are characterized by a combination of high plasma kinetic pressure, large fraction of self-driven current, and improved particle and energy confinement in a stationary condition. The advanced operation modes require control of plasma profiles to establish and to sustain the enhanced energy confinement and the non-inductive current fraction. Especially, the safety factor (q) profile control is essential to access and maintain the advanced operation modes [1]. In addition, the electron temperature (T_e) profile has to be also controlled to improve controllability of the q profile as well as to keep the high plasma pressure [2].

As the control of plasma profiles has to be robust against the evolution of the plasma state, a physics-based, fast and simple control algorithm which considers non-linearly coupled plasma profile evolutions and takes into account saturation and quantization of actuator powers, is preferable. The new approach to the real time plasma profile control [3] recently applied to the KSTAR experiment has remarkable features. It allows real time update of linearized plasma profile response models derived by simplifying the related physics with the dual assumption of linearity and time invariance. It has been invented as a physics-based adaptive control algorithm.

The KSTAR experiments have been initiated aiming at establishing a real time control system of multiple plasma profiles (T_e, q, and v_Φ profiles) using multiple actuators (NBI and EC) and to validate the applied physics-based control models. Our first attempt to apply the T_e profile control model to real experiments has been done in the 2013 KSTAR campaign. In

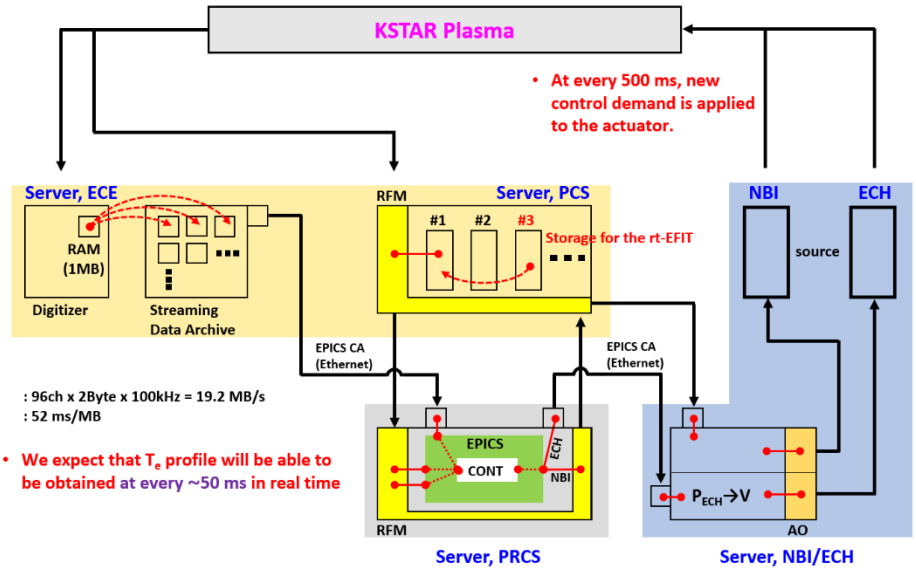

Figure 1 Schematic configuration of real time T_e profile control system in KSTAR.

these experiments, the real time T_e profile response model referred in [3] has been employed after modifying it to a non-adaptive version for simplicity. The adaptive profile control approach requires several equilibrium quantities to update the profile response models. As this requires dedicated tests and resources which were not available at the first attempt, the non-adaptive profile control approach has been applied in this work. Therefore, the profile response models and control matrix are prepared for an assumed plasma target state, such as H-mode or L-mode, and these were applied to control the T_e profile without updating them. In this paper, we introduce the dedicated control experiments performed in KSTAR and discuss the feasibility of the implemented real time profile control system.

2. Hardware and software systems for real time T_e profile control experiment in KSTAR

In this section, we explain how to implement the T_e profile control approach to the experiment in details. The real time T_e profile can be obtained from either the real time Electron Cyclotron Emission (rtECE) diagnostics or the real time Thomson Scattering (rtTS) diagnostics. Then this profile can be interpolated on to the flux coordinate for controls using the equilibrium data from the real time Equilibrium Fitting (rtEFIT) code.

Actually the KSTAR real time data acquisition system has not been yet fully developed for the real time profile control at the time we started this work. Therefore, we have temporarily implemented a dedicated hardware and software (HW/SW) system for our real time T_e profile control experiment. The schematic configuration of the HW/SW system is shown in Figure 1. The real time EFIT data containing the information of the poloidal magnetic flux at radial locations on the mid-plane is transferred by Reflect Memory (RFM) from the Plasma Control System (PCS) to the PRofile Control System (PRCS) sever at every ~7 ms. The ECE measurement provides the T_e profile at every ~50 ms. The sampling frequency for obtaining the T_e profile is limited by the size of RAM in the ECE digitizer. The data transfer from the RAM to the Streaming Data Archive which eventually uploads the data to the MDSplus server starts only when the RAM is full with the data. We have extracted the T_e profile right after transferring the data to the Streaming Data Archive. Therefore, we could obtain the T_e profile at every ~50 ms in our experiments. The extracted T_e profile is delivered to the PRCS server by the EPICS Channel Access (EPICS CA) which is a kind of Ethernet way. The T_e

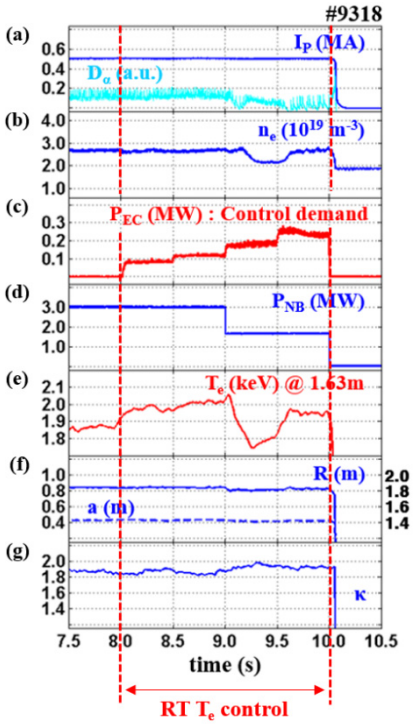

Figure 2 The description of discharge #9318. (a) I_P in MA and D_α signal in a.u., (b) n_e in 10^{19} m^{-3}, (c) P_{EC} in MW, (d) P_{NB} in MW, (e) T_e in keV at 1.63 m, (f) R_0 and a in m, and (g) κ.

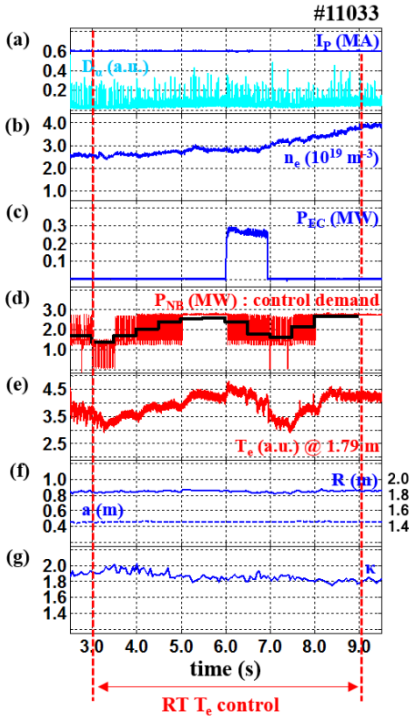

Figure 3 The description of discharge #11033. (a) I_P in MA and D_α signal in a.u., (b) n_e in 10^{19} m^{-3}, (c) P_{EC} in MW, (d) P_{NB} in MW, (e) T_e in a.u. at 1.79 m, (f) R_0 and a in m, and (g) κ.

profile control model has been implemented in the PRCS server. Based on the data obtained from rtECE and rtEFIT, the installed T_e profile control model calculates the control demand for the actuator action. Here, we have considered two actuators, EC and NBI. The new control demand on EC power is sent to the EC system control sever by the EPICS CA. One the other hand, the control demand on NBI power is firstly sent to the PCS using a RFM, then it is sent to the NBI system control server due to the safety issue.

The time sequence for real time T_e profile control in the KSTAR experiment is determined as follows. A relatively large control interval of 500 ms is chosen for the first application, not to impose pressures on other systems and actuators. During this control interval, firstly the T_e profile obtained from rtECE and rtEFIT is prepared and the ECE data is interpolated on to the normalized poloidal magnetic flux coordinate within 350 ms. In this period, several sets of T_e profile are accumulated with about 50 ms of the acquisition time. Therefore, the time averaged T_e profile is eventually prepared as the estimation of the current T_e profile and used to calculate the new control demands. Then, these control demands are held for 150 ms in a buffer. Finally the new control demands are sent to the actuators at every 500 ms. Once the real time profile control system is fully commissioned and stabilized, the control interval will be reduced.

3. Experimental results of real time T_e profile control in KSTAR

Several real time T_e profile control experiments have been carried out in the 2013 and 2014 KSTAR campaigns. Three main discharges are presented in this section. Discharge #9318 represents the real time T_e profile control experiment done using the EC power (P_{EC}) as an actuator while the NBI power (P_{NB}) was used as an external disturbance to the profile control. Discharge #11033 represents the real time T_e profile control experiment done using

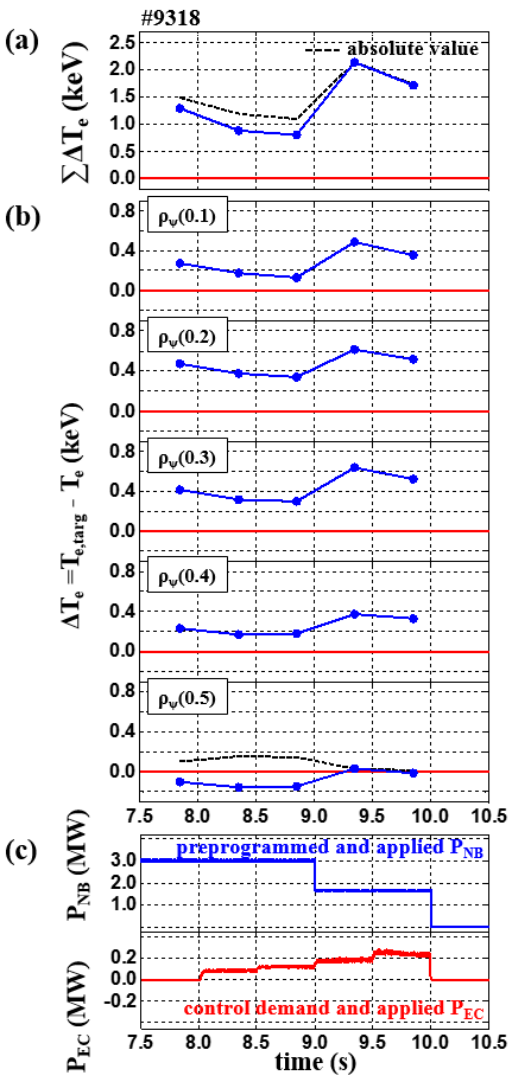

Figure 4 The error analysis of discharge #9318. (a) Total sum of control error in keV and (b) control error at each controlled position in keV. Their absolute values in black dashed line. (c) Actuator P_{EC} and disturbance P_{NB}.

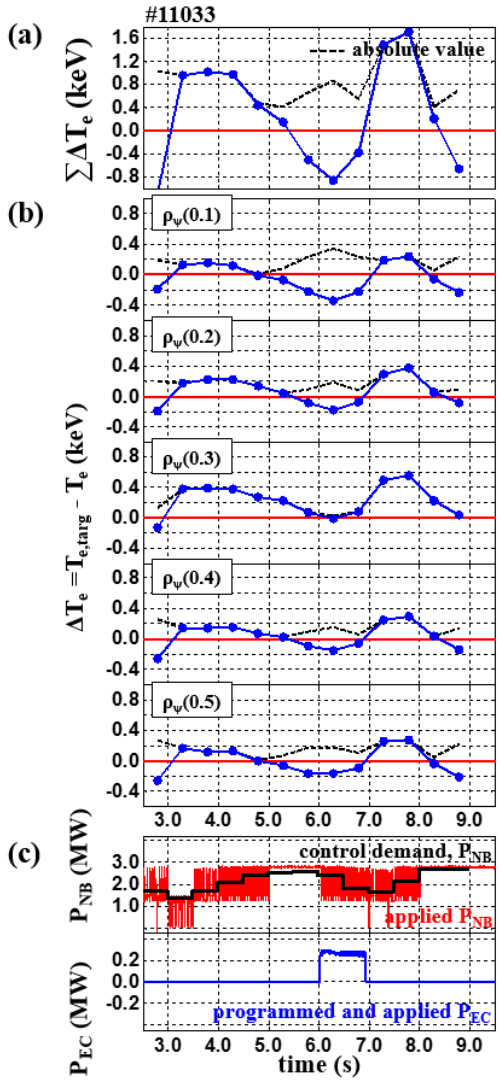

Figure 5 The error analysis of discharge #11033. (a) Total sum of control error in keV and (b) control error at each controlled position in keV. Their absolute values in black dashed line. (c) Actuator P_{NB} and disturbance P_{EC}.

the P_{NB} as an actuator while P_{EC} was used as a disturbance. Discharge #11036 represents the real time T_e profile control experiments done using both P_{EC} and P_{NB} as actuators. Figure 2 and Figure 3 show the descriptions of discharge #9318 and #11033, respectively. The total profile control period in the discharge #9318 was about 2.0 s, from 8.0 s to 10.0 s. Only 4 control actions have been applied during the control period. The total control period of discharge #11033 was about 6.0 s, from 3.0 s to 9.0 s, which includes 12 control actions during the control period. The control period in the discharge #9318 was limited to 2.0 s due to the availability of the EC source. These two discharges were stable in terms of the plasma states and applied control actions. The non-adaptive profile control matrix evaluated assuming the H-mode plasma state was working well in the experiments as the real plasma state was not deviated much from the one assumed for experiments.

The flat-top plasma in the discharge #9318 was in the H-mode with 500 kA of I_P as shown in Figure 2 (a). The NBI power (P_{NB}) is lowered from 3.0 MW to 1.7 MW at 9.0 s during the profile control (see in Figure 2 (d)) as it was pre-programmed as a disturbance to the control system. Note that the maximum available EC power was only 0.3 MW and this was much

smaller than the NBI power drop applied as the disturbance. P_{EC} was changed step by step in time with the control demand calculated by the real time physics-based non-adaptive control model. The plasma in the discharge #11033 was also in the H-mode with 600 kA of I_P as shown in Figure 3 (a). The EC power (P_{EC}) of ~0.3 MW was injected as a small disturbance from 6.0 s to 7.0 s during the control period (see Figure 3 (d)). Note that the maximum available NBI power was about 2.9 MW. In this experiment, the P_{NB} has been varied using the power modulation technique recently implemented for beta control. The discharge #11036 has been carried out with the same control conditions applied for the discharge #11033, however without assuming external disturbances as the both EC and NBI used as actuators.

In all these discharges, 5 locations were chosen as control points, from ρ_ψ=0.1 to 0.5 with 0.1 as an interval. The target T_e values in the discharge #9318 were 2.7, 2.5, 2.2, 1.7 and 1.2 keV from the plasma center. In the discharges, #11033 and #11036, these were 3.1, 3.0, 2.8, 2.6, and 2.5 keV. The 110GHz EC launcher deposited its power in to the plasma around ρ_ψ~0.2 at 2.0 T of B_T.. This provided a slightly off-axis heat source, while the NBI provided a broad on-axis heat source to the plasmas. The control ranges of the actuator powers were set to P_{NB}=~1.0-2.9 MW and P_{EC}=~0.0-0.3 MW. P_{NB} was set to be always above 1.0 MW to maintain the H-mode plasma state.

Both Figure 2 and Figure 3 show that T_e profiles were controlled by the T_e profile controller implemented using the physics-based non-adaptive T_e profile control model. The details of control performance are discussed in Section 4 with the error analysis of these discharges.

4. Error dynamics of real time T_e profile control discharges

Figure 4 and Figure 5 represent the error analysis of discharge #9318 and discharge #11033, respectively, to examine the control performance of our real time T_e profile control experiments. Total sum of control error is shown in Figure 4 (a) and Figure 5 (a), and the control error at each control position is shown in Figure 4 (b) and Figure 5 (b). In the figures, the black colored dashed line represents the absolute value of error. And actuator actions are shown in Figure 4 (c) and Figure 5 (c). The blue line represents the preprogrammed actuator power and the red line represents the applied actuator power following the control demands.

In the discharge #9318 (see Figure 4 (a)), the total sum of the control error decreases with the control action of EC power before the preprogrammed applied power of NBI is changed. When the preprogrammed NBI power decreases, the total sum of the control error increases significantly. Sudden changes in the P_{NB} have been recognized as a disturbance to the control system. At later step, the total sum of the control error is again reduced. Although there were no enough control actions applied after the disturbances, it appears that the T_e profile is controllable using the EC power as an actuator, even in the presence of a transient in the NBI power. Note that the T_e profile cannot reach to the target profile due to the availability of EC power.

In the discharge #11033 (see From Figure 5 (a)), the total sum of the control error decreases well before P_{EC} is injected. However, the total sum of control error increases when the P_{EC} is applied as a disturbance to the control system. This disturbance affects for about 4 control intervals (about for 2.0 s), as the P_{EC} is suddenly injected into the plasma and also removed from the plasma. After the disturbance is removed, the total sum of the control error is eventually reduced again. The T_e profile is controlled using the NBI power as an actuator in the presence of sudden injection and removal of the P_{EC}.

Figure 6 shows the error analysis of the discharge #11036. This discharge represents the real time T_e profile control by both EC and NBI as actuators. The error analysis of this

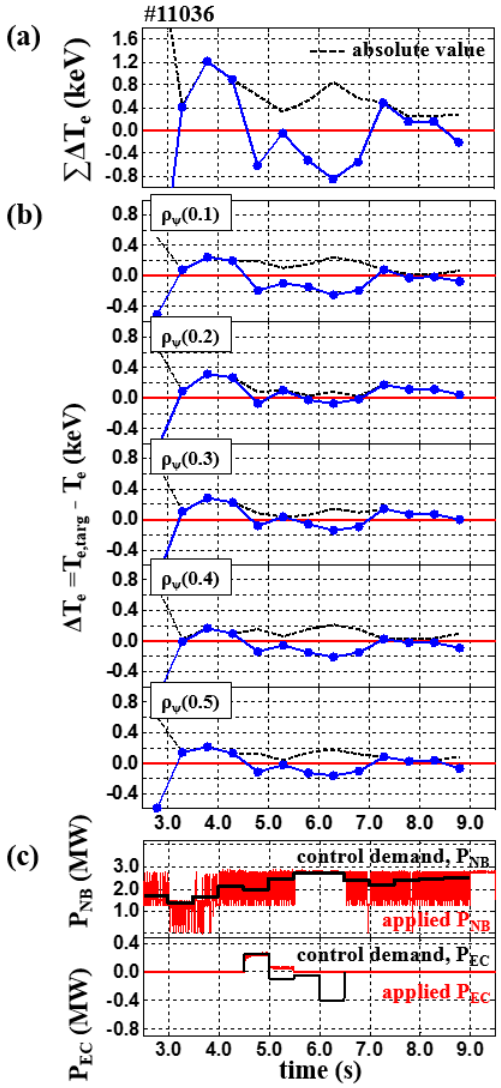

Figure 6 The error analysis of discharge #11036. (a) Total sum of control error in keV and (b) control error at each controlled position in keV. Their absolute values in black dashed line. (c) Actuators, P_{NB} and P_{EC}.

discharge is discussed step by step in detail. From 3.0 s to 4.5 s, the T_e profile is controlled using only one actuator, NBI, and the control error is reduced gradually. From 4.5 s to 6.5 s, the T_e profile is controlled using two actuators, NBI and EC. Since the central T_e is lower than the target profile, $T_{e,targ}$, at 4.5 s, increase of P_{EC} and decrease P_{NB} (as a compensation for P_{EC} increase) are requested from the control model for the next control interval, 4.5-5.0 s. It results in decreasing absolute control error. Here, we confirm that the real time T_e profile control is carried out successfully with both actuators. As the central T_e become higher than the target value at 5.0 s, the EC power control demand become reduced (even to an unrealistic negative value – black line), while the control demand for NB power is increased. However, in this experiment the available EC power saturation handling at the minimum available power has not been adequately set. Therefore, the routine for re-computing the control demands while setting the EC power at its minimum available power was not active. Although applied EC power was at its minimum power, the NBI power has not been re-computed. After 5.5s, the EC power become zero and excluded from the profile control. However, the NBI power was still working as an actuator for the profile control, and then when the control demand for EC become completely zero at 6.5 s (as the EC actuator was available only for 2 seconds), the profile control becomes effective again using the NBI power. Ironically, this demonstrates the robustness of applied physics-based profile control approach. Even with a fault in one actuator, if this has no overwhelming control actions, the other actuators (or a combination of actuators) can correct the potential faults and make the feedback control to be active and robust, as it has been demonstrated in the original modelling work [3].

5. Conclusion

The real time T_e profile control experiments have been conducted in KSTAR with the establishment of real time profile control system. The physics based non-adaptive control models have been implemented and NBI and EC have applied as actuators. We have shown that newly proposed T_e profile control approach is feasible for controlling the T_e profile in real time, even in the presence of disturbances. Furthermore, it has been also shown that the potential actuator faults can be partly covered if there are enough other actuators available for feedback control.

Disclaimer: The views and opinions expressed herein do not necessarily reflect those of the ITER organization

Acknowledgement
This research was supported by Ministry of Science, ICT, and Future Planning under KSTAR project and was partly supported by the JSPS-NRF-NSFC A3 Foresight Program (NRF No. 2012K2A2A6000443).

References

[1] Gormezano, C., et al., Nucl. Fusion **47** (2007) S285.
[2] Kim, H.-S, Ph. D. Dissertation, Seoul Nation. Univ. (2015).
[3] Kim, S.H., et al., Nucl. Fusion **52** (2012) 074002.

Characteristics of halo current in KSTAR

Jun-Gyo Bak[1], Heung-Su Kim[1], Sang-Hee Hahn[1], Jay-Hyun Kim[1]

[1]National Fusion Research Institute, Daejeon, Korea

Email : jgbak@nfri.re.kr

Small Rogowski coils as halo current monitors (HCMs) are used to measure halo currents (HCs) flowing through the support structures for the divertors between plasma and the wall of the vacuum vessel during the vertical displacement events (VDEs) which cause plasma disruption in the Korea Superconducting Tokamak Advanced Research (KSTAR) tokamak. The HC measurements are carried out during up / downward VDEs under the experimental conditions such as plasma current I_{p0} = 0.2 – 1.0 MA, toroidal field B_T = 1.5 – 3.0 T. The maximum value of total halo current $I_{h,max}$ is estimated up to 40 % of I_{p0} in the operational range of I_{p0} and B_T for elongated plasmas ($\kappa \geq 1.49$). The dependences of $I_{h,max}$ on plasma parameters (as plasma current, stored energy, plasma density, plasma shaping) are investigated. The toroidal peaking factor (TPF) is evaluated from the toroidal distribution of the local HC obtained at the inner /outer divertors. The maximum value of TPF × $I_{h,max}$ / I_{p0} is about 0.5. In this work, the KSTAR HCMs are briefly introduced, and results from the experimental investigations of the HCs during the campaign of 2014 in the KSTAR tokamak are presented.

1. Introduction

The vertical displacement events (VDEs), in which plasma generally moves upward or downward, can be usually occurred by the vertical instability due to a failure of vertical control or a result of the gross magnetic perturbation from a minor disruption for elongated plasmas. The VDEs eventually cause major plasma disruptions that generate large electromagnetic forces and high heat loads, which are critical issues in the future magnetic confinement device such as ITER. In the VDEs, the currents, called as halo currents, flowing into the vacuum vessel through in-vessel supporting structures were observed in tokamaks [1-5].

After the H-mode discharge was successfully produced in the KSTAR, the study on plasma disruption has been carried out because the disruption is critical issue for plasma current of higher than 1.0 MA with higher heating power that is required as one of missions in the KSTAR project. To study on the disruption due to the VDEs, small Rogowski coils, used as halo current monitors (HCMs) [6], were installed on the supporting structures of back-plates for divertors. However we could not get a clear signal from the HCM measurement due to low signal to noise ratio and noise pick-up from the power supply (with a switching frequency of 4kHz) for the in-vessel control coil (IVCC) until the experimental campaign of 2012 in KSTAR. These issues were clearly solved from the campaign of 2014 after the two improvements in the DAQ system for the HCM by changing the *RC* time-constant in the analog integrators for increasing the amplitude of the HCM signal and by adding electronic low pass-filters between the integrator and the digitizer for reducing noise pick-up from the IVCC. The HCM measurements were carried out during up / downward VDEs for elongated plasmas ($\kappa \geq 1.49$). In this work, the brief introduction of HCMs including supporting structures for divertors in KSTAR are reported and the initial results of the experimental investigations from the HCM measurements in the campaign of 2014 are presented.

2. Halo current monitors in KSTAR

The KSTAR divertor consists of inboard divertor (ID), central divertor (CD) and outboard divertor (OD), and each divertor has eight-sectored back-plates equally distributed in the toroidal direction. The supporting structures are mounted at the sectored back-plate for each divertor as following; two structures between two sectored back-plates at the ID, two structures between two sectored back-plates and two structures in the middle of each sectored back-plate at the CD, and one structure between two sectored back-plates and one structure in the middle of each sectored back-plate at the OD. The upper and lower divertors have same number of the supporting structures. Thus, total numbers of the supporting structure for each divertor are 16, 32 and 16 for ID, CD and OD, respectively. These sectored back-plates are electrically connected in the toroidal direction. Small Rogowski coils as halo current monitors (HCMs) were used to halo currents flowing the supporting structures at the divertors during vertical displacement

events (VDEs) in KSTAR. Each HCM was calibrated from the current measurement in a laboratory together with a commercial current sensor for pulse current of 100 – 200 A as mentioned in Ref. 6. The 32 HCMs were mounted on the supporting structures for inner and outer divertors and toroidal angle between two adjacent HCMs was 90° as shown in Fig. 1. Thus, the local HCs (at upper or lower divertor), such as $i_{h,ID}(\phi)$,$i_{h,innerCD}(\phi)$,$i_{h,outerCD}(\phi)$and $i_{h,OD}(\phi)$, were measured by four HCMs equally distributed in the toroidal direction at the ID, the inner and outer CDs and the OD, respectively. Here, the currents $i_{h,ID}(\phi)$and $i_{h,innerCD}(\phi)$ flow from plasma to wall through the supporting structure (called as 'sink current') and currents $i_{h,outerCD}(\phi)$and $i_{h,OD}(\phi)$ are called as 'source current'.

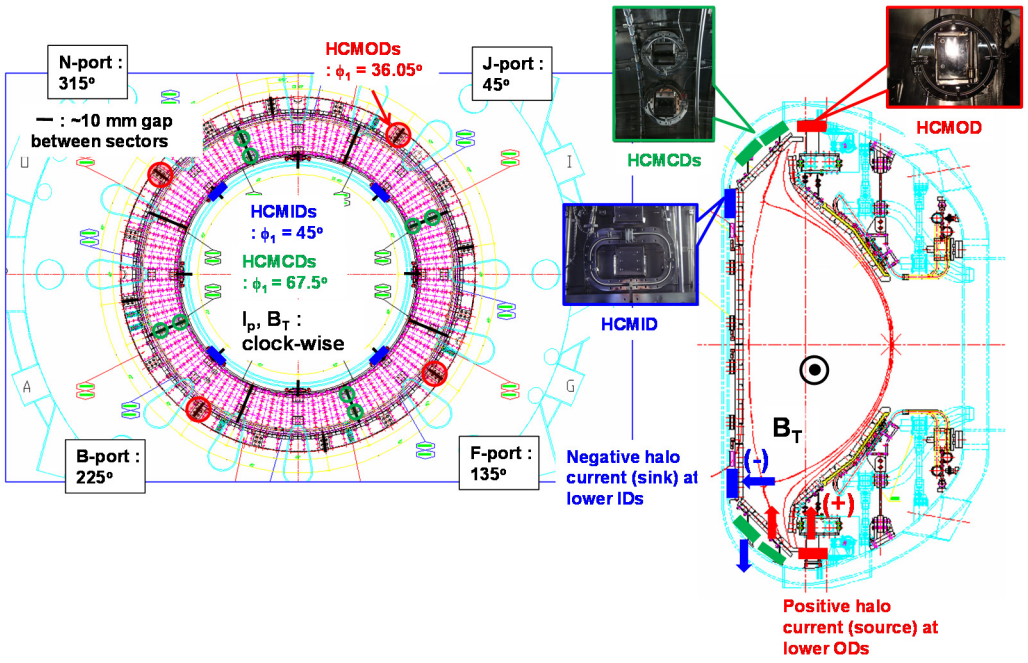

Fig.1. Halo current monitors in KSTAR.

3. Characteristics of VDEs

In the campaign of 2014, shots in where the VDE occurred 1s after plasma started up were selected for investigating characteristics of the VDEs in KSTAR. Total number of selected shots was 213; 136 and 77 shots for up and down VDEs, respectively. Figure 2 shows time slides of the TV camera that were taken during an upward VDE, together with plasma shapes reconstructed by the real-time EFIT.

The plasma parameters for the selected shots were following; I_{p0} = 0.2 – 1.0 MA, B_T = 1.5 – 3.0 T, q_{95} = 3.0 – 8.0, κ = 1.49 – 2.1. The maximum plasma current quench rate, $-(dI_p/dt)_{max}$ was up to 200 MA/s during VDEs. There is no clear correlation between $-(dI_p/dt)_{max}$ and dZ/dt as shown in Fig. 3(a). Here, dZ/dt means the vertical shift velocity of the plasma at time of maximum halo current, and the values were 10 – 110 m/s for the selected shots. In addition, there is the linear relationship between the current quench rate and plasma current before disruption for selected shots as shown in Fig. 3(b). From the relationship, the minimum plasma current decay time can be calculated by using $\tau_{p,min} = I_{p0} / -(dI_p/dt)_{max}$. The values of $\tau_{p,min}$ were 2 ~ 6 ms for up and down VDEs. For a target value of plasma current of 2.0MA in KSTAR tokamak, the maximum plasma current quench rate can be estimated as 522 MA/s from the relationship when the plasma disrupts due to the VDE.

4. Halo current and its parametric dependence

Since one supporting structure for the outer CD (or the OD), as a halo current channel, covers a toroidal angle of 22.5°, the total halo current I_h ('source current') in the plasma halo region at the outer CD and the OD was estimated from $360/22.5 \times (I_{h,outerCD} + I_{h,OD})$ where $I_{h,outerCD}$ and $I_{h,OD}$ were the average current

measured by four HCMs equally distributed in the toroidal direction at the outer CD and OD, respectively. Here, $I_{h,k}$ was obtained from local currents $i_{h,k}(\phi)$measured by the four HCMs. Two different ratios of maximum to the averaged halo current were obtained at outer CD and OD, and the higher one of two values was used as the toroidal peaking factor (TPF). Halo fraction, f, was obtained by the ratio of the maximum value $I_{h,max}$ in the time evolution of total halo current and the plasma current in the pre-disruption phase I_{p0}.

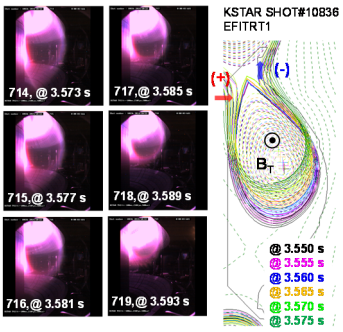

Fig.2. Upward vertical displacement event in KSTAR.

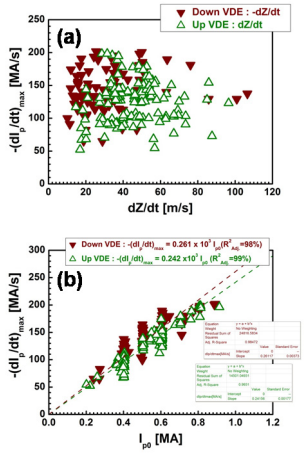

Fig. 3. (a) Maximum plasma current quench rate versus the vertical shift velocity of the plasma at time of maximum halo current, (b) Maximum plasma current quench rate versus plasma current before disrupt.

In the time evolution of total halo current from wall to plasma (as 'source'), its maximum magnitude $I_{h,max}$ mostly appeared before the time of $(dI_p/dt)_{max}$ as shown in Fig. 4. The time difference between two values in the time evolution of them was 0.2 ~ 5 ms. Fig. 4 also shows that halo current increases during thermal quench, and the maximum of the magnitude appear in the current quench phase, which is similar with the temporal behavior in the D_α signal. During VDEs, the vertical displacement became slower and increases after peak of halo current as shown in Fig. 5. Here, the value of TPF is about 2. Mostly, 'source' current was larger than 'sink' one in the HCM measurements.

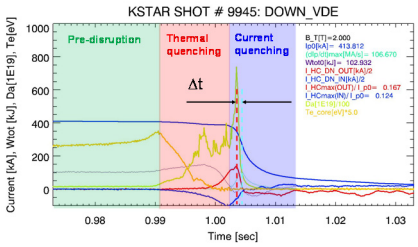

Fig. 4. Time evolutions of plasma current, core electron temperature, stored energy, D_α and halo current during down VDE.

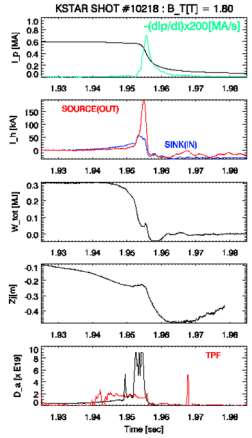

Fig. 5. Time evolutions of plasma current, halo current, stored energy, vertical displacement, D_α and TPF for downward VDE. Here, 'source' and 'sink' currents at the outer and inner divertors, respsectivly.

The values of TPF, f, and TPF × f for both up and down VDEs become smaller as plasma current before

disruption I_{p0} increases for $I_{p0} \geq 0.4$ MA as shown in Fig. 6. The values of TPF × f for both up and down VDEs slightly decrease as line averaged density and stored energy increase as shown in Fig. 7. The magnitude of the halo currents tended to decrease with the increase in stored energy just before the energy quench and with the line integrated electron density at the time of maximum halo current as reported in the JT-60U [3].

The values of TPF × f for both up and down VDEs slightly decrease as elongation and q_{95} increase as shown in Fig. 8. From the HCM measurements, the value of f is up to 0.4, and the maximum value of TPF is 5 as shown in Fig. 9. The value of TPF × f is 0.5, which is lower than the maximum value required in the ITER database (0.75).

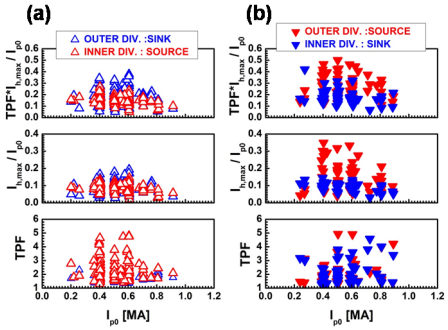

Fig. 6. Dependence of TPF× f, f and TPF (from top to bottom in figure) on pre-disrupted value of plasma current for (a) upward and (b) downward VDEs. Here, source means halo currents from wall to plasma and sink is the reversed current from plasma to wall.

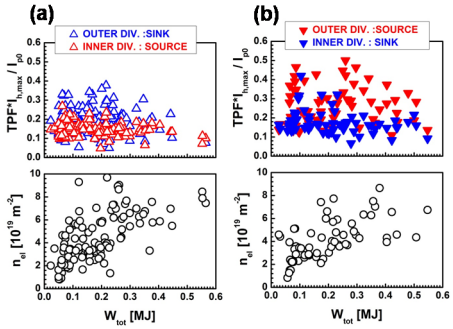

Fig. 7. Dependence of TPF× halo fraction on pre-disrupted value of stored energy (top), and line averaged density versus stored energy (bottom) for (a) upward and (b) downward VDEs.

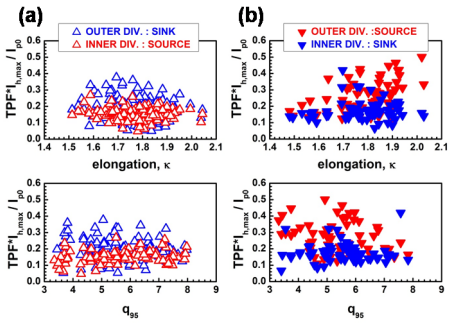

Fig. 8. Dependence of TPF × halo fraction on elongation (top), and q_{95} (bottom) for (a) upward and (b) downward VDEs.

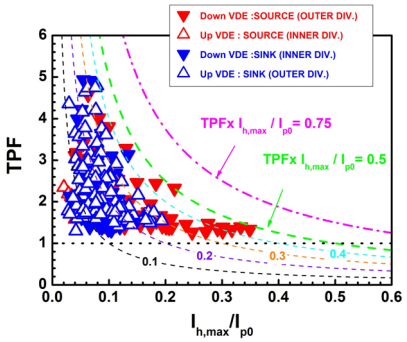

Fig. 9. TPF versus halo fraction.

5. Summary

Using 32 HCMs mounted on the supporting structures for inner and outer divertors, the HCM measurements were carried out in the operational range of I_{p0} and B_T (I_{p0} = 0.2 – 1.0 MA, B_T = 1.5 – 3.0 T) during up / downward VDEs for elongated KSTAR plasmas (κ ≥ 1.49). From the initial measurement, it was found that there were weak dependencies of halo current upon plasma parameters (as plasma current, stored energy, plasma density, plasma shaping). The halo fraction f was up 0.4 and the maximum value of TPF × f was about 0.5.

There are further works for the investigation of halo current characteristics in KSTAR as following; further investigation to understand the cause of the differences between ‘source’ and ‘sink’ currents, the

upper limit of halo current and plasma decay time during the plasma current quench, dependence of the magnitude of halo current on the vertical displacement velocity, possibility of rotating halo current in KSTAR, and behavior of electron temperature in the halo region.

Acknowledgements

This research was supported by Ministry of Science, ICT, and Future Planning under KSTAR project contract, and was partly supported by the JSPS-NRF-NSFC A3 Foresight Program in the field of Plasma Physics (NSFC: No. 11261140328, NRF: No. 2012K2A2A6000443).

References

[1] E.J. Strait, L.L. Lao, J.L. Luxon, and E.E. Reis, *Nuclear Fusion,* **31** (1991) 527.
[2] R.S. Granetz, I.H. Hutchinson, J. Sorci, J.H. Irby, B. Labombard, D. Gwinn, *Nuclear Fusion,* **36** (1996) 559.
[3] Y. Neyatani, R. Yoshino, Y. Nakamura and S. Sakurai, *Nuclear Fusion,* **39** (1999) 559.
[4] P.J. Knight, G.G. Castle, A.W. Morris, A. Caloutsis, C.G. Gimblett, *Nuclear Fusion,* **40** (2000) 325.
[5] V. Riccardo, et al., *Plasma Phys. Control. Fusion,* **46** (2004) 925
[6] J. G. Bak, et al., Korean Physical Society Meeting, 21st – 23th , October, 2009.

Development of the fusion-neutron diagnostics for the HL-2A tokamak

Y. Liu [1], W.L. Zhong [1], Z. B. Shi [1],Y.H.Xu [1], M. Isobe[2],Y. P. Zhang[1], W. Deng[1], X.Q. Ji[1]
1) *Southwestern Institute of Physics, P.O. Box 432, Chengdu 610041, China*
2) National Institute for Fusion Science (NIFS), Toki, Gifu, Japan

[1] *Southwestern Institute of Physics, P.O. Box 432, Chengdu 610041, China*
[2] *National Institute for Fusion Science, 322-6 Oroshi-cho, Toki 509-5259, Japan*

a) Corresponding author: YLiu, E-mial: yiliu@swip.ac.cn, Tel: +86-28-82850312, Fax: +86-28-82850300

PACS 52.70.Nc – Particle measurements
PACS 52.50.Gj – Plasma heating (beam injection, radio-frequency and microwave, ohmic, ICR, ECR, and current drive heating)
PACS 52.55.Fa – Tokamaks

Abstract: A new scintillator-based lost fast-ion probe (SLIP) has been developed and operated in the HL-2A tokamak [L. W. Yan et al, Nucl. Fusion 51, 094016 (2011)] to measure the lossess of neutral beam ions. The design of the probe is based on the concept of the α-particle detectors on Tokamak Fusion Test Reactor (TFTR) using scintillator plates. The probe is capable of traveling across an equatorial plane port and sweeping the aperture angle rotationally with respect to the axis of the probe shaft by two step motors, in order to optimize the radial position and the collimator angle. The energy and the pitch angle of the lost fast ions can be simultaneously measured if the two-dimensional image of scintillation light intensity due to the impact of the lost fast ions is detected. Measurements of the fast-ion losses using the probe have been performed during HL-2A neutral beam injection (NBI) discharges. The clear experimental evidence of enhanced losses of beam ions during disruptions has been obtained by means of the SLIP system. A detailed description of the probe system and the first experimental results are reported.

Keywords: fast ion, fast-ion-loss probe, NBI, disruptions, tokamaks

I. INTRODUCTION

Since the good confinement property of fast ions is an essential requirement for realization of an ignited fusion reactor, the behavior of fast ions in magnetically

confined fusion plasmas is one of the important research subjects in fusion studies.[1-3] Self-maintained fusion plasmas are expected to be heated mainly by D-T born α-particles. If α-particles are substantially lost from the plasma due to various reasons, the self-maintained state is inevitably terminated.[4] In addition, fast ions generated by plasma auxiliary heating systems such as neutral beam injection (NBI) and ion cyclotron resonance heating (ICRH) will support the plasma operation by additional heating and current drive. For efficient plasma heating, good confinement of the fast ions is required. In contrast, significant losses of fast ions will reduce the heating efficiency and NBI current drive.[5] Furthermore, the localized heat load on the plasma facing components (PFCs) due to the impact of the significant escaping fast ions may damage drastically the PFCs or pollute the plasma.[6] For all above reasons, understanding the physics of fast ions is crucial to achieve the safe operation for a fusion reactor.

The confinement, diffusion, convection and losses of the neutral beam-injected fast ions are a fundamental topic of plasma theory and experiment.[7] Measurements for the losses of the fast ions related to their confinement and plasma performance are thus crucial. Therefore, it is desirable to measure the losses of fast ions from the plasma, and furthermore to understand the mechanisms in an eventual hope to mitigate or eliminate those losses. Measurements of the fast-ion losses can be performed by a number of diagnostics, such as Faraday cups,[8,9] surface barrier diode detectors,[10,11] track detector,[12] exposure samples,[13] infrared imaging,[14] calorimeter probes,[15] and scintillator probes.[16-29] Among them, scintillator probes have the advantage to detect the energy and pitch angle of the lost ions as a function of time during a discharge. For a given magnetic field configuration, the orbits of the lost ions can be reconstructed, which may improve our understanding on associated physical processes. For this purpose a scintillator-based lost-fast-ion probe (SLIP) has been developed in the HL-2A tokamak.

The scintillator probe is based on the magnetic spectrometer concept.[30] The probe can disperse the incident fast-ions onto a scintillator plate and the strike points depend on their gyroradius (energy) and pitch angle. The gyroradius is taken to be $\rho_i = mv/Bq$, which is essentially a measure of the ion's energy. The pitch angle is defined as $\chi_i = \arccos(v_{//}/v)$, where v is the velocity of the ion and $v_{//}$ is the component along the magnetic field. Figure 1 illustrates the principle of the operation of a scintillator probe. The probe collimator has two entrance apertures, one behind the other. Charged particles that can pass through the collimator in the magnetic field will strike the scintillator plate. The collimator is chosen such that charged particles with certain gyroradius and pitch angle can hit the scintillator plate. In Fig. 1, two fast ions trajectories with different energies and pitch angles are diagramed to show the way the three-dimensional (3D) collimator working in the parallel and in the perpendicular direction with respect to the magnetic field. Energetic ions with larger gyroradius hit the scintillator screen farther from the apertures than those with smaller gyroradius. The strike points are dispersed across the line passing through the center of the two

apertures according to the pitch angles of ions. Fast ions striking the scintillator plate produce a pattern of light indicating the distribution of ions lost at the detected position. The light emitted from the scintillator will be transmitted via an optical path, and then, the image will be measured by a video camera and a photomultiplier array. This type of fast-ion-loss probes has been developed and operated in several devices so far, such as TFTR,[16-18] CHS,[19,20,22] LHD,[28] W7-AS,[21] ASDEX-U,[26] JET,[23] DIII-D,[29] NSTX,[24] KSTAR,[27] etc.

The purpose of this paper is to give a detailed description of the newly developed SLIP system in the HL-2A tokamak together with the first experimental results. Sec. II is dedicated to describe the setup of the HL-2A SLIP system. The first experimental results obtained from the SLIP system are presented in Sec. III. Finally, a summary is given in Sec. IV.

II. DIAGNOSTIC SETUP

The design of the HL-2A SLIP originates from the concept of the α-particle probe which has been developed by Zweben and used in TFTR for the first time.[16,17] The probe system mainly consists of a detector head, a long optical shaft system and a detection system. A schematic overview of the SLIP setup in the HL-2A tokamak is shown in Fig. 2. In the following the setup of the fast-ion-loss probe in HL-2A will be described.

The detector head is composed of a scintillator screen, a 3D ion collimator, a light-tight stainless steel box and a graphite armored box to prevent the heat load, as shown in Fig.3. The design starts with the shaping of the detector head. The proper geometry of detector head is key to measure the lost ions without blocking particles trajectories with a certain range of energy and pitch angle in the HL-2A device. The size of the scintillator screen must be close to the fast ion gyroradius. The energy of the deuterium neutral beam ions is typically about 40 keV in HL-2A, the gyroradius of the beam ions at the plasma boundary in the outer midplane is about 25 mm. Thus, the size of the scintillator screen is 25×25 mm^2.

Once the size of the scintillator screen is determined, the design of the 3D collimator is the next important step for the design of the detector head. The principle of the 3D collimator is shown in Fig. 1. The three dimension is considered in order that the lost fast ions can enter the slit opening without being stopped by the edge of the collimator. As we know, the soft x-ray may produce background noisy signals when the soft x-ray impact onto the scintillator screen. Note that the straight line of the x-ray light passing through the front and rear aperture is so constrained that it cannot intersect with the scitilator, and hence, avoiding the soft x-ray background noise. Many key properties of the detector head rely on the design of the 3D collimator in following points: (i) the resolution of the pitch angle is decided by the width of the front aperture and the range of the angle is determined by the orientation of the aperture together with the size of the scintillator screen; (ii) the resolution of the energy is determined by the height of the apertures and the range of the energy is

decided by both the height of the apertures and the size of the scintillator screen; (iii) the sensitivity of the detector head depends on the areas of the front and rear apertures. The Lorentz orbit code was used for the development of the 3D collimator. Fast ions have been traced backward in time starting randomly distributed along the front aperture within the appropriate gyrophase cone and with energies and pitch angles in the required range. The front aperture has a height of 0.8 mm and a width of 2.0 mm, and the distance between the front aperture center and the scintillator plate center is 25.5 mm. The rear aperture has a height of 0.8 mm and a width of 10 mm, and the distance between the rear aperture center and the scintillator plate center is 12.5 mm. The resolution with the current collimator geometry has been calculated and the results are shown in Fig.4. Figure 4(a) shows the calculated gyroradius distributions for 10, 15, and 20 mm at a pitch angle of 60°. The full widths at half maximum (FWHM) for this set of gyroradii are 2.0, 3.2 and 4.4 mm, respectively. It can be seen that the energy resolution becomes worst with increasing energy, which imply that the collimating effect of the 3D collimator becomes weaker for the ions with higher energy. Figure 4(b) shows the calculated pitch angle distributions for 80, 70 and 60 at a gyroradius of 20 mm. The results indicate that the pitch angle resolution is better than the energy resolution and the probe has the same FWHM ≈ 5° for all pitch angles. Furthermore, other collimators with different sizes can be made to get the desired pitch angle and energy resolution. In the design of the detector head in HL-2A, the collimator can be separated from the detector head. Therefore, the collimator can be conveniently replaced by another one with different size.

The ultimate time resolution of the SLIP system is decided by the decay time of the scintillation process of the scintillator material. The property of the material can significantly affect the SLIP performance. The scintillator material used for SLIP in fusion devices need to meet following requirements: (i) high sensitivity to fast ions such as NBI beam ions and α-particles; (ii) low sensitivity to the non-required particles such as electrons and neutrons, as well as the x-ray; (iii) fast response, particularly short decay time, because the MHD induced fast-ion losses are very fast processes; (iv) high saturation levels. Considering the manufacturability and the above-mentioned requirements of the scintillator screen, ZnS:Ag (P11 in EIA designation) has been selected as the scintillator material for the HL-2A SLIP. The emission peak and the decay time of ZnS:Ag scintillator are 450 nm and 70 ns, respectively.[31] ZnS:Ag scintillator phosphor was deposited onto a 25×25 mm^2 Aluminum substrate. The average thickness of the scintillator layer is 9 ± 1 μm. The scintillator plate is installed on the bottom of the light-tight stainless steel box with a graphite armor.

The detector head shown in Fig. 2 is mounted at the end of an adjustable long shaft. The entire head is capable of inserting into and withdrawing from the HL-2A vacuum chamber, and sweeping the aperture angle rotationally with respect to the axis of the long shaft in the vacuum chamber. Since the plasma discharge conditions, such as plasma configurations and the NBI power, are variable, the detector head need to be positioned in order to optimize the radial position and the incident angle of the collimator. To achieve the required capabilities of radial movement and angle rotation

in the vacuum vessel, the magnetic coupling drive system was adopted outside of the vacuum system. The long shaft is driven by two stepping motors shown in Fig. 2 via magnetic coupling, one motor is for the radial movement and the other is for the angle rotation. Figure 5 shows the photograph of the SLIP inside the HL-2A vacuum chamber. These motors can be precisely operated via a control panel. The step-size and step-angle are 1 mm and 1°, respectively. The long shaft is guided in the vacuum vessel by the rail to avoid the excessive vibration and deflection. The shaft system can provide a long traveling distance (2.7 m), which is very important in the actual operation because the available space in the vicinity of tokamak is limited.

The intermediate chamber shown in Fig. 2 has two functions: one is to observe the integrity of the detector head during the experimental campaign, and the other is for the convenience of the alignment, calibration and change of the detector head. When the detector head is located in the intermediate chamber, a manual gate vale isolates the SLIP system from the HL-2A main vacuum so that the SLIP can be vented to the air. The whole SLIP system is connected to the equatorial port of the HL-2A tokamak via a flange with the diameter of 50 mm and insulated from the electric potential of the device.

Lost fast ions enter into the detector head through the 3D collimator and produce a 2D light image on the scintillator screen. The image is focused by relay lenses onto a quartz image bundle fiber placed outside of the HL-2A vacuum and is carried to the detection section. The scintillation light is divided into two optical paths by an optical splitter located in front of the image plane. In the first path, the light emitting from the scintillator screen is then delivered to a photomultiplier (PMT) array by an optical fiber bundle. The array consists of 64 (8×8) channels and covers the whole scintillator plate. The array is a compact model (Hamamatsu Photonics K.K. Model H7546B-200) and its output is connected to a current amplifier (Hamamatsu Photonics K.K. Model IAM-64). The quantum efficiency (at 450 nm) and the gain factor dynamic range of the PMT are 37% and 2×10^6, respectively. The system can detect the total loss rate of fast ions as a function of time with frequency response up to 1 MHz. In the other path, the scintillation light is recorded by a high-speed video camera. The camera provides a rather slow video of the fast-ion-loss image but with a high energy-pitch angle resolution. The camera applied for this is a fast CMOS type (1280×800 pixels) with a 20×20 μm^2 pixel size, model V711-32GB by Phantom Inc. in USA. The quantum efficiency (at 450 nm) and the sensor dynamic range of the camera are 31% and 57.7 bB, respectively. The frame rate using full pixel (1,280×800) can up to 7,500 fps. The optical fiber bundles used for the two optical paths are wound fiber bundles (800×800 pixels) with visible light transmission rate 40%, wound fiber bundles 8×10 mm^2 format Part No. 1119144 by SCHOTT Inc. in USA.

The counts at the detector do not correspond to the light emitted by the scintillator as it is exposed to the flux of fast ions escaping the plasma. Therefore, if we want to obtain the flux information of fast ions per unit of energy and pitch angle, it is need to calibrate absolutely the SLIP system. The detection efficiency of the detector and the scintillation light conversion efficiency should be calibrated and determined. Then the linearity of the scintillator and detector can be calibrated and determined. This is a

meticulous work and will be done in the next-step work.

The main properties of the SLIP system at HL-2A are summarized and presented in Table I. The detector head was removed from the HL-2A vacuum chamber after the 2013 experimental campaign. The detector head was intact and the total SLIP system was well protected. The only minor problem is that the graphite armored box was slightly eroded by the impact of plasma flows.

Table I. Main properties of the SLIP system in HL-2A.

Scintillator material	*ZnS:Ag*
Scintillator screen size	25×25 mm
Detection energy range	10–70 keV
Detection pitch angle range	50-85°
Long shaft system	Radial movement, angle rotation
Photomultiplier array	8×8, 1 MHz
CMOS camera	7500 fps (at full pixel 1280×800)

III. INITIAL EXPERIMENTAL RESULTS

The HL-2A device is a medium-size tokamak with closed divertor chambers.[32] The main parameters of HL-2A are major radius R=1.65 m, minor radius a=0.4 m, and plasma current (I_p) up to 0.5 MA. Sixteen toroidal field coils can create and maintain a toroidal magnetic field (B_t) up to 2.8 T. The magnetic field is directed to be clockwise (top view), whereas the plasma current is counter-clockwise in the standard operation. The divertor of HL-2A is designed with two closed chamber. At present, it is operated with a lower single null configuration. An NBI is installed on the HL-2A tokamak with four-positive-ion sources.[33] Each ion source consists of a multi-pole plasma generator and an accel-decel extraction system. The beam injection energy is typically 40 keV and the total beam power can reach 2.0 MW. The neutral beam is tangentially co-injected with a radius of 1.4 m. Figure 6 depicts the arrangement of the NBI system together with the installation position of the SLIP. The main parameters of the SLIP experiment are shown in Table II.

The fast-ion-loss probe was put into application in the 2013 experiment campaign. However, the PMT array is still under development. Therefore, only experimental results obtained by the camera are presented in this paper.

Table II. Main parameters in the SLIP experiment in HL-2A.

Plasma current, I_p	*150-220 kA*
Central line-averaged electron density, n_e	(1-4) $\times 10^{19} m^{-3}$
Central electron temperature, T_e	1-3 keV
Toroidal magnetic field, B_t	1.3-1.5 T
NBI power	0.6-1.2 MW
Neutral deuterium injection energy	40 keV

A. Validation of the SLIP system

The SLIP system has been operated during the first phase of deuterium discharges heated by NBI pulses. The scintillation signals were collected by a low-speed camera with compact volume, which is for the convenience of the test and validation of the SLIP system. During this phase, the response of the detector was checked at different radial positions, collimator angles, and plasma conditions.

The light emitted from the scintillator plate during NBI has been observed in various cases. Figure 7 shows the prompt loss pattern produced by NBI on the scintillator screen. The plasma current was about 180 kA and the toroidal magnetic field was 1.3 T. The neutral deuterium beam with a power of 0.7 MW was injected into the plasma during the plasma current flat-top phase and lasted for about 400 ms. The camera has a frame rate of 3 fps, and hence, two pictures with available fast-ion losses can be obtained in one discharge, as shown in Fig. 7(a)-(b). The localized scintillation spot appears on the screen immediately after NBI turn-on. In the subsequent frame, the light spot becomes much brighter during the NBI phase, which is due to longer exposure time of the camera. After NBI turn-off, the scintillation light disappears as expected. Therefore, it is reasonably concluded that the measured scintillation light spot is caused by the impact of escaping beam ions. In addition, the orbits of the lost beam ions are calculated backward in time from the energy and pitch-angle, detected by the SLIP, as shown in Fig. 7(d). The wide bean shaped red curve is the envelope of the orbit of a beam ion. The impact area of the lost beam ions on the scintillator screen have been computed under the same plasma condition (B_t=1.3 T, I_p=180 kA), as depicted in Fig. 7(e). It can be found that the measurements are well consistent with the calculations.

B. Fast-ion losses during disruptions

Disruptions are a major concern for toakamks, not just for present-day machines, but even more so for ITER and future tokamak reactors.[34] During the disruption, both

plasma-stored-engery and the NBI ions are released drastically to the plasma facing components. The phenomenon gives a serious threat for the safe operation of a fusion reactor. Therefore, plasma disruptions in tokamaks have been extensively investigated.[35-37] However, previous studies mainly focused on the runaway electrons. In this study, the images of the fast-ion losses during disruptions with NBI have also been measured by the SLIP.

A typical plasma disruption with NBI is shown in Fig. 8, where the temporal evolution of the main parameters is plotted for shot 22614. A long NBI pulse with 1 MW was injected into plasma from 610 to 843 ms. A major disruption occurs at 833 ms and ends up at 848 ms. Thus, the NBI source is maintained for 10 ms during the disruption. The frame rate of the fast camera we used for this shot is 1 kfps. Therefore, some images of the beam-ion losses during the disruption can be obtained using the high-speed camera. Figures 9(a) and (b) shows two beam-ion-loss images on the scintillator screen before and during the disruption, respectively. Before the disruption, the energy and pitch angle of the lost beam ions are approximately 40 keV and 63°, respectively. The acceleration voltage of the NBI system in HL-2A is about 40 kV. Accordingly, the measurement results are in good agreement with the beam injection energy.

During the disruption, the scintillation light spot on the screen is significantly changed. Firstly, the brightness of the light spot is largely enhanced, indicating that the losses of the NBI beam ions dramatically increase during the disruption. Note that the present results provide the clear experimental evidence for the enhancement of fast-ion losses during a disruptions stage. Secondly, the shape of the light spot is changed tremendously and the area of the spot increases obviously during the disruption. The possible reason is that the transport of beam ions from the plasma core to the edge varies dramatically during the disruption because of strong magnetic perturbations and the change in the plasma current profile. Since the map of energy vs. pitch angle map is only available under quasi-steady state conditions, the map is not available during disruptions. In addition, the boundary of the scintillator screen is also identified during the disruption, as shown in Fig.9 (b). During the disruption, a large number of scattered x-ray photons are generated. The scattered photons can impact onto the scintillator screen and make the screen brighter, which permits to identify the actual boundary of the scintillator screen. The actual position of the screen boundary is well consistent with the calibration results.

IV. SUMMARY

A new fast-ion-loss probe system has been developed and operated in the HL-2A tokamak to measure the lost NBI ions. The design of the probe originates from the concept of the α-particle detectors on TFTR. The detector head is capable of inserting into and withdrawing from the HL-2A vacuum chamber, and sweeping the aperture angle rotationally by the magnetic coupling drive system. The 2D images of the scintillation light have been detected by means of an 8×8 PMT array and a fast CMOS camera.

The SLIP system has been implemented in the 2013 experiment campaign in the HL-2A tokamak. Measurements of the fast-ion losses using the SLIP system have been performed during NBI discharges. The 2D images of the scintillation light produced by the fast ions were detected and their energy-pitch angle information was obtained as well. The clear experimental evidence of enhanced loss of beam ions during a disruption has been achieved for the first time by the SLIP system. The transport of beam ions from the plasma core to the edge would be changed dramatically during disruptions due to the strong magnetic perturbations and the change of the plasma current profile. Moreover, the boundary of the scintillator screen is also identified during the disruption, which provides a direct verification for the calibration result. In the next campaign in HL-2A, a PMT array (8×8) with a bandwidth of 1 MHz will be applied and the effect of fast-ion driven MHD instabilities on fast-ion transport and/or loss will be investigated.

ACKNOWLEDGMENTS

The authors wish to thank the HL-2A experimental group and technical support team for their support in performing fast-ion-loss probe development and experiments in HL-2A. One of the authors, Y. P. Zhang, expresses sincere gratitude to Professor Y. Xu for his valuable support and helpful discussions. This work was partially supported by the National Science and Technology Major Project of the Ministry of Science and Technology of China (Grant Nos. 2010GB101000 and 2010GB101005), the National Natural Science Foundation of China (Grant Nos. 11005036 and 11375004), and it was also partially supported by Japan-China (post CUP) collaboration and the JSPS-NRF-NSFC A3 Foresight Program in the field of Plasma Physics (NSFC: No. 11261140328).

References

[1] W. W. Heidbrink, J. Kim, and R. J. Groebner, Nucl. Fusion **28**, 1897 (1988).

[2] W. W. Heidbrink, Phys. Fluids B **2**, 4 (1990).

[3] M. Isobe, K. Tobita, T. Nishitani, Y. Kusama, and M. Sasao, Nucl. Fusion **37**, 437 (1997).

[4] M. García-Muñoz, H.-U. Fahrbach, S. Günter, V. Igochine, M. J. Mantsinen, M. Maraschek, P. Martin, P. Piovesan, K. Sassenberg, and H. Zohm, Phys. Rev. Lett. **100**, 055005 (2008).

[5] C. B. Forest, J. R. Ferron, T. Gianakon, R. W. Harvey, W. W. Heidbrink, A. W. Hyatt, R. J. La Haye, M. Murakami, P. A. Politzer, and H. E. St. John, Phys. Rev. Lett. **79**, **427** (1997).

[6] D. S. Darrow, R. Majeski, N. J. Fisch, R. F. Heeter, H. W. Herrmann, M. C. Herrmann, M. C. Zarnstorff, and S. J. Zweben, Nucl. Fusion **36**, 509 (1996).

[7] L. Zhao, W. W. Heidbrink, H. Boehmer, R. McWillianms, D. Leneman, and S. Vincena, Phys. Plasmas **12**, 052108 (2005).

[8] O. N. Jarvis, P. Van Belle, G. Sadler, G. A. H. Whitfield, F. E. Cecil, D. Darrow, and B. Esposito, Fusion Technol. **39**, 84 (2001).

[9] W. W. Heidbrink, M. Miah, D. Darrow, B. LeBlanc, S. S. Medley, A. L. Roquemore, and F. E. Cecil, Nucl. Fusion **43**, 883 (2003).

[10] R. E. Chrien, R. Kaita, and J. D. Strachan, Nucl. Fusion **23**, 1399 (1983).
[11] J. D. Strachan, Nucl. Fusion **29**, 163 (1989).
[12] T. D. Murphy and J. D. Strachan, Nucl. Fusion **25**, 383 (1985).
[13] J. Zhu, G. M. McCracken, and J. P. Coad, Nucl. Instrum. Methods, Phys. Res. B **59/60**, 168 (1991).
[14] K. Tobita, Y. Neyatani, Y. Kusama, and H. Takeuchi, Rev. Sci. Instrum. 66, 594 (1995).
[15] D. M. Manos, R. V. Budny, S. Kilpatrick, P. Stangeby, and S. Zweben, Rev. Sci. Instrum. **57**, 2107 (1986).
[16] S. J. Zeben, Nucl. Fusion **29**, 825 (1989).
[17] S. J. Zweben, R. L. Boivin, M. Diesso, S. Hayes, H. W. Hendel, H. Park, and J. D. Strachan, Nucl. Fusion **30**, 1551 (1990).
[18] M. Tuszewshi, and S. J. Zweben, Rev. Sci. Intrum. **64**, 2459 (1993).
[19] D. S. Darrow, H. W. Herrmann, D. W. Johnson, R. J. Marsala, R. W. Palladino, and S. J. Zweben, Rev. Sci. Intrum. **66**, 476 (1995).
[20] M. Isobe, D. S. Darrow, T. Kondo, M. Sasao, K. Toi, M. Osakabe, H. Shimizu, Y. Yoshimura, C. Takahashi, S. Murakami, S. Okamura, and K. Matsuoka, Rev. Sci. Intrum. **70**, 827 (1999).
[21] A. Werner, A. Weller, D. S. Darrow, and the W7-AS Team, Rev. Sci. Intrum. **72**, 780 (2001).
[22] K. Shimohara, M. Isobe, and D. S. Darrow, Rev. Sci. Intrum. **77**, 10E521 (2006).
[23] S. Baeumel, A. Werner, R. Semler, S. Mukherjee, D. S. Darrow, R. Ellis, F. E. Cecil, L. Pedrick, H. Altmann, V. Kiptily, J. Gafert, and JET-EFDA Contributors, Rev. Sci. Intrum. **75**, 3565 (2004).
[24] D. S. Darrow, Rev. Sci. Intrum. **79**, 023502 (2008).
[25] D. Jiménez-Rey, B. Zurro, J. Guasp, M. Liniers, A. Baciero, M. García-Muñoz, A. Fernandez, G. Garcia, L. Rodrigurz-Barquero, and J. M. Fontdecaba, Rev. Sci. Intrum. **79**, 093511 (2008).
[26] M. García-Muñoz, H.-U. Fahrbach, H. Zohm, and the ASDEX Upgrade Team, Rev. Sci. Intrum. **80**, 053503 (2009).
[27] J. Kim, J. Y. Kim, S. W. Yoon, M. García-Muñoz, M. Isobe, and W. C. Kim, Rev. Sci. Intrum. **83**, 10D305 (2012).
[28] K. Ogawa, M. Isobe and K. Toi, J. Plasma Fusion Res. SERIES, 8, (2009) 655.
[29] R. K. Fisher, D. C. Pace, M. García-Muñoz, W. W. Heidbrink, C. M. Muscatello, M. A. Van Zeeland, and Y. B. Zhu, Rev. Sci. Intrum. **81**, 10D307 (2010).
[30] M. Isobe, M. Osakabe, T. Ozaki, M. Nishiura, P. V. Goncharov, E. Veshchev, K. Ogawa, K. Nagaoka, K. Saito, S. Murakami, T. Saida, M. Sasao, K. Toi, and LHD group, Fusion Sci. Technol. **58**, 426 (2010).
[31] See http://www.oken.co.jp/web_oken/Phosphors.htm for the physical characteristics of the ZnS:Ag scintillator.
[32] L. W. Yan, X. R. Duan, X. T. Ding, J. Q. Dong, Q. W. Yang, Yi Liu, X. L. Zou, D. Q. Liu, W. M. Xuan, L. Y. Chen, J. Rao, X. M. Song, Y. Huang, W. C. Mao, Q. M. Wang, Q. Li, Z. Cao, B. Li, J. Y. Cao, G. J. Lei, J. H. Zhang, X. D. Li, W. Chen, J. Chen, C. H. Cui, Z. Y, Cui, Z. C. Deng, Y. B. Dong, B. B. Feng, Q. D Gao, X. Y. Han, W. Y. Hong, M. Huang, X. Q. Ji, Z. H. Kang, D. F. Kong, T. Lan, G. S. Li, H. J. Li, Qing Li, W. Li, Y. G. Li, A. D. Liu,

Z. T. Liu, C. W. Luo, X. H. Mao, Y. D. Pan, J. F. Peng, Z. B. Shi, S. D. Song, X. Y. Song, H. J. Sun, A. K. Wang, M. X. Wang, Y. Q. Wang, W. W. Xiao, Y. F. Xie, L. H. Yao, D. L. Yu, B. S. Yuan, K. J. Zhao, G. W. Zhong, J. Zhou, J. C. Yan, C. X. Yu, C. H. Pan, Yong Liu and the HL-2A team, Nucl. Fusion **51**, 094016 (2011).

[33] H. Liu, J. Y. Cao, S. F. Jiang, C. W. Luo, L. X. Tang, G. J. Lei, J. Rao, and B. Li, Plasma Sci. Technol. **11**, 613 (2009).

[34] L.-G. Eriksson, P. Helander, F. Andersson, D. Anderson, and M. Lisak, Phys. Rev. Lett. **92**, 205004 (2004).

[35] V. Riccardo, and JET EFDA Contributors, Plasma Phys. Control. Fusion **45**, A269 (2003).

[36] B. Esposito, G. Granucci, P. Smeulders, S. Nowak, J. R. Martin-Solis, L. Gabellieri, FTU, ang ECRH teams, Phys. Rev. Lett. **100**, 045006 (2008).

[37] Y. P. Zhang, Yi Liu, G. L. Yuan, M. Isobe, Z. Y. Chen, J. Cheng, X. Q. Ji, X. M. Song, J. W. Yang, X. Y. Song, X. Li, W. Deng, Y. G. Li, Y. Xu, T. F. Sun, X. T. Ding, L. W. Yan, Q. W. Yang, X. R. Duan, Y. Liu, and HL-2A Team, Phys. Plasmas **19**, 032510 (2012).

Figure caption

FIG. 1. (Color online) Principle of the operation of a scintillator probe. The probe collimator has two entrance apertures, one behind the other. The collimator is chosen such that charged particles with certain gyroradius and pitch angle can hit the scintillator plate. The principle is similar to a magnetic spectrometer. Ions with larger energy hit the scintillator screen farther from the apertures than those with smaller energy.

FIG. 2. (Color online) A schematic overview of the fast-ion-loss diagnostic located at one cross section of the HL-2A tokamak. The probe system mainly consists of a detector head, a long optical shaft and a detection system.

FIG. 3. (Color online) (a) Schematic diagram of the detector head in HL-2A. (b)-(d) Assembly photograph and dissected views of the detector head. The detector head is composed of a 3D ion collimator, a scintillator screen, a light-tight stainless steel box and a graphite armored box.

FIG. 4. (a) The calculated gyroradius centroid distributions for 10, 15 and 20 mm at a pitch angle of 60°; (b) The calculated pitch angle distributions for 80°, 70° and 60° at a gyroradius of 20 mm.

FIG. 5. (Color online) Photograph of the SLIP inside the HL-2A vacuum chamber. The red labels highlight the available movements of the detector head while the white labels indicate the main probe components.

FIG. 6. (Color online) Top view of HL-2A, showing the NBI system and the installation position of the fast-ion-loss probe.

FIG. 7. (Color online) (a)-(c) Images emitted from the scintillator screen obtained by a low-speed camera with compact volume in a discharge with NBI. (a) right after NBI turn-on, (b) during NBI, (c) after NBI turn-off. (d) Calculated the envelope of the banana

orbit of the beam ions in HL-2A. (e) Calculated impact area of the lost beam ions on the scintillator screen in HL-2A (B_t=1.3 T, I_p=180 kA).

FIG. 8. (Color online) Time evolution of the main parameters in a plasma disruption with NBI in HL-2A. (a) plasma current I_p, (b) central line-averaged electron density n_e, (c) neutron emission rate measured by a neutron flux monitor (NFM), (d) NBI power. The disruption occurs at 833 ms and ends up at 848 ms.

FIG. 9. (Color online) The images of beam ion losses on the scintillator screen before (a) and during (b) the disruption in a NBI heated discharge.

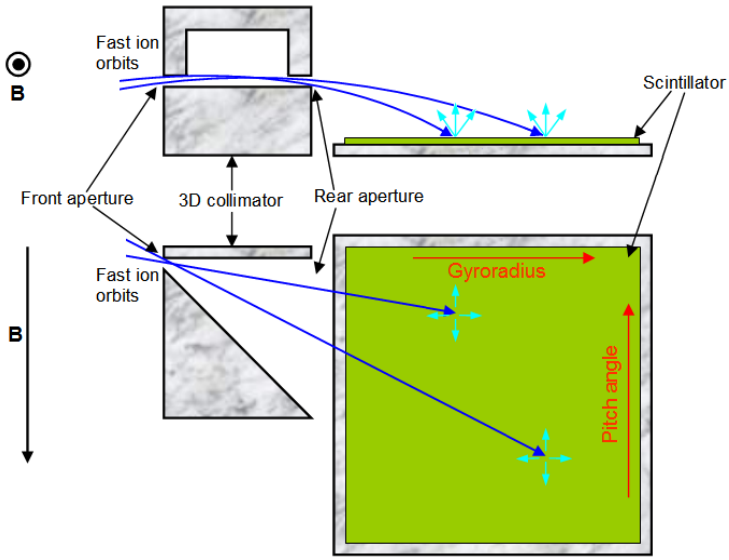

FIG. 1.

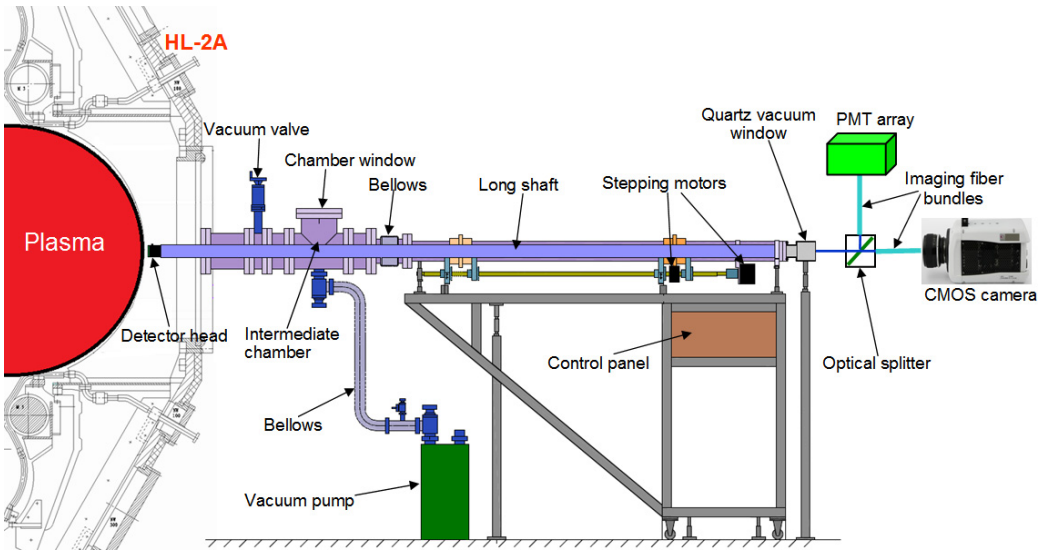

FIG. 2.

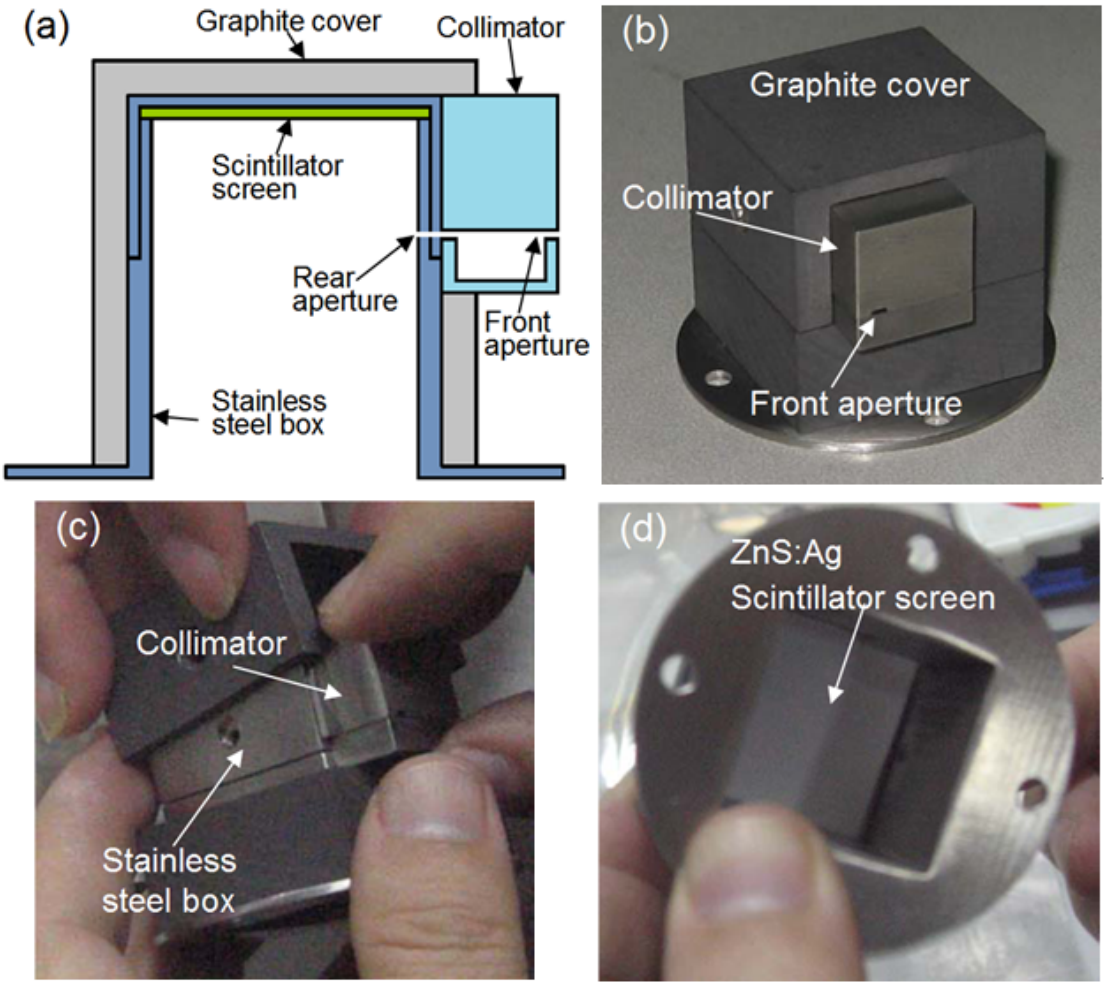
(a)
Graphite cover
Collimator
Scintillator screen
Rear aperture
Front aperture
Stainless steel box
(b)
Graphite cover
Collimator
Front aperture
(c)
Collimator
Stainless steel box
(d)
ZnS:Ag
Scintillator screen

FIG. 3.

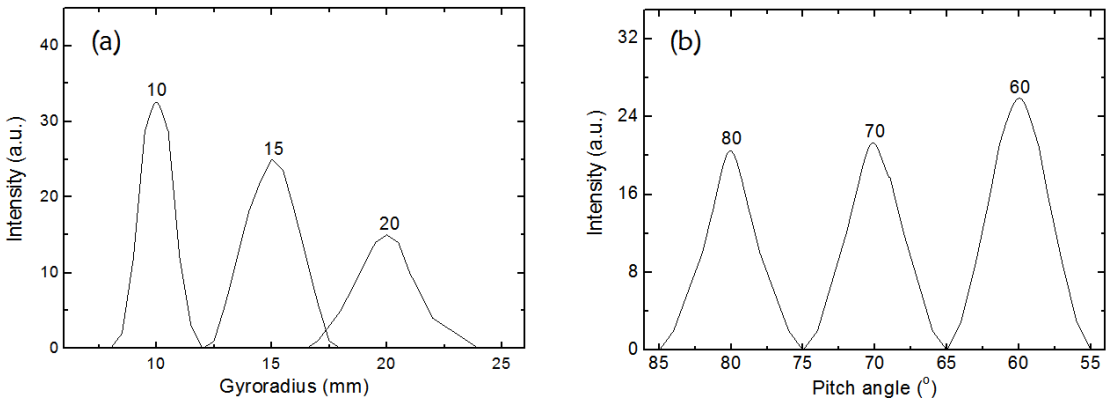
(a)
Intensity (a.u.)
Gyroradius (mm)
10
15
20
(b)
Intensity (a.u.)
Pitch angle (°)
80
70
60

FIG. 4.

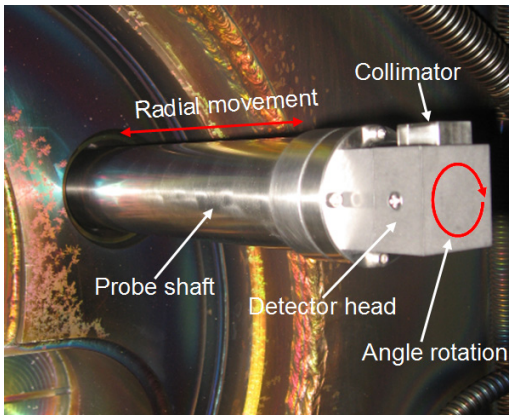

FIG. 5.

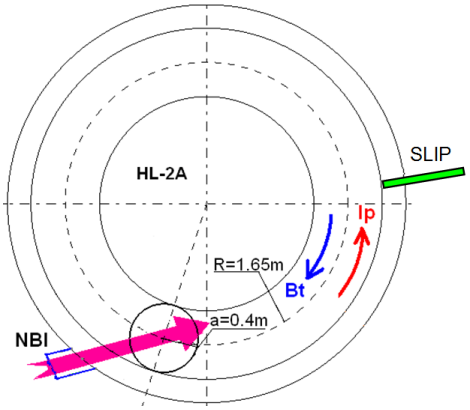

FIG. 6.

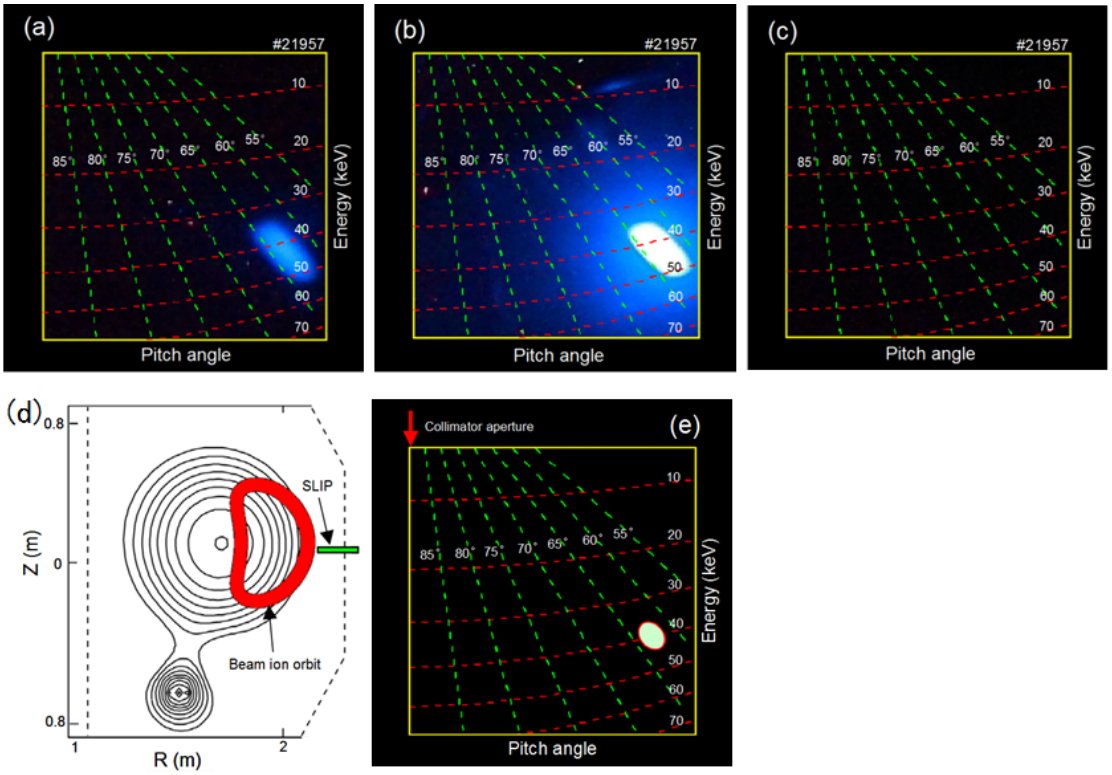

FIG. 7.

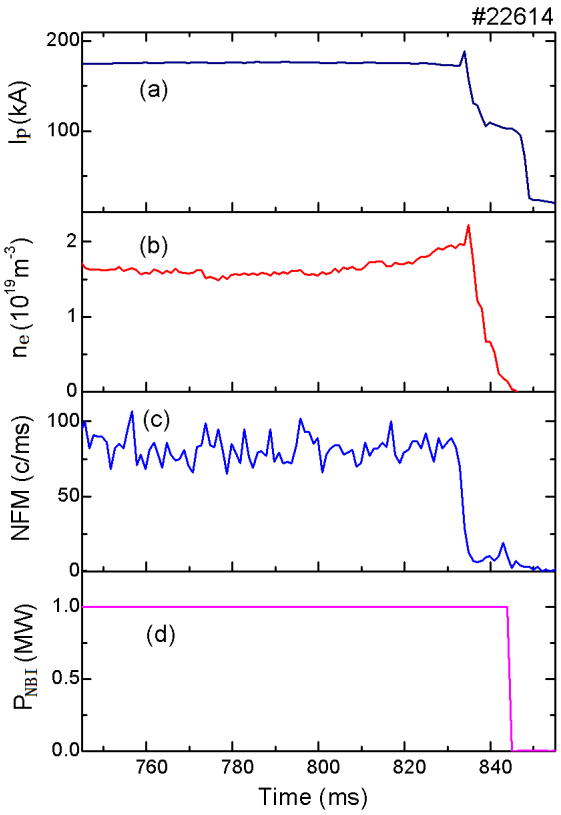
#22614
(a)
(b)
(c)
(d)
I_P (kA)
n_e (10^{19} m^{-3})
NFM (c/ms)
P_{NBI} (MW)
Time (ms)

FIG. 8.

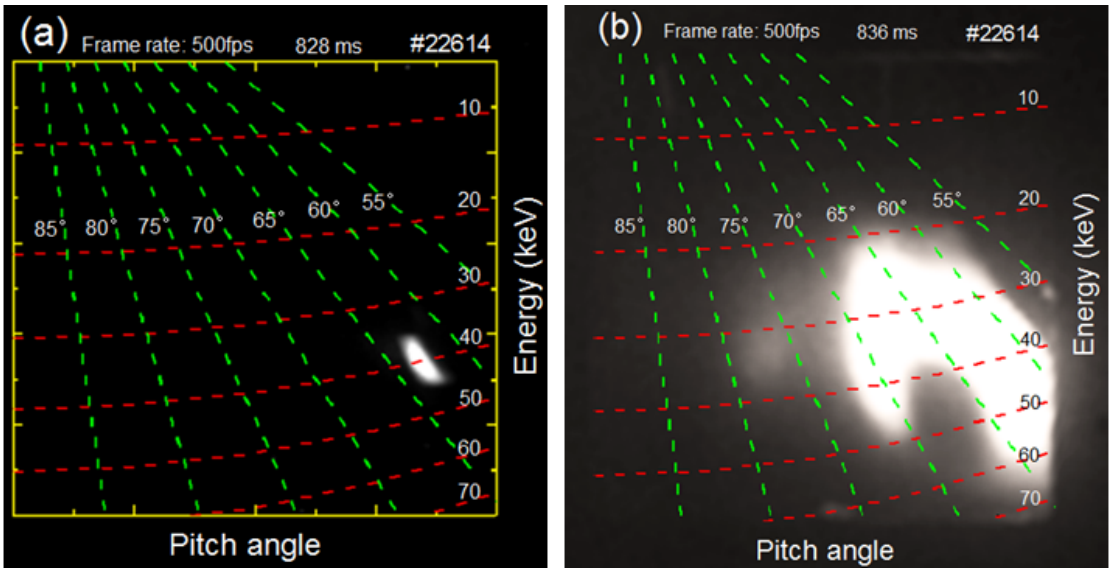
(a) Frame rate: 500fps 828 ms #22614
(b) Frame rate: 500fps 836 ms #22614
85° 80° 75° 70° 65° 60° 55°
10
20
30
40
50
60
70
Energy (keV)
Pitch angle

FIG. 9.

Long-term Simulation of Runaway Electrons in Toroidal Geometry

Jian Liu
Department of Modern Physics, University of Science and Technology of China

Abstract

The secular dynamics of runaway electrons in Tokamak electromagnetic field is studied. The radiation effect is added into a relativistic volume-preserving algorithm to gain long-term stability of calculation. The simulation results verify that the violent change of local magnetic field resulting from the high parallel speed of runaway electrons in Tokamak leads to the failure of the guiding-center theory. Meanwhile, the simulation reveals a mechanism that can cause the increase of perpendicular momentum, which indicates that part of energy provided by electric field is stored in the perpendicular direction and, as a result, the energy limit of runaway electrons will be higher than the prediction of guiding-center model.

Runaway electrons play an important role in the safe operation of Tokamak. It has been proved experimentally that large mounts of runaway electrons are generated during fast plasma shut down and [1] disruption [2]. Accelerated continuously by electric field [3], runaway electrons may carry considerably high energy up to tens of MeVs, which becomes a serious threat to the life of all the plasma-facing components (PFCs). The energy of a runaway electron cannot keep increasing but reach a stable point, known as energy limit, because, besides accelerated by electric field, the electrons face the energy dissipation through collision, synchrotron radiation and bremsstrahlung [4-8]. The whole life of a runaway electron is a physical process of multi-scale in both time and space. Therefore, theoretical and simulation studies are mostly based on guiding-center model which can, through averaging out the fast gyromotion, reduce the scale of timespace by two or three magnitude orders. Derived from guiding center theory [4,7], the test electron relaxation equations are traditional tools for studying the behavior of a runaway electron [5,6,8]. Through analyzing the singular points of the relaxation equations, the relation between energy limit and the loop electric field is predicted [5]. However, in the case where runaway electrons move in tokamak background electromagnetic field, because the parallel speed of a runaway electron can be accelerated to near the speed of light in a short time, the curved local magnetic field will rotate violently. As a result, the motion of runaway electrons has been out of the range of the assumption of gyrocenter approximation, which claims that the variation of magnetic field is of high-order. Therefore, the widely applied guiding-center theory may lead to results distorting the physical facts.

In our resent work, the relativistic Lorentz force equation with radiation effect for a runaway electron is solved under a typical 3-D electromagnetic field configuration of Tokamak. The collision resistance is ignored because of the high speed of runaway electrons [3,9]. In order to obtain long-term stability, our simulation is based on a relativistic volume-preserving algorithm (VPA), which is a kind of advanced geometric algorithms applied widely in plasma physics [4,7,10-14]. According to our simulation, while oscillating strongly, the perpendicular momentum will increase before reaching the stable point, which is quite different from the result of guiding center model which predicts that the perpendicular momentum keeps decreasing [4,5,8]. We find out that the weird evolution in momentum space results from the coupling between the rotation of momentum vector and the toroidal rotation of magnetic field. The different behavior of runaway electrons in momentum space may cause physical phenomena different from the results of guiding center model. Especially, the increase of perpendicular momentum means that part of energy provided by electric field is stored in the motion perpendicular to magnetic field. As a consequence, the simulated energy limit is higher than the prediction of relaxation equations [5]. In this letter, the model we used for the simulation is introduced firstly. Then, the secular dynamics of a runaway electron in momentum space is simulated and analyzed. Finally, the energy limit of runaway electrons is discussed.

The motion of a runaway electron is governed by the relativistic Lorenz force formula [15]. Within our consideration, the collision resistance is ignored because the speed of simulated runaway electrons is considerably high [3,9]. We assume that all the energy loss comes from the radiation emitted through the interaction between the electron and background field. In our model, a radiation drag force providing all the radiation energy loss is constructed, which leads to the

motion equation with radiation,

$$\begin{aligned} \frac{\mathrm{d}\mathbf{x}}{\mathrm{dt}} &= \mathbf{v}\,, \\ \frac{\mathrm{d}\mathbf{p}}{\mathrm{dt}} &= -e(\mathbf{E}+\mathbf{v}\times\mathbf{B})+\mathbf{F}_R\,, \\ \mathbf{p} &= \gamma \mathrm{m}_0\mathbf{v}\,, \end{aligned} \tag{1}$$

where **x, v** and **p** are, respectively, the position, velocity and mechanical momentum of a runaway electron, $-e$ denotes the charge of an electron, m_0 is the rest mass of an electron, **E** and **B** are the electric and magnetic field, and the Lorentz factor γ is defined as

$$\gamma = \sqrt{1+\frac{\mathrm{p}^2}{\mathrm{m}_0^2\mathrm{c}^2}} = \frac{1}{\sqrt{1-(v/\mathrm{c})^2}}. \tag{2}$$

Finally, $\mathbf{F}_\mathrm{R}$ denotes the radiation drag force, namely,

$$\mathbf{F}_\mathrm{R} = -P_R\frac{\mathbf{v}}{v^2}. \tag{3}$$

where P_R is the radiation power for relativistic charged particle[15],

$$P_{R0} = \frac{q_e^2}{6\pi\epsilon_0\mathrm{c}}\gamma^6\left[\left(\frac{\mathbf{a}}{\mathrm{c}}\right)^2-\left(\frac{\mathbf{v}}{\mathrm{c}}\times\frac{\mathbf{a}}{\mathrm{c}}\right)^2\right], \tag{4}$$

where ϵ_0 is the permittivity in vacuum, c is the speed of light in vacuum, $\mathbf{a}=\mathrm{d}\mathbf{v}/\mathrm{dt}$ denotes the acceleration of the particle.

To solve the system described by Eq. (1), tens of billion steps is necessary to simulate the whole life of a runaway electron, because the process crosses about 11 magnitude orders in time. In order to guarantee secular stability, our simulation is based on a relativistic volume-preserving algorithm where the radiation drag force is added in. To give a proper approximation to field in Tokamak, the motion of a runaway electron is calculated in a background electromagnetic field in the form of

$$\begin{aligned} \mathbf{B} &= \frac{B_0R_0}{R}\mathbf{e}_\xi - \frac{B_0\sqrt{(R-R_0)^2+z^2}}{qR}\mathbf{e}_\theta, \\ \mathbf{E} &= E_l\frac{R_0}{R}\mathbf{e}_\xi, \end{aligned} \tag{5}$$

where $R=\sqrt{\mathrm{x}^2+\mathrm{y}^2}$, ξ and z are, respectively, the radial distance, the azimuth and the height of cylindrical coordinate system, $\mathbf{e}_\xi$ and $\mathbf{e}_\theta$ are the unit vector on toroidal and poloidal direction, and q denotes the safety factor. In order to compare with the experimental observation, we choose the parameters based on EAST [16]. The center magnetic field intensity is chosen to be $B_0=3\mathrm{T}$, while the center loop voltage is $E_l=3\mathrm{V/m}$. The major radius is set as $R_0=1.7\mathrm{m}$. And the safety factor is $q=2$.

Our simulation focuses on how a runaway electron moves in Tokamak after it has been accelerated to a relative high speed. Therefore, the initial momentum of the electron is set to be $p_\parallel=5\mathrm{m}_0\mathrm{c}$, $p_\perp=1\mathrm{m}_0\mathrm{c}$ and the initial position is $R-R_0=0.1\mathrm{m}$, $\xi=z=0$. The evolution of the momentum of the runaway electron is depicted in Fig. 1. After about $0.4\mathrm{s}$, the momentum reaches to a stable point, the energy limit, where the effect of electric field is offset by the radiation loss. Before the energy limit, the parallel momentum keeps increasing and is far larger than the

perpendicular momentum. Considering the relation $p_\parallel^2 + p_\perp^2 = p^2$ and the fact that, in one gyro-period, the norm of momentum is approximately a constant, we have

$$\frac{\Delta p_\parallel}{\Delta p_\perp} = -\frac{p_\perp}{p_\parallel} \ll 1. \tag{6}$$

As a result, the oscillating amplitude of perpendicular momentum is larger than that of parallel momentum, which is obvious in Fig. 1. On the other hand, the evolution of perpendicular momentum shows three obvious characteristics, (1) rapid increase of oscillating amplitude at the beginning, (2) existence of a moment, named as *zero point*, when the perpendicular momentum touches zero, (3) the increase of the average value before the stable point.

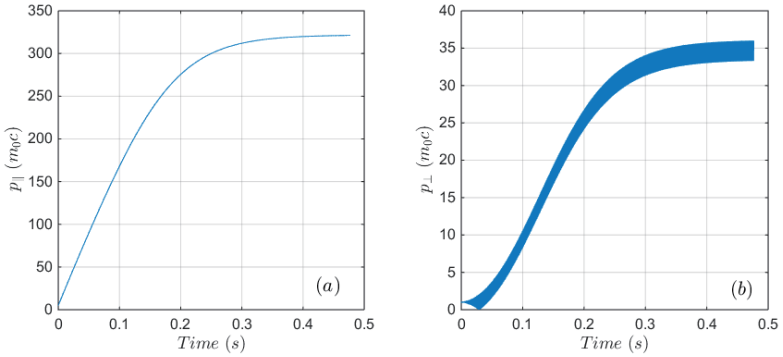

Fig. 1 Dynamics in momentum space for a runaway electron with initial position $R - R_0 = 0.1\mathrm{m}$, $\mathrm{z} = 0$,and initial momentum $\mathrm{p}_\parallel = 5\mathrm{m}_0\mathrm{c}$, $\mathrm{p}_\perp = 1\mathrm{m}_0\mathrm{c}$. (a) is the evolution of parallel momentum. (b) is the dynamics of perpendicular momentum.

The weird evolution of perpendicular momentum is caused by the coupling between the rotation of local magnetic field and the rotation of momentum of the runaway electron. To begin with, the oscillation frequency of momentum matches with gyro-frequency, which means that the oscillation results from the change of magnetic field caused by gyro-motion. As given in Eq. (5), the poloidal component B_θ is ignorable compared with the toroidal component B_ξ in Tokamak and the local magnetic field of a runaway electron can be expressed as $\mathbf{B} \approx B_\xi \mathbf{e}_\xi$. During one gyro-period, the acceleration of electric field, energy loss from radiation and the radial drift of runaway orbit are ignorable. Therefore, the toroidal magnetic field E_ξ, the norm of momentum p and the radial position R of the particle can be regarded as constants, which means that the runaway electron approximately runs along the circle of magnetic field line, as shown in Fig. 2. Because of the parallel motion of the runaway electron and the toroidal curvature of $\mathbf{B}$, the direction of local magnetic field line rotates quickly and the rate of change is approximately

$$\dot{\theta}_B = \frac{v_\parallel}{R}, \tag{7}$$

where $\square_\parallel$ is the parallel velocity. The gyro-period of the runaway electron is defined as

$$T_{ce} = \frac{2\pi\gamma \mathrm{m}_0}{\mathrm{eB}} \approx \frac{2\pi\gamma \mathrm{m}_0 R}{\mathrm{e}B_0 \mathrm{R}_0}, \tag{8}$$

where e is the unit of charge and the relation, $B \approx \mathrm{B}_0\mathrm{R}_0/\mathrm{R}$, is used. Combining Eqs. (7)-(8) and realizing that $p \approx p_\parallel = \gamma \mathrm{m}_0 \mathrm{v}_\parallel$, one obtains the change angle of the local magnetic field during one gyro-period,

$$\theta_B \approx \frac{2\pi p_{\parallel}}{eB_0R_0} = 0.0021 p_{\parallel n} \approx 0.0021\, p/m_0 c\,, \tag{9}$$

where $p_{\parallel n} = p_{\parallel}/m_0 c$ is the normalised parallel momentum. On the other hand, the effect of local magnetic field on momentum vector $\mathbf{p}$ is equivalent to the rotation operation in momentum space [11]. To be specific, in one gyroperiod, the dynamical equation of momentum in Eq. (1) can be written as

$$\frac{d\mathbf{p}}{dt} = -\omega_{ce}\mathbf{p} \times \mathbf{b}\,, \tag{10}$$

where the effects that change the energy, namely $\mathbf{E}$ and $\mathbf{F}_R$, are ignored, and $\omega_{ce} = eB/\gamma m_0$ denotes the gyro-freqency. This formula indicates that the changing rate of momentum interacting with magnetic field is approximately proportional to perpendicular momentum. As for a runaway electron, since the perpendicular momentum is of high order compared with the parallel momentum, the solid angle formed by the rotation in momentum space is also small. As shown in Fig. 2(a), if the parallel velocity of the particle is low enough, after one gyro-period, the unit vector of magnetic field $\mathbf{b}$ changes little and locates approximately on the axis of the cone formed by the track of rotated momentum $\mathbf{p}$. However, in the case of runaway electrons with high parallel momentum as depicted in Fig. 2(b), according to Eq. (9), even though one gyro-period is a short time, the toroidal rotation of magnetic field vector may be considerably large. If θ_B is large enough, the rotating momentum vector cannot catch up the turning magnetic field in the toroidal direction but keeps on the outside of the circle of magnetic field line.

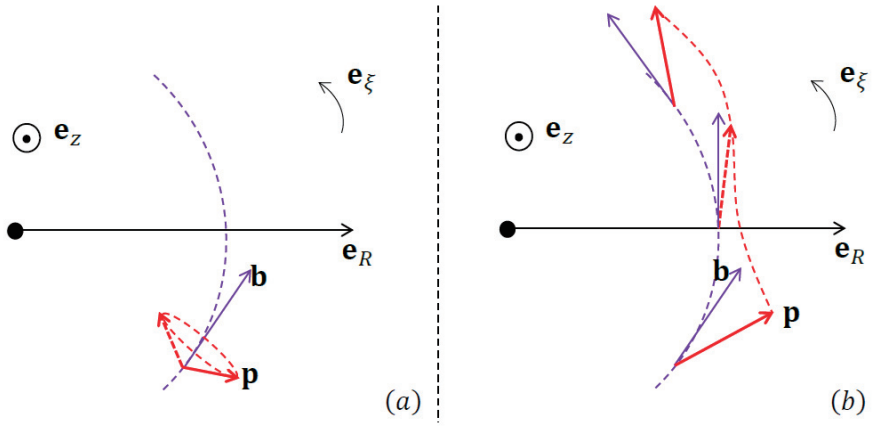

Fig. 2 The schematic diagrams for the rotation of momentum vector and local magnetic field during one gyro-period. The purple dashed lines depict approximately the magnetic line. The purple and red arrows represent, respectively, the direction of magnetic field and the momentum vector. (a) shows the case of particle with low parallel velocity and (b) is the case of runaway electron which has been accelerated to a high parallel speed.

To give a clear picture of the relation between rotation of $\mathbf{B}$ and the rotation of $\mathbf{p}$, we draw all the unit vectors of magnetic field in one gyroperiod at the same place while the relative positions of $\mathbf{b}$ and $\mathbf{p}$ keep unchanged, see Fig. 3. One should notice that all the phenomena in this letter are observed under rest reference framework and no coordinate transformation is involved. All we do in drawing Fig. 3 is just changing the angle of view. At the very beginning, depicted in Fig. 3(a), $\mathbf{b}$ changes little in one gyro-period and is near the axis of rotation cone. Therefore, the

perpendicular momentum is nearly a constant during one rotation. Because of the acceleration of electric field, the momentum rises, which leads to the increase of θ_B. As shown in Fig. 3(b), the cone of rotating momentum starts to move towards the radial direction. The difference between maximum and minimum perpendicular momentum, $\Delta p_\perp = \mathrm{p}_{\perp max} - \mathrm{p}_{\perp min}$, reveals the oscillation amplitude of perpendicular momentum. It is easy to see that $\Delta \mathrm{p}_\perp$ and the amplitude of oscillation keeps increasing while $\mathbf{b}$ moving towards the left side of the cone. When $\mathbf{b}$ touches the edge of the cone, depicted in Fig. 3(c), the minimum value of $p_\perp$ is 0. This moment is the zero point in Fig. 1(b). Because the solid angle spanned by momentum is small, it just needs about 0.03s, a short time compared with the whole life of the electron, to reach the zero point. If the increase of θ_B continues, $\mathbf{b}$ will move out of the cone and the angle between $\mathbf{b}$ and the axis of cone will become larger and larger. As a consequence, the projection of momentum on the perpendicular direction of $\mathbf{b}$ begins to increase while the change of $\Delta p_\perp$ slows down, see Fig. 3(d). This process reflects the mechanism that causes the increase of perpendicular momentum. However, since the effect of the radiation, the momentum of a runaway electron cannot increase forever but reach to a stable point where θ_B also becomes stable. Through the simplified model in Fig. 3, the simulation result of dynamics in momentum space can be explained clearly.

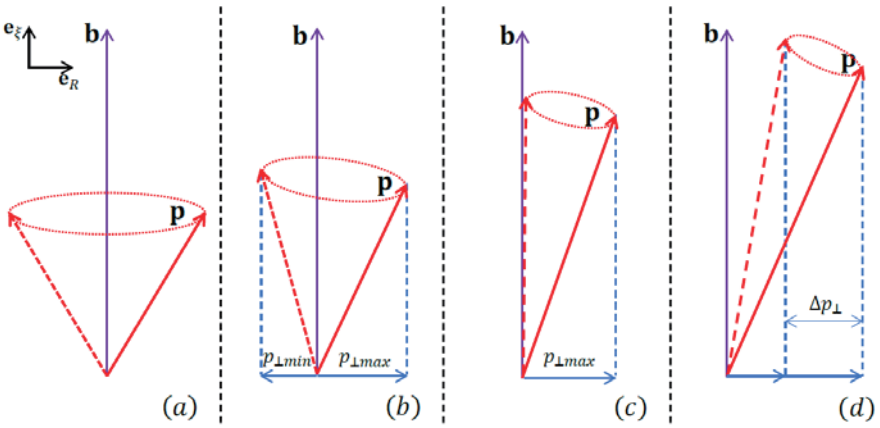

Fig. 3 The schematic diagrams for the relations between the magnetic field vector and the cone formed in one gyro-period by the rotation of momentum. In this figure, all the magnetic field vectors in one gyro-period are put together while the relative positions between $\mathbf{b}$ and $\mathbf{p}$ keep unchanged. (a) happens at the beginning of the simulation when the change of $\mathbf{b}$ in is slow. After the electron is accelerated by electric field, as shown in (b), $\mathbf{b}$ will move towards the edge of the cone. (c) is related to the "zero" point in evolution of perpendicular momentum. (d) shows the case where $\mathbf{b}$ is out of the cone and the average value of perpendicular momentum increases. All the phenomena are observed under rest reference framework. No coordinate transformation is involved in this figure.

A traditional way to study the dynamics of runaway electrons is to analyze the test electron relaxation equations which can be derived through guiding center model [4-8]. Within the assumption of guiding center approximation, the magnetic field changes slowly in time and space [17], i.e.

$$\frac{\rho_e}{L_B} \sim \epsilon \ll 1\,, \tag{11}$$

$$\frac{T_{ce}}{T_B} \sim \varepsilon \ll 1 ,$$

where ρ_e is the gyro-radius of an electron, L_B and T_B denote the various scale of magnetic field in space and time, respectively. One important result of the gyro-center approximation is that the magnetic momentum is an adiabatic invariant [17-21], which is one of the fundamental assumption in deriving the relaxation equations. By solving the relaxation equations, researchers are able to predict the evolution of runaway electrons in momentum space [4,5]. According to their analysis, before the energy limit, the perpendicular momentum keeps decreasing while the parallel momentum rises continuously. However, as discussed before, the change of the local magnetic field is violent, which implies that the motion of runaway electrons is out of the range of the assumption of gyrocenter approximation. We have shown a mechanism which causes the increase of the average value of perpendicular momentum, which cannot be described by guiding center model. Especially, if the radiation effect is excluded in simulation, the perpendicular momentum will never reach a balance point but keep growing. At the same time, the magnetic momentum defined as $\mu = \mathrm{p}_\perp^2/2\gamma \mathrm{m}_0 \mathrm{B}$ is not conserved in long time scale, see Fig. 4. All these simulated results imply that the predictions based on the guiding center model may distort the physical facts. To be specific, the analysis of the energy limit in Ref. [5] is not convincing, and, as we will discuss later, the maximum kinetic energy a runaway electron can reach has been underestimated.

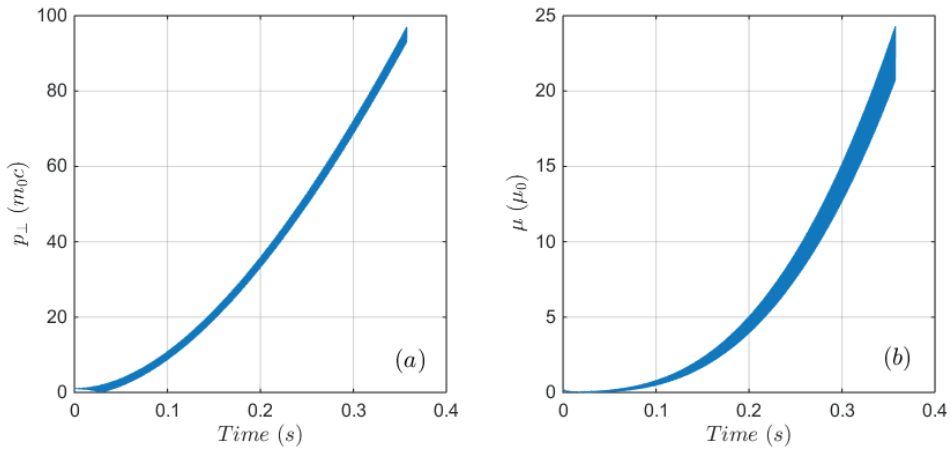

Fig. 4 The evolutions of perpendicular momentum(a) and magnetic momentum(b) without the radiation effect. The unit of magnetic momentum is $\mu_0 = \mathrm{m}_0\mathrm{c}^2/2\mathrm{B}_0$.

Energy limit of runaway electrons is widely concerned because electrons with high energy can damage the plasma-facing components (PFCs) in Tokamak. J. R. Martín *et al* [5] have studied the energy limit by analyzing the singular points of the test electron relaxation equations in 1998 and the relation of energy limit virus the loop electric field is given. According to their conclusion, if the electric field is much larger than the collision resistance, the radiation loss is provided mainly by the toroidal motion, which indicates that, the magnetic field has little effect on the final energy limit. However, as mentioned before, the guiding center model cannot cover all the details of the evolution of momentum. We have simulated the energy limit of a runaway electron based on our model. The magnetic field configuration is given in Eq. (5). Meanwhile, in order to eliminate the effect of different electric fields, the loop voltage is chosen to be uniform in radial direction,

namely, $\mathbf{E} = \mathrm{E_l}\mathbf{e_\xi}$ and $E_\mathrm{l} = 3\mathrm{V/m}$. Under the parameters of the EAST [16], namely, the density of electrons $\mathrm{n_e} = 10^{-19}\mathrm{m}^{-3}$ and the Coulomb logarithm $\ln\Lambda = 10$, the collision resistance is ignorable, compared with E_l. For runaway electrons with the same initial positions and momentums, we calculate the evolution of kinetic energy under different center magnetic field intensity, $\mathrm{B_0} = 1\mathrm{T}, 3\mathrm{T}, 7\mathrm{T}, 10\mathrm{T}$. In Fig. 5, the energy limit given by J. R. Martín *et al* is marked by the black dashed line and the solid lines are given by simulation. It can be seen from Fig. 5 that the energy limit given by our simulation is higher than J. R. Martín's result. The reason is that, because of the increase of perpendicular momentum, part of the energy provided by electric field is stored in the perpendicular direction. On the other hand, if the magnetic field intensity becomes larger and other physical conditions keep unchanged, the guiding-center approximation will get more appropriate [17]. Therefore, as Fig. 5 shows, the energy limit predicted by simulation goes closer to result of guiding-center theory as the magnetic field intensity increases.

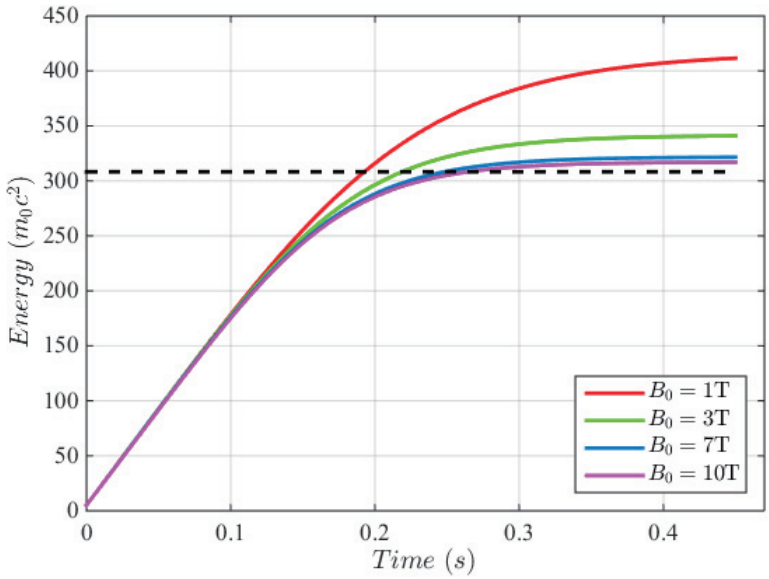

Fig. 5 Kinetic evolution of a runaway electron in different center magnetic field intensity. The black dashed line is the energy limit predicted by guiding-center model [5] for loop voltage $E_l = 3\,\mathrm{V/m}$, under the condition of EAST [16], namely, electron density is $10^{-19}\mathrm{m}^{-3}$ and Coulomb logarithm is 10. The solid lines are kinetic evolutions for a runaway electron in magnetic fields with different intensity, $1\mathrm{T}$, $3\mathrm{T}$, $7\mathrm{T}$ and $10\mathrm{T}$.

Even though gyrocenter approximation, as an elegant theory, is able to improve the efficiency of simulation and deepen our understanding of behavior of charged particles in magnetic field, it cannot be used everywhere. Besides the case of the runaway electrons in Tokamak, All of the secular dynamics of charged particles with high speed parallel to curved magnetic field cannot be described well via guiding-center model. In the future, in the study of runaway electrons, we will add bremsstrahlung into our model and develop corresponding codes used for guiding experimental observations. On the other hand, detail theoretical analyses will be done to the radiation model and modification of the guiding center theory shall be analyzed.

[1] R. Yoshino, T. Kondoh *et al.*, Plasma Phys. Control. Fusion **39**, 313 (1997).
[2] R. Jaspers, N. L. Cardozo *et al.*, Nucl. Fusion **36**, 367 (1996).
[3] H. Dreicer, Physical Review **115**, 238 (1959).
[4] X. Guan, H. Qin *et al.*, Phys. Plasmas **17**, 092502 (2010).
[5] J. Martín-Solís, J. Alvarez *et al.*, Phys. Plasmas **5**, 2370 (1998).
[6] J. Martín-Solís, B. Esposito *et al.*, Phys. Plasmas **6**, 238 (1999).
[7] J. Liu, H. Qin *et al.*, Phys. Plasmas **21**, 064503 (2014).
[8] M. Bakhtiari, G. J. Kramer *et al.*, Phys. Plasmas **12**, 102503 (2005).
[9] J. Connor and R. Hastie, Nucl. Fusion **15**, 415 (1975).
[10] H. Qin and X. Guan, Phys. Rev. Lett. **100**, 035006 (2008).
[11] Y. He, Y. Sun *et al.*, J. Comput. Phys. **281**, 135 (2015).
[12] H. Qin, S. Zhang *et al.*, Phys. Plasmas **20**, 084503 (2013).
[13] J. Xiao, J. Liu *et al.*, Phys. Plasmas **20**, 102517 (2013).
[14] R. Zhang, J. Liu *et al.*, Phys. Plasmas **21**, 032504 (2014).
[15] J. D. Jackson and J. D. Jackson, *Classical electrodynamics* (Wiley New York etc., 1962), Vol. 3.
[16] S. Wu, Fusion Eng. Des. **82**, 463 (2007).
[17] C. Grebogi and R. G. Littlejohn, Phys. Fluids **27**, 1996 (1984).
[18] V. I. Arnol'd, *Mathematical methods of classical mechanics* (Springer, 1989), Vol. 60.
[19] R. G. Littlejohn, J. Plasma Phys. **29**, 111 (1983).
[20] J. R. Cary and A. J. Brizard, Rev. Mod. Phys. **81**, 693 (2009).
[21] A. H. Boozer, Phys. Fluids 23, 1979.

Effect of 3D field on energetic particles in KSTAR

Jun Young Kim[a], Junghee Kim[a,b], T. N. Rhee[b], Won-Ha Ko[a,b],
S. W. Yoon[b], Y. M. Jeon[b], and M. Isobe[c]
[a]Korea University of Science and Technology, Daejeon, Korea
[b]National Fusion Research Institute, Daejeon, Korea
[c]National Institute for Fusion Science, Toki-shi, Japan
Email: nature1981@nfri.re.kr

Understanding of the fast ion loss behavior in the presence of the non-axisymmetric magnetic field by resonant magnetic perturbation (RMP) is being crucial since the RMP is the most optimistic method for ELM mitigation and/or suppression for ITER. In order to investigate the behaviors of the fast ions during RMP in KSTAR plasmas, fast-ion loss detectors (FILD) have been used intensively. Two sets of scintillator-based fast ion loss probe-heads have been installed inside of KSTAR vacuum vessel near C- and I-port to demonstrate the localized and asymmetric properties of the fast-ion loss by the applied edge magnetic perturbations (RMP). Simultaneous measurements of both FILD-1 and FILD-2 have produced the preliminary observations on the asymmetric loss rate during applications of various RMP spectra. In addition, the effect of toroidal rotation, which seems to be related to the fast-ion loss rate, will be presented.

1. Introduction

Resonant magnetic perturbation (RMP) is one of the most optimistic methods for ELM mitigation and/or suppression, resulting in reduction of the thermal load on a divertor. However, recent numerical simulation works and experimental results have shown that the beam ion loss in the presence of RMP is enhanced at the toroidally localized positions [1~5] depending on the perturbation configuration. In KSTAR, fast ion losses measured while the RMP have shown the enhanced signals exhibited on a FILD. In case of RMP mode locking, it was observed at least 1 order higher fast ion loss. In addition, fast ion loss rate was enhanced and suppressed depends on the RMP configuration on a localized position. Furthermore, the fast ion loss rate might be influenced strongly by toroidal rotation speed during RMP and it might be from the effect of the screening of external perturbation field penetration by the fast rotating plasma [6]. Since the reliable prediction of fast-ion transport becomes a crucial issue on potential damage to the first wall, [7] more detailed research on the fast-ion transport related to non-axisymmetric perturbation and/or Plasma locking should be analyzed and controlled. To investigate fast ion loss behavior during RMP, scintillator based fast-ion loss detectors (FILD) have been used at the peripheral of confined plasmas to understand the loss mechanisms of fast-ions.
Thus, this paper delineates KSTAR fast ion loss measurement results during RMP, Se ction 1 gives an introduction to the importance of understanding of the fast ion trans port during external magnetic perturbation. Section 2 describes the RMP coils and FI LD diagnostics system. Section 3 presents the experimental results of fast ion loss me asurement during RMP and finally, a short summary is given in Section 4.

2. RMP coils and fast ion loss detectors

KSTAR Field error correction (FEC) coils have been utilized for the magnetic resonant perturbation (RMP) [8]. FEC coils are consisted with total 12 coils that are 4 sections in toroidal direction and each section has top, middle and bottom coil. By using this

configuration of coils, n=1 or n=2 or mixture of n=1 and n=2 penetrations are applicable. Also three rows of the FEC coils can provide various poloidal magnetic spectra.

In 2014 KSTAR campaign, two FILD system are operated. FILD-1 is installed at the upper mid-plane (44cm above the mid-plane) of the C-port which is separated 202.5 degree from NBI in toroidal direction. The FILD-1 system consists of the probe head, the mounting system and the image detection system. The probe head of the FILD consists of a scintillator plate, aperture and collimator slits and a graphite thermal shield. The aperture of the three-dimensional collimator is aligned parallel to the local magnetic field. The three-dimensional collimator is acting as a magnetic mass spectrometer and it disperses the incident fast-ions on the scintillator plate according to their energies and pitch-angles. The perpendicular velocity component of a fast-ion to the magnetic field line is directly related to the gyro-radius of the lost ion and the distance from the collimator to the scintillator strike point is proportional to its gyro-radius. Pitch-angle is a ratio between the parallel and the perpendicular components of the total velocity of a fast-ion to the external magnetic field, and in a similar manner, as the pitch-angle varies, the ion will strike the different position on the scintillator even though the total ion energy is same. Consequently, it is possible to determine the pitch-angle and gyro-radius of escaping fast-ions from the measurement of the strike position on the scintillator. The mounting system enables controlling the radial position of the probe head by moving the shaft tube back and forth using an air motor. A graphite shield covers up the probe head of FILD system to protect the internal components from the excessive heat load. The graphite cover is shaped according to the plasma boundary to reduce the perpendicular heat load on to the protection cover. TG-green was chosen as a scintillator material for better emitting efficiency and it is coated on the stainless steel substrate. TG-green scintillator has already been used in the scintillator-based fast-ion loss detectors in AUG [9] and D□-D [10]. Cubic beam splitter divides scintillation light from the fast-ion bombardment into two and the CCD camera (up to 200 fps) utilized with a telescopic camera lens to captures one of the rays from beam splitter. Another ray is focused on the optical fiber bundle and it is connected to the 16-channel photomultiplier tube for fast measurement (up to 1MHz) of fast ion loss fluctuation. FILD-2 is also a scintillator based fast ion loss detector, but its probe-head is fixed at certain radial position. It is installed at I-port, lower mid-plane which is toroidally separated from for 135 degree from FILD-1. FILD-2 system has only fast camera system and APD (avalanche photo diode) cam will be installed for 2015 EXP.

3. Experimental results of fast ion loss measurement during RMP

Simultaneous measurement of two sets FILD systems enables identifying the toroidally asymmetric and localized fast ion loss pattern in non-axisymmetric magnetic field by RMP. For shot number 10921, n=1 +90 degree phasing RMP (2200_0220_0022) has been applied for 5.2s to 7s, gradually increase coil current from 0 to 4kA/t. The toroidal magnetic field and plasma current is kept as 2.0T and 400kA, respectively. As RMP turns on, immediately fast ion loss increases by factor of 2 has been observed both in FILD-1 & FILD-2. However, from the bifurcation point (RMP-induced mode locking), the intensity of fast ion prompt loss spot in FILD-1 is increased by at least by factor of 10. Meanwhile, the fast ion loss signal in FILD-2 is decreased. When n=1 RMP is applied with given polarity, the perturbation field, B_r direction at FILD-1 is toward to outside while its direction at FILD-2 is inward. So it seems that the fast ion loss pattern during RMP is affected by B_r direction. This toroidally asymmetric and localized fast ion loss is due to the symmetric breaking of magnetic field and can cause severe damage to the plasma facing component.

In case of mixed RMP, it has been shown similar results. For shot number 11111, we

applied four pulses of mixed RMP (2002_2020_2200); 1) middle coil only (n=2) with constant current, 2) all coils with constant current, 3) Top and bottom coils (n=1 with non-resonant component) with constant current and 4) constant middle coil current, plus top and bottom coil current scan. (Fig. 1) For the given RMP polarity, as soon as RMP is turned on, the fast ion loss rate in FILD-1 is immediately decreased to the base level except third pulse (T/B coil only). For shot number 11458, all the plasma parameters of #11111 are reproduced but RMP coil polarity. The RMP coil polarity has been changed by 180 degree (0220_0202_0022) and as RMP is turned on, fast ion loss rate in FILD-1 is increased for all four RMP pulses. The loss rate enhancement was biggest during the second pulse (all coils) and the first pulse (M-coil only) was followed. In a comparison of #11111 and 11458, it has been observed that the toroidal asymmetric fast ion loss can be regulated by changing RMP polarity. Also in the mixed RMP case, the middle-coil looks more effective to perturb the fast-ion orbit.

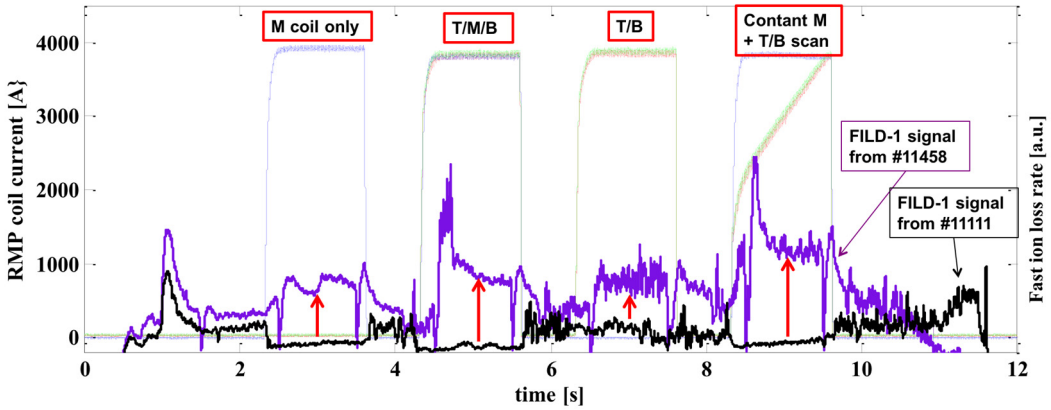

Figure 1. Fast ion loss rate measured by FILD-1 during mixed RMP. As RMP coil polarity changed, ion loss behavior is changed from 'suppression' to 'enhancement'.

To investigate the effect of the toroidal rotation on the external field screening effect and fast ion loss rate, electron cyclotron heating (ECH) has been used to change the rotation speed while the RMP is applied. During shot number 11465, n=2 middle coil was turned on during plasma current plate-top region and 110Ghz and 170 Ghz ECH has been launched to regulate the toroidal rotation velocity. Both in L- and H-modes, toroidal rotation dependency on the fast-ion loss has been shown clearly. As rotation increases, fast-ion loss decreases. (Fig. 2) In a low rotation or locking plasma, fast-ion loss level is enhanced and the possibility of severe damage on the first-wall and in-vessel components is increasing.

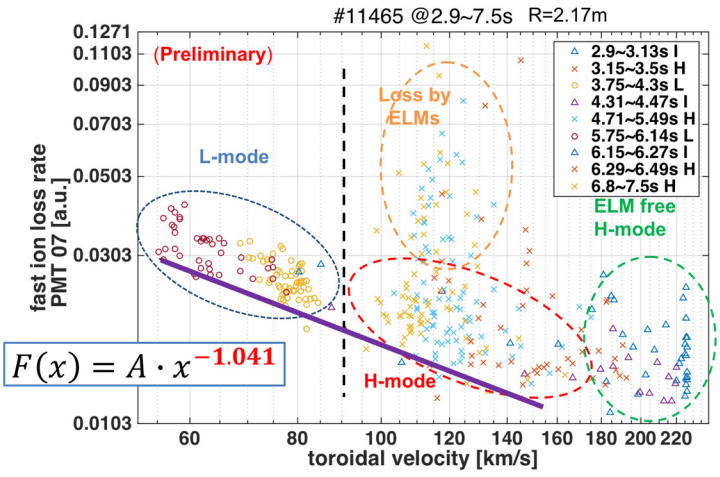

Figure 2. As toroidal rotation velocity is increase, the fast ion loss rate is decrease. The relation of fast ion loss rate and toroidal velocity is following exponential function and the loss patterns in L- and H-mode regime are well distinguished.

4. Summary

Various fast ion loss signatures during RMP application has been observed simultaneously by scintillator based fast ion lose detectors FILD-1 and -2 in KSTAR. Excessive fast ion loss with at least 1 order higher compare to conventional L-mode plasma during RMP mode locking was observed. Fast ion loss during RMP is non-axisymmetric and sensitive to the B_r direction. In addition, by changing RMP coil polarity, toroidally asymmetric fast ion loss can be regulated. It seems that the toroidal rotation and fast ion loss rate closely related. As rotation speed is increasing, fast ion loss rate is decreasing. Shielding effect of as external perturbation (RMP) field penetration needs to be more investigated. Toroidally asymmetric and localized fast ion loss due to RMP should be avoided to prevent the damage to the wall or vacuum vessel. Also low toroidal rotation velocity could enhance the fast ion loss rate and it could harm the fusion performance.

Acknowledgement
This research was supported by Ministry of Science, ICT, and Future Planning under KSTAR project and was partly supported by the JSPS-NRF-NSFC A3 Foresight Program (NRF No. 2012K2A2A6000443).

References
[1] K. Tani *et al*., Nucl.Fusion **52**, 013012 (2012).
[2] K. Shinohara *et al*., Nucl. Fusion **52**, 094008 (2012).
[3] J. Kim *et al*., Rev. Sci. Instrum. **83**, 10D305 (2012).
[4] M. Garcia-Munoz *et al*., Nucl. Fusion **53**, 123008 (2013).
[5] J. Kim *et al*., 10th ITPA Energetic Particles Topical Group Meeting (2013).
[6] Y. Q. Liu *et al*., Plasma Phys. Control. Fusion 54 (2012) 124013
[7] C.Z. Cheng, *et al*., in Fusion Energy 1996 (Proc. 16th Int. Conf. Montreal, 1996), Vol. **2**, IAEA, Vienna (1997) 953
[8] Y.M. Jeon *et al.,* Phys. Rev. Lett. **109,** 035004 (2012)
[9] M. Garcia-Munoz *et al.*, Rev. Sci. Instrum. **80**, 053503 (2009)
[10] R. K. Fisher *et al*., Rev. Sci. Instrum. **81**, 10D307 (2010)

Preliminary result and initial analysis on radial profiles of impurity line emissions measured with EUV spectrometer on HL-2A

Chunfeng Dong[1], Zhengying Cui[1], Shigeru Morita[2], Ping Sun[1], Kai Zhang[1], Bingzhong Fu[1], Ping Lu[1], Yan Zhou[1], Yuan Huang[1], Qingwei Yang[1] and Xuru Duan[1]

[1]*Southwestern Institute of Physics, P. O. Box 432, Chengdu 610041, China*
[2]*National Institute for Fusion Science, Toki 509-5292, Japan*

Abstract:
A space-resolved extreme ultraviolet (EUV) spectrometer has been developed on HL-2A to monitor the impurity behavior and to study the impurity transport. A gold-coated varied-line-spacing (VLS) holographic grating with curvature of 5600mm is adopted as a dispersion component and a back-illuminated charge-coupled device (CCD) with size of 6.6×26.6 mm^2 (1024×256 pixels) is utilized to record the spectral image. A two-stage wavelength scanning system is designed to enable the measurement in wider wavelength range of 30-600Å. The line of sight of the spectrometer is inclined to a downward direction to measure an entire profile of the impurity line emission at lower half (0≤Z≤-40cm) of HL-2A tokamak plasmas. The vertical profile of line emissions from several impurity spices such as carbon, oxygen, iron, copper and molybdenum is successfully observed with a good spacial resolution. The vertical profile of CIV (312Å) measured from limiter and divertor discharges show a slight different radial location at the peak intensity position. The intensity of CIV significantly increases in the limiter configuration because the graphite is used as the limiter material and further increases when the auxiliary heating of ECRH and NBI is turned on. A similar result is also observed in the CVI emission. When the discharge encounters the H-mode transition, the vertical profile of CIV and CVI indicates a substantial change. A preliminary result on the vertical profile of several impurity spices observed from a variety of discharges is presented with an initial analysis.

1. Introduction

Impurity transport study is one of the essential subjects to the magnetically confined fusion plasma research. Plasma confinement capability is strongly affected by the impurity behavior through radiation loss, plasma dilution. In addition, high-Z impurity accumulation at plasma core predicated by the neoclassical theory will have a serious damage to the device, such as ITER with tungsten divertor plates[1]. On the other hand, plasma performance can benefit from the presence of impurity at plasma edge, since head load onto divertor plates could significantly reduced by seeding impurities in divertor region[2]. Therefore, it is important to study impurity transport for impurity control in present device and ITER.

Spectroscopy plays an important role in both the impurity diagnostics and the impurity transport study. A normal incidence vacuum ultraviolet (VUV) spectrometer has been developed to measure edge impurity line emissions in the wavelength range of 300-3200Å in HL-2A in 2008. The electron temperature is dramatically increased in HL-2A due to the recently improved electron cyclotron resonant heating (ECRH) system and neutral beam injection (NBI) heating system. Wavelength of impurity line emissions radiated from plasma core shifts towards extreme ultraviolet (EUV) range (⩽500Å). Particularly for the high-Z material tungsten, the spectra are mainly measured below 100Å in the high temperature plasma from previous study [3-5]. On the other hand, a new method for the impurity transport study based on impurity profile measurement

[6,7] has been proposed, instead of tracing the time evolution of impurity line emission, which has been used as a conventional method for impurity transport study for years. Therefore, an EUV spectrometer with spatial resolution is desired for HL-2A tokamka.

2. Space-resolved EUV spectrometer system

HL-2A tokamak is a device with axi-symmetric X-point poloidal divertor configuration, and the major and minor radii of the tokamak are 1.65m and ~0.4m, respectively. The arrangement of space-resolved EUV spectrometer in HL-2A tokamak is shown in Fig. 1. The line of sight of the spectrometer is not perpendicular to the magnetic field line and has a angle of 76° with toroidal magnetic field direction. The distance between entrance slit and plasma center is about 7.37m along the horizontal direction. The space-resolved EUV spectrometer consists of an entrance slit, a spatial-resolution slit, a varied-line-spacing holographic grating and a CCD detector. A varied-line-spacing holographic grating with 1200 grooves/mm is equipped to this spectrometer. The detective area of CCD camera is 26.6×6.6mm^2 corresponding to 124×255 pixels. The width of entrance slit and space-resolved slit are 100μm and 0.5mm, respectively. The angle of incidence of this spectrometer is 87°. The distance between the entrance slit and grating center is 237mm and the distance from grating center to focal plane is 235mm. Two-stage wavelength scanning system for moving CCD position along the focal plane is designed to enable the vertical profile measurement in wavelength range of 30-600Å. Electric motor is externally controlled for the wavelength scan through LAN network.

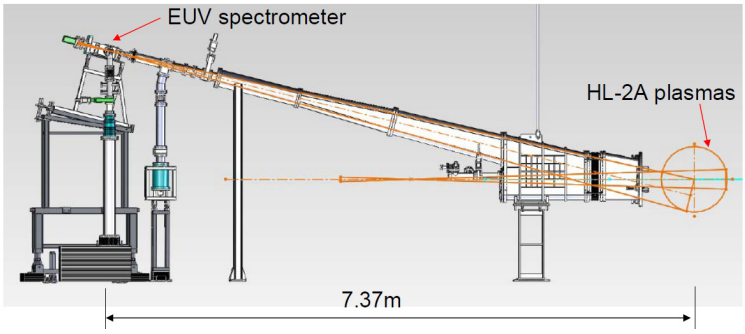

Fig. 1 The arrangement of space-resolved EUV spectrometer in HL-2A.

The impurity spectra emitted from lower half of HL-2A plasma (~40cm) is measured by the space-resolved EUV spectrometer, as shown in Fig.1. Figure 2 presents the poloidal cross section of HL-2A with lower divertor configuration, and the observable range of EUV spectrometer is denoted by the two blue lines. A metal bar with width of 3cm is installed at the diagnostic port position for the vertical position calibration of impurity profile. A sign will be produced in the impurity vertical profile as reference position. This bar could not be removed during the experiment since it is inside the machine vacuum. Therefore, all the profile analyzed here will be with a intensity well at Z=-15~-18cm, as shown in Fig. 3.

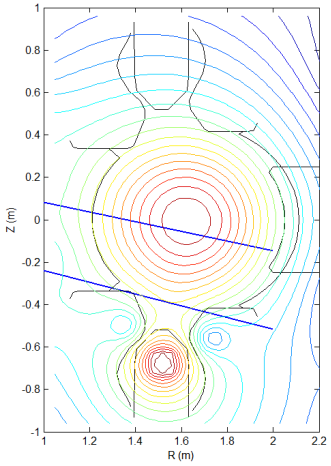

Fig. 2 Poloidal cross section of HL-2A tokamak.

3. Preliminary analysis on impurity profiles

The first wall of HL-2A tokamak is covered by graphite, and the divertor plates are made of copper with graphite baffle. The previous result shows that the impurity in HL-2A plasma is dominated by carbon in addition with oxygen and nitrogen, which are due to the air leakage. The vertical profile from carbon, oxygen and iron with different charge states are plotted in Fig. 3. The profiles of CIV (1s-2p: 33.73Å) shown in Fig. 3(a) has a clear difference with CVI ($1s^2 2s$-$1s^2 3p$: 312.4Å) due to the difference in ionization potentials of the two ions, i.e., 490eV for C^{5+} and 64.5eV for C^{3+}. In contrast, the profiles of OV (2s2p-2s3d: 192.8Å) and OVI ($1s^2 2s$-$1s^2 3p$: 150.09Å) show a similar pattern except the edge peak positions, since the ionization potentials for this two ions are close to each other, i.e., 113.9eV for O^{4+} and 138.12eV for O^{5+}. The profiles of FeXV ($3s^2$ -3s3p: 284.15Å) and FeXVI ($2p^6 3s$-$2p^6 3p$: 335.407Å) show a similar tendency as OV and OVI with the same reason of the similar ionization potentials for the two ions, i.e., 457eV for Fe^{14+} and 489.27eV for Fe^{15+}.

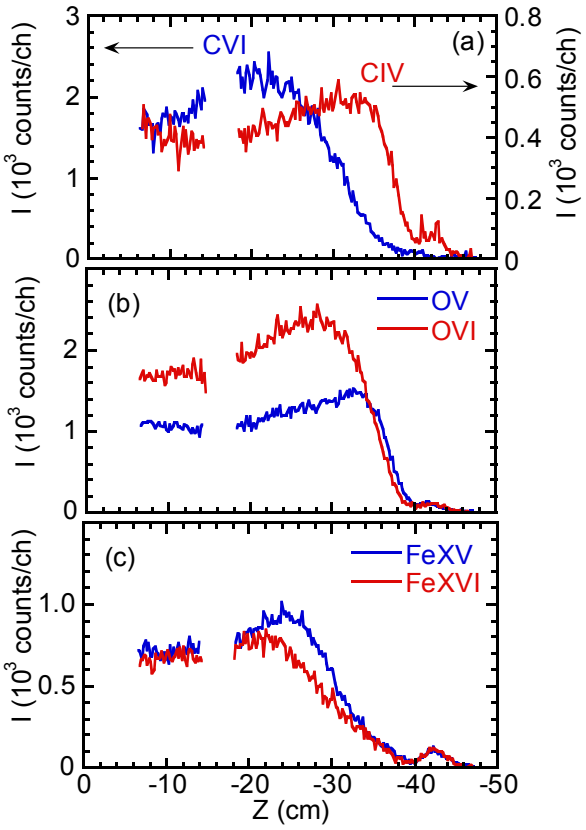

Fig. 3 Verical profiles of (a) CIV and CVI, (b) OV and CVI, (c) FeXV and FeXVI measured by space-resolved EUV spectrometer.

The plasma in HL-2A tokamak can be operated with two different configurations, i.e., limiter and lower null divertor and a clear difference in the two configuration has been observed in carbon profiles. The vertical profiles of CIV and CVI obtained from limiter and divertor configurations with similar plasma parameters are shown in Fig. 4, in which red line denotes limiter configuration and blue line denotes divertor configuration. Seen from Fig. 4(a), CIV profiles tends to be flat in limiter configuration and shows a sharp peak in divertor configuration. CVI vertical profiles shows similar distribution in two configurations. It has to be noted that the carbon intensity is enhanced in limiter configuration, since the limiter is

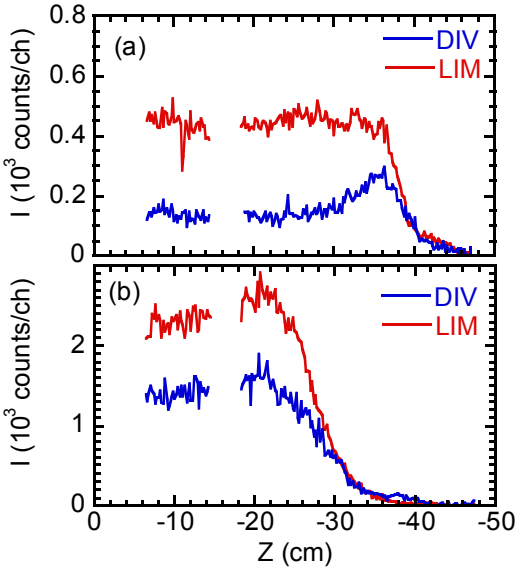

Fig. 4 Verical profiles of (a) CIV and (b) CVI obtained from divertor and limiter configurations.

covered by graphite in HL-2A.

The vertical profile of CIV with different vertical displacements from limiter configuration are plotted in Fig. 5, in which blue line denotes the small vertical displacement and red line denotes the large vertical displacement. Although the two profiles have similar pattern, a clear difference in edge of CIV vertical profile is observed. C^{3+} ion usually exists at the very edge of plasma with a narrow width due to its low ionization potential, in other word, the position of plasma boundary can be presented by the location of C^{3+} ion. When the plasma moves upwardly with the same minor radius, the position of plasma boundary is also shifted up. In contrast, the similar result is not observed in CVI profile.

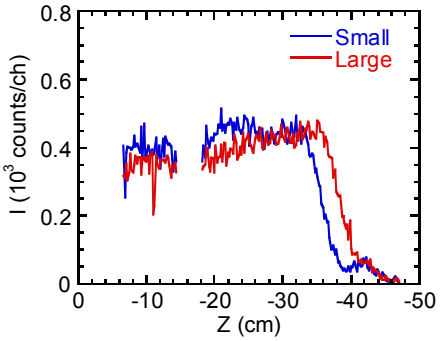

Fig. 5 Verical profiles of CIV obtained from discharges with small and large vertical displacements.

In order to increase the plasma stored energy and improve the plasma confinement, auxiliary heating is introduced in HL-2A tokamak. There are two different heating systems, i.e., electron cyclotron resonant heating (ECRH) with frequency of 65GHz and neutral beam injection (NBI) with positive ion source of 40keV. The intrinsic impurity, carbon, shows a different vertical profile for the different heating system. The vertical profiles of CIV and CVI obtained before and during ECRH heating are shown in Fig. 6. As we know, one of the advantages of ECRH heating is to avoid additional impurity introduced into plasma. However, the intensity of carbon is dramatically enhanced for both charge states of CIV and CVI during ECRH heating period as shown in Fig. 6.

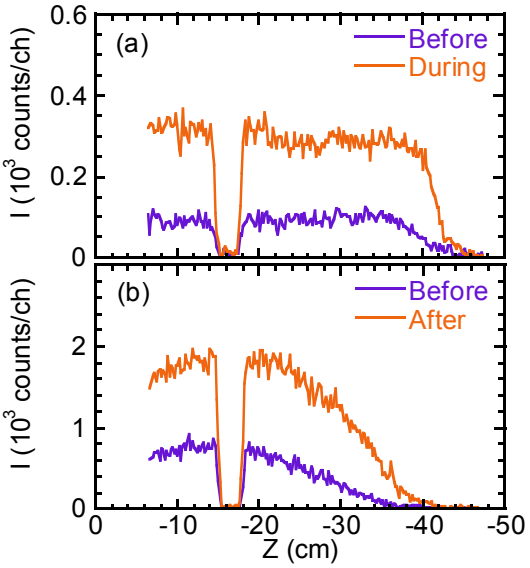

Fig. 6 Verical profiles of (a) CIV and (b) CVI obtained from plasma with ECRH heating.

In addition, the plasma size seems to be expanded as seen from CIV profile in Fig. 6(a). The plasma has a chance to touch the limiter or other parts covered with graphite inside the vacuum vessel when the plasma is expanded. Therefore, the carbon intensity is increased when ECRH is launched. On the other hand, according to the fluid model which is generally used to describe the impurity transport at plasma edge, the impurity transport is governed by the balance of friction force and thermal force. And the thermal force is proportional to the temperature gradient. The temperature profile measured by electron cyclotron emission (ECE) system shows that the temperature is significantly increased at plasma edge. Increased thermal force is also the possible reason for the increased carbon intensity. The detailed analysis will be done later.

The vertical profiles of CIV and CVI obtained before and during NBI heating are shown in Fig. 7. Time of 400ms (201-400ms) in Fig.7 denotes before NBI heating, 800ms (601-800ms) denotes during NBI heating phase, and in time interval of 600ms (401-600ms) NBI heating is just carried out in 501-600ms. The intensity of CIV in time interval of 800ms changes a lot due to

plasma performance and it has nothing to do with NBI heating. The increased carbon intensity during NBI heating period is also observed as the result in ECRH heating discharge. However, the plasma size seen from Fig. 7 is not expanded as ECRH heating case. The reason for the enhanced carbon intensity seems to be different from ECRH heating case. It is also found that the neutral beam could penetrate the plasma to hit the wall and bring the carbon into plasma.

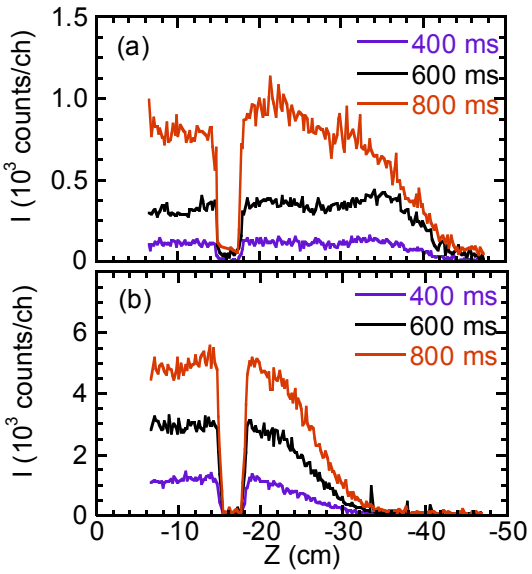

Fig. 7 Verical profiles of (a) CIV and (b) CVI obtained from plasma with NBI heating.

The H-mode plasma could be achieved by the combination of NBI and ECRH heating. The increased intensity of CIV and CVI are also observed as the ECRH and NBI heating, as shown in Fig. 8. The times in Fig. 8 have the same meaning as in Fig 7. It is seen that location of CIV and CVI is shifted outwardly in H-mode phase, and possibly this is due to the temperature profile is changed. On the other hand, increasement of CIV and CVI intensity is due to the confinement improvement.

4. Summary

A space-resolved EUV spectrometer is successfully developed in HL-2A for impurity profile measurement and impurity transport study. Vertical position of impurity profile is absolutely calibrated based on a metal bar. Vertical profiles emitted from various impurities are excellently measured. Carbon intensity in limiter configuration is significantly enhanced compared with divertor configuration. CIV profile at plasma edge shows a clear difference for different vertical displacement in limiter configuration. Carbon intensity is enhanced with auxiliary heating of ECRH and NBI. However, the mechanism for increasement of carbon intensity with different discharge conditions possibly is different. The carbon transport will be studied based on the EMC3-EIRENE code in the future.

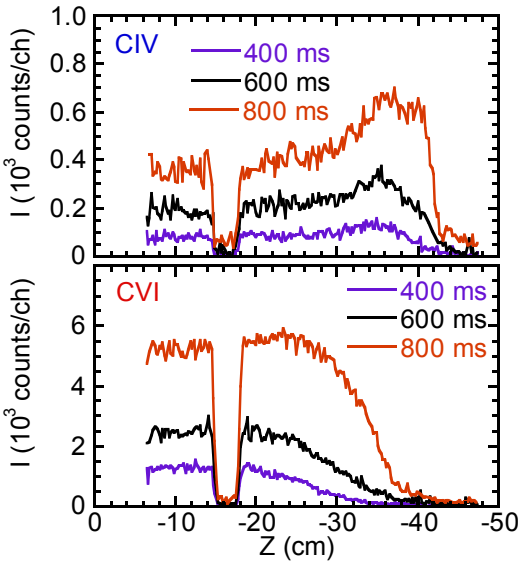

Fig. 8 Verical profiles of (a) CIV and (b) CVI obtained from H-mode plasma heated by ECRH and NBI.

Acknowledgement

The authors would like to thank X. Song for useful discussion about the magnetic structure reconstruction. This work was partly supported by the JSPS-NRF-NSFC A3 Foresight Program

in the field of Plasma Physics (NSFC: No.11261140328, NRF: No.2012K2A2A6000443).

Reference

[1] ITER Physics Basis Editors, Nucl. Fusion **39**, 2391 (1999).
[2] ITER Physics Basis Editors, Nucl. Fusion **39**, 2137 (1999).
[3] R. Isler et al., Phys. Lett. A **63**, 295 (1977).
[4] Hinnov et al., Phys. Lett. A **66**, 109 (1978).
[5] K. Asmussen, el al., Nucl. Fusion **38**, 967 (1998).
[6] C. F. Dong, et al., Jns. J. Appl. Phys. **51**, 010205 (2012).
[7] S. Morita, et al., Nucl. Fusion **53**, 093017 (2013).

Observation of plasma termination processes using stereoscopic fast framing cameras in the Large Helical Device

Mamoru SHOJI and the LHD Experimental Group
National Institute for Fusion Science, Oroshi-cho 322-6, Toki 509-5292, Japan
E-mail : shoji.mamoru@LHD.nifs.ac.jp

Abstract

The Large Helical Device has performed long pulse discharge experiments for more than one decade. Long pulse discharges in the previous experimental campaign in FY2013 were often terminated by the large amounts of carbon-rich dusts released from closed divertor regions, which were caused by exfoliation of mixed-material deposition layers. The plasma termination by the release of dusts was reduced by modification of the closed divertor configuration. Some long pulse discharges in the last experimental campaign in FY2014 were interrupted by iron-rich dusts released from stainless steel armor tiles on helical coil cans. Stereoscopic observations of the three-dimensional trajectories of the dusts revealed that the dusts penetrate into the main plasma through the ergodic layer and the Last Closed Flux Surface.

1. Introduction

The Large Helical Device (LHD) has a superconducting helical coil and three pairs of poloidal coils for producing plasma confinement magnetic fields, and toroidal plasma currents are not necessary.[1] It is quite advantageous for developing plasma heating systems and studying physics for long pulse discharge operation. One of main goals of the Large Helical Device (LHD) is demonstrating the feasibility of long pulse plasma discharge operation. The Large Helical Device has already achieved a long pulse plasma discharge for about 48 minutes in FY2013 with a plasma heating power of about 1.2 MW and a plasma density of about 1×10^{19} m^{-3}, corresponding to a world record of the highest input energy to plasmas of 3.4GJ.[2] One of the next targets of long pulse plasma discharge is 1 hour with a plasma heating power of 3MW. For achieving this target, understanding of physics for steady state plasma discharge operation, analyses of the particle/heat balance, impurity transport, plasma-wall interactions and dust formation/transport are indispensable. In the following sections, experimental results on the above last two topics in the previous (FY2013) and the last (FY2014) experimental campaigns are presented.

2. Experimental setup for long pulse plasma discharges

Recent long pulse discharges have been performed mainly by Ion Cyclotron Heating (ICH) using three antennas. Total heating sources of the ICH for long pulse discharges has been upgraded to about 3 MW with 6 transmission lines. For monitoring the plasmas and plasma-wall interactions in the vacuum vessel, totally about thirty visible CCD cameras (30 fps) have been mounted in some view ports in upper, lower, outer and tangential ports.[3] In addition to these cameras, fast-framing CMOS cameras have been installed for observing the plasmas with high frame rates (>1,000 fps) as shown in Figure 1. Fast framing cameras in an outer port (3-O) and an upper port (7.5-U) are stereoscopic cameras for measuring the three-dimensional

trajectories of dusts in the vacuum vessel.

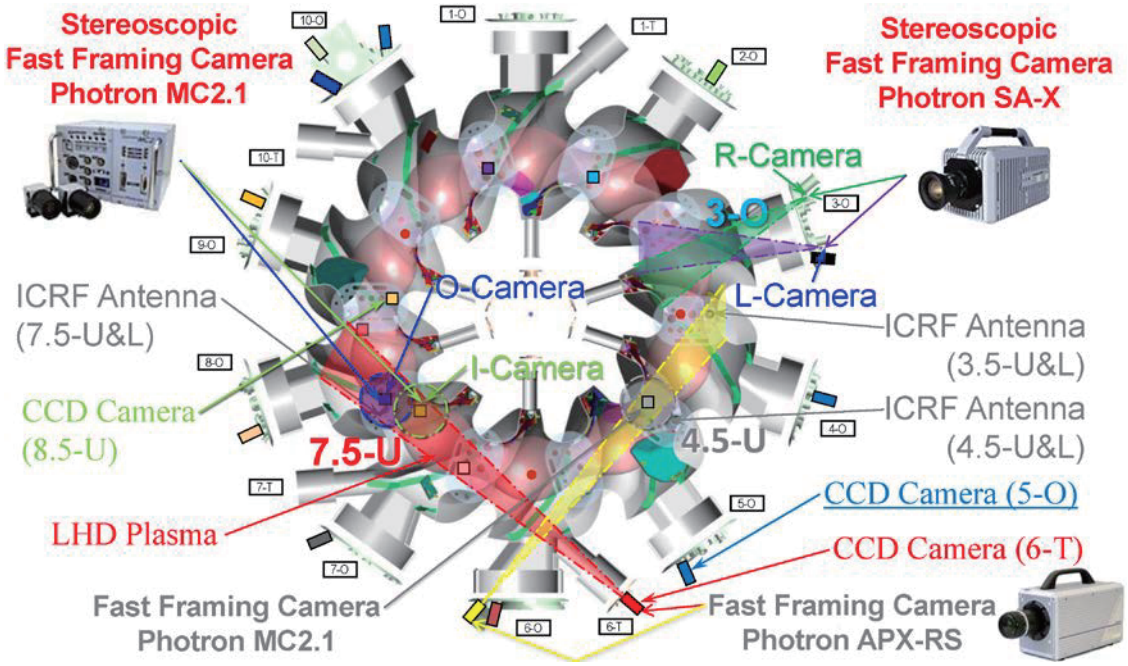

Fig.1 Top view of the experimental setup of plasma heating systems (ICRF antennas), visible CCD cameras and fast framing CMOS cameras for monitoring long pulse plasma discharges and plasma-wall interactions in the vacuum vessel, etc.

3. Control of deposition layers in closed divertor regions

Long pulse discharges in FY2013 were often terminated by release of large amounts of dusts from closed divertor regions. A fast framing camera installed in an upper port (4.5-U) proved that the dusts were released from the closed divertor region in the inboard side of the torus near a lower port (4.5-L).[4] Just before the plasma termination in this long pulse discharge, a visible spectrometer detected significant increase in carbon ion emission (CIII) with moderate rise in iron ion emission (FeXVI), which indicates that impurities included in the dusts triggered radiation collapse to terminate the long pulse discharge. After this experimental campaign, traces of exfoliation of carbon-rich deposition layers was found in the closed divertor region near a lower port (4.5-L) where the release of the dusts was observed with the camera.[5]

The configuration of the closed divertor near lower/upper ports which is enclosed by a dome structure and inclined divertor plates could be the main cause of the formation of the deposition layers. Some plasma-wall interactions could induce the exfoliation of the deposition layers to lead to the release of large amounts of dusts from the closed divertor region. In order to control the deposition layers, the configuration of the closed divertor near the lower/upper ports was modified such that the front surface of some inclined divertor plates to face to the main plasma after the previous experimental campaign. The deposition layers in the closed divertor region were successfully reduced after the modification in the last experimental campaign (FY2014). And, plasma termination due to the release of the dusts from the closed divertor regions near lower/upper ports was not observed in the last campaign (after the modification).

4. Plasma termination with iron ion emission increase

A different termination process of long pulse discharge from that in the previous experimental campaign (FY2013) was observed in the last experimental campaign (FY2014). The plasma was terminated with increase in iron ion emission which preceded carbon ion emission rise as presented in Figure 2 (a). In this long pulse discharge, a number of incandescent flying dusts were observed with a fast framing camera installed in an outer port (6-O). Figure 2 (b) is a representative image just before the plasma termination. Seeing the moving pictures taken with the fast framing camera, the flying dusts were likely to be released from a lower port (5.5-L). These observations suggest that iron-rich dusts released from around the lower port triggered termination of the long pulse discharge. After the last experimental campaign, arc traces were found on the surface of stainless steel armor tiles on a side wall of a helical coil can near the lower port. The main cause of these arc traces can be Electron Cyclotron Resonance Heating (ECRH) from an upper port (5.5-U). Because of no ECRH during the time of the plasma termination, it is possible that the arc traces itself enhance plasma-wall interactions causing erosion of the surface on the armor tiles to release iron-rich dusts to the main plasma.

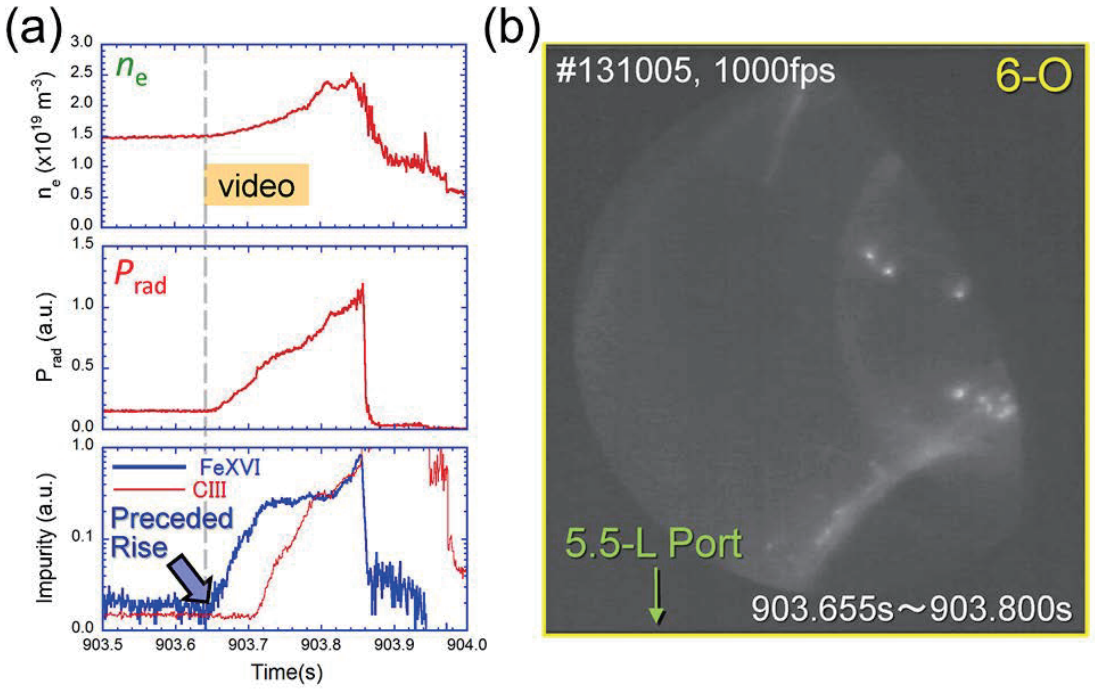

Fig.2 (a) Time evolution of the average plasma density, the radiation power, and the intensity of impurity emission (iron and carbon) measured just before a long pulse discharge in the last experimental campaign, (b) Image of flying dusts observed with a fast framing camera installed in outer port (6-O).

5. Stereoscopic observation of dust trajectories with a fast framing camera

A stereoscopic fast framing camera installed in an outer port (3-O) observed the termination process of a long pulse plasma discharge in the last experimental campaign (FY2014). The camera detected that sparks were initiated from a position of a gap of armor tiles on a side wall of a helical coil can in the inboard side of the torus close to an inner port (3-I). The sparks expanded and moved to near the top of the

helical coil can, which finally led to the release of dusts as shown a sequential image in Figure 3. In this discharge, the visible spectrometer observed abrupt increase in iron ion emission just before the plasma termination. The rate of the increase was much larger than that in carbon ion emission. These observations suggest that the sparks initiated at the gap triggered the release of iron-rich dusts from near the top of the helical coil can, which induced radiation collapse to terminate the long pulse discharge. The trajectories of some observed dusts was in the field of the view of the stereoscopic fast framing camera, which enables to derive the three-dimensional positions of the dusts using a pin-hole camera model.[6]

Figure 4 shows a poloidal cross-section of the LHD peripheral plasma for a typical magnetic configuration (the radial position of the magnetic axis R_{ax}=3.60m) and the vacuum vessel with showing the derived dust positions. The stereoscopic observations revealed that the most of the dusts locate in the inboard side of the tours and the dusts penetrate into the main plasma confinement region inside the ergodic layer and the Last Closed Flux Surface (LCFS). The large amounts of the iron-rich dusts released from the helical coil can could induce radiation collapse to terminate the long pulse discharge.

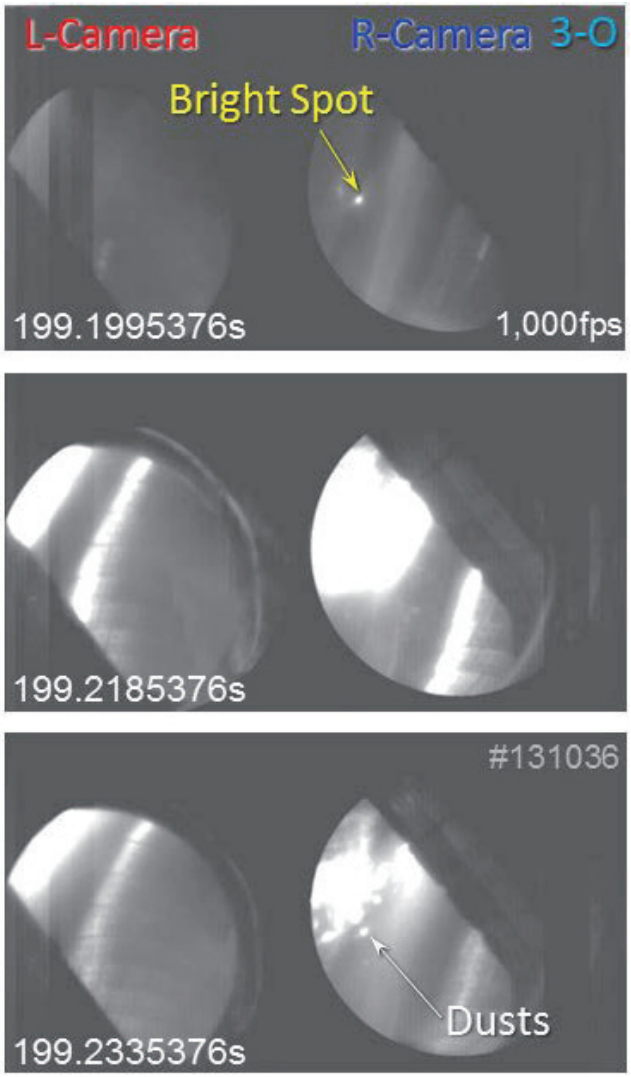

Fig.3 Sequential images of the plasma termination process of a long pulse discharge in the last experimental campaign observed with a stereoscopic fast framing camera installed in an outer port (3-O).

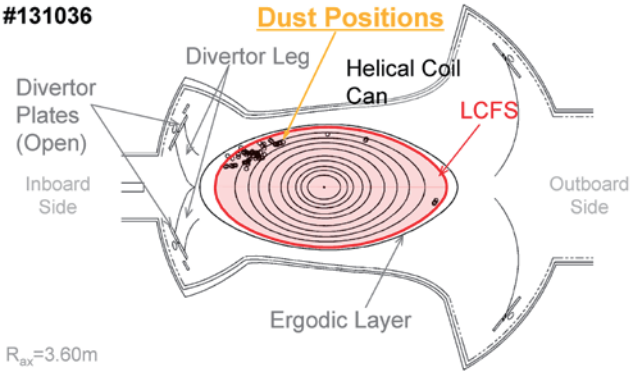

Fig.4 Poloidal cross-section of the LHD peripheral plasma for R_{ax}=3.60m and the vacuum vessel, and the positions of some observed dusts derived using a stereoscopic fast framing camera.

Acknowledgments

The corresponding author thanks the LHD group at the National Institute for Fusion Science (NIFS) for their helpful support for this research. This work was financially supported by NIFSULPP015 and by NIFS/NINS under the project of Formation of International Scientific Base and Network with an international

collaboration research framework between NIFS and CIEMAT in Spain. It was partly supported by the JSPS-NRF-NSFC A3 Foresight Program in the field of Plasma Physics (NSFC: No.11261140328, NRF: No.2012K2A2A6000443).

References

[1] A. Komori et al., 2010 Fusion Sci. and Technol. **58**, 1.

[2] H. Kasahara et al., 2014 EX/7-3, presented at 25th IAEA Int. Conf. on Fusion Energy St Petersburg.

[3] M. Shoji et al., 2015 J. Plasma and Fusion Res. SERIES **10**, 3402040.

[4] M. Shoji et al., 2015 Nucl. Fusion **5**, 053014.

[5] M. Tokitani et al., 2014 I10, presented at 21st Int. Conf. on Plasma Surface Interactions Kanazawa.

[6] R. Sakamoto et al., 2005 Rev. Sci. Instrum. **76**, 103502.

Current Status of Magnetic Island Feedback Control System Using ECH in KSTAR

Min Ho Woo[a], J.H.Jeong[a], M.Joeung[a], S.H. Hahn[a] , Y.S.Bae[a], W.R.Lee[a], J.G. Bak[a], H.S. Kim[a], Y.J.Kim, M.L. Walker[b], A.S. Welander[b], A. Humphreys[b]

[a]*National Fusion Research Institute, Daejeon, Korea*

[b]*General Atomics, San Diego CA, USA*

Email address: mhwoo@nfri.re.kr

In KSTAR 2014 campaign, we have successfully implemented magnetic island feedback control system into the plasma control system (PCS) [1] and tested its performance in real experiment. Detailed specs of the hardware for both mirror and power controllers are illustrated and their signal transmission lines and some important parameters like mirror speed, response time and calculation times are discussed in detail. Also, preliminary result for mirror controller test has been illustrated.

1. Introduction

Main purpose magnetic island feedback control is to suppress n=1 or n=2 islands that generally discriminates plasma performance or even cause disruption. Two MC probes that have toroidal phase difference have been chosen to estimate rough size of the island and 170GHz gyrotron is used as actuator to suppress the mode. Feedback control algorithms are implemented in PCS that is capable of achieving MC signal in real time and control mirror and power simultaneously during the plasma discharge. Two feedback control algorithms have been tested in the experiment [2]. The first one is “active tracking” that mirror is following specific q-flux surface along the resonance vertical line and ECH power is injected as island size has exceeded some critical value. The second one is “search and suppress” that determines where should mirror move depending one current island size or its difference compared to previous step.

2. Real time control of the 170GHz ECH using PCS

In KSTAR, PCS is the main device that controls both PF coils and heating. Especially for the 170GHz ECH, control of the steering mirror and power is done in a different way. For the mirrors, reflective memory (RFM) is used to transmit data from PCS to mirror control sever through optical cable. Mirror angle command data so called encoder values from PCS is written into RFM in every 50us and mirror control server reads data from RFM every 200us (5kHz). Also mirror control server writes current mirror angle data into the RFM using same sampling speed. Mirror control sever communicates with individual mirror controller in different location through MOXA by RS422 port and optical cable. Mirror response time for such data transmission system is about 18~20ms. In figure 1 we have shown basic layouts for data communication system.

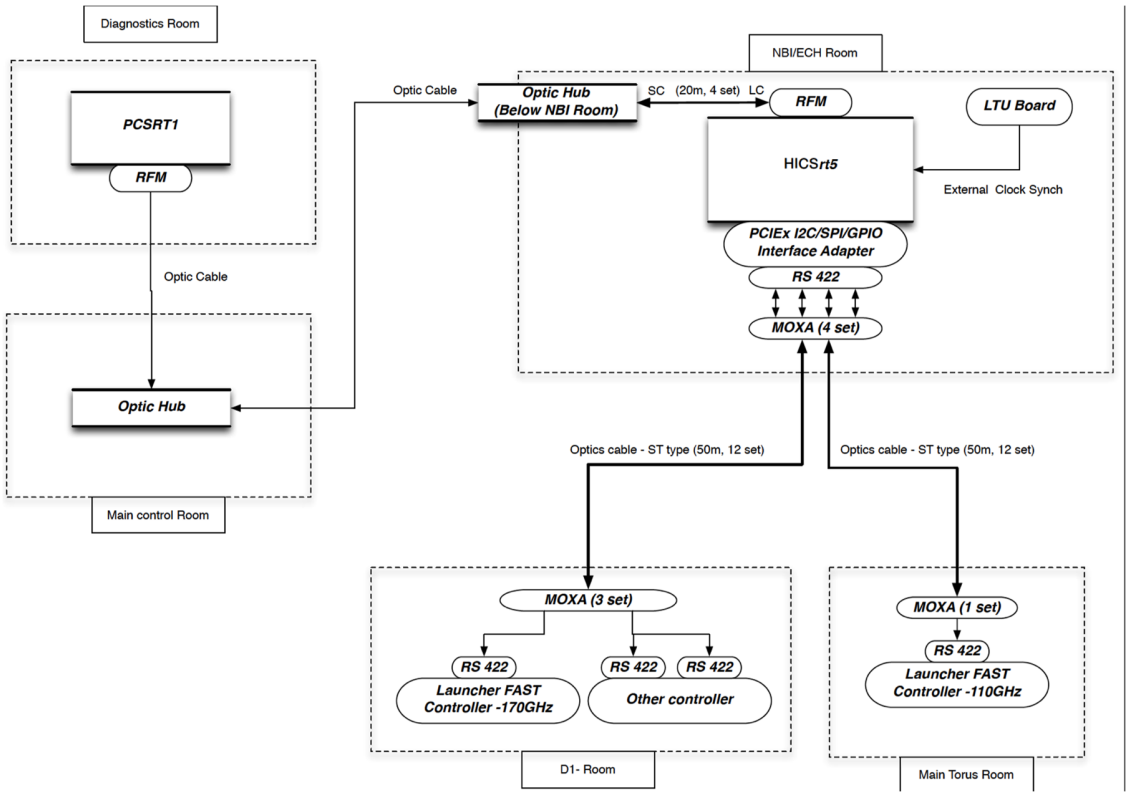

Figure 1. Hardware layout for data communication between PCS, mirror control server and mirror controller

PCS only gives commands to the mirror controller server and mirror control server checks if these commands are safe and guarantee that mirrors do not move out of the operation regime. Also mirror controller checks current mirror status and move the mirror only when controllers are ready.

In figure.2 we have shown results for the real time steering of the mirror by PCS. In the figure, blue/black line is mirror angle command designed in PCS and red/green line is actual mirror angle. We can see that mirrors moves towards its target as fast as they can. But after moving to target position, there is a small oscillation which is believed to be because of mechanical encoder. Also, in the figure green line is the mirror with water cooler and red line is without water cooler and their speed is different because mirror become heavier with cooler. Since KSTAR 170GHz ECH is designed to operate for more than 50s, water cooler is essential and we expect green line will be the normal mirror speed in real time. Assuming resonance lines in plasma center as 1.8m, approximate mirror vertical scan speed without cooler is 30cm/s and 10cm/s with cooler and vertical minimum and maximum position is -25~45cm.

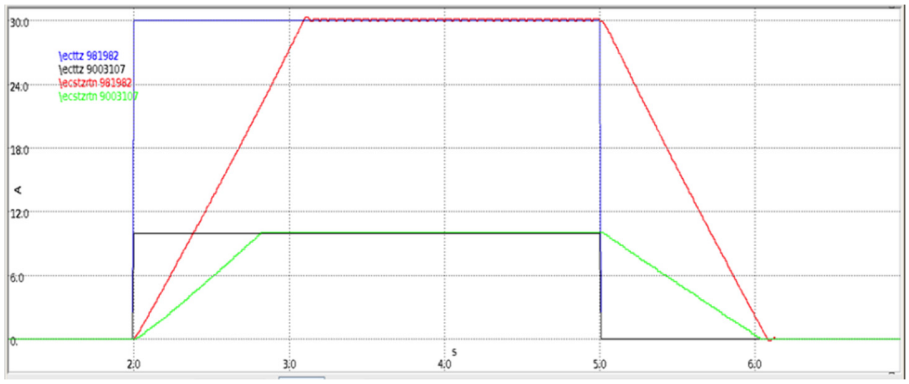

Figure 2. Blue and black line is mirror command from PCS and red and green line actual mirror angle

For the power control system, digital ou12tput from PCS is used to give only ON/OFF command to power control system. Then AFL 300 is used to transmit these data to the power control system where APS voltage is controlled to inject ECH. Detailed hardware system layout is given in figure.3. Response time this ECH power control system is less than 1ms.

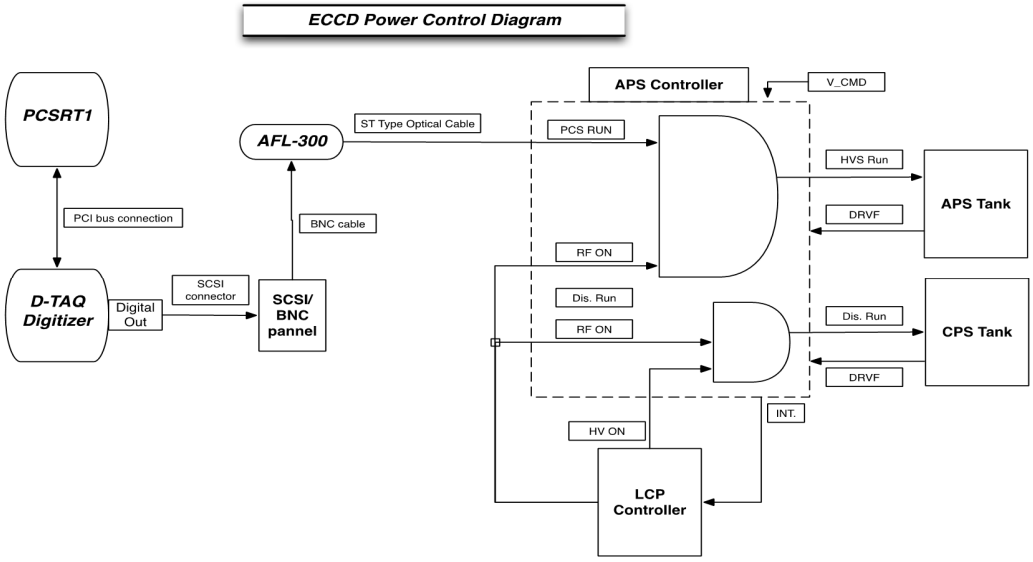

Figure 3. Hardware system layout for ECH power controller

3. Real time MCs and mode amplitude estimation

In KSTAR there are four dedicated MCs in different toroidal position but in same poloidal position. Their toroidal angles are given as (0,90,210,270) and poloidally they are located at lower-outboard passive plate. These MCs measure time derivative of magnetic fluctuation in time and ACQ245-ELF fast real time digitizer is used to achieve data to the PCS in real time to calculate mode number and amplitude. Spectral analysis of two probes is used to calculate mode number and corresponding mode amplitude [3].

Firstly, we Fourier transform two signals from the MC and denote them as $X_1(\omega), X_2(\omega)$.

Then compute cross-spectrum as

$$C_{12}(\omega) =< X_1(\omega)X_2^*(\omega) >_{\Delta\omega}$$

Here <> is average over some small interval of frequency (typically $3\delta\omega$ where $\delta\omega$ is sampling frequency divided by sample number for each FFT window). Then phase of this cross-spectrum indicates average phase difference between two probes for specificω. Mode number is found trivially by dividing phase difference with toroidal phase difference.

$$n = \frac{\Delta\phi_{12}}{\Delta\Phi} \text{ where } \Delta\phi_{12} = \arg(C_{12}(\omega))$$

Then mode amplitude for corresponding frequency is given as

$$P_{12} = |C_{12}(\omega)|$$

Also coherence is calculated to ignore signals that are lower thatn 95% confidence correlation level. In figure.4 we have shown different mode amplitude for toroidal mode number n=2 and n=1 using method described above. Also, these mode amplitudes are normalized by their frequency and square root is taken to reveal the fact that we are interested rough estimation of the island size rather than fluctuation itself.

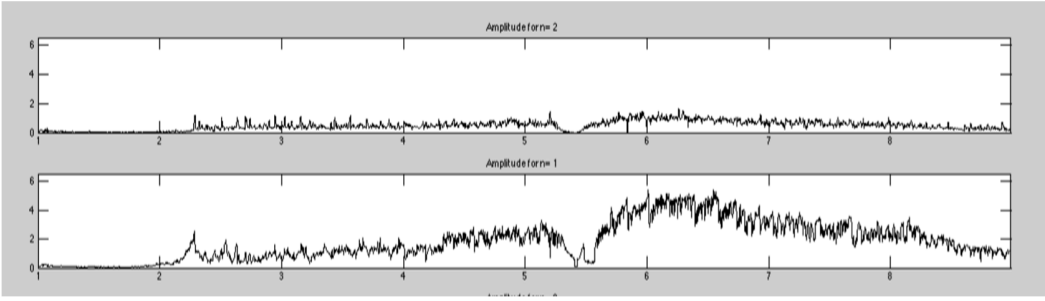

Figure 4. Magnetic island mode amplitude for n=2 and n=1 toroidal mode number

4. Real time feedback control of the magnetic island

The rough estimation of island size using MC in previous section can be used as input for magnetic island controller that is implemented in KSTAR PCS. 170GHz gyrotron and mirrors are used as actuator to suppress the mode. Currently, two types of magnetic island control algorithms are present in KSTAR[2].

The first one is “search and supress” (S&S) algorithm that moves mirror in a stepwise way depending on current mode amplitude with optimized dwell time and step size. In figure 5, we have shown commissioning result of S&S algorithm. We can see that when mode is not suppressed, mirror moves all the way to certain maximum, and then it reverses its direction, continues moving until controller has found position where mode amplitude is smaller than critical value. Then mirror stops moving and dwell there as long as mode amplitude is small enough.

The second one is “active tracking” algorithm. Using this algorithm we can follow specific q-flux surface along the resonance line of the 170GHz ECH. With compensations from off-line analysis of the magnetic island position, we can roughly aim at most probable island position and

shoot ECH as magnetic island appears. In Figure 6, we have shown the tracked mirror position together with command. This algorithm has limitations because flux surface is calculated from rtEFIT and magnetic field structure estimation includes lots of uncertainty. But with help of real time profile measurement (MSE etc…) and heating position calculation code like rt-torbeam, we can expect much better performance.

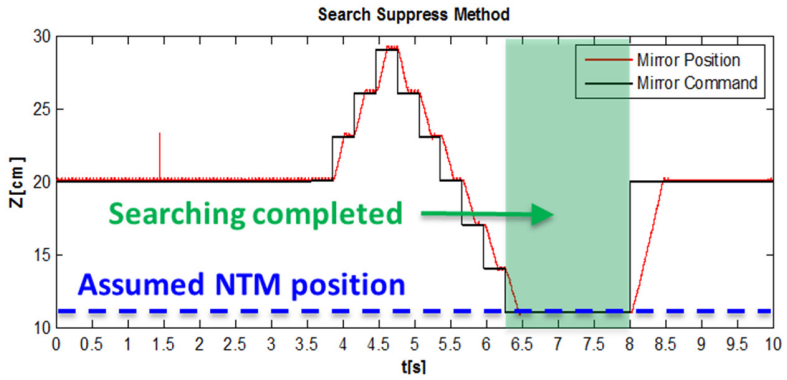

Figure 5. Mirror motion by "Search and Suppress" algorithm. Here red line is actual mirror position and black line is target position

For the injection of ECH power, we specify some critical mode amplitude and inject ECH power as mode amplitude exceeds this critical amplitude. In figure7, we can see that ECH is injected right after mode amplitude grows beyond critical amplitude.

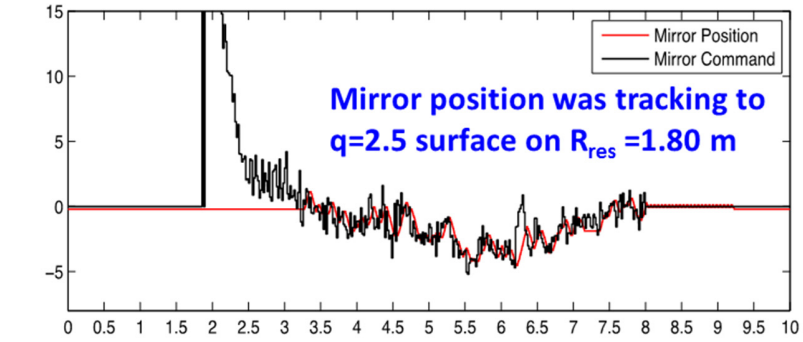

Figure 6. Mirror motion by "active tracking" algorithm. Red line is vertical position of the q=2.5 line at R=1.80m and black line is actual mirror position

Though "S&S" and "active tracking" for mirror can be used independently, we have found it more effective to use these algorithm altogether with power control algorithm. For example, we turn on "active tracking" algorithm before onset of the magnetic island mode without ECH. Then when the magnetic island appears and grows above critical value, we inject ECH and mirror control algorithm switches into "S&S" algorithm to get optimized position for suppression. If the mode is suppressed successfully, then we turn off ECH and switch to "active tracking" again.

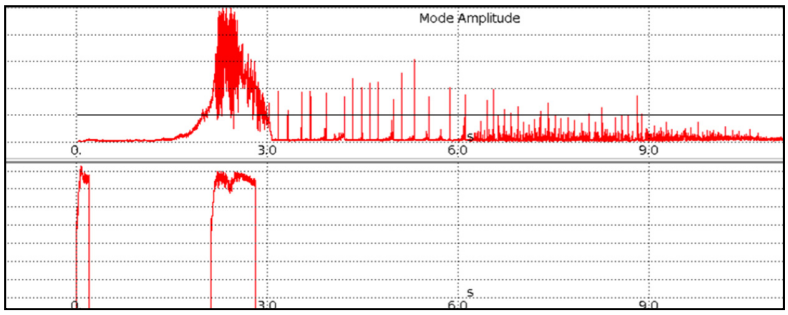

Figure 7. In upper figure, red line is mode amplitude and black line is critical amplitude. Lower figure is injected ECH power at the same time axis

5. Conclusion

With control algorithms listed above for mirror and ECH power, we are ready to use these control systems routinely in real experiment. With increasing heating power and better performance of the plasma, we are expecting magnetic island would become one of the most severe issues from the viewpoint of steady state, high beta operation. Thus commissioning of such real time feedback control system of the mirror and ECH power provides us firm background for extended operation regime for the high beta plasma and avoidance of the disruption.

Acknowledgement

This research was supported by Ministry of Science, ICT, and Future Planning under KSTAR project and was partly supported by the JSPS-NRF-NSFC A3 Foresight Program(NRF No. 2012K2A2A6000443).

References:

[1] S. Hahn, A.S. Welander, S.W. Yoon *et al*, "Progress and improvement of KSTAR plasma control using model-based control simulators", Fusion Engineering and Design 89, 542-547 (2014).
[2] D.A. Humphreys,*et al*, "Active control for stabilization of neoclassical tearing modes",Phys. Plasmas13, 056113 (2006)
[3] J.S.Kim et al., Plasma Phys. Control. Fusion **41** (1999) 1399–1420

Path to Resolve the Non-axisymmetry Issues in Tokamaks

Yongkyoon In
National Fusion Research Institute, Daejeon, Korea
Email : yongkyoon@nfri.re.kr

The presence of the non-axisymmetric field influences the axisymmetric tokamak in terms of stability and transport implicitly and sometimes explicitly. Hence, when the underlying level of intrinsic non-axisymmetric field becomes an order of magnitude lower, quite a few uncertainties in the relevant physics themes are expected to be resolved. The KSTAR, which has the lowest error field and toroidal field ripple among tokamaks, is well suited for such non-axisymmetry study. Nonetheless, to realize a future reactor sooner rather than later, it is deemed important to identify the path to passively robust plasma profiles that can be resilient against the influence of non-axisymmetric field, as well as to have active control capability of non-axisymmetric field.

1. Introduction

The understanding of non-axisymmetric fields on fusion plasmas has been greatly enhanced for the last couple of decades, but the lingering uncertainties still affect almost every aspect of axisymmetric tokamak physics [1]. While the sustainment of high performance axisymmetric fusion plasmas is subject to stability and transport issues, the presence of non-axisymmetric fields is directly or indirectly involved. Specifically, a majority of MHDs, such as tearing modes, resistive wall modes, locked modes, and disruption, are associated with non-axisymmetric ($n \geq 1$) fields. Also, momentum transport (e.g. plasma rotation) varies quite significantly, depending on either resonant or non-resonant non-axisymmetric fields, in addition to neoclassical toroidal viscosity (NTV) effects.

Meanwhile, it is quite interesting that such non-axisymmetric fields can be either beneficial or detrimental, depending on the 3D configuration. For example, the error field can be defined as unwanted non-axisymmetric field that is dominantly associated with kink-resonant components, while resonant magnetic perturbation (RMP) is an intentionally applied non-axisymmetric field that would be typically configured to maximize the pitch-resonant components [2]. Thus, it is of high interest to know what determines such vastly contrasting non-axisymmetric field impacts on tokamak plasmas.

In a typical tokamak, the intrinsic level of non-axisymmetric field is in the order of $<\delta B>_{m/n=2/1}/B_0 \sim 10^{-4}$, while an effective RMP would reach an order of magnitude higher, $<\delta B>_{m/n=2/1}/B_0 \sim 10^{-3}$. Here, $<\delta B>_{m/n=2/1}/B_0$ refers to the pitch-aligned component at m/n=2/1 surface, unless otherwise specified throughout this paper. It is quite common to try to establish an actively controlled (and/or removed) non-axisymmetry, while no or little attention is paid to the importance of passively robust profiles. However, in spite of a measurable level of non-axisymmetric field, it is not a secret to observe some discharges that do not have MHD likely due to strong rotational stabilization benefits [3] but, very importantly, still possess deformed flux surface, leading to NTV effects (rotation damping).

In that regard, should a device be equipped with an order of magnitude lower intrinsic error field (i.e. $<\delta B>_{m/n=2/1}/B_0 \sim 10^{-5}$), we may be able to resolve the uncertainty of non-axisymmetric fields more rigorously. In Section 2, the non-axisymmetric fields of KSTAR is discussed to see if it is suitable for this type of study. Then, Section 3 will discuss several

physics themes that may take advantage of the low level of non-axisymmetric fields, as well as an alternative view against conventional approach. A short summary is given in Section 4.

2. Low level of intrinsic non-axisymmetric fields in KSTAR

Ever since KSTAR reported an extremely low level ($<\delta B>_{m/n=2/1}/B_0 \sim 10^{-5}$) of intrinsic non-axisymmetric field after 2013 run-campaign, an outlier excluded from compass scan error field measurements was the source of ambiguity that should be addressed [2]. Hence, another compass scan using mid-RMP coils was done in 2014 run-campaign, which confirmed the record-low intrinsic EF in ohmic plasmas in KSTAR. Meanwhile, the intrinsic error field in H-mode plasmas has been diagnosed by monitoring the angular momentum variations. Specifically, an iso-surface of $n_e\Omega$ near q=2 surface, proportional to angular momentum, suggests the error field in typical neutral-beam-injected (NBI) H-mode plasmas (relevant to RMP ELM-controlled discharges) at $\beta_N \sim 1.6$ would be a factor of 2-3 larger than in Ohmic plasmas (at $\beta_N \sim 0.4$) [4]. Similar results are reached, even when the iso-surfaces near q= 3 and 4 surfaces are considered.

Although a routine operation in KSTAR does not exceed $\beta_N \sim 2.0$ yet, the low level of intrinsic EF is expected to allow us to easily access the no-wall stability limit (nominally $\beta_N \sim$ 2.6 in KSTAR) without having any dedicated error field correction. Considering that recent DIII-D experiments showed that the linearity of the plasma response is validated not only below no-wall limit [5], but also up to a substantial β_N above the no-wall limit (when the kinetic effects are included [6]), the linear projection beyond $\beta_N \sim 3.0$ is also likely to be valid ($\delta B/B_0 \sim 5\text{x}10^{-5}$) in KSTAR, as shown in Figure 1.

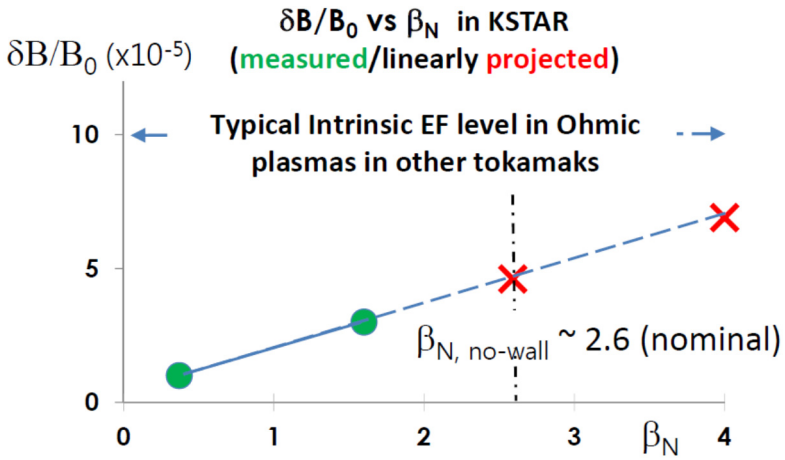

Figure 1. Intrinsic error field measurements and linear projection. Two green circles are the measured n=1 intrinsic error fields in Ohmic and H-mode plasmas respectively. Assuming that the linear dependence of $\delta B/B_0$ on β_N is valid, the linear projection for high β_N has been made in red cross marks. It is to be noted that even at $\beta_N \sim 4$, the projected error field level is lower than a typical value ($\delta B/B_0 \sim 10^{-4}$) in Ohmic plasmas in other tokamaks.

Nonetheless, it is to be noted that the n=1 intrinsic error field level is still much lower than a typical intrinsic error field level ($\delta B/B_0 \sim 10^{-4}$) measured in tokamaks. Besides, despite no dedicated measurement yet in KSTAR, similarly low level of $n > 1$ harmonics is expected, in that no source of non-axisymmetry, as well as higher plasma rotation in Ohmic and H-mode plasmas, has been identified.

Moreover, KSTAR has been characterized with the lowest toroidal field ripple ever. While a typical order of toroidal field ripple (δ_{TF}) is around 0.5 % in a majority of the tokamaks (DIII-D, JT-60U, and ITER), the ripple factor of 32 TF coil operations in JET was distinctively low at 0.08 %, which was attributable to very high Mach number, 0.65 [7]. In KSTAR (with δ_{TF} = 0.05 %), the fastest Mach number was recently measured at 0.8 [8,9]. Overall, the high toroidal rotation at pedestal top is likely due to both low EF & TF ripple in KSTAR. In fact, when core toroidal rotation in KSTAR is compared with those in DIII-D and AUG (of similar size and aspect ratio), we found that it is indeed faster than in the other tokamaks with similar NBI powers. To make a more direct comparison with other devices, momentum transport experiments are being planned in KSTAR with similar NBI torque levels (rather than NBI powers) .

3. Venues to address the non-axisymmetry issues actively and passively

Undoubtedly, active control capability of non-axisymmetric fields has been and will be an ideal tool to address the issue of how the presence of non-axisymmetry affects fusion plasmas. In this regard, when the underlying level of non-axisymmetry is insignificant, there are many interesting stability and transport themes we can clarify.

First, the purest plasma response against well-controlled non-axisymmetric field can be unambiguously measured. Also, the momentum transport (i.e. plasma rotation) and energy confinement dependence on 3-D field can be rigorously studied. Similarly, neoclassical toroidal viscosity (NTV) physics is to be elucidated, in that exclusively resonant or non-resonant components would be readily configured without the uncertainty of the other components.

For example, specifically deformed nested flux surfaces due to 3-D fields can be configured without driving magnetic islands. Thus, various 3-D neoclassical transport codes can be verified and validated. Also, the transport and turbulence associated with 3-D field is likely to be surgically diagnosed. Especially, the edge transport changes with and without ELM-suppression/mitigation would be of high interest.

Arguably, the most influential theme would be the RMP-ELM control/physics, where the physics mechanism and details need to be clarified. Recent KSTAR studies [2] suggest that the distinction between kink-resonant and pitch-aligned components might explain the unique observation of n=1 RMP ELM-control in KSTAR. In fact, recent DIII-D experiment results are also supportive to such hypothesis, in that the n=2 RMP ELM suppression conditions were separable from the kink-dominant conditions [10]. Meanwhile, the mid-plane in-vessel coils in KSTAR is rather uniquely positioned, likely attributable to another unique result (n=2 single mid-plane row RMP ELM-suppression) [8].

On the other hand, it is also important to take into account the existence of plasma profiles that are much more resilient against the influence of non-axisymmetric field [3]. Such passively favorable profiles, once identified, would be much more desirable, in that robust fusion plasma operations would be feasible without the need of actively controlled non-axisymmetric field. Throughout numerous stability experiments, it is not uncommon to have difficulty in identifying the destabilization conditions with seemingly similar conditions [3]. This implies that quite a few discharges survive without encountering the unstable conditions, whose plasma profiles are the ones that can be much more valuable in a reactor point of view. So far, we are used to a paradigm that the lower error field is desirable, while the RMP field strength should be minimally used, even if non-axisymmetric fields can be actively controlled. However, the ultimate future reactor among tokamaks is likely to be determined by both

active and passive criteria; *conventionally solid (extremely low EF with minimal use of RMP) and robust profiles (less susceptible to δB-variations)*.

4. Summary

The presence of intrinsic non-axisymmetric field has been recognized as influential on axisymmetric tokamaks. Thus, when the underlying level of non-axisymmetric field becomes an order of magnitude lower, quite a few interesting stability and transport themes can be explored and potentially resolved.

In that regard, the KSTAR, which has the lowest-level of error field and toroidal field ripple, is expected to provide the purest plasma responses against actively controlled non-axisymmetric fields. Thus, a systematic study of 3D field impacts on both transport and stability in KSTAR may help us not only to resolve the uncertainties of the non-axisymmetric field on axisymmetric tokamak performance, but also to potentially create/explore the knowledge and understanding of error-field-insignificant tokamak physics. On the other hand, a search for passively robust plasma profiles (against non-axisymmetric field) should be also sought in parallel to realize the future reactor sooner rather than later.

Acknowledgement
This research was supported by Ministry of Science, ICT, and Future Planning under KSTAR project and was partly supported by the JSPS-NRF-NSFC A3 Foresight Program (NRF No. 2012K2A2A6000443). We acknowledge significant contributions from KSTAR colleagues, appreciating the successful operation and team efforts in KSTAR. The content may not necessarily reflect the official opinions from any affiliated institutions, but can be rather regarded as a personal perspective of the author.

References
[1] T.C. Hender *et al*., Nucl. Fusion **47,** S12 (2007)
[2] Y. In *et al*, Nucl. Fusion **55,** 043004 (2015)
[3] Y. In *et al, "Holistic approach against performance-limiting instabilities in steady state plasmas"* at ReNew Workshop on March 23-27, 2009, https://www.burningplasma.org/web/ReNeW/whitepapers/2-53%20HolisticApproachReNew_v5.pdf
[4] Y. In, KSTAR Conference 2015
[5] M. Lanctot, Phys. Plasmas **18**, 056121 (2011)
[6] J.K. Park, private communication (2015)
[7] P.C. de Vries *et al*, Plasma Phys. Control. Fusion **48**, 1693 (2006)
[8] S.W. Yoon *et al*, IAEA-FEC (2014)
[9] S.G. Lee, private communication (2015)
[10] C. Paz-Soldan *et al*, Phys. Rev. Lett. **114**, 105001 (2015)

The progress of on-building ECRH system on J-TEXT *

Z. J. Wang , D. H. Xia, C. H. Liu, Z. J. Wang, M. Zhang, W. Zheng, L. Q. Jiang, D. L. Sun, Z. Zeng, F. T. Cui, Z. X. Yu, G. Zhuang, K. X. Yu, Y. Pan
State Key Laboratory of Advanced Electromagnetic Engineering and Technology
Huazhong University of Science and Technology
Wuhan, China
Corresponding author e-mail: Wangzj@hust.edu.cn

***Abstract*—As a flexible and controllable auxiliary heating method, electron cyclotron electron heating and current drive has been widely used in various plasma confinement devices and also will be used on J-TEXT. The main parts of the J-TEXT electron cyclotron systems under development are donated by the Culham Science Center, including six 60 GHz/200 kW/5 s (0.5 s) gyrotrons, six magnets and anode power supplies for the gyrtrons, transmission parts, etc. For these systems, the output mode of the gyrotron is TE_{02} mode and converted to TE_{01} mode for low loss transmission. Then the HE_{11} mode for efficient coupling is obtained at the end of the transmission lines by a TE_{01} - TE_{11} - HE_{11} mode conversion sequence. A 100kV/60A pulse step modulation power supply has been developed to feed all the six gyrotrons. The control system based on the Compact Reconfigurable I/O - 9068 platform of National Instruments for monitoring, timing and protection is being designed. Other units such as the cooling loops, a new quasi-optical launcher and a spared auxiliary power supply are on the way. It hopes that four to six EC subsystems can be finally used on the J-TEXT tokamak, and the first one is scheduled to be completed at the end of 2015.**

Keywords—J-TEXT tokamak; ECRH; rebuilding

I. INTRODUCTION

In recent years, owing to development of high power electron cyclotron electron heating (ECRH) systems on various magnetic confinement devices, especially tokamaks and stellarators [1]-[5], ECRH has been proved to be a useful and attractive method for plasma heating, start up, current profile control, stabilization of MHD instabilities, etc. To expand the operation region of J-TEXT tokamak, ECRH systems composed of six 60 GHz/200 kW/5 s (0.5 s) subsystems is under construction.

J-TEXT tokamak has a major radius of 105 cm and a minor radius of 25 ~ 29 cm with a movable silicon-carbide coated graphite limiter [6]. The centre-line toroidal field for normal discharge is about 2.0 T. Thus at J-TEXT, with an operation frequency of 60 GHz, the electron cyclotron waves will be mainly used for heating and current drive by the fundamental ordinary mode.

The ECRH systems on J-TEXT are rebuilt based on those systems of the former COMPASS-D tokamak at the Culham Science Center (CSC) [7]. For the on-going 60 GHz ECRH systems, a negative high voltage power supply (100 kV / 60 A) [8], a spared gun-anode power supply, a cooling system, a controlling system and a launcher has been designed excepted the donated parts from CSC. This paper gives a brief introduction of ECRH systems under development on J-TEXT tokamak.

II. WAVE SOURCES AND AUXILIARY UNITS

A. Gyrotrons

As a major part of donation from CSC, six gyrotrons are shipped to the site of J-TEXT tokamak, which will used as high power millimeter wave sources for ECRH systems. Fig. 1 is a photograph of one gyrotron.

Fig. 1. Paragraph of one 60 GHz gyrotron from CSC on the site of J-TEXT

TABLE I. GYROTRON PARAMETERS

Parameter	Value
Frequency	60 GHz
Output power	200 kW
Beam Voltage	80 kV
Beam Current	8 A
Efficiency	~ 32%
Pulse length	0.5 s (VGE-8006C); 5s (VGE-8006G)
Duty	1.46% (VGE-8006C); 1.8% (VGE-8006G)

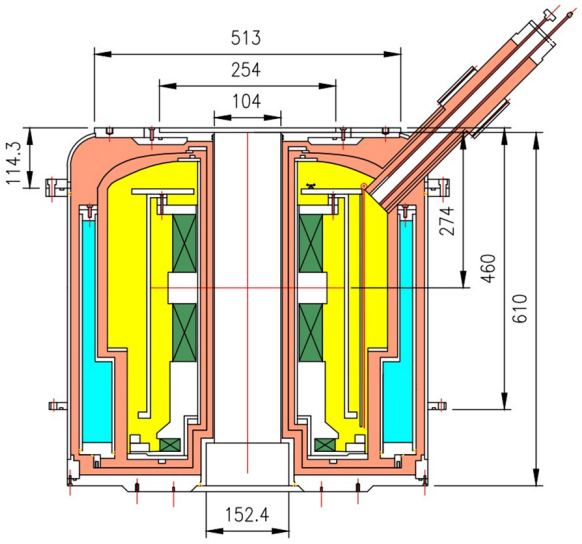

Fig. 2. A schematic cross-section drawing (unit: mm) of the SCM for 60 GHz gyrotron.

TABLE II. PARAMETERS OF COILS

Coil	No. of turns	Inductance (H)	Max currents (A)
Cavity coil 1	10452	18	40
Cavity coil 2	10452	18	40
Gun coil	3186	3	10

All these gyrotrons, including two VGE-8006C gyrotrons in the 1980s and four VGE-8006G gyrotrons in the 1990s, are produced by the former Varian Associates, Inc.. The VGE-8006C and VGE-8006G gyrotrons have similar parameters, only with different pulse length and duty. The main parameters of gyrotrons are summarized in Table I according to the manual of these two kinds of gyrotrons.

B. Magnets

For operation of a gyrotron, a superconducting magnet (SCM) is needed to provide the desired magnetic field profile. The SCM matched with the 60 GHz gyrotron is a traditional one, where the coils are immersed in a liquid helium bath to maintain the superconducting state [9].

Fig. 2 shows a schematic cross-section drawing of the SCM according to the manual of the manufacturer (Oxford Instruments). In Fig. 2, the main dimensions and the position of coils are given. For this magnet, seven coils, including two main cavity coils, a gun coil and two pairs of trim coils, are used to produce and optimize the magnetic field. Here the main magnetic field is generated by the cavity coils and gun coil, while the alignment of the field is finished by the trim coils.

Table II gives the main parameters of the cavity and gun coils. When max currents in Table II are added to these coils, a magnetic field of about 3.5 T will be produced in the center region of the magnet.

C. Power supplies

For operation of VGE-8006C and VGE-8006G gyrotrons, filament, cathode and anode power supplies should be applied as shown in Fig. 3, where the filament power supply is a AC current source (I_f) and other supplies (V_c, V_{ga} and V_b) are DC voltage source.

In Fig. 3, the beam voltage in Table I is provided by V_c which has been developed by the J-TEXT lab based on the pulse step modulation (PSM) technology; V_{ga} is mainly used to control output power of the gyrotron and the bias supply V_b is applied for easy control of the gyrotron beam; the filament is fed by I_f for emission of electrons. Although power supplies excepted V_c have been donated by CSC, a spared auxiliary power supply for anode and filament has been designed and will be finished in a few months. Table III summaries the main parameters for these power supplies.

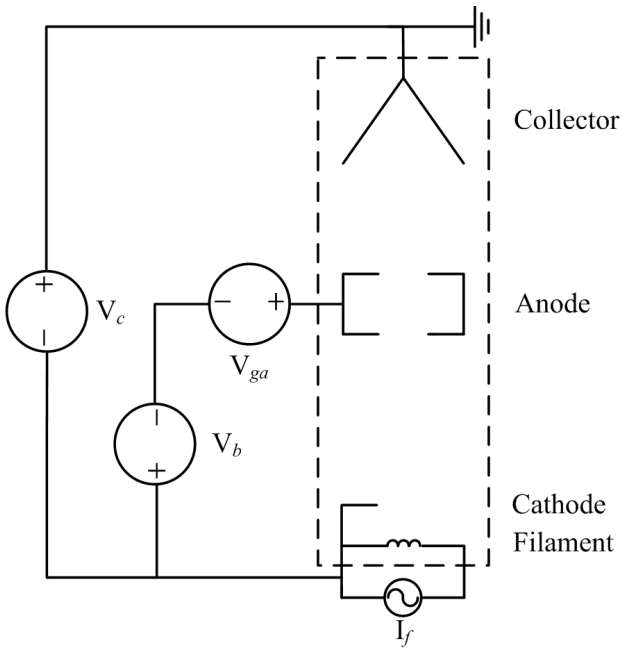

Fig. 3. Wiring Diagram of filament (I_f), cathode (V_c) and anode (V_{ga} & V_b) power supplies for the gyrotron.

TABLE III. PARAMETERS OF COILS

Coil	No. of turns	Inductance (H)	Max currents (A)
Cavity coil 1	10452	18	40
Cavity coil 2	10452	18	40
Gun coil	3186	3	10

TABLE IV. PARAMETERS OF POWER SUPPLIES FOR 60 GHZ GYROTRONS

Power supply	Parameters
Cathode (V_c)	100 kV / 60 A[a], stability <1%, ripple <1%
Anode (V_{ga})	33 kV / 100 mA, stability <0.5%, ripple < 0.5%
Bias (V_b)	3 kV / 100 mA
Filament (I_f)	10 A / 12 V, stability <1%

[a]. Designed to feed all the six gyrotrons

TABLE V. REQUIRMENTS OF COOLING

Units	Requirements		
	Coolant	*Flow rate (L/min)*	*Pressure (MPa)*
Collector	deionized water	568	< 1.5
Body	deionized water	60	< 0.75
Window	FC-40	27	< 0.15

D. *Control system*

For safe operation of an ECRH system, especially the gyrotron, a control system is needed. To improve the integration and expansibility, a control system based on the Compact Reconfigurable I/O (cRIO) - 9068 platform of National Instruments (NI) is designed for the J-TEXT ECRH systems. All signals needed to be monitored or processed will be sent to this platform with principle as follows:

- Monitoring: condition of all the devices, especially those related to the gyrotron for interlock and protection.
- Timing: making sure that devices, especially the power supplies in Table III, are opened in sequence.
- Fast protection: arc, over-current or -voltage of the cathode or anode power supplies; response time < 10 μs based on Field Programmable Gate Array (FPGA) integrated in cRIO.
- Slow protection: all other fault signals except those for fast protection; response time < 1 ms based on the processor of cRIO.
- Signal transmission: stability and accurate transmission with fiber isolation technology.

E. *Cooling*

As shown in Table I, efficiency of the gyrotron is about 32%, and most of the power fed to the gyrotron is deposited in the body and collector. To avoid damage of the gyrotron and its window, a cooling system for four gyrotrons with two coolants (deionized water and FC-40) has been designed according to requirements of gyrotrons' cooling in Table IV. For this system, the resistivity and total flow rate of deionized water is 5 MΩ·cm and 250 m^3/h respectively. In addition, this system can be upgraded in the future if six gyrotrons should be used.

III. TRASIMMSION LINE AND LAUNCHER

To inject high power millimeter waves to the plasma of J-TEXT tokamak, high efficiency transmission lines (TLs) and quasi-optical launcher (QOL) are needed [10]. Considering space of the hall and port of the J-TEXT tokamak, a design of four TLs and a launcher for one beam injection is proposed as shown in Fig. 4, which gives the layout of the four TLs and also the position of port for the launcher.

The length of each line is about 30 m from the window of the gyrotron to the port for beam injection on the J-TEXT tokamak. The four TLs have the similar composition as shown the in Fig. 5. The output mode of the gyrotron is TE_{02} mode with a few spurious modes, which will be filtered. Then The pure TE_{02} mode will be converted to TE_{01} mode for low loss transmission and finally converted to HE_{11} at the end of the TL for efficient coupling with the plasma. In addition, arc detectors and power monitors are used for safe operation; a bellow is applied for easy installation of TLs and a switch is installed to cut off the connection between the TL and the plasma under fault conditions.

After the wave beam is transmitted to the tokamak, a QOL is needed. Since only one gyrotron will be firstly operated, a QOL for one beam is designed in Fig. 6. This launcher will be replaced by a new one when test of all the four gyrotrons in Fig. 4 is finished. The launcher in Fig. 6 is mainly composed of a polarizer, a ellipsoidal mirror, a flat mirror, a gate valve and related drivers for the polarizer and flat mirror. When the beam is transmitted to the launcher by the TL, the desired polarization is firstly obtained by the polarizer [11]; then the beam is focused by the ellipsoidal mirror and injected into the plasma with certain torodial & poloidal angles by the flat mirror. To make the real time control of injection angles [12] of the beam, pushrods are used for fast movement of the flat mirror.

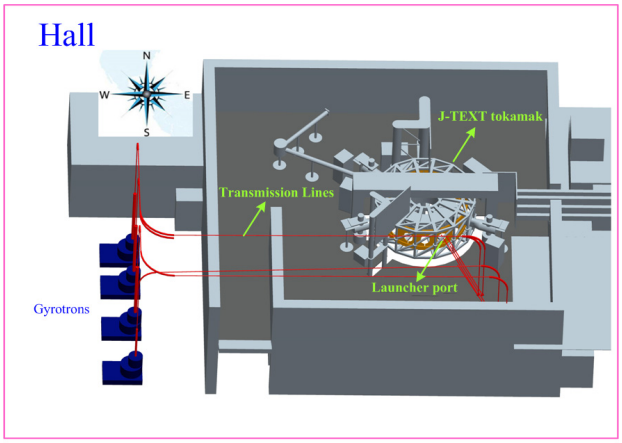

Fig. 4. Layout of four tranmission lines and the launcher for the J-TEXT ECRH systems.

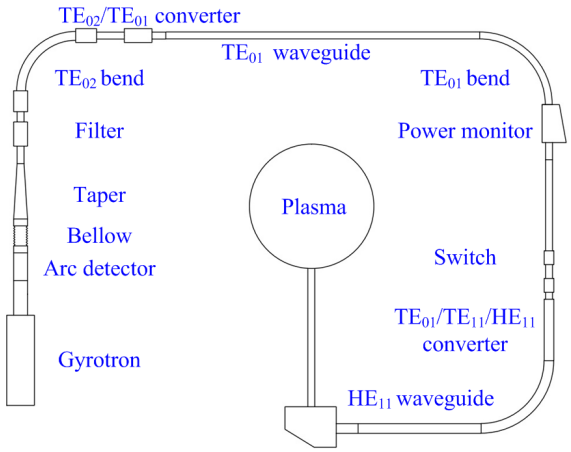

Fig. 5. Schematic of the 60 GHz transission line on J-TEXT ECRH system.

IV. Conclusion

Based on the donated components of ECRH systems from the CSC, including six 60 GHz/200 kW/5 s (0.5 s) gyrotrons, six magnets and anode power supplies for the gyrtrons, transmission parts, etc, reconstruction of the 1.2 MW / 60 GHz ECRH systems are now on-going for the J-TEXT tokamak.

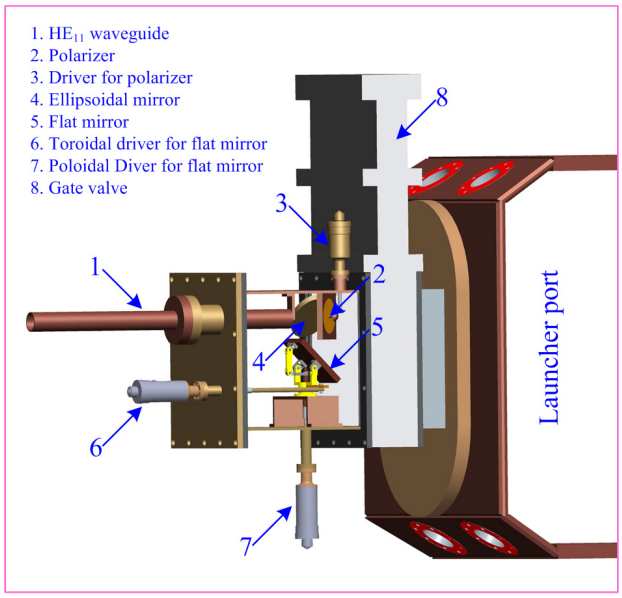

Fig. 6. Structure of the designed launcher on J-TEXT ECRH system.

To operate the system, the main negative power supply (100 kV/ 60 A) by PSM technology, a spared auxiliary power supply, a control system, a cooling system and a launcher have been designed. Currently, the main negative power supply has been finished and other subsystems are under developed. It hope that operation of the first 200 kW ECRH system can be done at the end of 2015 and four to six 200 kW ECRH systems can be finally used for the J-TEXT tokamak.

Acknowledgment

The authors would like to thank the J-TEXT team and Julian Hawes (CSC, Abingdon) for valuable discussions during the reconstruction of the ECRH systems. This work was supported by the ITER Special Fund of China (No. 2013GB106001 and No. 2013GB106003) and partly supported by the JSPS-NRFNSFC A3 Foresight Program in the field of Plasma Physics (NSFC No. 11261140328).

References

[1] R. Prater, "Heating and current drive by electron cyclotron waves," Phys. Plasmas, vol. 11, pp. 2349-2376, 2004.

[2] T. Omori, M. A. Henderson, F. Albajar, S. Alberti, U. Baruah, T.S. Bigelow et al., "Overview of the ITER EC H&CD system and its capabilities," Fusion Eng. Des., vol. 86, pp. 951-954, 2011.

[3] M. Cengher, J. Lohr, Y. A. Gorelov, R. Ellis, E. Kolemen, D. Ponce et al., "Performance and upgrades for the electroncyclotron heating system on DIII-D," IEEE Trans. Plasma Sci., vol. 42, pp. 1964-1970, 2014.

[4] D. Wanger, J Stober, F Leuterer, F. Monaco, M. Münich, D.S. Lorch et al., "Recent upgrades and extensions of the ASDEX Upgrade ECRH system," J. Infrared. Millim. Te., vol. 32, pp. 343-357, 2011.

[5] T. Shimozuma, H. Takahashi, S. Kubo, Y. Yoshimura, H. Igami, Y. Takita et al., "ECRH-related technologies for high-power and steady-state operation in LHD," Fusion Sci. Technol., vol. 58, pp. 530-538, 2010.

[6] G. Zhuang, K. W. Gentle, P. Diamond, J. Chen, B. Rao, L. Wang et al., "Overview of the recent research on the J-TEXT tokamak," Nucl. Fusion, vol. 55, pp. 104003, 2015.

[7] S J Fielding, M Valovic, P G Carolan, D A Gates, C Hunt, P Leahy et al., "H-modes on COMPASS-D with high-power ECRH," Plasma Phys. Control. Fusion, vol. 40, pp. 731-735, 1998.

[8] S. X. Ma, M. Zhang, L. L. Xia, D.H. Chen, Z. Zeng, X.L. Zhang et al, "Overview of 100 kV/60 A High-Voltage Power Supply utilized for the ECRH System on J-TEXT Tokamak," IEEE Trans. Plasma Sci., vol. 42, pp. 656-663, 2014.

[9] D.H. Xia, M. Huang, J. Zhou, X.Y. Bai, T.L. Zheng, J. Rao et al, "The 5.8T cryogen-free gyrotron superconductin magnet system on HL-2A," Plasma Sci. Technol., vol. 16, pp. 410-414, 2014.

[10] M.K. Thumm, W. Kasparek, "Passive high-power microwave components," IEEE Trans. Plasma Sci., vol. 30, pp. 755-786, 2002.

[11] D.H. Xia, M. Huang, J. Zhou, J. Rao, G. Zhuang, "The coordinate transformation method for design of polarizers on HL-2A electron cyclotron resonance heating and current drive systems," Rev. Sci. Instrum., vol. 84, pp. 103504, 2013.

[12] F. Felici, T. P. Goodman, O. Sauter, G. Canal, S. Coda, B.P. Duval et al., "Integrated real-time control of MHD instabilities using multi-beam ECRH/ECCD systems on TCV," Nucl. Fusion, vol. 52, pp. 074001, 2012.

Effect of the RMP on the ELM-like activities observed in the high beta H-mode of LHD

S. Ohdachi, S. Sakakibara and LHD experiment Group
National Institute for Fusion Science

Formation of the edge transport barrier is the key to achieve high confinement plasma in Tokamaks. H-mode transition in the Large Helical Device (LHD) was also realized in relatively low beta condition, beta up to 2.5%, with the vacuum magnetic location Rax = 3.6m~3.9m [1]. In the last experimental campaign, operational regime in more inward shifted configurations, e.g., Rax = 3.56m, is investigated. Operational condition with Rax = 3.56 m was found to be favourable for obtaining high beta plasma with relatively large magnetic field (Bt = 1T) condition (Fig. 1). H-mode transition with higher beta = 3.0% (1T) ~3.5% (0.75T) was clearly observed in this regime and this transition is necessary to achieve plasmas with good confinement. With the transition, the rapid increase in the electron density is observed in the very peripheral region (Fig. 2). That region is definitely outside the plasma boundary or the last closed flux surface of the vacuum magnetic field. After the transition, strong ELM-like edge MHD instabilities localized in the magnetic stochastic layer are activated from the increase of the pressure gradient, as shown in Fig. 3. The increase of the stored energy is limited by this excitation of the edge MHD instabilities. Coherence between the magnetic fluctuations and the fluctuating component of the ion saturation currents measured at the divertor plate also suggests that the ELM-like activities are responsible for enhancing the transport in the peripheral region (Fig. 4).

In the lower beta experiments, suppression of the non-resonant RMP application was found to be effective to suppress the instabilities localized in the magnetic stochastic region [2]. In the LHD with no-net current, the pressure-driven modes, e.g., resistive interchange modes in the edge region are always unstable since the edge plasma region stays in the magnetic hill. Experimentally, MHD instabilities localized in the edge region are constantly observed. Typical amplitude of the MHD instabilities is of 10^{-4} of the toroidal magnetic field. From the mode number of activities (poloidal / toroidal mode number m/n = 2/3, 1/2, 2/4), the location of corresponding rational surface, determined by HINT2 equilibrium prediction, is near the LCFS or definitely outside the

iota = 1 surface Parameter dependence of the saturation level is then examined for evaluation of the impact of MHD activities on confinement. The saturation level increases with the increase of the pressure gradient. The mode amplitude decreases with the decrease of the collisionality. The amplitude is also affected by the magnetic field topology. When the magnetic field is disturbed by the m/n RMP field to affect the magnetic topology, the amplitude of the modes is found to be decreased even though the pressure profile at the mode rational surface is unchanged. The mechanism for this stabilization has not been fully understood. However, we have noticed several changes in the magnetic fluctuations in addition to the reduction of the amplitude. The interval of the busts of the MHD activities becomes longer with the increase of the external field. The amplitude of the each burst is also decreased as well as shown in Fig. 5. If we assume that the bursting of the MHD activities enhances the transport, the pressure gradient becomes transiently flatter with the bursting. This is one possible hypothesis why the MHD activities with m/n = 2/3 mode becomes less frequent with RMP. Also the peak of the each burst is reduced. The relation of the amplitude of the activities with the enhanced flux driven by the MHD activity might be also modified by the Stochastization of the magnetic field.

Application of the m/n = 1/1 RMP is tested to control the large amplitude ELM-like activities observed in the high-beta H-mode However, the effect on the amplitude of the MHD activities is not large (Fig. 6). However, a reduction of the fluctuating component of the particle flux onto the divertor is observed. That effect is favourable for the protection of the divertor plate. When the RMP field is large so that m/n = 1/1 island is formed, the H-mode cannot be achieved. Detailed analysis for the effect of the RMP on the MHD activities will be made soon.

Acknowledgements;

This work was This work was supported by NIFS budget code ULPP028 and is also partially supported by the Ministry of Education, Science, Sports and Culture, Grant-in-Aid for Scientific Research 26249144 and is partly supported by the

JSPS-NRF-NSFC A3 Foresight Program in the field of Plasma Physics (NSFC: No.11261140328, NRF : No.2012K2A2A6000443).

References

[1] K. Toi, et. al., Fusion Sci. Tech., **58** (2010), 61

[2] S. Ohdachi, et. al., "Pressure Driven MHD Instabilities in Intrinsic and Externally Enhanced Magnetic Stochastic Region of LHD", in proceeding of the 25th IAEA FEC, Oct. 13-18, 2015, St Petersburg, Russia, EX/P6-29, submitted to Nucl. Fusion.

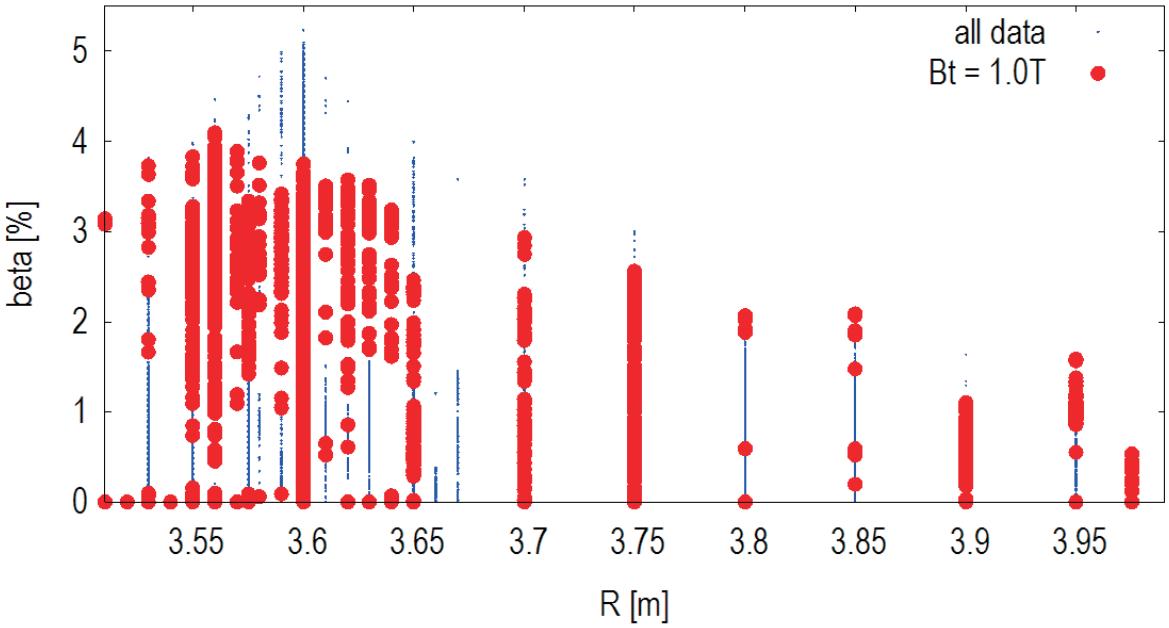

Fig. 1: Achieved beta value as a function of the magnetic axis location.

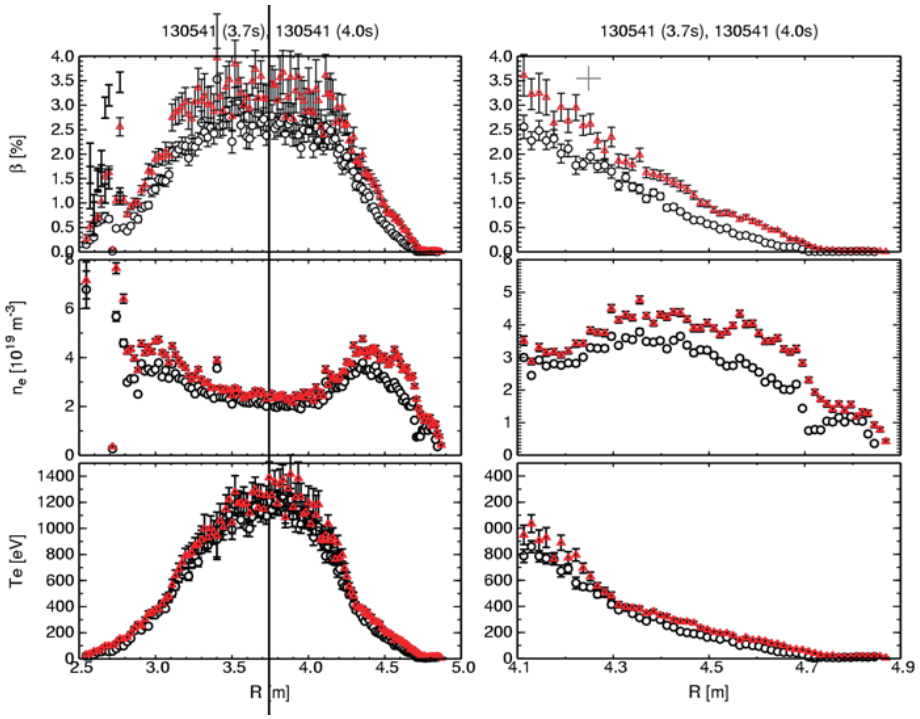

Fig: 2 Change of the profile of beta, the electron density and the electron temperature with H-mode transition. (H-mode: Red, L-mode: Black)

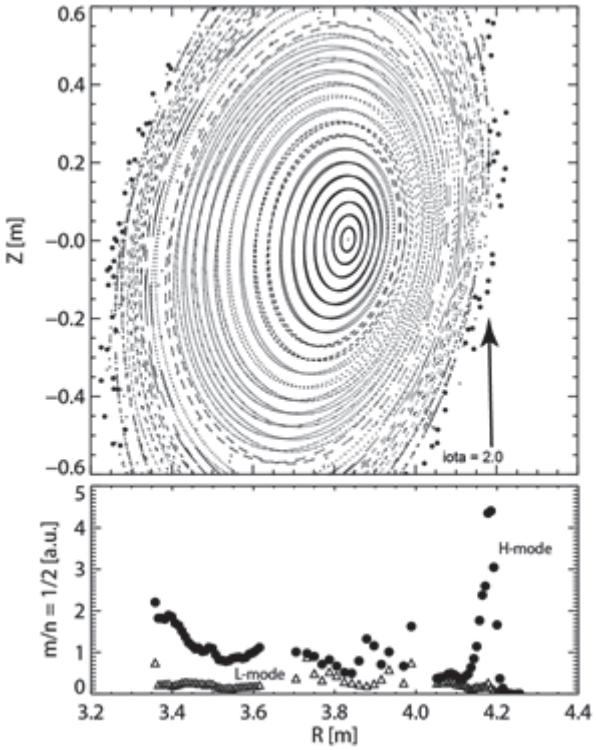

Fig. 3: Poincarre map of the magnetic field estimated by HINT2 and the fluctuation amplitude of the m/n = 1/2 MHD instabilities measured by the CO2 laser imaging interferometer.

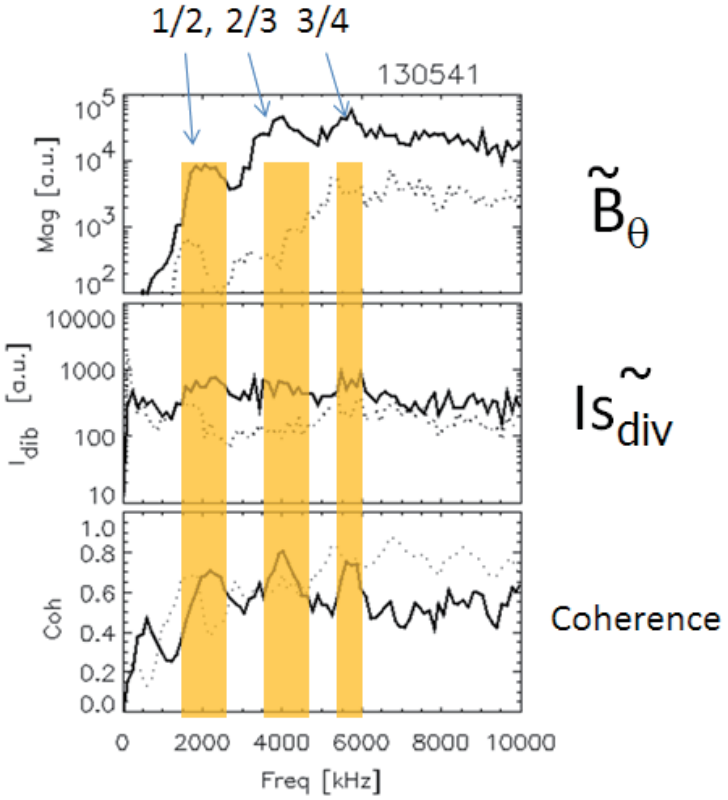

Fig. 4: Spectrum of the magnetic fluctuations, the ion saturation current measure at the divertor plate and the coherence between these two quantities.

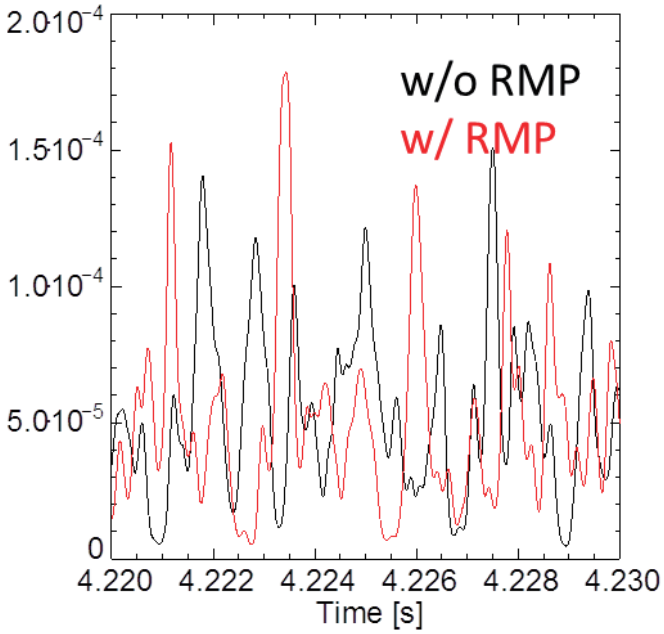

Fig. 5: Time evolution of the mode amplitude with and with tout RMP application.

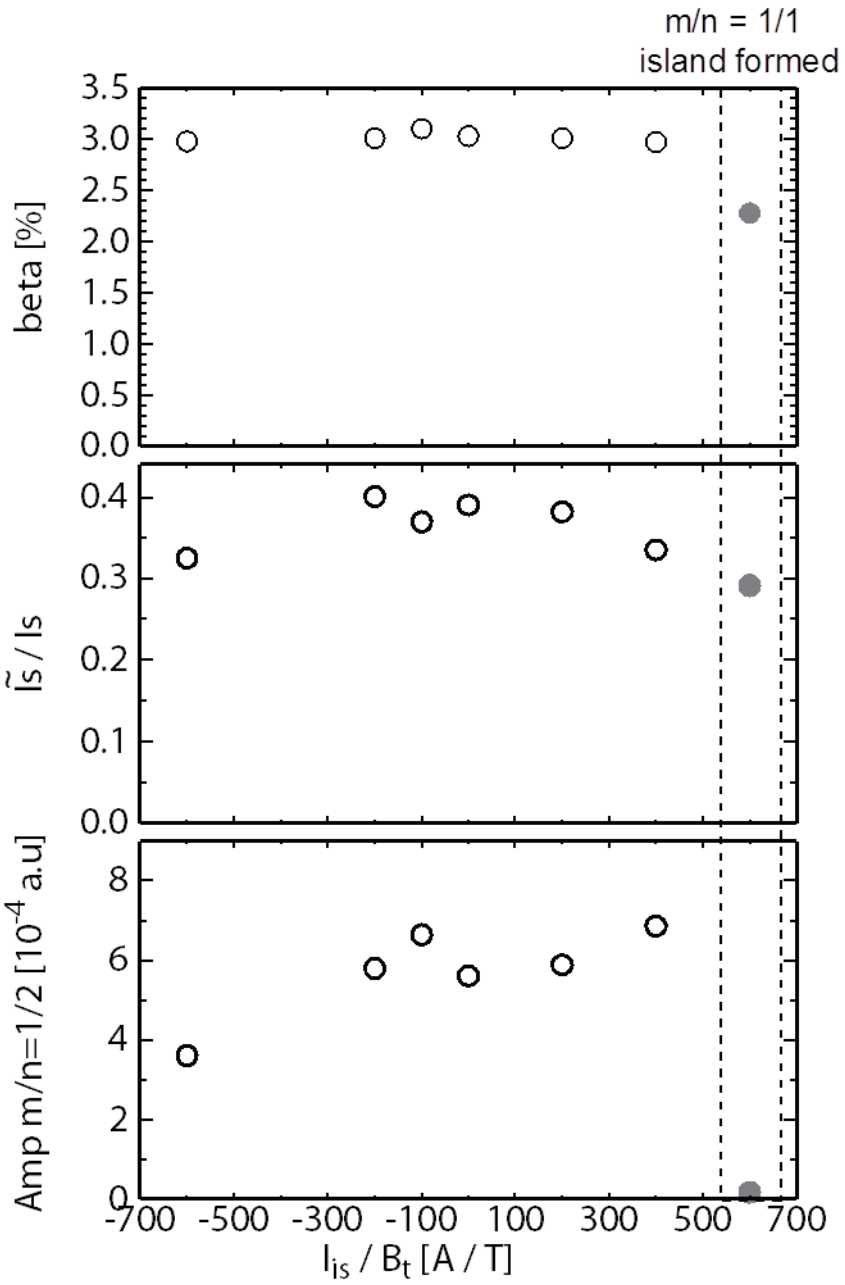

Fig:6: Achieved beta value and the fluctuation level of the ion saturation current and the amplitude of the m/n = 1/2 MHD activities as a function of the current of the RMP coil system.

Upgrade of 2D Microwave Imaging Reflectometry (MIR) in KSTAR

June-eok Leem
Pohang University of Science and Technology, Pohang, Korea
Email : juneeokleem@gmail.com

An advanced diagnostic concept for the electron density fluctuation measurement, microwave imaging reflectometry (MIR), has been developed to overcome the shortcomings of conventional microwave reflectometry. MIR system adopts a large-aperture probing and imaging optics in order to launch the probing beam properly and collect the majority of the reflected beam while minimizing the interference problem [2-4]. Measurement of semi-2D (radial and poloidal) electron density fluctuations can be realized in MIR system through the combination of the large-aperture optical system and the array of detectors (and one another for 2D measurement). From the 2014 KSTAR campaign, KSTAR MIR system has been upgraded to have doubled radial channels for investigating the radial structures of the plasma turbulence. In order to expand the detection channels, most components of the KSTAR MIR system such as I/Q electronics, optics, probing source and also DAQ system have been modified or replaced. In this work, the details of upgrading KSTAR MIR system will be addressed and discussed.

1. Introduction

Microwave reflectometry is a relatively simple technique that measures phase shifts of the reflected beam from the density-dependent cut-off layer. The fluctuating component of the measured phase can be given by the 1D geometric optics approximations [1]

However, in the case of multidimensional, large amplitude and high wave number turbulent fluctuations, which are more practical case for magnetic fusion plasmas, the interpretation of reflectometry data is still a remaining issue due to diffraction and complex interferences patterns of the reflected beam [2,3]

An advanced diagnostic concept for electron density measurement, microwave imaging reflectometry (MIR), has been developed to overcome the shortcomings of conventional microwave reflectometry. MIR system adopts a large-aperture probing and imaging optics in order to launch the probing beam properly and collect the majority of the reflected beam while minimizing the interference problem [2,3]. Measurement of semi-2D (radial and poloidal) electron density fluctuations can be realized in MIR system through the combination of the large-aperture optical system and the array of detectors (a number of microwave detectors are aligned vertically) at the imaging plane.

2. Measurement of plasma turbulence

It is commonly believed that the plasma turbulence is the main key factor of inducing energy transport in magnetically confined plasmas. Plasma eddies generated by plasma turbulence and micro-scale instabilities transport the heat and particles confined in plasma from the plasma core to the outer region, and therefore degrade the plasma confinement. Recent researches on plasma turbulence revealed that obtaining a well-confined plasma, also

known as H-mode, is closely related to the sheared flow and its product. It is claimed that when the sheared flow reaches to the radially elongated eddies, which trigger long-distance transport in bad curvature direction, the sheared flow eventually makes eddies less effective or break up, and help plasma confinement [5]. In order to verify the connection between the sheared flow and plasma confinement, temporal measurement of 2D wavenumber spectrum and correlation length of plasma turbulence is demanded.

In general, turbulence measurements are often limited to one dimension or are line-integrated. Plasma diagnostic which has a capability of measuring simultaneous 2D density fluctuation in the poloidal and radial direction is essential for understanding the underlying turbulence instabilities. BES(beam emission spectroscopy), reflectometry and ECE(electron cyclotron emission) radiometer are major diagnostics in this point of view. D3-D group has reported a detailed assessment of several characteristics of localized 1D and 2D measurements of long wavelength ($k_\perp \rho_i \leq 1$) density fluctuations in L-mode plasmas [6]. From this report, the measured poloidal turbulent structure has a constant peak at $k_p \sim 0.3$, radial correlation length in L-mode plasmas has a range from 2 to 6 cm, the measured de-correlation rate is found to be less than 45 kHz near the core where it is comparable to or less than the E X B shear rate, and this confirms that the E X B velocity dominates the poloidal advection of the turbulence [6].

3. MIR system upgrade in 2014

Before 2013, KSTAR MIR system capability was not sufficient to measure and analyze the long wavelength plasma turbulence whose physical scales are comparable to the reported result of D3-D group. In order to enhance the system capability of measuring and investigating micro-instabilities and plasma turbulence, three big changes has been adopted to MIR system in 2014. First, the number of radial channels has been increased from 2 to 4. Second, radial spacing between adjacent channels has been smaller by adjusting the narrower frequency gap between probing beam. Basically, radial detection positions of MIR system is determined by the frequencies of MIR probing beams and their corresponding density cut-off in the plasma[1]. Finally, time resolution has been also improved to trace the time evolution of turbulence properties. Upgrading details and corresponding descriptions is as follows;

The detector array of MIR system is changed. There are several important updates in the new detector array compared to the old one. First, the front lens has been changed from large-hemispherical type to mini-parabolic type. This change helps gathering the beam heading to the area of lens aperture more efficiently and enhances the signal level. Also, those individual mini-lenses in front of individual detectors make the signal overlap between adjacent channels less to have better channel-independence and spatial resolution in vertical direction. Second, the design and the specifications of micro-strip dual dipole antenna and schottky diode, working as a balanced mixer, have been changed to have broader detection bandwidth. Enhanced frequency range of array response leads to the wider dynamic range of measurable radial position.

MIR electronics and data acquisition systems are totally upgraded. For better radial measurement of plasma turbulence, the number of radial channels has been increased and the frequency gap between probing beams has been reduced from 4 GHz to 1.8 GHz. As a result of these changes, MIR I/Q demodulator (second stage mixer) is completely redesigned to process the 16 vertical channels. Each vertical channel handles 4 inter-mediate frequencies, corresponding to the 4 radial channel, at once and demodulate the in-phase and quadrature-

phase from the each frequency. Therefore, the new I/Q demodulator now has totally 16 X 4 X 2 = 128 outputs. DAQ(data acquisition system) is also upgraded to have more channels with higher sampling rate which leads the system to have better time resolution.

The receiving optics of MIR system has been redesigned. Dimension changes on detection system, especially the entrance size difference between the new detector array (210 mm) and the old one (31 mm), forced the receiving optics to be redesigned. The verification of the new optics has been done in the laboratory by putting the point source on the plasma position, scanning the intensity profile, and making a comparison between the measurement and the simulation. Consequently, adopting the new detector array with the new receiving optics made total vertical span and spacing between adjacent channels doubled (from 90 mm to 185 mm). This means that the maximum detectable poloidal wavenumber of the system got worse. MIR system was able to resolve the coherency of plasma turbulence along poloidal direction in L-mode plasmas in 2013, but was not resolvable for the most of L-mode plasmas in 2014. After upgrading, the experiment results during 2014 KSTAR campaign gave us the perspectives of future tasks.

4. Summary

KSTAR MIR system has been upgraded to have doubled radial channels with narrower radial channel spacing for investigating the radial structures of the plasma turbulence in 2014. Most components of the KSTAR MIR system such as I/Q electronics, optics, probing source and DAQ system have been modified or replaced. As a result of upgrading, the new MIR receiving optics and detector array made worse the maximum detectable poloidal wavenumber, and therefore the poloidal coherency of plasma turbulence was hardly resolvable. To achieve higher spatial and temporal resolution for MIR system in 2015 KSTAR campaign, the new design of receiving optics is now in progress.

Acknowledgement
This research was supported by NRF Korea under grant no. NRF-2014M1A7A03029865 and was partly supported by the JSPS-NRF-NSFC A3 Foresight Program under grant no. NRF-2012K2A2A6000443)

References

[1] H. Park *et al*. : Rev. Sci. Instum., Vol. 74, No. 10, October (2003).

[2] E. Mazzucato : Nucl. Fusion Vol. 41, No. 2 (2001)

[3] E. Mazzucato, T. Munsat, H. Park, B. H. Deng, C. W. Domier, N. C. Luhmann, Jr. , A. J. Donn´e and M. J. van de Pol : Phys. Plasmas Vol. 9, No 5 (2002)

[4] W. Lee *et al* : Nucl. Fusion Vol. 54 (2014) 023012.

[5] H. Biglari, P. H. Diamond, and P. W. Terry : Phys. Fluids B 2, 1 (1990)

[6] M. W. Shafer *et al* : Phys. Plasmas Vol. 19, 032504 (2012)

[7] T. L. Rohdes *et al* : Phys. Plasmas Vol. 9, 2141 (2002)

2D potential measurement with Heavy Ion Beam Probe on the Large Helical Device

A. Shimizu, T. Ido, M. Nishiura[1], S. Kato and the LHD experiment Group
National Institute for Fusion Science, Oroshi-cho, Toki, Gifu, 509-5292, Japan
[1]The University of Tokyo, Kashiwa, Chiba, 277-5651, Japan

Abstract

Two-dimensional potential profiles in the Large Helical Device (LHD) was measured with a heavy ion beam probe (HIBP). To measure the two-dimensional profile with the HIBP, the probe beam energy is required to be changed. It is not easy to change the probe beam energy because the beam transport line of our HIBP system is about 20m, and many electrostatic deflectors are required to be adjusted to optimize the beam orbit in the beam transport line. To reduce this adjustment time, a PC based automatic beam adjustment system was developed. Using this system, the time to change the probe beam energy was dramatically reduced and two-dimensional potential profiles were successfully measured with HIBP.

1. Introduction

In the confinement physics of magnetically confined plasmas, the radial electric field E_r is important. The E_r is correlated to plasma flow through $\boldsymbol{E} \times \boldsymbol{B}$ flow, and many theoretical researches have shown that the reduction of turbulence by flow shear is important to improve confinement property of the device [1]. There are many experimental results that support these theoretical researches, such as H-mode, internal transport barrier (ITB) [2-3]. On the other hand, flow makes an effect on the structure of magnetic field, for example, island formation, healing phenomena, and the stochastic character of magnetic surface are influenced by the plasma flow [4,5]. Two-dimension measurement of E_r is very effective to study the effect of the plasma flow on those characters of magnetic field. In this report, two-dimensional potential profile measurement with a heavy ion beam probe (HIBP) [6] is suggested and experimental results are reported [7].

HIBP is a useful tool to study the physics related to E_r, because it can measure the potential with good time and spatial resolution, without perturbing the plasma. Usually, one-dimensional potential profile is measured with HIBP by changing the incident angle of probe beam [8]. By changing the probe beam energy, the observation region is extended and two-dimensional profile of potential can be measured with HIBP.

In the large helical device (LHD), an HIBP system was installed and developed to study E_r formation physics in helical plasma [9,10]. The HIBP system in the LHD has a long beam transport line (about 20 m), and there are many electro static deflectors and lenses to adjust the beam trajectory along the transport line. It is not easy to change the probe beam energy, because voltages

of many electric deflectors must be optimized simultaneously. To reduce the required time for this adjustment, a PC-based automatic adjustment system was developed and applied to our HIBP system. The details of the automatic adjustment system and experimental results of two-dimensional potential measurement are reported in section 3 and 4.

2. Heavy Ion Beam Probe on the LHD

For an HIBP diagnostic, singly charged particles are injected into the plasma (primaries). In the plasma, primaries are further ionized to produce doubly charged particles (secondaries). In the outside of the plasma, the secondaries are detected and their energies are analyzed. Due to the energy conservation law, the difference of energy between primaries and secondaries corresponds to the potential energy at the ionized position in the plasma. The energy analyzer has a slit that allows only secondaries ionized at a given plasma position to reach the detector through the slit. Therefore, potential localized at the ionization point is possible to obtain.

The LHD is a helical device, of which maximum strength of toroidal magnetic field is about 3T, and the typical major/minor radius is 3.6 m/0.6 m. The required probe beam energy reaches 6 MeV to inject primaries into the center of plasma, when we use the gold (A_u^+) beam. To generate this high energy beam, the tandem accelerator is used to reduce the required accelerator voltage to be half. The high energy beam generated by the tandem accelerator is transported to an injection port of LHD through the beam transport line, of which length is about 20 m. A schematic view of the HIBP system in the LHD is shown in Fig. 1. Many electro deflectors and quadrupole lenses are equipped in the beam transport line to adjust the beam orbit. The beam incident angle to plasma is changed by the 8-pole electrostatic deflector located at the injection port. At the ejection port, we have another 8-pole electrostatic deflector and adjust the beam direction to inject the beam into the energy analyzer with a suitable angle. In Fig. 2, the observation points of LHD-HIBP are shown with magnetic surfaces. The actual observation points are arranged three-dimensionally, so in this figure a projection of observation points on the horizontally elongated cross section for simplicity. Generally, the probe beam energy is fixed and the injection/ejection angles are changed to measure a one-dimensional profile. For

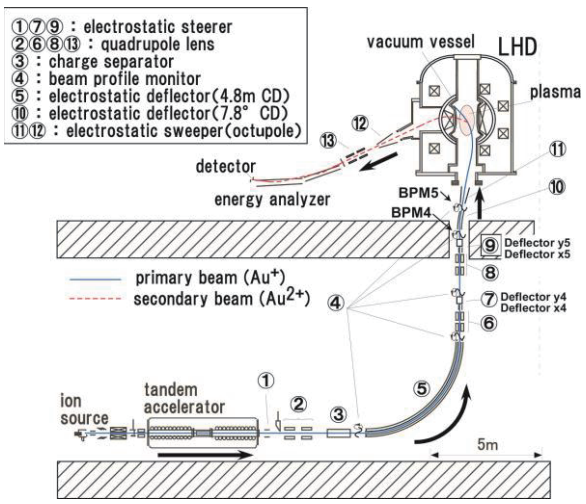

Figure 1 Schematic view of HIBP system on LHD. There are many electro deflectors along the beam line to adjust the beam orbit in it.

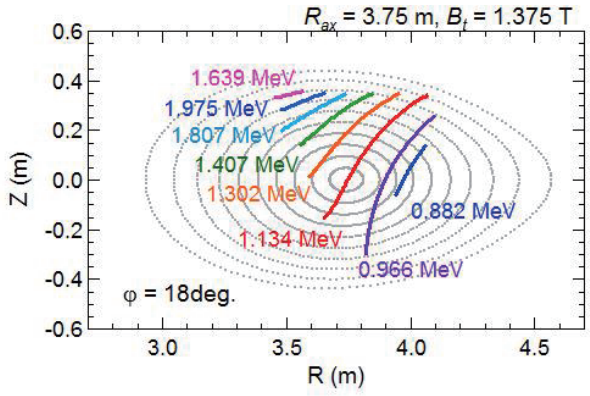

Figure 2 Observation points by LHD-HIBP system are shown. The injection/ejection angle is swept to scan the observation points along a line of corresponding beam energy.

example, if the probe beam energy is fixed at 1.134 MeV, the observation point is scanned along the line of 1.134 MeV shown in Fig. 2. If the probe beam energy is changed, we can measure another one-dimensional potential profile along the different line in the figure. By changing the beam energy shot to shot, two-dimensional potential profile can be obtained.

3. PC based automatic beam adjustment system

As stated above, the beam transport line of LHD-HIBP system is about 20 m, and there are many electrostatic deflectors in it. When the probe beam energy is changed, the beam orbit in the beam transport line must be adjusted by using these deflectors. Voltages applied to these deflectors are basically changed in proportion to the probe beam energy, however, effects of leaked magnetic field from the LHD are not negligible, therefore subtle adjustment is required. To adjust many deflector voltages easily, a PC based automatic adjustment system was developed. In the beam transport line, we have 14 electrostatic deflectors, but in the region far from the LHD the effects of leaked magnetic field are small. Therefore, 4 deflectors near the injection port are used to optimize the beam orbit, and other voltages, such as the quadrupole lens and deflectors at further positons, are changed in proportion to the probe beam energy. The beam position in the beam transport line is measured with beam profile monitors (BPMs). The BPM detector comprises a helical winding wire, a turn table, and a shield. The helical winding wire rotates with the turn table and the beam current is detected with the wire. The beam profiles in two orthogonal axes are measured with BPM.

Displacements of the beam at the point i are defines as Δx_i, Δy_i in the x and y axes, respectively. These displacements have basically linear dependence on the deflector voltages V_{xj}, V_{yj}. When two pairs of x and y deflectors and two BPMs are used, the displacements of beam can be expressed as follows,

$$\begin{pmatrix} \Delta x_4 \\ \Delta y_4 \\ \Delta x_5 \\ \Delta y_5 \end{pmatrix} = \begin{pmatrix} A_{11} & A_{12} & A_{13} & A_{14} \\ A_{21} & A_{22} & A_{23} & A_{24} \\ A_{31} & A_{32} & A_{33} & A_{34} \\ A_{41} & A_{42} & A_{43} & A_{44} \end{pmatrix} \begin{pmatrix} \Delta V_{x4} \\ \Delta V_{y4} \\ \Delta V_{x5} \\ \Delta V_{y5} \end{pmatrix}. \quad (1)$$

Here ΔV_{xj}, ΔV_{yj} are the change in the deflector voltage j. The transport matrix A_{ij} can be calculated theoretically, but in the actual operation, components of A_{ij} obtained from the calibration experiment

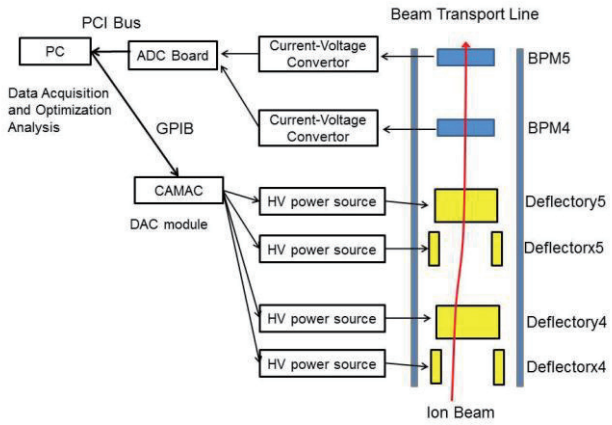

Figure 3 Simple diagram of the PC-based beam optimization system is shown.

were used.

A simple diagram of the PC-based optimization system is shown in Fig. 3. Raw signals from BPMs are acquired through ADC board of which sample frequency is 1 kHz. The displacements of beam, Δx_i, Δy_i, are calculated from these signals. The deflector voltage to adjust the beam position to be at the center of the beam transport line is calculated by using the inverse of matrix **A**, as $\mathbf{\Delta V} = \mathbf{A}^{-1}\,\mathbf{\Delta x}$. The calculated voltages are applied to high voltage power supplies of deflectors through CAMAC DAC modules connected with the PC through GPIB controller. After that, the probe beam positions are measured with BPMs again, and the next optimization loop is repeated. When distances between the center of beam and the transport line axis at BPMs is less than 1 mm, this optimization process finishes. Using this automatic beam adjustment system, the required time to optimize the beam orbit in the beam transport line can be reduced to 3 minutes so we can change the beam energy between each discharge of LHD.

4. Experimental results

By changing the probe beam energy shot to shot, a two-dimensional potential profile was measured. Parameters of magnetic configuration of LHD are as follows: The toroidal magnetic field strength B_t = 1.375 T, the major radius of magnetic axis R_{ax} = 3.75 m, the quadrupole component of magnetic field B_q = 100 %. The plasma is produced and sustained by neutral beam injection (NBI) heating. Auxiliary heating of electron cyclotron heating (ECH) is applied after 1.1 s of neutral beam injection. Typical line averaged density and the central electron temperature in NBI + ECH phase are 0.4×10^{19} m^{-3} and 4 keV. Two-dimensional potential profile was measured in NBI + ECH phase by varying the probe beam energy shot to shot as shown in Fig. 4. Potential profile data from seven shots were used to obtain this experimental result. These experimental data are compared with the theoretical calculation result based on neoclassical theory, and the experimental data coincides with the theoretical prediction well.

The potential profile in magnetic islands was tried to be measured in other experiments. An example of one dimensional potential profile measured with HIBP is shown in Fig.5, in which the electron temperature profile is also shown for reference. In the temperature profile, in the region of

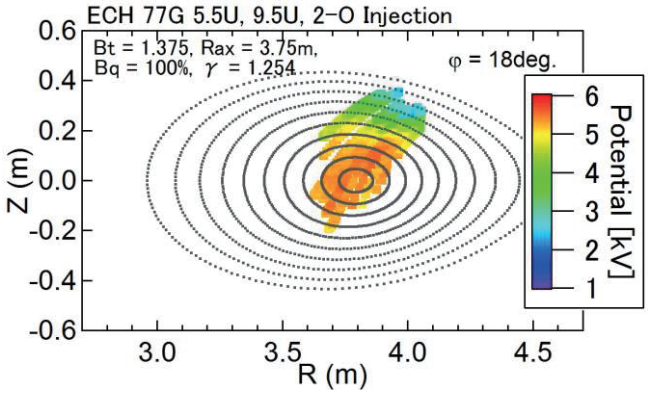

Figure 4 Two-dimensional potential profile in NBI + ECH phase measured with HIBP

$0.3 < r_{eff} / a_{99} < 0.6$, the flat profile is observed, of which structure is considered due to islands ($m/n = 2/1$). The temperature profile is asymmetry for the magnetic axis. It is considered that the phase of islands is not symmetric for the axis in this cross section. The potential profile is also shown in this figure, and the flat profile can be seen in the region of $0.3 < r_{eff} / a_{99} < 0.5$. This region roughly coincides with the flat region in the temperature profile.

In other experiments, two-dimensional potential profile was tried to be measured, however, we were not able to obtain enough shot data to see the clear structure of islands. Experimental results are shown in Fig.6, in which magnetic surfaces are also shown as reference. In this experiment, RMP field was applied to enlarge the size of islands, and magnetic surfaces shown in Fig. 6 are calculated ones on the vacuum condition. In the electron temperature profile of this experiment, the flat region was narrow, therefore plasma might respond to decrease the size of islands in this experiment. In the future, more detail two dimensional structure in islands will be measured to study the effect of plasma flow on islands.

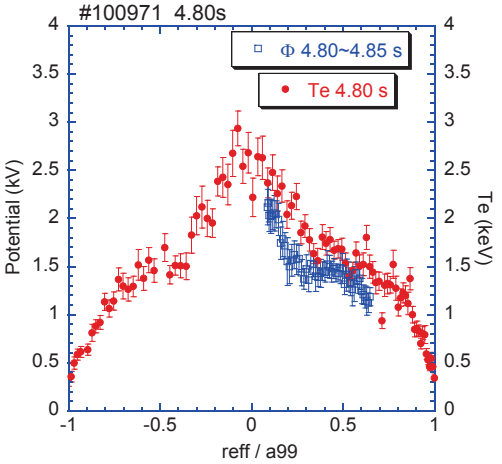

Figure 5 Potential profile (blue rectangles) when islands appear. For the reference, temperature profile (red circles) is also shown.

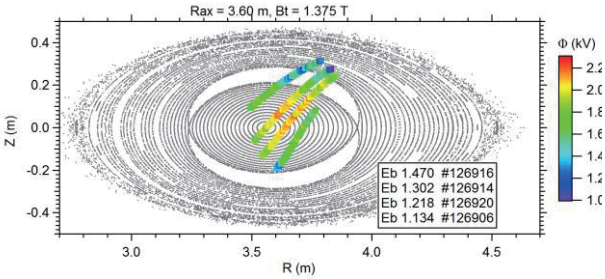

Figure 6 Two dimensional potential profile is shown when RMP field was applied to enlarge the size of islands. Magnetic surfaces on the vacuum condition are also shown for reference.

5. Summary

To measure two-dimensional potential profile with HIBP system, an automatic beam adjustment system has been developed. By using this system, the adjustment of beam orbit in the beam transport line can be finished within 3 min after the probe beam energy is changed. The probe beam energy was changed shot to shot, and two-dimensional potential profile was successfully measured. The two-dimensional potential profile in magnetic islands was tried to be measured, however, clear structure of islands was not seen in the experimental results. In the future, more precise two-dimensional profile in islands will be measured to study the effect of flow on islands.

Acknowledgement

This work was partially supported by the JSPS-NRF-NSFC A3 Foresight Program in the field of Plasma Physics (NSFC: No.11261140328, NRF : No. 2012K2A2A6000443) and also supported by the NIFS under Contract Nos. ULHH 020, 023, and by JSPS KAKENHI Grant Nos. 24561031, 25820441.

Reference

[1] K. H. Burrell, Phys. Plasmas **4**, 1499 (1997).

[2] T. Ido, K. Kamiya, Y. Miura, Y. Hamada, A. Nishizawa, and Y. Kawasumi, Phys. Rev. Lett. **88**, 055006 (2002).

[3] A. Fujisawa, H. Iguchi, T. Minami *et al*., Phys. Rev. Lett. **82**, 2669 (1999).

[4] K. Ida, M. Yoshinuma, H. Tsuchiya, T. Kobayashi, C. Suzuki *et al*., Nature Communications **6**, 5816 (2015).

[5] Y. Narushima, F. Castejon, S. Sakakibara, K. Y. Watanabe, S. Ohdachi, Y. Suzuki, T. Estrada *et al*., Nucl. Fusion **51**, 083030 (2011).

[6] G. A. Hallock, R. L. Hickok, and R. S. Hornady, IEEE Trans. Plasma Sci. **22**, 341 (1994).

[7] A. Shimizu, T. Ido, M. Kurachi, R. Makino, M. Nishiura, S. Kato, A. Nishizawa, Y. Hamada, Rev. Sci. Instrum. **85**, 11D853 (2014).

[8] A. Fujisawa, H. Iguchi, M. Sasao, Y. Hamada, J. Fujita, Rev. Sci. Instrum. **63**, 3694 (1992).

[9] T. Ido, A. Shimizu, M. Nishiura, A. Nishizawa, S. Katoh, K. Tsukada, M. Yokota, H. Ogawa, T. Inoue, Y. Hamada *et al*., Rev. Sci. Instrum. **77**, 10F523 (2006).

[10] A. Shimizu, T. Ido, M. Nishiura, H. Nakano, I. Yamada, K. Narihara, T. Akiyama, T. Tokuzawa, K. Tanaka *et al*., Plasma Fusion Res. **2**, S1098 (2007).

Calibration and uncertainty analysis of magnetic measurement for plasma shape reconstruction on EAST

(The paper will be submited to Fusion Engineering and Design)

Biao Shen, Jinping Qian, youwen Sun, Tonghui Shi, Dalong Chen
Institute of Plasma Physics, Chinese Academy of Sciences
PO Box 1126, Hefei, Anhui, 230031, P.R.China
Email: biaoshen@ipp.ac.cn

Abstract: Magnetic diagnostics is one of basic measurement systems for Tokamak plasma current and shape control. The accuracy of magnetic data will influence the plasma shape reconstruction. In this paper, the calibration of magnetic diagnostics is carried out on the EAST Tokamak. The overall uncertainties of magnetic sensors are analyzed from the calibration and vacuum shots. The uncertainty results are used as fitting weight in plasma shape reconstruction code (EFIT). Based on EFIT simulation and experiment data fitting results, the sensitivity of the magnetic data uncertainty in the plasma shape reconstruction is analyzed.

1. Introduction:

Magnetic diagnostics is the basic and essential parts in Tokamak device. On EAST superconducting Tokamak, the magnetic diagnostics includes plasma current rogowski coils, magnetic pickup coils, mirnov probes, poloidal flux/saddle loops, diamagnetic loops, Halo current monitors, and poloidal field coil current sensors. The configuration of EAST magnetic diagnostics is showed in figure 1[4].

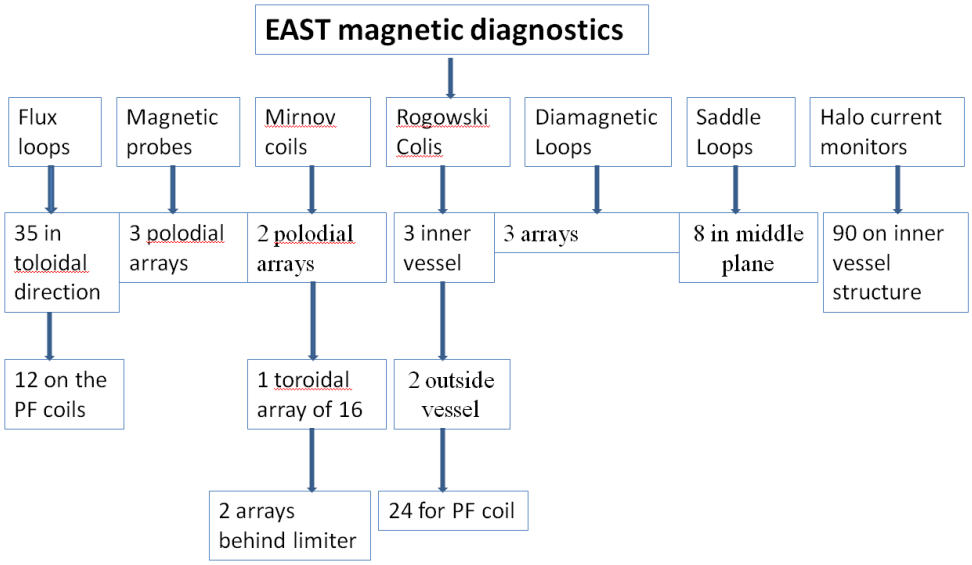

Figure 1. EAST magnetic diagnostic configration

In magnetic diagnostics, sensors which are used for equilibrium reconstruction contain: plasma current rogowski coil, 38 poloidal magnetic probes, 35 poloidal flux loops and 12 poloidal field coil currents.

The basic principle to reconstruct the plasma shape is to solve the Grad-Shafranov equation[1], the parameters are determined from magnetic data by minimizing the fitting error:

$$\chi^2 = \frac{1}{k}\sum_{i=1}^{k}\frac{\left(X_i^c - X_i^e\right)^2}{\sigma_i^2} \quad (1)$$

$$X^c = G\left(\vec{r}_d, \vec{r}_{PF}, \vec{r}_{plasma}, \vec{r}_{eddy}\right) \times I \quad (2)$$

Where X_i^c and X_i^e are the computational and experimental values of magnetic measurement. Fitting weight σ_i should stand for the offset $\Delta_i = X_i^c - X_i^e$. G is matrix of green functions, I and $\vec{r}$ are the matrix of currents and positions.

The total offset comes from green functions and measurement:

$$\Delta = \Delta^c + \Delta^e \approx G\left(\vec{r}_d, \vec{r}_{PF}\right) \times I_{PF}^{\Delta} + G^{\Delta} \times I_{PF} + \sigma_d \quad (3)$$

The offset contains the effects of all uncertainty sources. They can be divided into two parts, the system uncertainties and the random uncertainties. The system uncertainties include PF current, and uncertainty of magnetic diagnostics σ_d. The uncertainty of magnetic diagnostics contains the error of diagnostics active areas, the error of integrator-acquisition system, the signal attenuation of the 70m twisted pair, and the imperfection of the diagnostics. The mainly random uncertainties are base on the positions of poloidal field(PF) coils and magnetic sensors[2].

In EAST magnetic diagnostics system, the system uncertainty parameters which are needed to be calibrated are listed in following: sensors effective area, integrator and amplifier, signal transfer line. Different methods for calibration are introduced in detail in this paper.

For flux loop, $\phi = \int V_s dt = \frac{G}{RC}\int V_s dt \cdot T_{das\_fl}$

For magnetic pickup coil and rogowski coil, $\begin{cases} B = \frac{1}{NS}\int V_s dt = \frac{G}{RC}\int V_s dt \cdot T_{das\_probe} \\ I = \frac{1}{2\pi r_0}\cdot\frac{1}{NS}\int V_s dt = \frac{G}{RC}\int V_s dt \cdot T_{das\_PF} \end{cases}$

Where: ϕ is the measurement result of the flux loop, and G is additional gain of the amplifier, and RC is the time constant of the integrator, NS is the magnetic probe's effective areas, and T_{das} is the translation coefficient of the data acquisition system.

The random uncertainties are base on the PF coils and sensors positions, and cannot be obtained by measured directly. For example, when the superconducting coils are cooled down from room temperature to 4.5K, the coils positions will be changed because of contraction. Also, the sensors positions will be changed when the vacuum vessel baked or pumped. These changes will influence the green functions. A lot of vacuum shots will used to analyze and estimated the error of plasma shape reconstruction.

2. Calibration of EAST magnetic diagnostics

In the whole magnetic measurements circuit, there are several system uncertainties sources from the sensor to signal processing unit. It includes following side: the effective area of pickup coil or flux loop, the integrator parameter (RC) and amplifier factor (G), the influence of 70m twist signal transfer line, the current of poloidal field (PF) and plasma current rogowski coils. The details of all these calibrations are list as following:

(1) Calibration of 12 poloidal field rogowski coils

These rogowski coils are calibrated by a same HALL current sensor. The error of the absolute coefficient is determined by the accuracy of the Hall sensor. The error of the absolute coefficient is about 0.5%. All PF coils current were tested with 9KA/turn close to full scale of Hall sensor(10KA).

(2) Calibration of pickup coils

The effective areas(NS) of pickup coils are calibrated by a solenoid coil[5]. Figure 2 shows the parameters of the solenoid. A standard pickup coil and measured pickup coil are put in the centre of a solenoid coil with 200Hz AC power supply. The figure 2 shows the parameters of solenoid coil, the positions of standard and measured pickup coil, the field uniformity at the center of solenoid. The NS value of measured pickup coil is obtained by compare the induced voltages of two pickup coils. The uncertainty of NS value is about 0.5%. The calibration system is showed in Figure.3.

Conductor size	Coil turns	Coil Inner diameter	Coil Length	Coil resistance
2.8×4mm	200×2=400	200mm	1000mm	0.562Ω

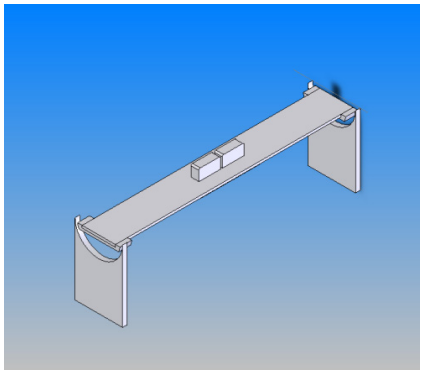

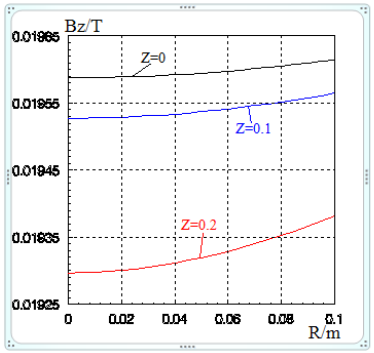

Figure 2. the parameters of solenoid

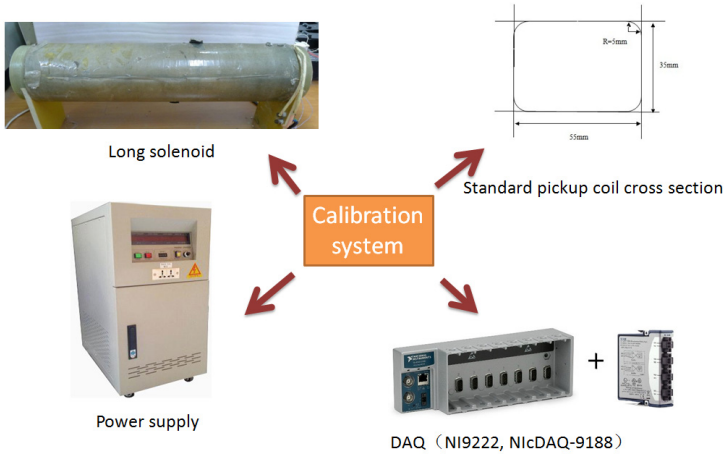

Figure 3. The calibration system of picket coils

(3) Calibration of integrator and amplifier

The integrator–amplifier-digitizer were calibrated before the experiment operation. Different RC values are designed base on the different effective area of pickup coil and flux loop. RC=20ms is set for pickup coils and RC=200ms is set for flux loop. In the calibration, the reference input signal is a 3V (100 Hz form pickup coils and 10Hz for flux loops) square-wave, which is checked by a high precision voltmeter. The value of RC/G is obtained from the output triangle wave (calculate the slop, shown in

Fig. 4). The uncertainty of the RC/G calibration can be ignored (less than 0.00001).

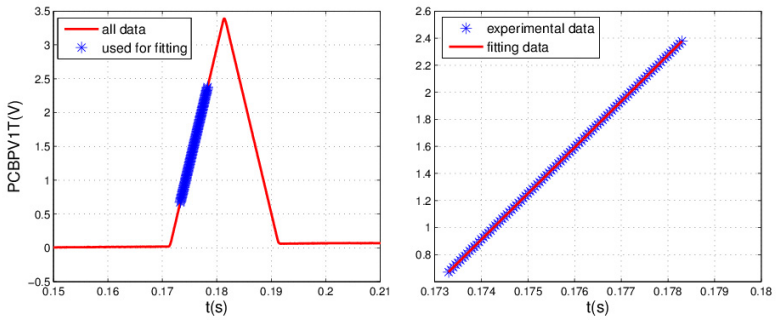

Figure 4. Calibration of integrator

(4) The influences of 70m twist signal transfer line

From the magnetic measurement system which installed inside the vacuum vessel to the integrator and DAQ system, there are about 70m length. To improve the anti-interference ability of the signal, the twisted-pair line with shield is used for signal transfer. An electric model is built to analyze the influences of signal transfer, and the experiment result is given too[3]. It is showed in Figure 5.

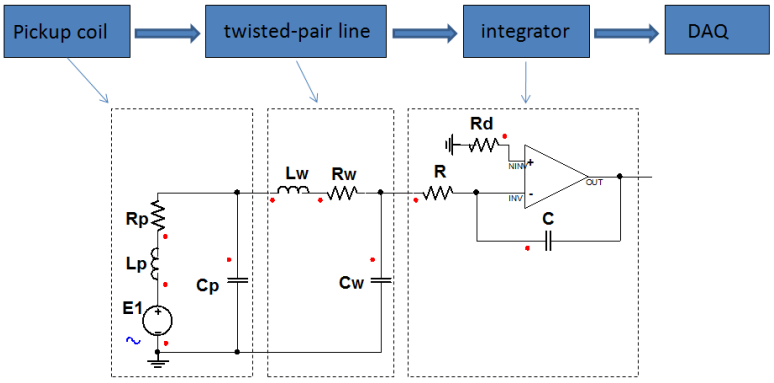

Figure 5. the circle model of 70m transfer line

In the circuit model, the parameters of twisted-pair line are measured as following:

$$R_w = 5.825\Omega, L_w = 0.1713mH, C_w = 0.2nF$$

For 10KHz magnetic signals for plasma shape reconstruction, the impedance of twisted-pair line compare integrator is very small. The influence to the signal is small than 0.03%, it can be ignored.

3. Random uncertainties analysis for plasma shape reconstruction

(1) The uncertainties analysis base on the vacuum shot

To estimate the positions influence of pickup coils and flux loops to green function (see the equation 2), many vacuum shots were carefully designed and performed before each machine operation. 37 different vacuum shots were used in the analysis which including: individual PF coil powered shots; un-down symmetric PF coils co/counter powered shots; other special designed vacuum shots. They are designed to obtain high signal-to-noise ratio of the signal to do the analysis. All the PF currents used are 8-9KA/turn. The vacuum shots are shown in Fig. 6. To avoid eddy current on the vessel and some other structure, the yellow area signals data which in the current flat are used.

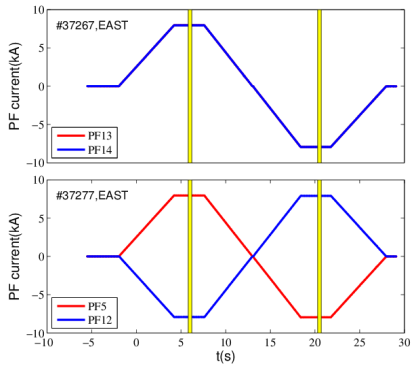

Figure 6. PF coil current for vacuum shot

By statistics from poloidal field vacuum shot-database, random uncertainty of flux loops and pickup coils on EAST are shown in Fig.7. The random uncertainties of most of pickup-coils are less than 10G, while random uncertainties of most of flux loops are less than 10mWb. The 6 sensors (pb19, pb38, fl 12,33-35) will not be used in equilibrium reconstruction.

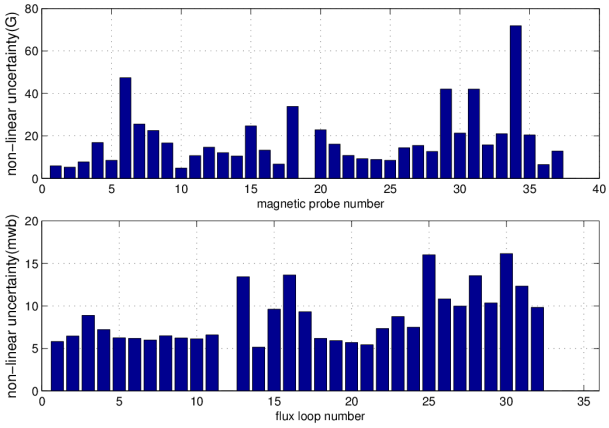

Figure 7. The random uncertainty of the magnetic probe and flux loops

(2) Equilibrium reconstruction based on uncertainty analysis

The equilibrium reconstruction on EAST is accomplished by EFIT, using 2- and 3-knot spline representation for P' and FF'. The uncertainty values of sensors are used as fitting weight in EFIT. In the simulation, plasma equilibrium shot is set as the reference, and the magnetic data from the reference will be used as accurate calculated data. The calculate data add the uncertainty value is set as the measurement data to do the reconstruction simulation. At last, the uncertainty is obtained by statistics of the difference between the reconstruction results and the reference equilibrium. The uncertainty parameters of two X-points, 4 strike points and 6 control gaps in Plasma Control System (PCS) will be presented.

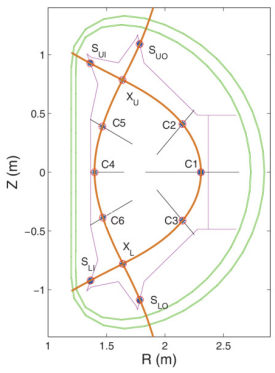

Fig.8 The cross-section of EAST. The green lines, pink lines, the orange lines and the black lines are the vacuum vessel, the limiter, the last close magnetic surface and the SOL control lines separately, and C1-C6, X_U , X_L , S_{UI} , S_{UO} , S_{UI} , S_{LI} , S_{LO} , are 6 control gaps, 2 X-points, and 4 strike point separately.

There were 3 equilibriums used as reference. The key parameters are shown in table 1. Shot 42059 is one of the normal discharges on EAST in last campaign, and shot 3000 and 1000 are 2 simulation results for comparison. These three equilibriums have similar plasma shapes and pressure and current profiles, and different plasma total currents and B_T.

Table 1. Key parameters of the reference equilibriums

Shot	type	R	B_T	I_p	l_i	β_T	κ	q^*
3000	simulation	1.9m	3.5T	1MA	1.4	0.66	1.7	4.9
1000	simulation	1.86m	1.9T	500kA	1.15	0.039	1.7	5.3
42059	experiment	1.86m	1.8T	400kA	1.23	0.19	1.75	6.6

The results of the uncertainty of equilibrium reconstruction are summarized in Fig.7. The uncertainties of the gaps on low field side and the strike points are larger than others uncertainties. The uncertainty of the gap on low field side (C1) is larger because the sensors are farther away from this gap. In the discharges with plasma current of about 400-500kA, the uncertainties uncertainty is 0.5~1.4cm for 6 control gaps, less than 0.8cm for X-points, and 1.0~1.6cm for strike points (95% confidence). However, as the plasma current increasing, the signal to noise ratio of the diagnostics system is larger, which will lead to the reducing of the uncertainty of equilibrium reconstruction. It's clarified that in the discharges with plasma current of 1MA, the uncertainties are less than 0.7cm for 6 control gaps, less than 0.4cm for 2 X-points, and less than 1.0cm for 6 strike points, for 1MA discharge (95% confidence).

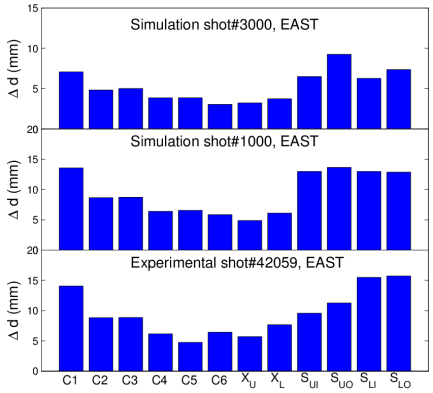

Fig.9 position uncertainties of these 12 points from the equilibrium scan (95% confidence).

4. Conclusion

The calibration of magnetic measurements is carried out on the EAST Tokamak. The uncertainties of magnetic measurements are analyzed on EAST by comparison between experimental and green-function calculations based on vacuum shots. The overall uncertainty and its origins are analyzed from the calibration. The sensitivity of the magnetic data uncertainty in the plasma shape reconstruction is analyzed based on EFIT fixed boundary and fitting mode by applying overall uncertainty as fitting weight in EFIT.

This work is supported by National Natural Science Foundation of China (Grant No.

11475002）.

Reference:

[1] L. Lao, H. John, R. Stambaugh, A. Kellman, and W. Pfei_er, Nuclear fusion 25, 1611 (1985).

[2] E. Strait, Review of scientific instruments 77, 023502 (2006).

[3] X. J. Dai, B. Shen, and G. J. Liu, Nuclear Fusion and Plasma Physics 30, 360 (2010).

[4] W. B. Xi, S. T. Wu, B. Shen, B. N. Wan, Nuclear Fusion and Plasma Physics 1, 014 (2008).

[5] J. Y. Sun, B. Shen, G. J. Liu, Nuclear Fusion and Plasma Physics 3,34 (2014)

Topics: *Stability of edge plasma*

MHD Stability of Edge Region of H-mode Plasmas in LHD and Comparison with the Characteristics in Tokamaks

K. Toi, S. Ohdachi and LHD Experiment Group
National Institute for Fusion Science, Toki 509-5292, Japan

Abstract

Clear reduction of magnetic fluctuations due to resistive interchange modes (RICs) is observed in ELM (edge localized mode) free phase of the H-mode plasma in an outward-shifted configuration of LHD, in which plasma a steep pressure gradient is generated at the plasma edge in magnetic hill. When the transition from H-phase to L-phase occurs, the RICs are suddenly enhanced although the edge pressure gradient is reduced considerably. Moreover, when the L-phase goes into so-called improved L-mode transiently, the RICs are again suppressed clearly, having a modest ETB structure in very edge. The ELM free phase is quenched by a large amplitude ELM where RICs grow explosively with a short time scale of the order of ~ 0.1ms. Possible mechanisms for the edge stability against RICs in the ELM-free phase are discussed based on a linear restive MHD theory, that is, an inward movement of the ETB foot away from the low order rational surface of ι=1 surface (ι: rotational transform). Other kinetic effects such as diamagnetic and/or ExB flows and the sheared flows may also play an important role in RIC-suppression and explosive growth observed experimentally.

1. Introduction

MHD stability of the edge region in H-mode plasmas with steep pressure gradient is crucially important for burning plasmas based on a tokamak or stellarator/helical concept. Once MHD instabilities are excited in the pedestal or edge transport barrier (ETB) region, strong degradation of plasma performance takes place and might lead to quenching D-T burning in the most serious situation. As commonly observed in major toroidal confinement devices, such MHD instabilities often trigger large amplitude edge localized modes (ELMs) which affects seriously the life of divertor target plates and other plasma facing components [1]. In tokamak plasmas, there is a consensus that MHD instabilities to trigger so-called type I ELMs are ballooning and peeling modes and their combination [2]. These instabilities are driven

by pressure gradient and toroidal current density at the pedestal/ETB region. On the other hand, ELMs are also observed in H-mode plasmas of stellarator/helical devices. In contrast to tokamak H-modes, pressure driven modes are predominantly destabilized in the plasma edge, and the current driven modes can be excluded due to very low net toroidal plasma current. Resistive interchange mode (RIC) is thought to be the most likely candidate of an ELM trigger, as discussed in W7-AS and LHD H-mode plasmas [3-5]. In this paper, we present experimental results on clear suppression and explosive growth of RICs in an H-mode having long ELM free phase achieved in a specific magnetic configuration of LHD and try to interpret the observations with help of a linear resistive MHD theory.

2. Suppression and explosive growth of RICs in an H-mode

In LHD, an H-mode plasma is first obtained in so-called inward-shifted magnetic configuration where the magnetic axis position in the vacuum field R_{ax} is pre-set around R_{ax}=3.6 m. Although good energetic particle confinement is achieved in this configuration, the MHD stability is worse due to the presence of higher magnetic hill and RICs are easily destabilized, in particular, in the edge region of H-mode plasmas. In this configuration, RIC having m=2/n=3 structure is always destabilized just after the ETB formation by the L-H transition where the low order rational surface of ι=3/2 resides in the ETB region [4], where m and n are the poloidal and toroidal mode numbers, respectively. It is known that the eigenfunction has a character of a mode localized at the mode rational surface. If the low order rational surface is placed away from the steep pressure gradient region, RIC activities would be considerably reduced to an acceptable level although kinetic effects such as plasma flow and its shearing effects might be needed to get complete suppression. In LHD, a specific outward-shifted configuration, i.e., the R_{ax}=3.9m configuration places the low order rational surface ι=1 just outside the last closed flux surface (LCFS) of the vacuum field. It should be noted that only lesser numbers of low order rational surfaces exist around ι=1 surface even in the configurations having finite edge magnetic shear, such as LHD. The character of the H-mode in this configuration is different from that of the H-mode in the inward-shifted configurations, that is, it has an ELM free phase much longer than global energy confinement time [5]. A marked difference in edge MHD stability for both H-modes obtained in the inward- and outward-shifted configurations is the sudden excitation or suppression of RIC just after the ETB formation. A typical discharge waveform of the H-mode with long ELM free phase is shown in Fig.1. In this figure, the confinement improvement factor is also shown for the international stellarator

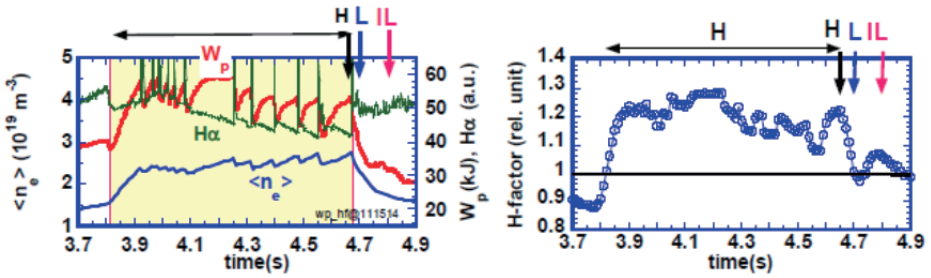

Fig.1 (Left) Typical waveform of an H-mode with long ELM free phases and large amplitude ELMs in the outward-shifted magnetic configuration of R_{ax}=3.9m, where W_p, $<n_e>$ and $H\alpha$ are the plasma stored energy, line averaged electron density and Hα-emission, respectively. (Right) The improvement factor of the global energy confinement for the ISS2004 scaling.

scaling ISS2004 which has a character of gyro Bohm type confinement [6]. In this shot, we pay attention three time slices in characteristic confinement phases marked with "H" at t=4.666s, "L" at t=4.700s and "IL" at t=4.800s which stands for an improved L-mode. The radial profiles of n_e, T_e and the electron pressure P_e in these time slices are compared in Fig.2. As seen from Fig.2, an obvious ETB having very steep gradient is formed in the electron density (n_e-) profile at t=4.666s in the ELM-free H-phase, but is not formed in T_e profile. Nevertheless, the P_e-profile has a clear ETB structure. On the other hand, in the IL phase an ETB structure is found in T_e-profile, while the ETB structure does not develop in n_e-profile. The character in the IL phase is similar to that of I-mode [7]. The P_e-profile of this phase has an ETB structure with the modest height in the edge. In L phase, no ETB structure is found in both T_e- and

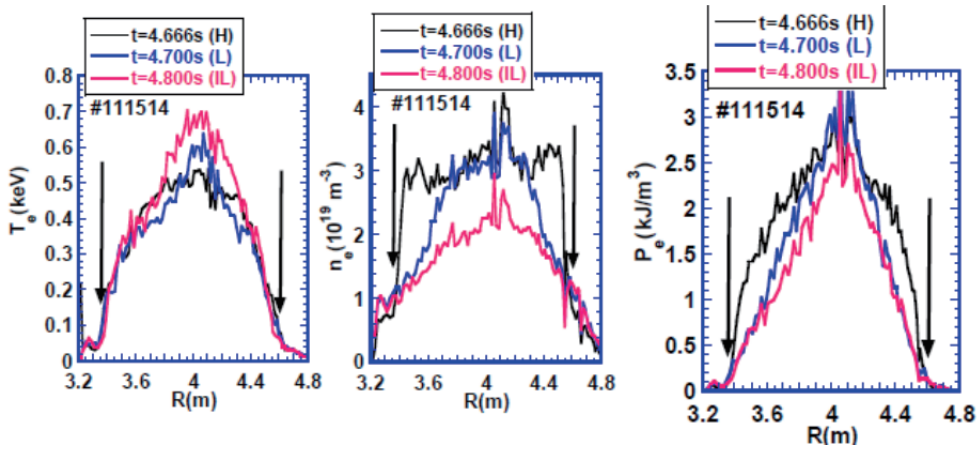

Fig.2 Radial profiles of electron temperature (T_e), electron density (n_e) and electron pressure (P_e) in three characteristic phases, "H", "L" and "IL" on the H-mode.

n_e-profiles, accordingly also not in P_e-profile. Note that the vertical arrows in Fig.2 show the inferred location of the ι=1 mode rational surface. Edge MHD stability is easily investigated by monitoring low frequency magnetic fluctuations less than 10 kHz on LHD. Time evolution of the magnetic fluctuations is shown in Fig.3 together with the volume averaged toroidal beta value measured by a diamagnetic loop $<\beta_{dia}>$ in this H-mode with long ELM free phases and large isolated ELMs. We focus on three time slices indicated with arrows in Fig.3. Just before the H-L back transition at t=4.670 s, the magnetic fluctuation amplitude is in the lowest level. The back transition is triggered by a large ELM and the L-phase appears having the amplitude enhanced by a factor of ~3 for that in the H-phase. After the L-phase for ~100 ms, a characteristic

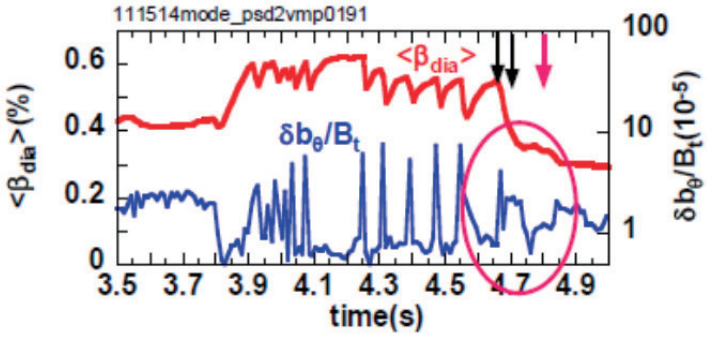

Fig.3 Time evolution of the volume-averaged toroidal beta measured by diamagnetic diagnostic $<\beta_{dia}>$ and the magnetic fluctuations amplitude related to RICs in the H-mode shot shown in Fig.1.

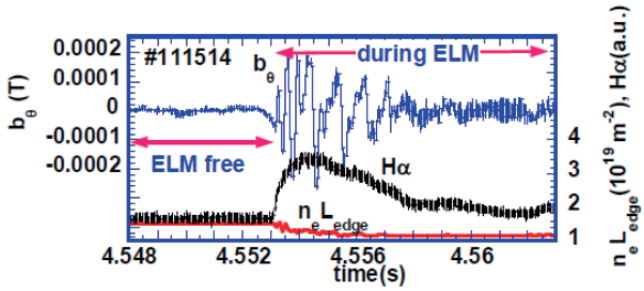

Fig.4 Zoomed waveforms of magnetic probe signal, $H\alpha$-emission signal and line electron density just outside the ETB foot in a large amplitude ELM event.

phase is suddenly generated with again reduced magnetic fluctuation amplitude similar or slightly higher level compared with the H-phase one. This suppression of RIC contributes to modest confinement improvement, as shown in Fig.1. It should be noted that the quiescent phase without RICs is interrupted by explosive growth of RICs triggering a large ELM pulse, as seen from Figs. 1 and 3. In the ELM event, the

magnetic fluctuations rapidly grow in a short time scale of the order of 0.1ms, as shown in Fig.4. The amplitude of the magnetic fluctuations during the ELM is enhanced by a factor of ~10 higher than the H-phase level and ~3 times higher than the L-phase level. This suggests that the steep pressure gradient achieved during ELM free phase would supply large free energy for RIC destabilization and lead to the explosive growth.

3. Stability analysis with a linear resistive MHD stability theory

In this section, the stability of resistive interchange modes is analyzed using the pressure profile data obtained experimentally. The rotational transform profile is used that calculated by the HINT2 code where the plasma response is taken into account but not plasma rotation effects [8]. When the location of the ι=1 surface is just outside the LCFS of the vacuum field, a global resistive MHD code [9] is not applicable to the equilibrium profile data for stability analysis against resistive interchange modes. To avoid this difficulty, the effective minor radius is defined so that the location of the ι=1 surface is placed at ρ=0.95 inside the LCFS determined by the minor radius. By this code, the eigenfunctions of unstable RICs are calculated, together with the growth rates. The pressure profile is given using the P_e-profile so that the volume averaged beta calculated from the profile should match with the diamagnetic beta value, i.e., 0.6 % in the present analysis. In other words, the radial profile of the local beta β(ρ) thus determined is used in the code analysis. In Fig.5, the radial profiles of the rotational

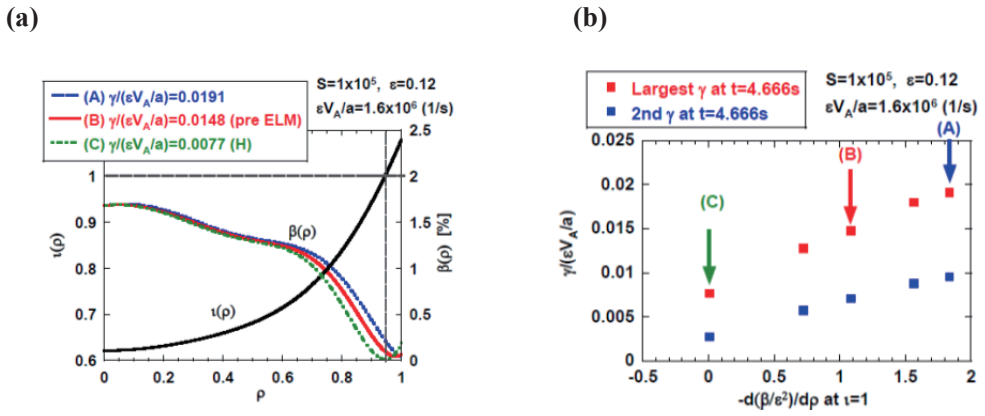

Fig.5 (a) β(ρ) profiles (A) to (C) having the different gradient at the ι=1 surface which locates at ρ=0.95. (b) The 1st and 2nd growth rates of m=1/n=1 RIC calculated for the profiles, where the magnetic Reynolds number is assumed to be S=10^5.

transform and the local beta value are shown for the profile in the H-phase, where three model profiles (A), (B) and (C) of the local beta $\beta(\rho)$ are provided from the experimental data by changing the ETB foot location slightly with a fixed highest

gradient magnitude near the edge. These profile data enable us to study the effect of the gradient at the ι=1 surface on the RIC stability. The 1st and 2nd largest growth rates for the profiles (A) to (C) are given in Fig.5(b) with three vertical arrows. When the gradient at the ι=1 surface $|\nabla\beta|$ is vanished as in the profile (C), the growth rate is reduced by a factor of ~3 from the highest case (A). The eigenfunctions of the scalar potential $\phi(\rho)$ have a character of a localized at the ι=1 surface, as shown in Fig.6. It is also seen from Fig.6 that the eigenfunctions expand in the region with steep $\nabla\beta$ inside the ι=1 surface and on the other hand they quickly decay in the very edge region outside the surface. The eigenfunction of the radial displacement ξ_r is similar with the shape of $\phi(\rho)$, because ξ_r is expressed as $\xi_r(\rho)=\frac{im}{\gamma a B_\varphi}\frac{\phi(\rho)}{\rho}$ where γ, a and m are respectively the growth rate, averaged minor radius and poloidal mode number. It should be noted that this linear calculation does not provide any information of the differences of the radial displacement magnitude for three profiles (A) to (C) because the magnitude is determined by nonlinear saturation of RICs. If the profile (C) corresponds to the profile in the ELM free H-phase and evolves to the profile (B) caused by a slightly increased volume averaged beta, the radial displacement might be dramatically enhanced with a short rise time. This should be confirmed with more detailed experimental data. In the L-phase, the eigenfunction is more localized because of gentle gradient of $\beta(\rho)$ near the ι=1 surface.

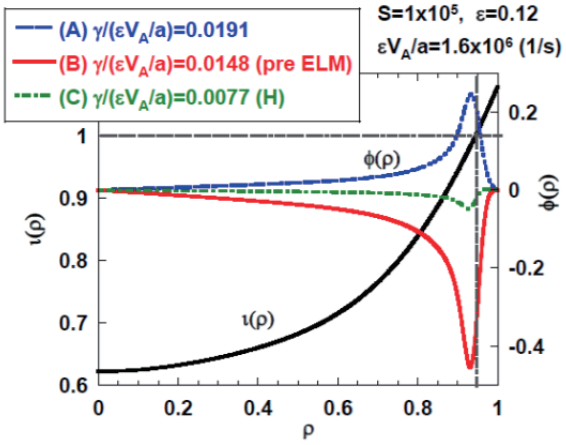

Fig.6 Eigenfunctions of $\phi(\rho)$ for three $\beta(\rho)$ profiles (A), (B) and (C) shown in Fig.5(a).

4. Comparison of the edge MHD stability with that in tokamak H-modes

Edge MHD stability of H-mode plasmas is determined by a certain kind of MHD instabilities depending on toroidal magnetic configuratios such as

stellarator/helical or tokamak devices. The instabilities in the pedestal or ETB region can induce ELMs through the nonlinear evolution. In LHD H-mode plasmas edge MHD stability is mainly determined by destabilization of resistive interchange modes which are pressure driven modes and are usually localized at the mode rational surface in bad curvature region, i.e., magnetic hill [3-5]. Current driven modes are excluded in net current free plasmas as H-mode plasmas on LHD. This is a clear contrast to the situation of H-mode plasmas in tokamaks. As the MHD instabilities, one is peeling mode which is a kind of kink mode and mainly destabilized by large totoidal current density in the pedestal region [1,2]. The other one is ballooning mode which is mainly driven by pressure gradient in local bad curvature region of a tokamak plasma having the flux-averaged magnetic well over a whole region of $1/\iota>1$, i.e., in the outboard side of the torus [1,2]. The edge toroidal current in the pedestal is dominated by bootstrap current which is driven by the steep pressure gradient there. Accordingly, these instabilities are driven by both toroidal current density and pressure gradient in the pedestal region in a complex way. Large amplitude ELMs, i.e., so-called type I in tokamaks should be controlled through sophisticated control of these driving free energy resources. In LHD and other stellarators, ELMs induced by RICs might be controlled with a simpler way, compared with a tokamak.

5. Summary

In a specific magnetic configuration of LHD where the $\iota=1$ surface is placed just outside the LCFS of the vacuum field, an H-mode has been observed having a long duration of ELM free phase where RICs are clearly suppressed. This H-mode character exhibits a clear contrast to the H-modes observed in the so-called inward-shifted configuration where RICs are immediately enhanced by the ETB formation. The long ELM free phase is often interrupted by explosive growth of RICs triggering large amplitude ELMs. The H-phase returns to L-phase by the H-L transition triggered by a large ELM event. After the L-phase, the improved L-phase (IL-phase) without clear drop of Hα-emission is often realized with an ETB structure in T_e-profile not in n_e-profile. In the IL-phase, the magnetic fluctuations of RICs are again suppressed considerably. The observed behaviors of RICs are analyzed using a global resistive MHD code. A qualitative comparison has been done between the experimental results and those of the numerical analyses. Other kinetic effects such as diamagnetic and E x B flows and their shear should be taken into account for more improved understanding of the edge MHD stability of ETB region on LHD. Edge MHD stability and ELMs are determined by different instabilities in stellarators/helicals

(LHD and others) and tokamaks (EAST, KSTER and others), i.e., resistive interchange modes in the former and peeling-ballooning modes in the latter. Experimental and theoretical studies of edge MHD stability, mainly, ELMs in both toroidal configurations are important and would give us many important hints to control ELMs with different approaches, reliably and effectively,.

Acknowledgements

We acknowledge the LHD technical team for their support to this research. This research is supported in part by LHD project budget (NIFS10ULHH011, NIFS14KLPP037) and the Grant-in-Aid for Scientific Research from JSPS (No. 24360386). It is also supported by the JSPS-NRF-NSFC A3 Foresight Program in the field of Plasma Physics (NSFC: No.11261140328, NRF: No. 2012K2A2A6000443).

References

[1] E.J. Doyle et al., Nucl. Fusion **47**, S18 (2007).
[2] P.B. Snyder et al., Phys. Plasmas **9**, 2037 (2002).
[3] A. Weller et al., Phys. Plasmas **8**, 931 (2001).
[4] K. Toi et al., Fusion Sci. Technol. **58**, 61 (2010).
[5] K. Toi et al., Nucl. Fusion **54**, 033001 (2014).
[6] H. Yamada et al., Nucl. Fusion 45, 1684 (2005).
[7] D.C. Whyte et al., 2010 Nucl. Fusion **50** 105005.
[8] Y. Suzuki et al., Nucl. Fusion 46, L19 (2006).
[9] R. Ueda et al., Phys. Plasmas **21**, 052502 (2014).

Intermittent edge plasma transport in the Large Helical Device

H. Tanaka[1, 2] and the LHD Experiment Group

[1] *National Institute for Fusion Science, 322-6 Oroshi-cho, Toki, 509-5292, Japan*
[2] *SOKENDAI (The Graduate University for Advanced Studies, Department of Fusion Science), 322-6 Oroshi-cho, Toki, 509-5292, Japan*

Abstract

In order to evaluate an internal electric field inside the blob-like structures observed in the Large Helical Device (LHD), we have measured electrostatic fluctuations around the LHD divertor leg by using a three-pin reciprocating Langmuir probe. In the vicinity of the low-field side edge of the divertor leg, negative and positive spikes of an ion saturation current fluctuation were observed in the divertor leg and the private region, respectively. By employing the conditional averaging technique for the ion saturation current and two floating potentials, we have confirmed the existence of the internal electric field insise the blobs and quantitatively estimated the propagation speed.

I. INTRODUCTION

Accurate prediction of the divertor heat flux width, which is proportional to the wetted area on the divertor plate, is one of the essential issues for ITER and future DEMO reactor. Therefore, multi-machine scaling of the scrape-off layer (SOL) width has been actively discussed recently. This result suggests that the SOL width in ITER attached divertor discharge will be quite narrow (~1 mm)[1]. Moreover, cross-field transport of the heat flux in between the X-point and the divertor plate plays an important role for determination of the heat flux width on the divertor plate as well as the upstream SOL width.

On the other hand, recent edge plasma experiments in tokamaks indicate that there is an intermittent transport inside the private region in addition to the blobby plasma transport in the low-field side (LFS) SOL[2]. The latter is well-known phenomenon as the cross-field intermittent transport of filament structures ("blobs"). Blobs propagate toward the LFS direction because of the $\mathbf{E} \times \mathbf{B}$ drift with an induced electric field ($\mathbf{E}$), which is generated by the gradient and curvature of the magnetic field ($\mathbf{B}$)[3]. In order to improve the prediction of the heat flux width on the divertor plate, mechanisms and characteristics of such transports appearing around the divertor region should be understood in detail.

In the Large Helical Device (LHD), distribution of the magnetic field strength is essentially different from that in tokamak devices. Past studies in LHD indicated that blob-like structures appear in the private region from the measurements by using the divertor probes[4], the lithium beam probe[5], and a fast scanning Langmuir probe (FSP)[6]. However, there had been no measurement of the internal electric field inside the blob-like structures.

In this study, we have investigated such intermittent transports appearing around the LHD helical diverter by using the FSP. In order to confirm an existence of the internal electric field, we installed a probe head with three probe tips on the FSP and measured an ion

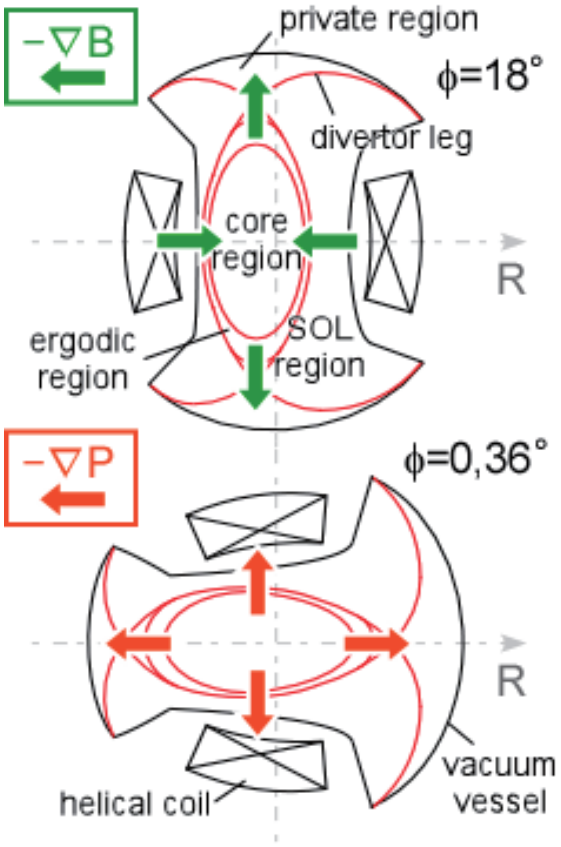

FIG. 1. Vertical and horizontal cross sections in LHD[7]. They appear alternatively every 18 degrees in the toroidal direction. Vectors of $-\nabla B$ and $-\nabla P$ are roughly depicted.

saturation current (I_{sat}) signal and two floating potentials simultaneously. The electric field was estimated by applying the conditional averaging technique.

II. EXPERIMENTAL SETUP

We used the world's largest heliotron-type device LHD. In LHD, the magnetic geometry inside the vacuum vessel is mainly determined by the two superconducting helical coils with a toroidal number of m = 10. Figure 1 shows vertically and horizontally elongated poloidal cross sections. In the same figure, gradients of the magnetic field strength (B) and the plasma pressure (P) are denoted by arrows. The core plasma is surrounded by the ergodic region with complex magnetic geometry. The two SOLs except for the ergodic region are located in front of the helical coils; the magnetic field strength becomes strong as increasing the distance from the last-closed flux-surface (LCFS) on the helical mid-plane. Thus, SOLs in LHD are similar to the high-field side (HFS) SOL in tokamaks. The other magnetic structures are the divertor leg and the private region that is lying between the two divertor legs. In the private region, which is the furthermost from the helical coils, the LFS direction from the divertor leg points to the lower plasma-pressure side[7], as shown in Fig. 1. Therefore, the private region has similar positional relationship with the LFS SOL in tokamaks.

In order to investigate the existence or non-existence of the internal electric field in the blob-like structures observed in the private region, we installed a fast scanning Langmuir probe (FSP) with three probe tips. Figure 2(a) shows a two-dimensional (2-D) distribution of the connection length (L_c) of the magnetic field line around the insertion trajectory of the FSP. The 2-D plane is roughly perpendicular to the magnetic field on an upper X-point. The standby position of the probe head was set in the private region. During the flat-top phase in a discharge, the probe head was inserted downward at a speed of approximately 1.5 m/s. The probe head firstly cuts across the divertor leg and then passes through the edge surface layers and the ergodic region.

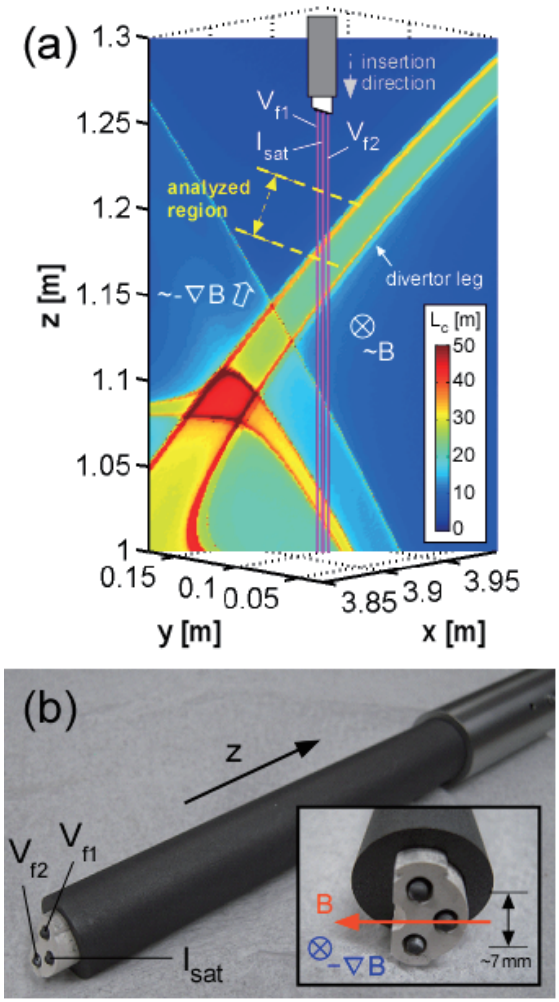

FIG. 2. (a) 2-D distribution of L_c around the insertion trajectory of the FSP head for R_{ax} = 3.6 m. (b) Photograph of the probe head[8].

In order to obtain the electric field inside the blobs, we arranged three probe electrodes on a plane that is perpendicular to the magnetic field gradient around the divertor leg, as shown in Fig. 2(b). The center tip measured an ion saturation current (I_{sat}) fluctuation. The others obtained the floating potentials (V_{f1}, V_{f2}) simultaneously. Distance between the latter two tips (d) was approximately 7 mm. By assuming the electron temperatures (T_e) of a passing blob on these two tips were the same, the internal electric field across the magnetic field on the probe surface can be deduced by $E_\perp = (V_{f1} - V_{f2}) / d$. Here, the sign of $E_\perp$ becomes positive when the blobs propagate toward the LFS direction due to the $\mathbf{E} \times \mathbf{B}$ drift. The sampling frequency was 1 MHz.

III. MEASUREMENT OF THE ELECTRIC FIELD INSIDE THE BLOB-LIKE STRUCTURES

Figure 3(a) shows the I_{sat} distribution as a function of the height (z) from the mid-plane. A single I_{sat} peak at $z \sim$ 1.18 m corresponds to the upper L_c peak inside the divertor leg (see Fig. 2(a)). An upper region of $z >$ 1.18 m is in the private region. Figures 3(b) and (c) show the fluctuation level and the skewness of I_{sat} defined by

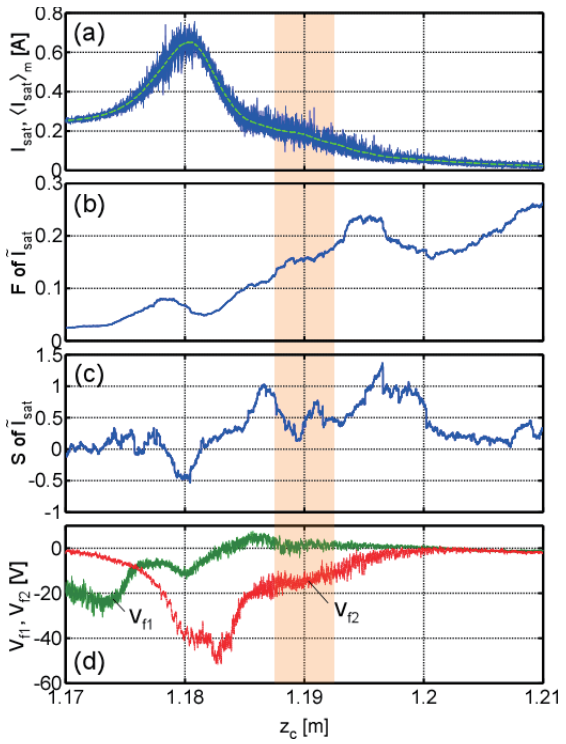

FIG. 3. (a) Distribution of I_{sat}, (b) F, (c) S of I_{sat}, (d) V_{f1} (solid line) and V_{f2} (dashed line) around the LFS edge of the divertor leg[8]. The hatched region was analyzed with conditional averaging technique in Fig. 5.

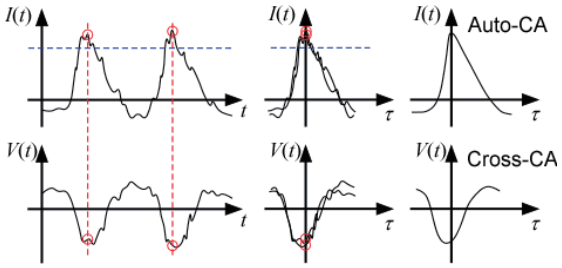

FIG. 4. Schematic of the conditional averaging technique.

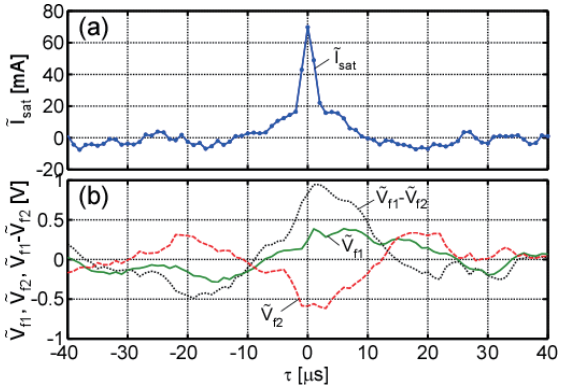

FIG. 5. (a) Auto-conditional averaged shape of I_{sat}. (b) Cross-conditional averaged shapes of V_{f1} (solid line), V_{f2} (dashed line), and ($V_{f1} - V_{f2}$) (dotted line)[8].

$F = \left\langle \tilde{I}_{sat}^2 \right\rangle^{1/2} / \left\langle I_{sat} \right\rangle$ and $S = \left\langle \tilde{I}_{sat}^3 \right\rangle / \left\langle \tilde{I}_{sat}^2 \right\rangle^{3/2}$, respectively.

From $z \sim 1.18$ m to 1.2 m, F gradually increases and S becomes negative to positive as increasing z. The negative and positive S indicate appearances of hole-like and blob-like structures, respectively. Thus, hole-like and blob-like structures were detected inside the divertor leg and the private region as with the past researches in LHD[4–6]. Regrettably, there were large high-frequency ($f > 100$ kHz) background noise components in the I_{sat} fluctuation in this discharge. Thus, the skewness drops to ~0 at $z > 1.2$ m mainly caused by the noise components. Figure 3(d) shows the simultaneously measured V_{f1} and V_{f2}. The negative V_f reflects the large sheath potential with high T_e inside the divertor leg.

In order to estimate the internal electric field, we applied the conditional averaging technique illustrated in Fig. 4. Figure 5 shows the conditional averaged shapes of I_{sat}, V_{f1}, V_{f2}, and ($V_{f1} - V_{f2}$). In this calculation, time points of passing of blobs were detected when the I_{sat} fluctuation has a positive peak larger than a standard deviation for more than 3 μs. Then, subsets of each signal around the detected time points were collected and averaged in the same time domain. The thin peak of the conditional averaged I_{sat} with three points is partly attributed to the high-frequency noise. Conditional averaged V_{f1} and V_{f2} have positive and negative values at $\tau \sim 0$; therefore, ($V_{f1} - V_{f2}$) has a positive peak of approximately 1 V. Because of some detection errors from the background noise, it should be noted that this voltage is an underestimated value.

From the conditional averaged result, the underestimated electric field is estimated as $E_\perp \sim 1/7 \sim 143$ V/m; the $\mathbf{E} \times \mathbf{B}$ drift speed is $v_b \sim E_\perp / B \sim 110$ m/s. Duration time of the positive spike of the averaged I_{sat} seems to be < ~20 μs; size along the magnetic field gradient is estimated as ~2.2 mm.

IV. SUMMARY

We have used the three-pin-head FSP in order to evaluate the internal electric field inside the blob-like structures observed in the private region next to the the LFS edge of the divertor leg in LHD. Near the LFS

edge of the divertor leg, negative and positive skewness were observed. This tendensiy is similar to that observed near between the LCFS and the LFS SOL in tokamaks[9–11] and stelalleters[12]. By applying the conditional averaging technique to simultaneously measured electrostatic fluctuations, an existence of the electric field was confirmed and estimated quantitatively. The revealed electric field is consistent with the prediction that the blobs propagate toward the LFS direction due to the $\mathbf{E} \times \mathbf{B}$ drift in common with tokamaks. Estimated size along the magnetic field gradient is somewhat small compared with that in the LFS SOL of tokamaks. This might be influenced from the large mangetic shear and/or short connection length inside the private region in LHD. Therefore, a modification effect of the divertor heat flux width due to the blobby plasma transport inside the private region might be small in the helical system. In contrast, we had confirmed an enhancement of an intermittent transport and the broadening of the divertor particle flux distribution under the detached divertor condition in the past study of LHD[13]. The broadening effect should be promptly clarified because ITER will be operated on a highly-recycling divertor with the plasma detachment in order to preserve the tungsten divertor target from the initial period.

ACKNOWLEDGMENTS

This work was supported by KAKENHI (23860064 and 25820440). This research was also performed under the auspices of the LHD project financial support (NIFS12ULPP029 and NIFS13KLPP028) and NIFS/NINS under the project of Formation of International Network for Scientific Collaborations. This work was partly supported by the JSPS-NRF-NSFC A3 Foresight Program in the field of Plasma Physics (NFSC: No. 11261140328, NRF: No. 2012K2A2A6000443).

REFERENCES

[1]T. Eich *et al*., Nucl. Fusion **53**, 093031 (2013).
[2]J.R. Harison *et al*., J. Nucl. Mater. (in press).
[3]S.I. Krasheninnikov, Phys. Lett. A **283**, 368 (2001).
[4]N. Ohno *et al*., Contrib. Plasma Phys. **46**, 692 (2006).
[5]H. Tsuchiya *et al*., Plasma Fusion Res. **5**, S2078 (2010).
[6]H. Tanaka *et al*., J. Nucl. Mater. **438**, S563 (2013).
[7]H. Tanaka *et al*., Plasma Fusion Res. **7**, 1402152 (2012).
[8]H. Tanaka *et al*., J. Nucl. Mater. (In press).
[9]J.A. Boedo *et al*., Phys. Plasmas **10**, 1670 (2003).
[10]G.S. Xu *et al*., Nucl. Fusion **49**, 092002 (2009).
[11]J. Cheng *et al*., Plasma Phys. Control. Fusion **52**, 055003 (2010).
[12]B. Nold *et al*., Plasma Phys. Control. Fusion **52**, 065005 (2010).
[13]H. Tanaka *et al*., Plasma Phys. **17**, 102509 (2010).

Versatile controllability of magnetic perturbation to ELM experiments

Hyunsun Han*, Y.M. Jeon, Y. In, J. Kim, S.W. Yoon, S.H. Hahn, H.S. Ahn, M.H. Woo, B.H. Park, and J.G. Bak
National Fusion Research Institute, Daejeon, Korea
Email : hyunsun@nfri.re.kr

New feature of in-vessel control coil (IVCC) system by introducing new alternating current (AC) power supplies with a patch-panel is presented and its application to the ELM (Edge localized mode) experiments using the RMP (Resonant magnetic perturbation) are discussed. Until the last campaign, the 3D magnetic field configuration could not be changed easily as well as the possible configuration was restricted to few setups due to the limited capability of the direct current (DC) power supply system. In the coming KSTAR campaign, comparing to the previous experimental condition, the new upgraded IVCC system will easily cope with the various demands for the peaked toroidal angle and the poloidal phasing of the 3D magnetic field in a shot.

1. Introduction

In the H-mode plasmas, the transient event called ELM which released almost 20% of the plasma stored energy to walls [1] becomes main issue to solve for protection of the wall. Among many attempts to avoid ELMy situation, or to mitigate them, the RMPs is one of the most effective method in current tokamak experiments [2-5], though the theoretical model or mechanism for that has not been established perfectly. For example, it is not clear if the ELM suppression and mitigation can be interpreted in a same way. Also, the change of the plasma stability by the perturbed field has to be investigated in the concrete. In regard to these theoretical uncertainties, a phenomenal understanding has been achieved using a slowly varying magnetic field configuration [6].

The ELM response study by the 3D magnetic field has been studied in KSTAR for many years utilizing three poloidal rows of coils dividing four sectors in toroidal direction with DC power supply system [2,7]. Though, using the n=1 and n=2 magnetic field configuration, some important physical indication for the ELM suppression condition have been observed, the limited feature of the power source and the hardness of the change of the current configuration should be enhanced for the flexible experiment plan to investigate the physical feature intensively. For this purpose, we will have installed new broad-band power supply systems with an IVCC patch panel system for the various magnetic configuration setup and field control. The basic functionalities of this flexible 3D field control system will be delivered in the coming campaign, except some real-time control capability which will be developed and provided in future.

This article structured as follows. The newly installed power supply system as well as the patch panel system is first described, with emphasis on the flexibility of the magnetic configuration. In the next section, we introduce some experiment plan in the coming campaign using the new feature of the 3D magnetic configurations. The final part, section 3, summarizes our plan with discussions.

2. New features of 3D magnetic field coils

Figure 1 shows the schematic diagram of flexible IVCC patch panel using the four power supplies. In the picture, the IVCC patch panel can change the current flow connection between the coil segments physically, while the four power supplies can be used to modify

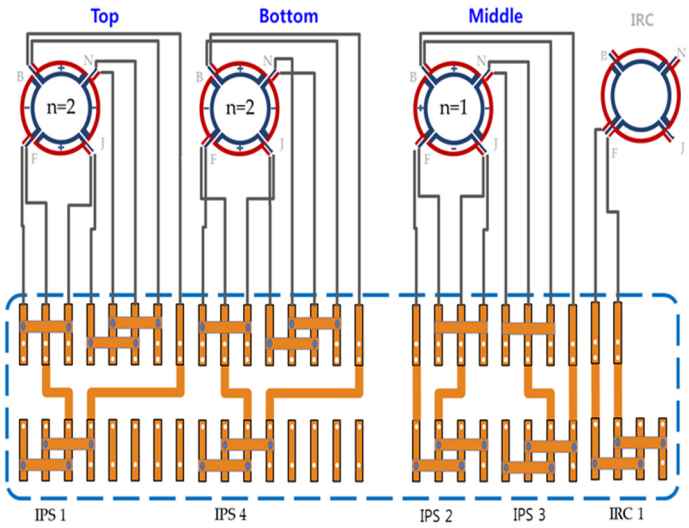

Figure 1. IVCC configuration with the patch panel of which bottom is linked power supplies, IPS1-4. (IRC is related to the radial position control.)

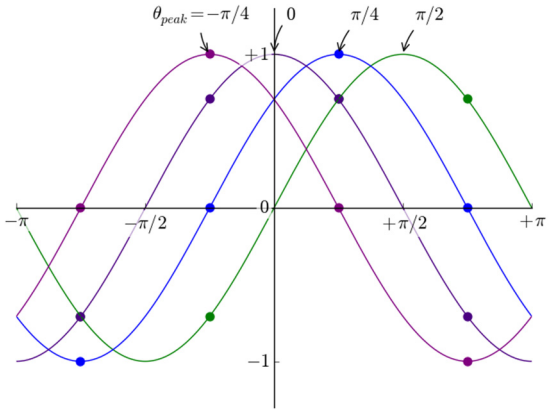

Figure 2. Relative currents on the IVCC coils (dots at toroidal angle with –3π/4,–π/4, π/4, 3π/4) to make various toroidal peak angle (Θ_{peak}) of n=1 perturbed magnetic field.

the amount of the current including even the direction (i.e. -5kA to 5kA). Each power supply can be divided two stacks which can connect to the coil with half capability, respectively (i.e. -2.5kA to 2.5kA). The operation of power supplies will be integrated to our plasma control system (PCS) for various feedback operations as well as the convenience of the shot design. By the combination of the patch panel setup and the currents on the power supplies, we can configure the toroidal phase and the poloidal phasing of the 3D magnetic field. To help understand the featuring way, if each power source is connected to each middle coil respectively, we can make n=1 perturbed magnetic field with arbitrary toroidal peaked angle by adjusting the currents of power sources according to a one-cyclic sinusoidal function (see figure 2). In this case, we ignore the side-band effect of higher n-modes. It is noticeable that some coil segments should be tethered in a same power supplies due to the mismatch of the number between the IVCCs and the power supplies. This mechanical condition can limit the degree of freedom in the poloidal coil rows or the affordable current level. Related to the previous case in figure 2, using the periodicity of the n=1 mode (i.e. f(x+π)=-f(x)), two power supplies can handle with the n=1 mode instead of four power supplies. One power supplies

have two stacks which can link to the IVCC independently. Therefore, for n=1 mode, we can adjust the toroidal peak angle of each row coils. Until now, total eight kinds of patch panel setup are prepared considering the experimental purpose and convenience of shot design.

3. 3D magnetic field experiments related to ELM using the new functionality

In this section, we discuss some experimental plans in which the new functionality of the 3D magnetic field control system will be applied. The first plan is to investigate the plasma response in both of global and local properties to the various or moving n=1 poloidal phasing magnetic configuration. We have been identified the favorable n=1 poloidal phasing magnetic configuration is existed to make the ELM suppression in KSTAR, though the selectable phasing angle is limited to four kinds with $-\pi/2$, 0, π /2, and π. In the coming KSTAR campaign, to explore in more detail with the new functionality, we can scan the plasma response varying the poloidal phasing slowly. Figure 3 shows the degree of resonant between the plasma and the magnetic perturbation with various phasing using the vacuum superposition method [8]. We expect to find the similar phenomena with the recently reported experimental results of DIII-D where the rapid bifurcations between ELMy and ELM suppression state are observed by slowly varying n=2 magnetic fields [6]. This operational capability can use to investigate the distinction between kink-resonant and pitch-aligned resonant configuration which can be determined by the relative position between the plasma q-profile (e.g. dot lines in figure 3) and the resonant contour for the poloidal mode numbers.

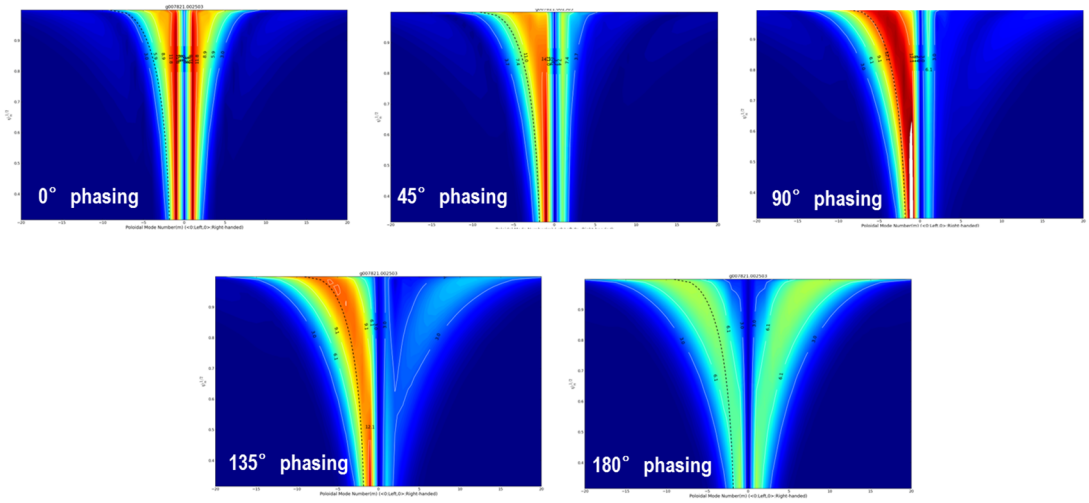

Figure 3. Poloidal mode spectra comparison between the poloidal phasing (n=1 peak angle difference between the top and the middle coils). Dot line means the plasma q-profile.

As well as n=1 case, n=2 effect will be also investigated focusing on the effects by the top or bottom coils or mixed field effect adding n=1 field. Last campaign, we have obtained ELM-suppressed shot by only mid-plane coils, and it was also found that the mixed field configuration can act on the ELM suppression differently depending on the plasma condition such as plasma confinement. To study on this phenomena in more detail, based on the n=2 ELM suppressed shot, we can add the top or/and bottom coils with even or odd configuration in a same shot. Related to the study on the mixed effect, it will be possible to add the n=1 field if the power supplies which are initially reserved to the top and bottom coils are connected to the mid-plane coils to obtain the other field topology. It will be also thinkable to

add the n=1 field on the top and bottom coils, which is same configuration used in the last campaign.

Next plan is to employ the capability of the 3D magnetic field rotation or traveling. From the previous experiments in the last two campaigns, it is identified that the error field of KSTAR is too low to make a meaningfully different effect on the plasma as the toroidal peaked angle of the perturbed field [7]. Therefore it is not relevant to choose a fixed toroidal peak angle which will be the reference position to make a poloidal phasing between the coils. But it can be useful in the view point of measurement. For example, we can determine the extent of the plasma response when the perturbed field push the plasma or pull it by changing the toroidal phase. Or we can determine whether the diagnostic signature directly came from the 3D magnetic field effects or not by tracking the signal with the rotation of toroidal phase. The ability of the perturbed field rotation can use to identify the role of the $\omega_{\perp,e}$ ($\equiv \omega_{ExB} + \omega_{e,dia}$) for the onset condition of ELM suppression. It is believed that the $\omega_{\perp,e} = 0$ condition is important to the ELM suppression by the perturbed field. Therefore, we will rotate the perturbed field configuration which suppresses the ELMs, then we check the $\omega_{\perp,e}$ which shoud be changed to the field rotation speed to support the assumption. As a final option that we suggest, rotating the 3D magnetic field can be a passive method to control the load by ELM, since it causes the strike point splitting to distribute the particle and heat flux over the divertor [9].

4. Summary

Until the last campaign, though there were impressive experimental results on the ELM control experiments using the 3D magnetic field, the field configuration could not be changed in a shot and the accessible configuration was restricted to few setups due to the limit of power supplies. In the coming KSTAR campaign, the new upgraded IVCC system equipped the current connection patch panel with four broadband power supplies will easily cope with the various demands for the peaked toroidal angle and the poloidal phasing of the 3D magnetic field in a shot. It make possible to explore the plasma response in more detail and to help the understanding of the ELM behaviors by the RMP. It is also deserve to mention that the new feature of our IVCC system can be applied to the other MHD physics such as RWM(Resistive Wall Mode) stabilization.

Acknowledgement
This research was supported by Ministry of Science, ICT, and Future Planning under KSTAR project and was partly supported by the JSPS-NRF-NSFC A3 Foresight Program (NRF No. 2012K2A2A6000443).

References
[1] A. Loarte *et al*., Nucl. Fusion **54,** 033007 (2014)
[2] Y.M. Jeon *et al.,* Phys. Rev. Lett. **109,** 035004 (2012)
[3] T.E. Evans *et al.,* Phys. Rev. Lett. **92,** 235003 (2004)
[4] W. Suttrop *et al.,* Phys. Rev. Lett. **106,** 225004 (2011)
[5] A. Kirk *et al.,* Nucl. Fusion **53,** 043007 (2013)
[6] R. Nazikian *et al.,* Phys. Rev. Lett. **114,** 105002 (2015)
[7] Y. In *et al.,* Nucl. Fusion **55,** 043004 (2015)
[8] D. Kim *et al.,* Plasma Phys. Control. Fusion **52,** 095009 (2010)
[9] A.J Thornton *et al., To be published in* J. Nucl. Mater (doi:10.1016/j.jnucmat.2014.09.079)

Development of Silicon on Insulator Type X-ray CMOS Sensor for LHD

S. Muto[1], T. Miyoshi[2, 4], N. Tamura[1], H. Nakanishi[1, 4], Y. Itoh[1], K. Tsukada[3], R. Nishimura[4], T. Tsuru[5], Y. Ono[6], Y. Arai[2, 4], and LHD Experimental Groups[1]

[1]*National Institute for Fusion Science, 322-6, Oroshi, Toki, Gifu, JAPAN*
[2]*Institute of Particle and Nuclear Studies, High Energy Accelerator Research Organization (KEK), 1-1 Oho, Tsukuba, Ibaraki, JAPAN*
[3]*Department of Technical Support, Nagoya Institute of Technology, Gokiso, Showa, Nagoya, Aichi, JAPAN*
[4]*The Graduated University for Advanced Studies, Hayama, Kanagawa, 240-0193, JAPAN*
[5]*Physics, Kyoto Univ., Kitashirakawa-Oiwake-Cho, Sakyo, Kyoto, JAPAN*
[6]*Graduate School of Frontier Sciences, Division of Transdisciplinary Sciences, The University of Tokyo, Hongo, Bunkyo, JAPAN*

To study impurity transport, a new kind of X-ray detector is required. The detector must measure the radial profiles of time-resolved soft X-ray spectra [1]. High temperature plasmas emit strong soft x-ray spectra in an energy range from 1.0 keV to 10 keV. The spectra consist of continuum as bremsstrahlung emitted from electrons and K_α lines emitted from the impurities such as ionized argons, and transition metals.

An energy resolved X-ray video camera has been developed for LHD. The camera is equipped with a Silicon-On-Insulator pixel detector (SOIPIX). Structure of the SOIPIX is shown in Fig. 1. The SOIPIX has both thick high-resistive radiation sensor and CMOS readout circuit in a single chip [2].

To get good energy resolution, the SOIPIX must be cooled to around -50 ºC, so it is mounted within a vacuum chamber (Fig. 2). A pulse tube refrigerator is used as a cooling system. We confirmed the detector has been cooled below -50 ºC in few hour.

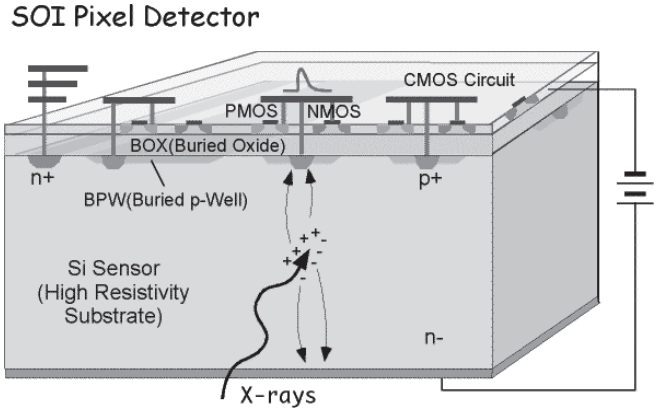

Fig. 1. Structure of the SOIPIX [3].

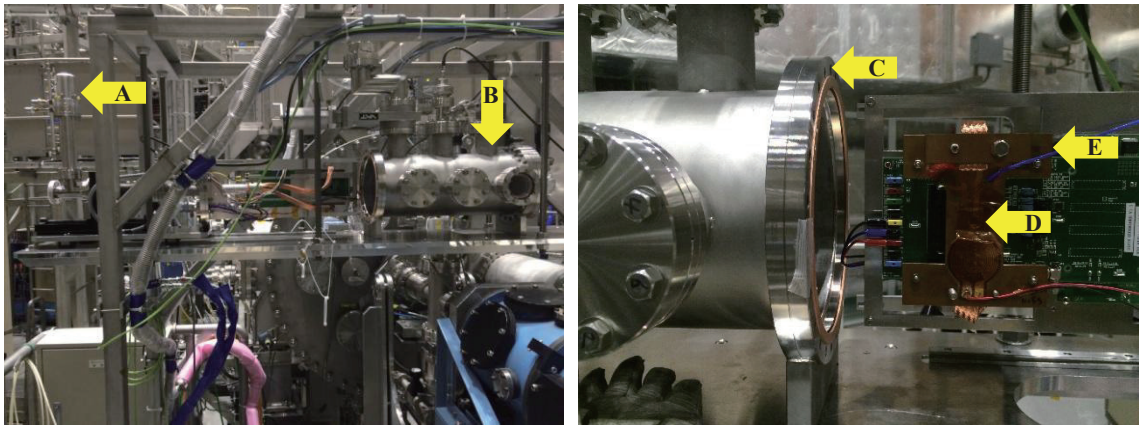

Fig. 2. Photograph of the vacuum chamber (left) and the SOIPIX sensor board (right), which is mounted in the chamber. The parts indicated by the signs "A" to "E" are a refrigerator, the vacuum chamber, a vacuum flange in a size of ICF253, the SOIPIX, and a heat sink made of copper for cooling [4].

We start to measure the x-ray by means of SOIPIX at 7-O horizontal port in LHD. The signal is read out in a fast time of 1 μs/pixel. The detector installed at the port is 264×264 pixels of 14 μm square. The thickness of the sensor is 500 μm to obtain the x-ray in a range from 1.0 keV to 10 keV, effectively. The data and control signals are transferred through an Ethernet I/F consisting of an on-board FPGA. The SOIPIX is cooled to less than -10 °C to reduce leakage current.

The plasma image is measured with the SOIPIX through a 100-μm-diameter pinhole and a 250-μm-thick beryllium filter. The filter separates vacuum between the LHD and the detector system, and reduces the flux of low-energy x-rays. The transmission of argon K_α (E = 3.2 keV) and iron K_α (E = 6.7 keV) emitted from high temperature plasma are 18.4 % and 85.3 %, respectively. The distances between the pinhole and the plasma center (R_{ax} = 3600 mm), the pinhole and the sensor are 16.85 m and 65.5 mm respectively. At the plasma center, the SOIPIX approximately covers 0.8-m-square region. The position of the pinhole is manually adjustable against the SOIPIX in perpendicular and horizontal precisions of 10 μm and 100 μm, respectively.

The first measurement of an x-ray image has been tried at a cycle (17^{th} LHD experimental campaign). Figure 3 shows the first experimental result obtained from an ICRF heated plasma of approximately 40 minutes heating pulse duration (LHD#124530, $T_e^{center} \approx 3.0$ keV, $n_e \approx 10^{19}$ cm^{-3}). The total exposure time of the SOIPIX is 16 sec. In Fig.3 is also shown the spectrum obtained with the Si(Li) x-ray pulse-height analyzer (PHA) installed at 2-O port. In the figure the surface intensities are adjusted to be equal at iron K_α. Consequently, the peak intensities are proportional to the energy resolutions of $E/\Delta E$. As a result, the energy resolution of SOIPIX is approximately 70 % in compared with the PHA.

In the figure the counting rates per a single chord are also presented. The parameter of "X" indicates the number of pixels in the single chord. In the case of the PHA, one chord is corresponding to one pixel. In the case of the SOIPIX, one chord is considered to consist of 8×8 pixels. The surface of 8×8 pixels are approximately comparable with that of the pin hole. From the figure, the counting rates of SOIPIX with 250-μm-thick-beryllium filter and PHA with 1000-μm-thick-beryllium filter are estimated to be 1.1 kcps/chord and 0.6 kcps/chord, respectively. As a result, the SOIPIX makes it possible to study the impurity transport with two times larger counting rate than the PHA. In the typical transport study the counting rate is approximately one order larger than the long pulse discharge. The pile up rejection at the main amplifier for the PHA is 5.0 % at 8.0 kcps in a shaping time of 4.0 μs. At the counting rate, that of the SOIPIX will be 15 kcps/chord.

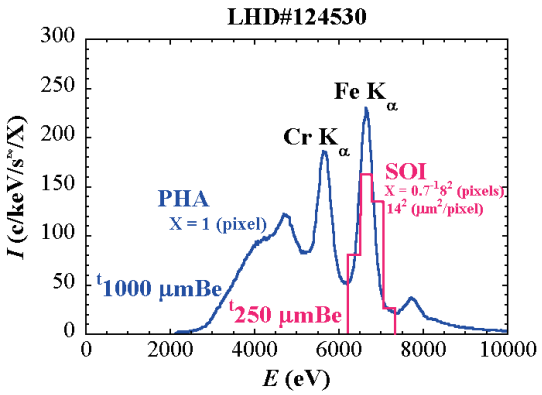

Fig.3. Spectra measured with the SOIPIX and the conventional Si(Li) x-ray pulse-height analyzer in the LHD. The horizontal and vertical axes mean the photon energy and the intensities, respectively. The thicknesses of the beryllium filters are 1000 μm for the PHA and 250 μm for the SOIPIX, respectively [5].

It is an advantage of the CMOS sensor that the pixel size is small. By the advantage, the radial profile of x-ray spectra can be measured with the SOIPIX. In order to measure the spectra, it is important that the counting rate in an exposure time is less than 1 photon/pixel. The counting rate of 15 kcps/chord is corresponding to that of 4.8×10^{-1} photon/pixel in an exposure time of 2.05 ms. This exposure time means the reading time for 256×8 pixels in the SOIPIX. The 256×8 pixels is used as 32 chords in the radial direction. The number of chords will become approximately one order better than the PHA which has three chords motional in the radial direction. With the PHA, it has been necessary for the transport study to carry out more than ten times fixed discharges. Then, the SOIPIX is expected to analyze impurity transport in a single shot.

Figure 4 shows the two images, one (to the left) obtained from a long pulse heated plasma of approximately 40-minutes pulse duration (LHD#124530), and the second (to the right) obtained from a long pulse heated plasma of approximately 10-minutes pulse

duration (LHD#131052). The total exposure time of the SOIPIX is 12.139 sec. The square frame indicates the whole region covered with the sensor. In the present measurement, the position of the sensor was perfectly adjusted.

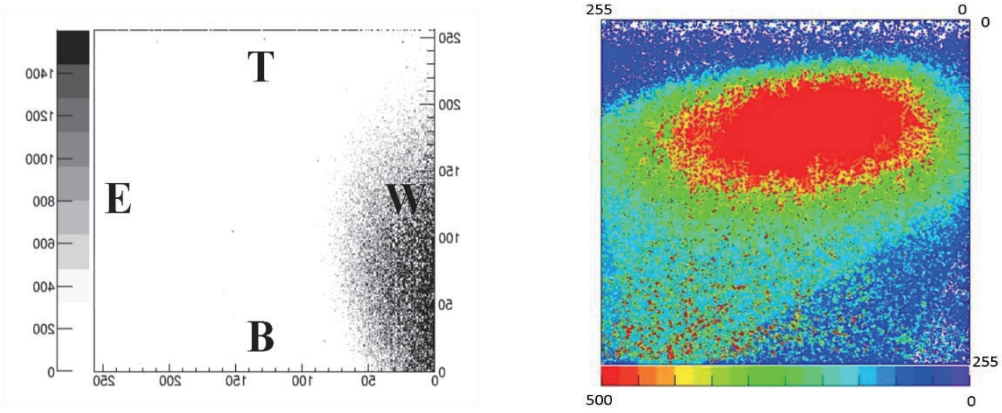

Fig. 4. LHD plasma X-ray images taken with the SOIPIX camera system (left: in 17th LHD experimental campaign, right: in 18th campaign). The vertical and horizontal axes are corresponding to the Z and toroidal direction of the plasma, respectively. The signs of "T", "B", E", and "W" mean the top, bottom, 6-O side, and 8-O side of the sensor. At the sensor the X-ray image of LHD plasma is reversed due to the pinhole camera configuration [4].

The SOIPIX is a kind of LSI which is developed by circuit, layout diaphragms, and manufacturing process. Typically, the pixel size and the number of pixels can be improved. In addition, the reading time of the SOIPIX will be improved to be 2 times faster. It is better for avoiding pile up that the counting rate will be improved to be 2.4×10^{-1} photon/pixel.

A compact PHA has been also introduced in the vacuum chamber for the SOIPIX, and the system can directly calibrate the X-ray counting rate in the LHD experiments.

References

1) "Impurity Transport Study of Medium-Z Argon by means of Soft X-ray Pulse Height Analyzer in LHD", S.Muto *et al*., Plasma and Fusion research **2,** S1069, 2007.
2) "Development of SOI Pixel Process Technology", Y. Arai, *et al*., Nucl. Instr. and Meth A. Vol. 636, Issue 1, Supplement, pp. S31-S36. doi:10.1016/j.nima.2010.04.081.
3) "Development of Energy Resolved X-ray Video Camera", Y. Arai, *et al*., Annual Report 2012 (NIFS).
4) "Energy Resolved X-ray Video Camera system in LHD", Y. Arai, *et al*., Annual Report 2014 (NIFS).
5) "Development of Energy Resolved X-ray Video Camera in the LHD", Y. Arai, *et al*., Annual Report 2013 (NIFS).

Acknowledgement

This work was partly supported by the JSPS-NRF-NSFC A3 Foresight Program in the field of Plasma Physics (NSFC: No.11261140328, NRF : No.2012K2A2A6000443).

Installation and commissioning of the neutron spectrometry system in KSTAR

H. Tomita[a], Y. Nakayama[a], S. Hayashi[a], F. Yamashita[a], Y. Yamamoto[a], Y. Sakai[a], K. Morishima[a], M. Isobe[b,c], K. Ogawa[b,c], MunSeong Cheon[d], JungMin Jo[e], K. Ochiai[f] and T. Iguchi[a],

[a]Nagoya University, Japan

[b]National Institute for Fusion Science, Japan

[c]SOKENDAI (The Graduate University for Advanced Studies), Japan

[d]Diagnostics Technology Team, ITER Korea, Republic of Korea

[e]Seoul National University, Republic of Korea

[f]Fusion Research and Development Directorate, Japan Atomic Energy Agency, Japan

1. Introduction

In the coming LHD deuterium experiment, energetic-particle physics research will be extended by fusion products diagnostics. Because energetic D^+ related DD reactions are dominant in fusion deuterium plasma heated by neutral deuterium beam injection, measurement of the 2.5 MeV neutrons (DD neutron), which is one of the fusion products of the DD fusion reaction, is useful to understand behaver of energetic D^+. We are developing two types of DD neutron energy spectrometer (NES)[(1)]: One is nuclear emulsion based NES[(2-4)] based on time integrated record of recoiled proton tracks caused by elastic scattering of DD neutrons and off-line analysis of the tracks after development of the nuclear emulsion. The other is an associated particle coincident counting NES (APCC-NES)[(5-7)] based on coincident detections of a scattered neutron and a recoil proton associated to an event of neutron elastic scattering. The NES systems for DD neutron are plan to be installed in LHD. In order to demonstrate DD neutron measurement at fusion plasma experimental device, the prototypes of these NES systems were installed at J-port in an experimental fusion device Korea Superconducting Tokamak Advanced Research (KSTAR) at National Fusion Research Institute and the commissioning was performed.

2. Time integrated nuclear emulsion-based NES and its performance

The detector system consists of nuclear emulsion plates and a pinhole collimator as shown in Figure 1. Using the pinhole collimator made of a tungsten alloy, most neutrons are incident into the emulsion layer after passing through the pinhole. An incident neutron interacts with a hydrogen atom in the emulsion plate (OPERA film) by elastic scattering[(8,9)]. Here, energy of recoiled proton caused by fast neutron depends on its scattering angle. After development of the emulsion plate, tracks of the recoiled protons are analyzed by automatic scanning system called S-UTS[(10)].

The recoiled proton energy E_{rp} can be calculated from the track length of the recoiled proton, and the scattering angle θ of a neutron can be derived from the angle between the vector directed from the pinhole to the start point of the recoiled proton track and the vector pointing along the track. Thus, the incident neutron energy $E_n = E_{rp}/cos^2\theta$ can be estimated. In addition, the combination of the pinhole collimator and the nuclear emulsion also works as a pinhole camera for fast neutron.

The commissioning test was conducted in 2012-2013 KSTAR experimental campaign. Figure 2 shows the experimental setup in KSTAR. The detector set at J-port of KSTAR, viewing the plasma perpendicularly. The distance between the plasma center and the detector was 3.9 m. Figure 3 shows the dependences of number of recoiled proton tracks obtained during several shots on the integrated counts of a Neutron Flux Monitor (NFM). Here, NFMs based on the ^{3}He proportional counter and the fission chamber were located on basement floor of KSTAR. Integrated track number was proportional to the NFM counts, *i.e.* total number of neutrons emitted from deuterium fusion plasma during the shots. Here, a number of recoiled proton tracks N_{rpt} can be described as

$$N_{rpt} = \eta_{emulsion} \times SA \times S_n \times t_{meas} \qquad (1)$$

where $\eta_{emulsion}$ is the efficiency of nuclear emulsion (tracks/n), SA is the solid angle, S_n is the neutron birth rate (neutron/s), and t_{meas} is the measurement time. Average neutron birth rate of #8963-#8969 shots in KSTAR plasma in 2013 was estimated to be in the order of 10^{13} neutron/s. The rate is in agreement with maximum neutron birth rate of around 10^{14} neutron/s during 2013 experimental campaign estimated by MCNP simulation and activation foil measurements [11].

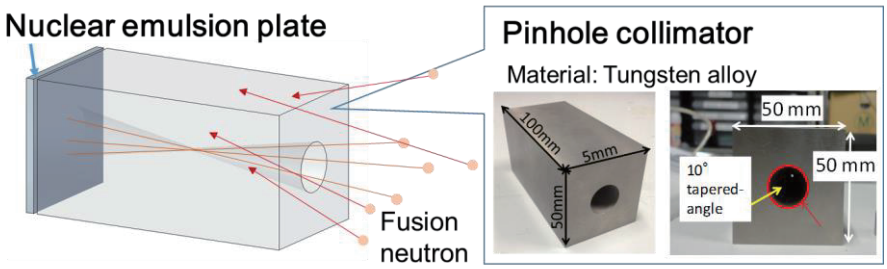

Fig.1 Overview of the NES combined with a nuclear emulsion plate and a pinhole collimator.

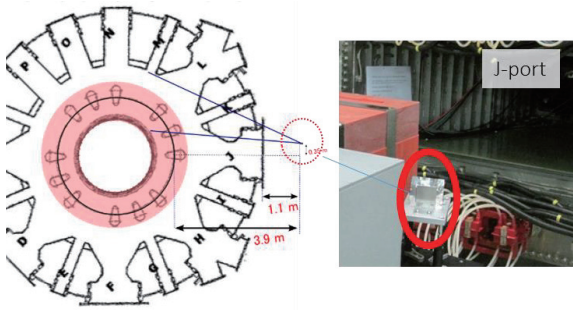

Fig.2 Experimental setup at J-port in KSTAR.

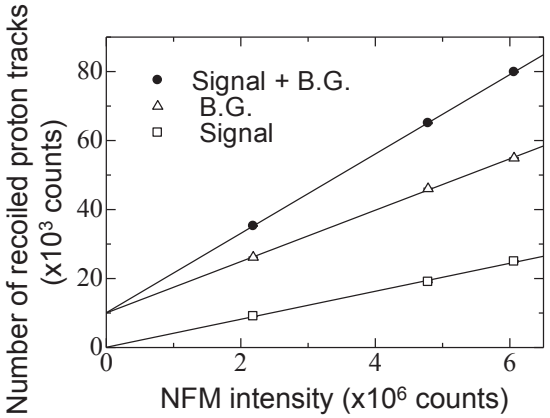

Fig.3 Dependence of number of recoiled proton tracks obtained during several shots on the integrated counts of the NFM.

3. Associated particle coincident counting (APCC) NES

Figure 4 shows an overview of the APCC-NES system. The system is based on coincident detections of a scattered neutron and a recoil proton associated to an event of neutron elastic scattering. The incident neutron energy E_{in} is simply derived from the sum of the recoil proton energy E_{rp} and the scattered neutron energy E_{sn}. Therefore the system consists of three detectors: a thin plastic scintillator worked as an incident neutron target and ΔE detector for recoiled protons (called as a radiator), a Si surface barrier detector for recoiled proton detection (RPD), and a plastic scintillator for scattered neutron detection (SND). The recoiled proton energy is derived from the deposited energy in the radiator and the deposited energy in the PRD. The scattered neutron energy is measured by time-of-flight (TOF) method between the radiator and the SND.

We used a waveform digitizer (DT5720, CAEN) for on-line DSP of outputs of these detectors. The digitizer allows analog to digital conversion and following on-line DSP for the charge integration. A fast

preamplifier was used for photomultiplier tube (PMT) output for the radiator. For output of the RPD, a preamplifier and a spectroscopy amplifier were used. Figure 5 shows a schematic diagram of on-line DSP in the digitizer for the APCC-NES. Long gates for inputs for the detectors were optimized for the better energy resolution and time resolution. For the RPD output, the integration time of the spectroscopy amplifier was also optimized. List mode data, i.e. series of the timing and pulse height of each pulse was recorded in PC. After the measurement, the pulse height spectrum with/without coincidence events and the time-of-flight spectrum were obtained by off-line data analysis. The energy resolution of the RPD and the radiator, and the time resolution by the radiator and the SND were comparable with those by data acquisition based on a conventional multi-channel analyzer.

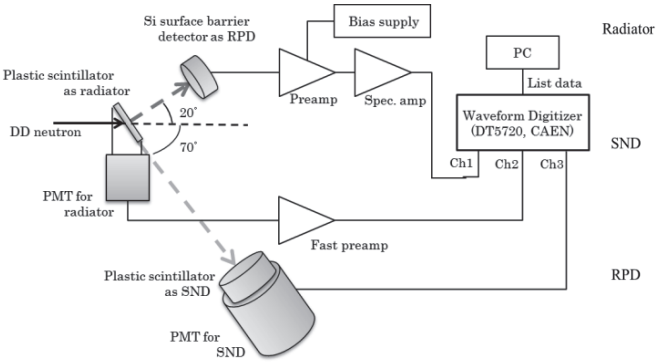

Fig.4 Overview of the APCC-NES

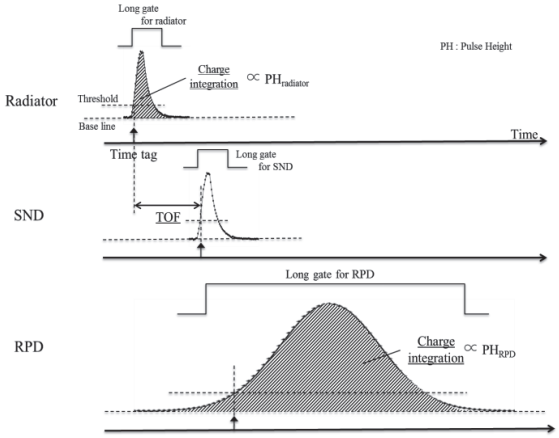

Fig.5 Schematic diagram of on-line DSP in the digitizer for the APCC-NES.

The DSP was applied to the prototype of the APCC-NES system installed at J-port in the KSTAR during the 2014 experimental campaigns. Figure 6 shows typical time trend of plasma current, NBI power, and count rate of NFM. We obtained the time trend of radiator (red line), SND (blue line) and RPD (green line) by application of an online DSP system. Figure 7 shows dependence of counting rate in between NFM and the radiator. The APCC-NES system using a waveform digitizer worked properly at counts rate of up to 10^5 cps.

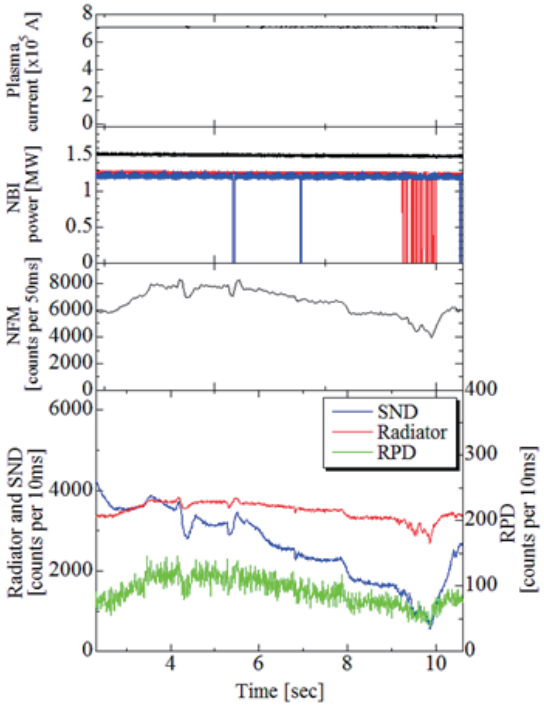

Fig.6 Typical time trend of plasma current, NBI power, NFM, APCC-NES detector in the KSTAR during 2014 experimental campaign (Shot No. 10576).

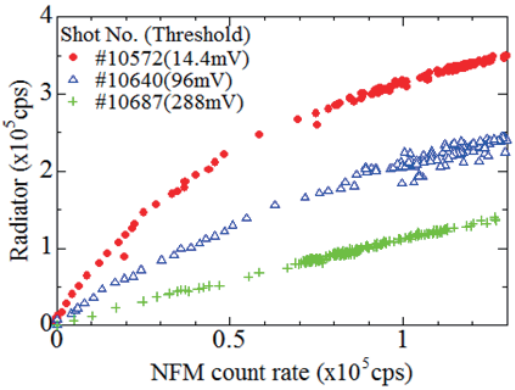

Fig.7 Dependence of counting rate between neutron flax monitor and the radiator.

4. Summary

For deuterium plasma operation in KSTAR and toward LHD deuterium phase, two types of DD neutron energy spectrometer (NES), the time integrated nuclear emulsion-based NES and the associated particle coincident counting (APCC) NES, is under development. The prototypes of these NES systems were installed at J-port in KSTAR. In the nuclear emulsion NES, the number of recoiled proton tracks recorded in the emulsion was proportional to the integrated counts of a neutron flux monitor. Average neutron birth rate in 2013 experimental campaign was roughly estimated to be in the order of 10^{13} n/s by the nuclear emulsion NES. Using data acquisition system with on-line digital signal processing, the detectors of APCC-NES worked properly at counts rate of up to 10^5 cps. The off-line data analysis obtained by APCC-NES is now ongoing.

5. Acknowledgements

This work is performed with the support and under the auspices of the NIFS Collaboration Research program (NIFS 12KOAH029, 15KOAH033, 11KLEH011) and Cooperation between Japan and Korea in the Area of Fusion Energy Research and Related Fields. Also, this work is partly supported by the JSPS-NRF-NSFC A3 Foresight Program in the field of Plasma Physics (NSFC: No.11261140328, NRF: 2012K2A2A6000443).

6. References

(1) H. Tomita, *et al*., Rev. Sci. Instrum. **85**, 11E120 (2014).
(2) Y. Nomura *et al*., Plasma Fusion Res. **6**, 2402148 (2011).
(3) H. Tomita *et al*., Plasma Fusion Res. **8**, 2406095 (2013).
(4) Y. Nakayama *et al*., Physics Procedia **80**, 81 (2015).
(5) H. Tomita, *et al*., Rev. Sci. Instrum. **81**, 10D309 (2010).
(6) Y. Yamamoto *et al*., Progress on Nucl. Sci. Tech., **4**, 679 (2014).
(7) S. Hayashi, *et al*., Proc. of PLASMA2014, 19PB-066 (2014).
(8) M. Isobe *et al*., Plasma Fusion Res. **8**, 2402068 (2013).
(9) K. Morishima *et al*., Plasma Fusion Res. **8**, 2402164 (2013).
(10) K. Morishima *et al*., JINST **5**, P04011 (2010).
(11) M. S. Cheon *et al*., JINST **7**, C05009 (2012).

Simulation study of Alfvén eigenmodes in an LHD plasma

Y. Todo[1,2], D. A. Spong[3], Y. Suzuki[1,2], and N. Nakajima[1]

[1] National Institute for Fusion Science, Toki, Japan

[2] SOKENDAI (The Graduate University for Advanced Studies), Toki, Japan

[3] Oak Ridge National Laboratory, Oak Ridge, United States

E-mail: todo@nifs.ac.jp

Abstract. Alfvén eigenmodes destabilized by energetic particles in an LHD plasma are investigated using a magnetohydrodynamic hybrid simulation code MEGA. The most unstable toroidal mode number depends on the location of spatial gradient of the energetic particle pressure profile. The resonance condition between energetic particle and an Alfvén eigenmode is clarified with the analysis of the transit frequencies of resonant particles. It is found that the drive from trapped particles to the Alfvén eigenmode is strong.

1. Introduction

Energetic particle driven instabilities are one of the most important issues for burning plasmas because they lead to energetic alpha particle redistribution and losses. Energetic particle driven instabilities have been studied in LHD experiments [1]. In this work, we investigate Alfvén eigenmodes (AEs) destabilized by energetic particles and the resonance condition between the AE and energetic particles in an LHD plasma using a magnetohydrodynamic (MHD) hybrid simulation code MEGA [2]. The creation of hole and clump pairs in an energetic ion energy spectra associated with AEs was examined using the neutral particle analyzer (NPA) on the LHD shot #47645 [3]. We use the equilibrium data of this LHD plasma.

In the hybrid simulation model employed in the MEGA code, the bulk plasma is described by the full MHD equations and the energetic particles are simulated with particle-in-cell (PIC) method. The energetic particle effects on the MHD fluid are taken into account through the energetic particle current density included in the MHD momentum equation. The energetic particle dynamics is governed by the electromagnetic field given by the MHD equations.

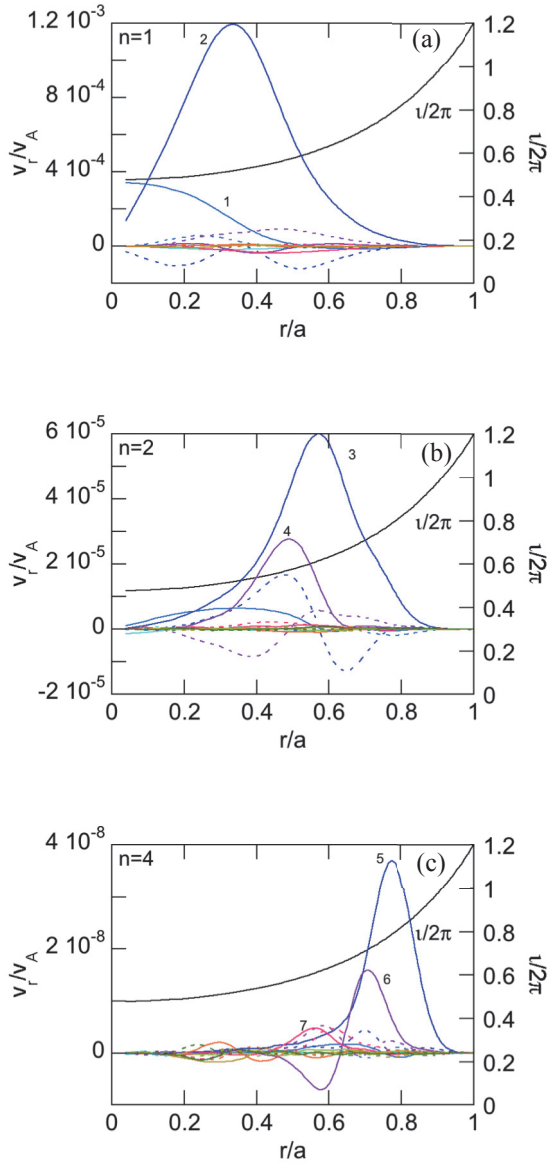

Fig. 1 Spatial profiles of the most unstable Alfvén eigenmode for (a) r_0/a=0.4, (b) 0.6, and (c) 0.8.

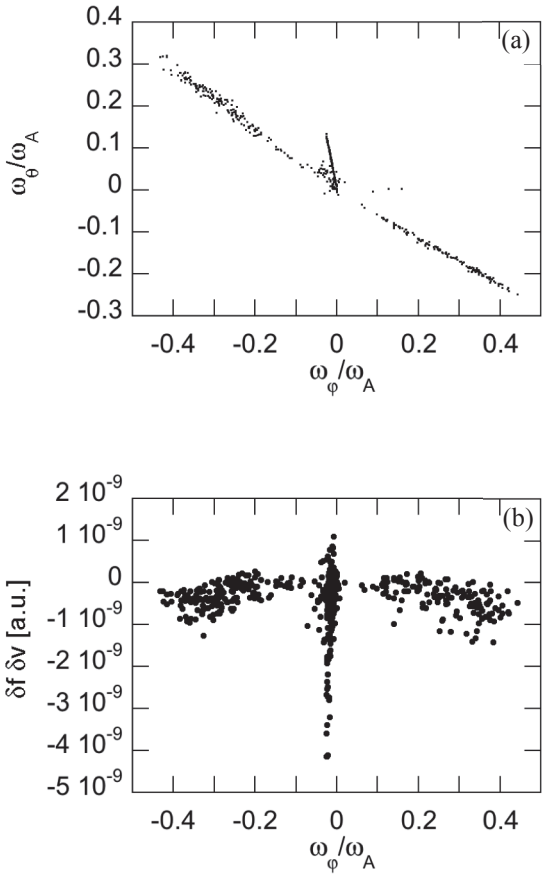

Fig. 2 Transit frequencies of resonant particles; (a). The horizontal and vertical axes are toroidal and poloidal transit frequencies, respectively. Energetic particle drive of the resonant particles; (b). Negative value in the vertical axis indicates the drive to the toroidal Alfvén eigenmode.

MEGA can simulate the energetic particle driven instabilities in LHD plasmas.

2. Simulation Results

2.1. Unstable Alfvén eigenmodes in an LHD plasma

We simulate Alfvén eigenmodes destabilized by energetic particles in the LHD discharge

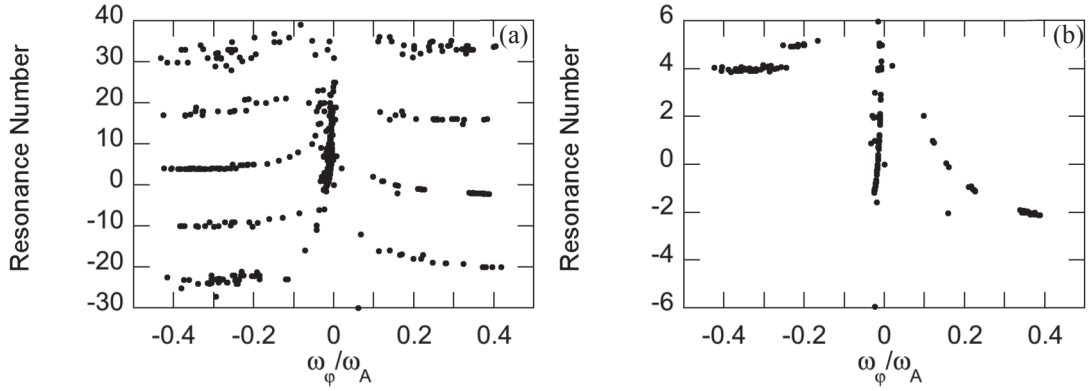

Fig. 3 Right-hand side of Eq. (3) versus toroidal transit frequency for the resonant particles. The branches for jv=-2, -1, 0, 1, 2 are plotted in panel (a). Panel (b) focuses on the branch for jv=0, which is similar to the resonance in tokamak plasmas.

#47645 [3]. We investigate the dependence on the initial energetic particle spatial profile. The initial energetic particle pressure profile is assumed

$$P_h = P_{h0}\frac{1}{2}\mathrm{erfc}\left[\frac{r-r_0}{\Delta r}\right], \tag{1}$$

to localize the spatial gradient with the scale length $\Delta r = 0.1a$. The velocity distribution of energetic particles is an isotropic slowing down distribution. The most unstable modes for *r/a=0.4, 0.6, 0.8* are shown in Fig. 1. We see the most unstable toroidal mode numbers are *n=1, 2, and 4*, respectively. The *n=1* mode for *r/a=0.4* is dominated by only one poloidal harmonic, which suggests the mode is a global Alfvén eigenmode (GAE). The peak location of this mode is different from the location of the rotational transform 2/3 (*q=1.5*) expected for a toroidal Alfvén eigenmode (TAE) with *n=1*. The *n=2* and *4* modes for *r/a=0.6* and *0.8* are located at the TAE gaps, and consist of two major poloidal harmonics, which indicate they are TAEs.

2.2. Resonance condition between energetic particle and TAE

We investigate toroidal and poloidal transit frequencies of the particles resonant with the *n=2* TAE shown in Fig. 1(b). The transit frequencies of the resonant particles are shown in Fig. 2(a). We see both the co-passing particles with positive toroidal transit frequency and the counter-passing particles with negative toroidal transit frequency are resonant with the TAE.

We also see the trapped particles with $\omega_\theta = -5\omega_\varphi$ are resonant. The toroidal transit frequency of trapped particles is small and negative. The energetic particle drive to the TAE is shown in Fig. 2(b). The negative value indicates the particle is driving the TAE. We see the drive from the trapped particles is strong.

A resonance condition proposed in Ref. [4] is given by

$$\omega - (n + jvN)\omega_\varphi - (m + j\mu)\omega_\theta = 0, \tag{2}$$

where *N=10* for the LHD plasmas, and j, ν, μ are arbitrary integers. Equation (2) is rewritten to

$$(m + j\mu) = \lfloor \omega - (n + jvN)\omega_\varphi \rfloor / \omega_\theta . \tag{3}$$

We plot in Fig. 3 the right-hand side of Eq. (3) for the resonant particles shown in Fig. 2. The branches for *jv=-2, -1, 0, 1, 2* are plotted in Fig. 3(a). It is demonstrated that the right-hand side of Eq. (3) takes integers for resonant particles. Figure 3(b) focuses on the branch for *jv=0*. We see the resonance for *jv=0* is similar to that in tokamak plasmas investigated in Ref. [2].

ACKNOWLEDGMENTS

Numerical computations were performed at the Plasma Simulator of National Institute for Fusion Science, and the Helios of the International Fusion Energy Center. This work was partly supported by the JSPS-NRF-NSFC A3 Foresight Program in the field of Plasma Physics (NSFC: No.11261140328, NRF: No. 2012K2A2A6000443).

References

[1] Toi K. *et al* 2011 *Plasma Phys. Control. Fusion* **53** 024008

[2] Todo Y. and Sato T. 1998 Phys. Plasmas **5** 1321

[3] Osakabe M. *et al* 2006 *Nucl. Fusion* **46** S911

[4] Kolesnichenko Ya. I. *et al* 2002 *Nucl. Fusion* **42** 949

Program of the 7th A3 Seminar

(May 19-22, 2015, Chuncheon, Korea)

18 May 2015 (Monday)

Welcome Reception: **18:30-20:00**

19 May (Tuesday)

Session 1 (Opening & Category I-1) Chair: S. Morita	08:50	**Yeong-Kook Oh** (NFRI)	**Announcement & Introduction**
	09:00	**Keeman Kim** (NFRI)	**Welcome address**
	09:10	**Hyeon K. Park** (UNIST)	**Welcome address**
	09:20	**Liqun Hu** (ASIPP)	Recent progress of the EAST Project
	09:45	**Yeong-Kook Oh** (NFRI)	Plan of KSTAR 2015 campaign
	10:05	**Liqun Hu** (ASIPP)	Chinese achievements in the A3 program
Coffee Break 10:30-10:50			
Session 2 (Category I-2) Chair: Y.K.Oh	10:50	**Bojiang Ding** (ASIPP)	Extended LHCD Capability towards Steady-State Plasma in EAST
	11:15	**Nong Xiang** (ASIPP)	Effects of Trapped Electrons on Lower Hybrid Wave Current Drive
	11:40	**Young-soon Bae** (NFRI)	Preliminary design study of Off-midplane LHCD for KSTAR
	12:05	**Xiaodong Zhang** (ASIPP)	ECRH Heating System on the EAST Machine
Group Photo & Lunch Break 12:30-13:40			
Session 3 (Category IIa-1) Chair: J.G. Bak	13:40	**Shigeru Morita** (NIFS)	Analysis of tungsten density in plasma core of LHD
	14:05	**Naoko Ashikawa** (NIFS)	Characterizations of surface contaminations on tungsten exposed to EAST plasma and progress of PWI studies
	14:30	**Bo Lyu** (ASIPP)	Observation of ICRF Effect on Toroidal Plasma Rotation on EAST
	16:55	**Jung-Hoon Son** (SNU)	Density limits in KSTAR
Coffee Break 15:15-15:35			
Session 4 (Category IIa-2) Chair: C. Dong	15:35	**Tetsutaro Oishi** (NIFS)	Observation of flow and ion temperature of carbon impurities in the ergodic layer of LHD
	16:00	**Haiqing Liu** (ASIPP)	First Results of Polarimeter-Interferometer System for Current Density Measurement on EAST
	16:25	**Ichihiro Yamada** (NIFS)	Current status and future application of the LHD Thomson scattering system
	16:50	**Jae-Sun Park** (KAIST)	Application of neural network technique to KSTAR plasma diagnostics
Discussion & Summary	17:10	Open discussion	
Dinner 18:00			

20 May (Wednesday)			
Session 5 (Category I-3) Chair: L. Hu	08:40	**Zhijiang Wang** (HUST)	Recent RMP Research on J-TEXT
	09:00	**Bingjia Xiao** (ASIPP)	Enhancement of EAST plasma control capabilities
	09:25	**Yong-Su Na** (SNU)	Exploration of Advanced Tokamak Operation in KSTAR
	09:50	**Hyun-Seok Kim** (SNU)	Real-time electron temperature profile control using NBI and EC in KSTAR
	10:15	**Jun-Gyo Bak** (NFRI)	Characteristics of halo current in KSTAR
Coffee Break 10:40– 10:55			
Session 6 (Category III) Chair: K. Toi	10:55	**Yi Liu** (SWIP)	Link between L-H transition and fishbone Mode in the neutral beam heated HL-2A plasmas
	11:20	**Jian Liu** (USTC)	Long-term simulation of runaway electrons in toroidal geometry
	11:45	**Jun-Young Kim** (NFRI/UST)	Effect of 3D field on energetic particles in KSTAR
	12:05	**Chunfeng Dong** (SWIP)	Observation of tungsten line emission with lower ionization state using EUV-II spectrometer on HL-2A
Lunch 12:30-13:30			
Session 7 (Category I-4) Chair: Y.K. Oh	13:30	**Mamoru Shoji** (NIFS)	Observation of plasma termination processes using stereoscopic fast framing cameras in the Large Helical Device
	13:55	**Yuan Huang** (SWIP)	Optimization of data acquisition for Thomson scattering diagnostic on HL-2A
	14:20	**Minho Woo** (NFRI)	Current status of Tearing Mode control in KSTAR
Coffee Break 14:45– 15:00			
Session 8 Discussions on A3 program Chair: Y.K.Oh S.Morita L.Q.Hu	15:00-17:00 Plenary meeting on future collaboration at each category for A3 Foresight Program on Critical Physics Issues Specific to Steady State Sustainment of High-Performance Plasmas **Category I:** Steady state sustainment of magnetic configurations (Current drive and profile control) **Category II:** Edge and divertor plasma control Category IIa: Transport of edge and divertor plasmas Category IIb: Stability of edge plasma		
Banquet dinner 18:00			

21 May (Thursday)			
Session 9 (Category IIb-1) Chair: B. Xiao	08:40	**Yongkyoon In** (NFRI)	Path to resolve the non-axisymmetry issues in tokamaks
	09:05	**Zhijiang Wang** (HUST)	The progress of onbuilding ECRH system on J-TEXT
	09:30	**Satoshi Ohdachi** (NIFS)	Effect of the RMP on the ELM-like activities observed in the high beta H-mode of LHD
	09:55	**Jayhyun Kim** (NFRI)	ELM suppression by mixed non-axisymmetric fields in KSTAR
Coffee Break 10:20 - 10:35			
Session 10 (Category IV) Chair: Y. Todo	10:35	**Gun-su Yun** (POSTECH)	Key features of nonlinear MHD dynamics measured by fast imaging diagnostics on KSTAR
	11:00	**June-Eok Leem** (POSTECH)	Upgrade of 2D Microwave Imaging Reflectometry in KSTAR
	11:20	**Akihiro Shimuzu** (NIFS)	2D potential measurement with heavy ion beam probe on the LHD
	11:45	**Taemin Jeon** (KAIST)	Current status of soft X-ray camera diagnostics on KSTAR
	12:05	**Biao Shen** (ASIPP)	The current state of EAST magnetic diagnostics
Lunch Break 12:30 - 13:40			
Session 11 (Category IIb-2) Chair: Y. In	13:40	**Kazuo Toi** (NIFS)	MHD stability of edge region of H-mode plasmas in LHD and comparison with the characteristics in tokamaks
	14:05	**YoungMu Jeon** (NFRI)	Physics insight of RMP-driven ELM-suppression in KSTAR
	14:30	**Hirohiko Tanaka** (NIFS)	Intermittent edge plasma transport in the Large Helical Device
	14:55	**Hyun-Sun Han** (NFRI)	New features of ELM-RMP experiments in KSTAR 2015
Coffee Break 15:20-15:35			
Session 12 (Category III+IV) Chair: S. Ohdachi	15:35	**Sadatsugu Muto** (NIFS)	Development of Silicon on Insulator type X-ray CMOS Sensor for LHD
	16:00	**Yoichiro Nakayama** (Nagoya Univ.)	Installation and commissioning of the neutron spectrometry system in KSTAR
	16:25	**Yasushi Todo** (NIFS)	Simulation study of Alfven eigenmodes in an LHD plasma
	16:50	**Jae-Min Kwon** (NFRI/WCI)	Gyrokinetic Simulation Study of Turbulence Spreading and its Control by External Flows
Discussion & Summary	17:15	Open discussion	
Dinner 18:00			

22 May (Friday)	
Session 13 Discussions on A3 collaboration Chair: Y.K.Oh S.Morita L.Q.Hu	08:30-12:00 Plenary meeting on future collaboration at each category for A3 Foresight Program on Critical Physics Issues Specific to Steady State Sustainment of High-Performance Plasmas **Category III:** Confinement of alpha particles (Interaction of energetic particle and bulk plasma) **Category IV:** Theory and simulation
Lunch Break 12:00 – 13:00	
Session 14 Discussions on A3 collaborations	13:00-17:00 Discussion on the next phase A3 program plan - Discussion on personnel exchange - Discussion on future study related to A3 collaboration - Discussions with young scientists and PHD students - Education of young scientists - Discussion on budget and administrative works - Discussion on annual report of A3 collaboration - Discussion on machine operation schedules - Discussions on next seminar and workshop plans
Closing & Adjourn	17:00 Closing